January 2010

Geochemical Conditions Affecting Uranium(VI) Fate And Transport In Soil And Groundwater In The Presence Of Phosphate

Abhas Singh
Washington University in St. Louis

WASHINGTON UNIVERSITY IN ST. LOUIS

School of Engineering and Applied Science

Department of Energy, Environmental & Chemical Engineering

Dissertation Examination Committee:
Daniel Giammar, Chair
William Buhro
Jeffrey Catalano
Cynthia Lo
Palghat Ramchandran
Jay Turner

GEOCHEMICAL CONDITIONS AFFECTING URANIUM FATE AND TRANSPORT IN SOIL AND GROUNDWATER IN THE PRESENCE OF PHOSPHATE

by

Abhas Singh

A dissertation presented to the
Graduate School of Arts and Sciences
of Washington University in
partial fulfillment of the
requirements for the degree
of Doctor of Philosophy

August 2010

Saint Louis, Missouri

ABSTRACT OF THE DISSERTATION

Geochemical Conditions Affecting Uranium Fate and Transport in Soil and Groundwater in the Presence of Phosphate

by

Abhas Singh

Doctor of Philosophy in Energy, Environmental & Chemical Engineering

Washington University in St. Louis, 2010

Research Advisor: Professor Daniel Giammar, Chair

Soil and groundwater contamination with actinides like uranium is a serious environmental concern. Phosphate addition to uranium-contaminated soil and groundwater can potentially provide long-term in-situ U(VI) immobilization by precipitation of low solubility U(VI)-phosphates. Reactions at the iron (oxy)hydroxide-water interface can control macroscopic transport and long-term stability of uranium.

First, the interactions among phosphate, U(VI), and goethite (α-FeOOH) were investigated in a year-long batch experimental study. Dissolved U(VI) and phosphate concentrations were interpreted within a reaction-based modeling framework. U(VI) uptake mechanism varied with the aqueous composition. For most initially supersaturated conditions, chernikovite, $H_3O(UO_2)(PO_4)\cdot 3H_2O_{(s)}$, nucleated homogeneously, but heterogeneous nucleation probably occurred in cases of mild supersaturation. For conditions undersaturated with respect to chernikovite, phosphate-

enhanced U(VI) adsorption indicated the formation of a U(VI)-phosphate-Fe(III) oxide ternary surface complex.

Second, molecular-scale structures of adsorbed and precipitated U(VI) from batch experiments were probed using X-ray absorption fine-structure (XAFS) spectroscopy for different total U(VI) concentrations over a pH range 4-7 in the absence and presence of phosphate. The structure of precipitated U(VI) fit the meta-autunite group structure. While U(VI) adsorbed as bidentate edge-sharing $\equiv Fe(OH)_2UO_2$ and bidentate corner-sharing $(\equiv FeOH)_2UO_2$ surface complexes in the absence of phosphate, it formed a ternary surface complex $(\equiv FeO)_2UO_2PO_4$ in the presence of phosphate.

Third, the effect of transport on U(VI) uptake and remobilization mechanisms and rate was examined. Continuous-flow stirred tank reactor (CFSTR) experiments at pH 4 were conducted under conditions supersaturated and undersaturated with respect to chernikovite and analyzed using a combination of measured dissolved concentrations, microscopy, and XAFS spectroscopy. The rates of dominant U(VI) and phosphate uptake and remobilization mechanisms in the absence and presence of goethite were quantified using a flow-through reactor model.

Finally, the effects of simultaneous Fe(III) uptake on iron (oxy)(hydr)oxides on U(VI) and phosphate uptake and remobilization were investigated at pH 4. Goethite-coated sand packed columns and goethite-containing CFSTRs were used to simulate environmental conditions favoring the growth of iron (oxy)(hydr)oxide. While the presence of co-influent Fe(III) increased the extent and rate of phosphate uptake its presence not only decreased U(VI) uptake on goethite but also limited the formation of stable phosphate-induced uranium surface species.

Acknowledgments

I take this opportunity to express my sincere gratitude to my advisor, Dr. Daniel Giammar, for providing me a wonderful learning opportunity during the past five years at Washington University and for being an excellent mentor. His positive attitude, unwavering support and encouragement have been a constant source of strength while completing this work. I also thank my dissertation committee including Dr. William Buhro, Dr. Jeffrey Catalano, Dr. Cynthia Lo, Dr. Palghat Ramchandran, and Dr. Jay Turner, for giving their valuable time and insightful suggestions in guiding me through the several stages of my research. In particular, I sincerely appreciate the time and help of Dr. Jeffrey Catalano while teaching me X-ray absorption fine-structure (XAFS) spectroscopy.

I sincerely acknowledge the National Science Foundation (Award No. CBET-0546219) for supporting my dissertation work and Washington University School of Engineering and Applied Science for providing me the ENVIRSAN fellowship during my first year of doctoral studies. I also recognize the Advanced Photon Source at the Argonne National Lab, Chicago for the XAFS experiments I performed there.

I truly acknowledge my colleague Dr. Kai-Uwe Ulrich for all his help and mentorship during the course of my Ph.D. Many thanks are due to all the past and present labmates who helped me during the course of my PhD, especially Wei Wan, Dr. Beizhan Yan, James Noel, Dr. Hui Zeng, Dr. Liyun Xie and Yanjiao Xie. I convey my sincere appreciation to the technical support at Washington University - Patty Wurm, Tyrone Daulton, Paul Carpenter, Lawrence Norcio, Jim Flynn and Joe Furlong and at the

Advance Photon Source – Nadia Leyarovska and Mahalingam Balasubramanian that was instrumental in the smooth completion of my work. I was fortunate to have shared my office with Shaohua Hu, Liyun Xie, Jeff Fornero and Yin Wang and I thank them for the camaraderie, stimulating discussions and help during my stay here.

I acknowledge Dr. Brian Wrenn for all his mentorship during the early stages of my Ph.D. and for impressing upon me the need to do good statistical analysis while interpreting data. I also pay my gratitude to all the professors who taught me courses at Washington University. The lectures were intellectually stimulating and have helped me in a better understanding of the subject. I thank Dr. Giammar for providing me the opportunity to teach some lectures while I was a Teaching Assistant for a couple of his courses. I am also grateful to Dr. Pratim Biswas and Dr. Young-Shin Jun for their mentorship and constant encouragement. Many thanks are due to all the departmental and university staff members who have directly or indirectly helped me in administrative work; in particular, Rose Baxter and Beth Mehringer.

Finally, and most importantly, I thank all my friends and family members whose unflinching support and understanding during the several stages of my Ph.D. made it happen. In particular, the sacrifices, support, and love of my parents and my wife, Anamika Rathore, provided me the utmost strength and motivation to stop not until the goal was achieved.

Abhas Singh

Washington University in St. Louis
August 2010

Dedicated to my late grandfather, Dr. Fateh Singh, whom I lost during the course of earning my Ph.D., but who was, and will always remain an inspiration to me.

Table of Contents

List of Figures

List of Tables

Chapter 1 Introduction and Overview

1.1. Introduction

1.1.1. Background

Widespread contamination of soil and groundwater with toxic heavy metals is a serious environmental concern due to their possible migration and contamination of drinking water sources and natural ecosystems. Natural uranium is radioactive and can be toxic to human health. The Safe Drinking Water Act has set the uranium drinking water standard at 30 ppb (μg/L) [1]. Sources of uranium contamination of soil and groundwater include the mining and refining of uranium ores and the waste disposal practices as part of nuclear weapons and energy programs [2, 3]. Furthermore, nuclear waste disposal and long-term storage remains a critical issue, and information is needed to predict the fate of uranium emplaced in long-term repositories. To put effective uranium containment strategies in place, an understanding of the geochemical conditions and immobilization mechanisms affecting uranium's long-term stability and transport is required.

1.1.2. Uranium geochemistry

Uranium (U) is predominantly found in the +VI and +IV oxidation states in the environment. U(VI) is generally more soluble and consequently more mobile than U(IV) [4]. Depending on the redox conditions and the pH of the environment, uranium can exist in different predominant forms as shown in Figure 1.1.

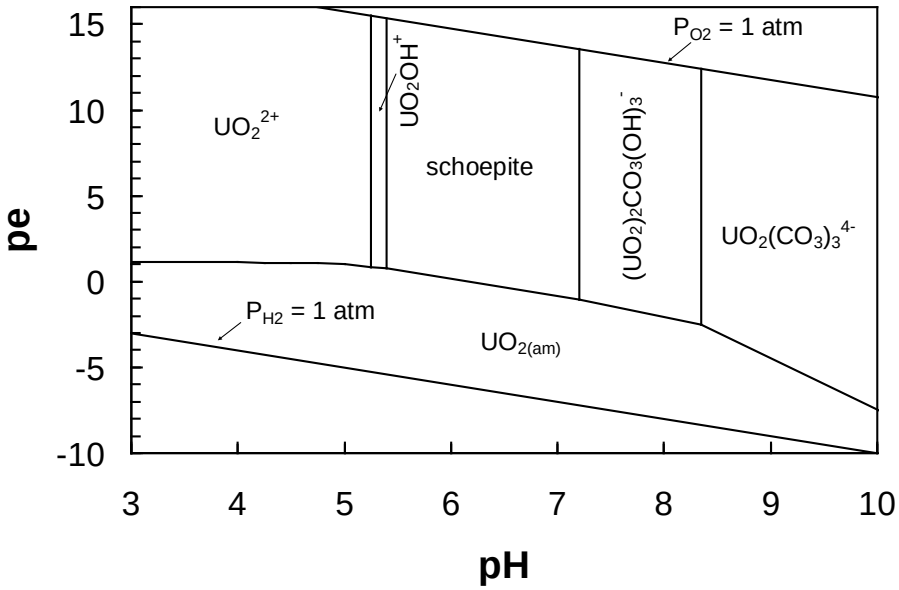

Figure 1.1. pe-pH diagram showing predominant uranium forms for TOTU = 5μM, $P_{CO2} = 10^{-3.5}$ atm, and ionic strength, I = 0.01 M.

Under oxic conditions, uranium is primarily present as the uranyl ion UO_2^{2+} and its associated hydroxyl complexes for low pH values. For sufficiently high total uranium concentrations at near-neutral pH, U(VI) can precipitate as schoepite [$UO_3 \cdot 2H_2O_{(s)}$]. In the presence of high phosphate concentrations, U(VI) can form uranyl phosphate solids that are less soluble than other U(VI) solids [5]. For undersaturated conditions, U(VI) can be solubilized by forming dissolved uranyl-phosphato complexes. U(VI) can readily adsorb to iron(III) oxyhydroxides such as ferrihydrite, goethite, and hematite and clay minerals [4]. Adsorption to iron-bearing minerals is favored by the high binding affinity of uranyl ion to geomedia [6-9]. Iron(III) oxyhydroxides like goethite are common minerals in soil and groundwater. They act as strong adsorbents for heavy-metals because of their reactive surfaces and high specific surface areas [10]. U(VI) adsorption to iron oxides typically increases from low to near neutral pH conditions. However, at higher pH values, in the presence of inorganic carbon, U(VI) forms stable dissolved complexes with carbonates that can limit U(VI) adsorption to iron oxyhydroxides and increase

the solubility of U(VI) precipitates [11]. At reducing conditions, uranium exists primarily as the mineral uraninite, $UO_{2(s)}$, which may be oxidized to more mobile U(VI) species when exposed to oxidizing conditions [11].

1.1.3. Uranium remediation strategies and use of phosphates

Due to the distributed nature of uranium contamination at many sites, remediation strategies often focus on in-situ immobilization. Treatment on site saves the costs otherwise associated with excavating sub-surface media. In-situ immobilization is also likely to promote the most stable solid associated forms of uranium.

Based on its geochemistry there are different potential approaches to immobilizing U(VI). It can be reduced to the relatively immobile U(IV) under reducing conditions by microbial activity [12] and by chemical reductants [13, 14]. When sustaining reducing conditions is not feasible, reduced U(IV) may remobilize by oxidizing to U(VI) species [15-18]; other in-situ remediation approaches are needed. Phosphate addition is a potential strategy for in-situ uranium immobilization for oxidizing conditions. The injection of phosphate-containing compounds may facilitate formation of uranyl phosphate solids [19, 20]; these solids have relatively low solubilities and are expected to form stable precipitates. This strategy could be particularly useful for sites at low pH when carbonate effects are not dominant and uranyl phosphates may precipitate out readily [11]. Because phosphate is not abundant in most soils and aquatic systems, a source of orthophosphate must be added to the subsurface. Orthophosphate can be obtained from minerals [11] or from organic compounds [21]. A recent study reported uranyl phosphate precipitation as a result of bacterial phosphatase activity; bacteria use an organophosphate compound for their metabolism and in-turn produce

orthophosphate that can combine with uranium [22]. Uranyl phosphate precipitates were also observed in an oxidizing bedrock aquifer resulting from interactions with iron oxyhydroxide [23]. Use of phosphates to treat uranium contaminated aquifers at the U.S. Department of Energy's (DOE) Hanford site has been pilot-tested [24].

One of the research areas related to phosphate-promoted in-situ remediation concerns the long-term stability of the immobilized uranium. If the immobilized uranium is unstable, it could eventually end up being a significant source of contamination for down gradient regions. Therefore, it is important to know the factors controlling the stability of immobilized uranium forms like uranyl phosphates. An understanding of the mechanisms of immobilization at the microscopic and molecular levels and their relation to macroscopic remobilization rates could prove helpful in addressing this concern.

1.1.4. Possible mechanisms of U(VI) immobilization

Reactions at the mineral-water interface can control the mobility of uranium in soil and groundwater. U(VI) may interact with mineral surfaces through adsorption, surface precipitation or co-precipitation. Whereas adsorption involves the association of dissolved U(VI) species with the mineral surface, surface precipitation is the precipitation of a pure U(VI)-containing phase on the surface of the substrate mineral (here, goethite). Unlike adsorbed species, surface precipitates have long-range order. Co-precipitation of U(VI) is its precipitation by either the formation of a solid solution with the substrate solid or by encapsulation of pure microcrystalline phases within the substrate matrix. Figure 1.2 shows the different mechanisms by which uranium mobility could be limited as well as the expected remobilization processes.

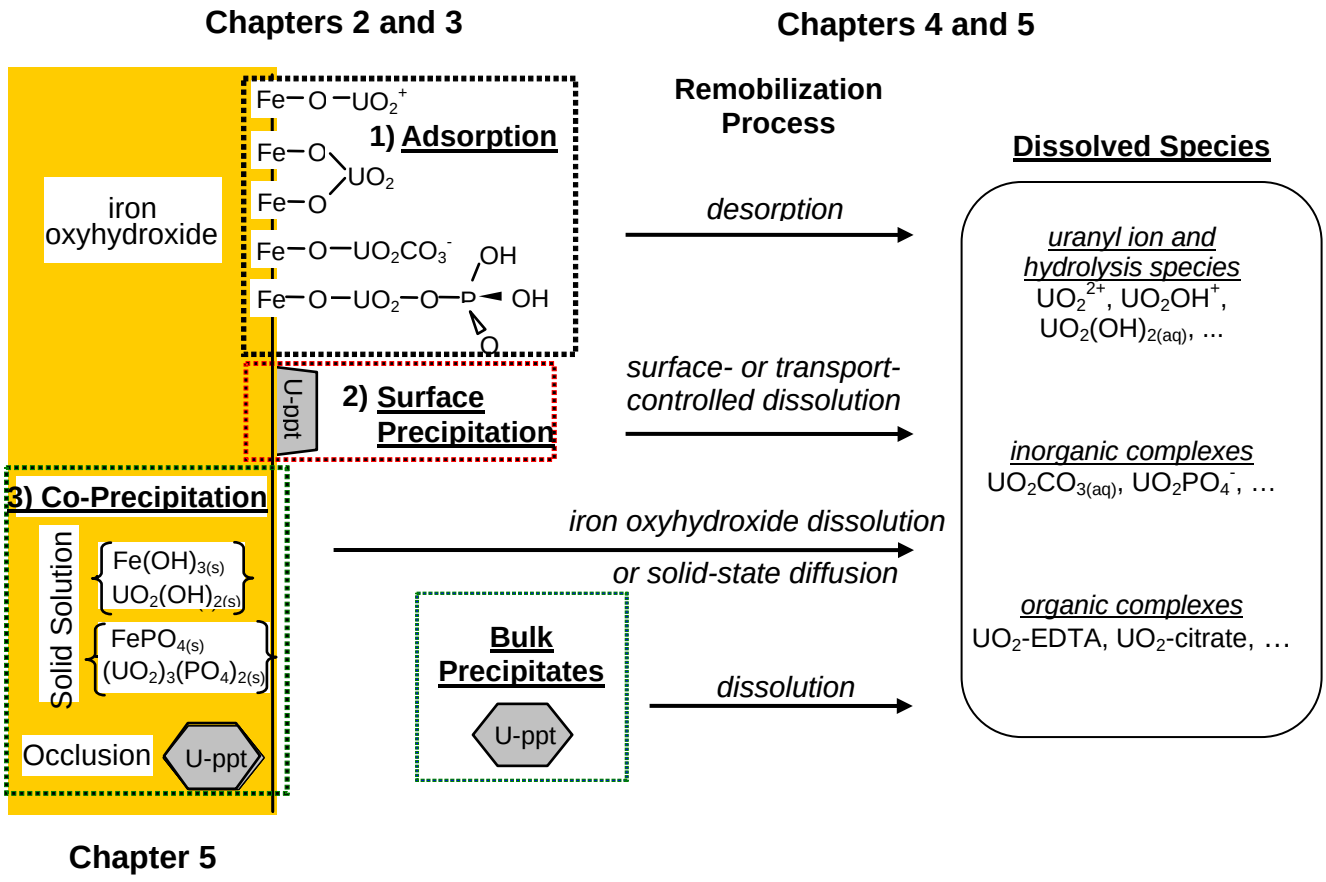

Figure 1.2. Immobilization mechanisms and remobilization processes. 1) Adsorption as monodentate, bidentate, and ternary surface complexes; 2) Precipitation of discrete phases at the surface, which may become occluded within the substrate; 3) Co-precipitation to form a solid solution or occluded phases; 4) Bulk precipitation due to homogeneous nucleation. Chemical and physical remobilization processes are determined by the immobilization mechanism.

U(VI) adsorption to Fe(III) oxides and oxyhydroxides has been studied extensively [7-9, 25, 26]. Some of the U(VI)-phosphates investigated and characterized include chernikovite [$H_3O(UO_2)(PO_4)\cdot 3H_2O_{(s)}$], uranyl orthophosphate [$(UO_2)_3(PO_4)_2\cdot 4H_2O_{(s)}$], autunite [$Ca(UO_2)_2(PO_4)_2\cdot 11H_2O_{(s)}$], and sodium meta-autunite [$Na_2(UO_2PO_4)_2\cdot xH_2O_{(s)}$] [4, 5]. A few studies have suggested that uranyl phosphate micro-precipitates nucleated on the surfaces of iron oxyhydroxides in geological settings [27, 28] and formed co-precipitates in an iron oxyhydroxide matrix [29].

The long-term stability and remobilization behavior of immobilized uranium depends on the actual mechanisms of immobilization. While desorption would govern remobilization of adsorbed uranium, the remobilization of precipitated uranium would be limited by either the solubility of the precipitated mineral (for bulk or surface precipitated uranium) or by the dissolution of the iron oxyhydroxide matrix (for coprecipitated or occluded uranium) (Figure 1.2). Although equilibrium modeling of U(VI) immobilization behavior in static systems can potentially be done by any of the three mechanisms of immobilization without providing information on the actual mechanisms [30-32], in the context of predicting reactive transport of contaminants in subsurface environments, reactive transport models should be able to account for the actual mechanism of immobilization.

1.2. Objectives of research

Immobilization mechanisms can significantly affect the transport and long-term stability of uranium in contaminated zones. Processes at the molecular scale may affect macroscopic transport. Although there have been studies to probe the immobilization mechanisms dominant in laboratory as well as field settings, very few of those have focused on relating them to uranium remobilization. This work attempted to bridge this gap by investigating the dominant mechanisms of uranium immobilization under different geochemical conditions and later relating them to uranium release rates.

The overall objectives of the research were 1) to quantify the effects of geochemical conditions and reaction time on phosphate-induced immobilization mechanisms of uranium at the iron (oxy)(hydr)oxide-water interface; 2) to identify the immobilization mechanisms of uranium at the molecular-scale in the absence and presence of phosphate, and as a function of

pH; 3) to quantify the rates of dominant U(VI) and phosphate uptake and remobilization mechanisms in the absence and presence of goethite; 4) to mimic environmental conditions favoring the growth of iron (oxy)(hydr)oxide and evaluate the effect of these conditions on uranium fate and transport.

1.3. Overview of dissertation

This dissertation contains four research themes addressing phosphate-amended uranium remediation of sediments and groundwater. The first two themes focus on identifying the dominant mechanisms of uranium uptake in the presence of phosphate and goethite and relating macroscopic observations with processes at the molecular-scale. The other two themes center on quantifying the kinetics of uranium and phosphate uptake and remobilization mechanisms by understanding the effects of transport and conditions favoring the growth of iron oxides on these mechanisms.

Chapter 2 focuses on identifying macroscopic uranium uptake mechanisms. The objective was to quantify the effects of geochemical conditions and reaction time on uranium immobilization mechanisms in the presence of goethite and phosphate. Particular emphasis was placed on distinguishing adsorption from precipitation pathways. The interactions among phosphate, U(VI), and goethite (α-FeOOH) were investigated in a year-long series of batch experiments at pH 4. Reaction time, total U(VI), total phosphate, and the presence and absence of goethite were systematically varied to determine their effects on the extent of U(VI) uptake and the dominant uranium immobilization mechanism. Dissolved U(VI) and phosphate concentrations were interpreted within a reaction-based modeling framework that included dissolution-precipitation reactions and a surface complexation model to account for adsorption.

The best available thermodynamic data and past surface complexation models were integrated to form an internally consistent framework. Additional evidence for the uptake mechanisms was obtained using scanning electron microscopy and X-ray diffraction.

Chapter 3 probes the coordination environment of uranium immobilized by adsorption and precipitation mechanisms discussed in Chapter 2. The objective of this study was to identify the immobilization mechanisms of uranium at the molecular-scale in the absence and presence of phosphate, and as a function of pH. XAFS (X-ray Absorption Fine Structure) spectroscopy was used to investigate the molecular structure of U(VI) immobilized with goethite and phosphate. In preparation for XAFS analysis, goethite suspensions were equilibrated with U(VI) in the presence and absence of phosphate over a pH range of 4-7, which is environmentally relevant but a range over which U(VI)-carbonate complexes are not significant. The EXAFS (Extended X-ray Absorption Fine Structure) analysis was used to distinguish between the chemical structures of precipitated and adsorbed uranium forms. A structural model for the adsorbed uranium surface complexes in the absence and presence of phosphate has been proposed.

Chapter 4 examines the effect of transport on U(VI) uptake and remobilization mechanisms and rates. The objectives were to quantify the rates of dominant U(VI) and phosphate uptake and remobilization mechanisms in the absence and presence of goethite. Continuous-flow stirred tank reactor (CFSTR) experiments were conducted under conditions that were supersaturated and undersaturated with respect to chernikovite. U(VI) adsorption was distinguished from U(VI) precipitation using a combination of macroscopic concentration data, microscopy, and XAFS spectroscopy. Rates for U(VI) adsorption-desorption and U(VI)-phosphate precipitation-dissolution mechanisms were calculated by modeling the flow-through reactor data.

Chapter 5 investigates the effect of continuous Fe(III) uptake on iron (oxy)(hydr)oxides on U(VI) uptake and remobilization in the absence and presence of phosphate. The objectives were to mimic environmental conditions favoring the growth of iron (oxy)(hydr)oxide and evaluate the effect of these conditions on uranium fate and transport. Uptake and remobilization experiments were conducted using goethite-coated sand columns and CFSTR configurations enabling different modes of contact of uranium, phosphate and Fe(III) that approximated the sequence associated with phosphate-based uranium immobilization strategies.

Chapter 6 provides a summary of the results from the four themes. Recommendations for future work are also included.

References

1. USEPA, National Primary Drinking Water Regulations; Radionuclides; Final Rule. In USEPA: 2000; Vol. 40 CFR Parts 9, 141 and 142, pp Fed. Regist. Vol. 65: 76707-76753.
2. Riley, R. G.; Zachara, J. M. *Chemical contaminants on DOE lands and selection of contaminant mixtures for subsurface science research*; DOE/ER-0547T; U.S. Dept. of Energy, Office of Energy Research: Washington, DC, 1992, 1992.
3. U.S.DOE, *Linking legacies: connecting Cold War nuclear weapons processes to their environmental consequences*. U.S. Department of Energy, Office of Environmental Management: 1997.
4. Finch, R.; Murakami, T., Systematics and Paragenesis of Uranium Minerals. In *Uranium: mineralogy, geochemistry and the environment*, Burns, P. C.; Finch, R., Eds. Mineralogical Society of America: Washington, DC, 1999; Vol. 38, pp 91-180.
5. Guillaumont, R.; Fanghänel, T.; Fuger, J.; Grenthe, I.; Neck, V.; Palmer, D. A.; Rand, M. H., *Update on the chemical thermodynamics of uranium, neptunium, plutonium, americium and technetium*. OECD Nuclear Energy Agency (ed.), Elsevier, Amsterdam: 2003.
6. Bostick, B. C.; Fendorf, S.; Barnett, M. O.; Jardine, P. M.; Brooks, S. C., Uranyl surface complexes formed on subsurface media from DOE facilities. *Soil Science Society of America Journal* **2002,** *66*, (1), 99-108.
7. Duff, M. C.; Amrhein, C., Uranium(VI) adsorption on goethite and soil in carbonate solutions. *Soil Science Society of America Journal* **1996,** *60*, 1393-1400.
8. Payne, T. E.; Davis, J. A.; Waite, T. D., Uranium adsorption on ferrihydrite - Effects of phosphate and humic acid. *Radiochimica Acta* **1996,** *74*, 239-243.
9. Wazne, M.; Korfiatis, G. P.; Meng, X. G., Carbonate effects on hexavalent uranium adsorption by iron oxyhydroxide. *Environmental Science & Technology* **2003,** *37*, (16), 3619-3624.
10. Schwertmann, U.; Cornell, R. M., *The Iron Oxides: Structure, Properties, Reactions, Occurrences and Uses*. Second ed.; Wiley-VCH: New York, NY, 2003.
11. Langmuir, D., *Aqueous environmental geochemistry*. Prentice-Hall, Inc.: Upper Saddle River, New Jersey, 1997.
12. Wu, W. M.; Carley, J.; Gentry, T.; Ginder-Vogel, M. A.; Fienen, M.; Mehlhorn, T.; Yan, H.; Caroll, S.; Pace, M. N.; Nyman, J.; Luo, J.; Gentile, M. E.; Fields, M. W.; Hickey, R. F.; Gu, B. H.; Watson, D.; Cirpka, O. A.; Zhou, J. Z.; Fendorf, S.; Kitanidis, P. K.; Jardine, P. M.; Criddle, C. S., Pilot-scale in situ bioremedation of uranium in a highly contaminated aquifer. 2. Reduction of U(VI) and geochemical control of U(VI) bioavailability. *Environmental Science & Technology* **2006,** *40*, (12), 3986-3995.
13. Gu, B.; Liang, L.; Dickey, M.; Yin, X.; Dais, S., Reductive precipitation of uranium (VI) by zero-valent iron. *Environ. Sci. Technol* **1998,** *32*, (21), 3366-3373.
14. Hua, B.; Xu, H.; Terry, J.; Deng, B., Kinetics of uranium (VI) reduction by hydrogen sulfide in anoxic aqueous systems. *Environ. Sci. Technol* **2006,** *40*, (15), 4666-4671.
15. Ginder-Vogel, M.; Criddle, C. S.; Fendorf, S., Thermodynamic constraints on the oxidation of biogenic UO_2 by Fe(III) (hydr)oxides. *Environmental Science & Technology* **2006,** *40*, (11), 3544-3550.
16. Gu, B. H.; Yan, H.; Zhou, P.; Watson, D. B.; Park, M.; Istok, J., Natural humics impact uranium bioreduction and oxidation. *Environmental Science & Technology* **2005,** *39*, (14), 5268-5275.

17. Zhong, L. R.; Liu, C. X.; Zachara, J. M.; Kennedy, D. W.; Szecsody, J. E.; Wood, B., Oxidative remobilization of biogenic uranium(IV) precipitates: Effects of iron(II) and pH. *Journal of Environmental Quality* **2005,** *34*, (5), 1763-1771.
18. Zhou, P.; Gu, B. H., Extraction of oxidized and reduced forms of uranium from contaminated soils: Effects of carbonate concentration and pH. *Environmental Science & Technology* **2005,** *39*, (12), 4435-4440.
19. Arey, J. S.; Seaman, J. C.; Bertsch, P., Immobilization of uranium in contaminated sediments by hydroxyapatite addition. *Environmental Science & Technology* **1999,** *33*, (2), 337-342.
20. Fuller, C. C.; Bargar, J. R.; Davis, J. A.; Piana, M. J., Mechanisms of uranium interactions with hydroxyapatite: Implications for groundwater remediation. *Environmental Science & Technology* **2002,** *36*, (2), 158-165.
21. Turner, B.; Paphazy, M.; Haygarth, P.; McKelvie, I., Inositol phosphates in the environment. *Philosophical Transactions B* **2002,** *357*, (1420), 449.
22. Beazley, M. J.; Martinez, R. J.; Sobecky, P. A.; Webb, S. M.; Taillefert, M., Uranium biomineralization as a result of bacterial phosphatase activity: Insights from bacterial isolates from a contaminated subsurface. *Environmental Science & Technology* **2007,** *41*, (16), 5701-5707.
23. Jerden, J. L.; Sinha, A. K., Phosphate based immobilization of uranium in an oxidizing bedrock aquifer. *Applied Geochemistry* **2003,** *18*, (6), 823-843.
24. Wellman, D.; Fruchter, J.; Vermeul, V. *Experimental Plan: Uranium Stabilization Through Polyphosphate Injection 300 Area Uranium Plume Treatability Demonstration Project*; PNNL-16101, Pacific Northwest National Laboratory (PNNL), Richland, WA (US): 2006.
25. Giammar, D. E.; Hering, J. G., Time scales for sorption-desorption and surface precipitation of uranyl on goethite. *Environmental Science & Technology* **2001,** *35*, (16), 3332-3337.
26. Hiemstra, T.; Van Riemsdijk, W. H.; Rossberg, A.; Ulrich, K. U., A surface structural model for ferrihydrite. II. Adsorption of uranyl and carbonate. *Geochemica et Cosmochimica Acta* **2009,** *73*, 4437-4451.
27. Murakami, T., Ohnuki, T., Isobe, H. and Sato, T., Mobility of uranium during weathering. *American Mineralogist* **1997,** *82*, 888-8999.
28. Murakami, T.; Sato, T.; Ohnuki, T.; Isobe, H., Field evidence for uranium nanocrystallization and its implications for uranium transport. *Chemical Geology* **2005,** *221*, (1-2), 117-126.
29. Duff, M. C.; Coughlin, J. U.; Hunter, D. B., Uranium co-precipitation with iron oxide minerals. *Geochimica et Cosmochimica Acta* **2002,** *66*, (20), 3533-3547.
30. Dzombak, D. A.; Morel, F. M. M., *Surface Complexation Modeling*. Wiley-Interscience: New York, 1990.
31. Farley, K. J.; Dzombak, D. A.; Morel, F. M. M., A Surface Precipitation Model for the Sorption of Cations on Metal Oxides. *Journal of Colloid and Interface Science* **1985,** *106*, (1), 226-242.
32. Sposito, G., Distinguishing Adsorption from Surface Precipitation. In *Geochemical Processes at Mineral Surfaces*, Davis, J. A.; Hayes, K. F., Eds. American Chemical Society: Washington, DC, 1986; Vol. 323, pp 217-228.

Chapter 2 Impact of phosphate on U(VI) immobilization in the presence of goethite

(Results of this chapter were submitted to *Geochimica et Cosmochimica Acta* in January 2010)

2.1. Introduction

Contamination of soil and groundwater with uranium is a serious environmental concern due to possible uranium migration and contamination of drinking water sources and ecosystems. Uranium contamination of soil and groundwater has resulted from inadvertent releases associated with mining, refining, and processing of uranium and from past waste disposal practices of nuclear weapons and energy programs [1, 2]. Due to the distributed nature of uranium contamination at many sites, remediation strategies often focus on in-situ immobilization to promote the most stable solid-associated forms of uranium. Treatment on site can avoid costs associated with excavating, treating, and transporting subsurface media. Design and implementation of effective uranium containment strategies requires an understanding of the geochemical conditions and immobilization mechanisms affecting the long-term stability and transport of uranium. Knowledge of long-term stability is also important to geological storage of spent nuclear fuel and radioactive waste.

The optimal approach to in-situ immobilization will depend on site-specific geochemistry. When reducing conditions are present or can be induced and sustained, the reduction of U(VI) to the less mobile oxidation state, U(IV), may be an effective immobilization strategy [3]. U(VI) reduction by microbial activity has been

demonstrated in sediments from contaminated field sites [4, 5]. Reduced U(IV), however, may be oxidized to U(VI) species when exposed to oxidizing conditions, resulting in remobilization of uranium [6-9]. Other in-situ remediation approaches are needed when sustaining reducing conditions is not feasible.

Under oxic conditions U is primarily present as the uranyl ion UO_2^{2+} and associated complexes with hydroxide and carbonate. With increasing total uranium, U(VI) can precipitate as schoepite [$UO_3 \cdot xH_2O_{(s)}$] with minimum solubility at near-neutral pH for most conditions. U(VI) forms soluble uranyl-phosphato complexes and can precipitate in uranyl phosphate solids if the phosphate and U(VI) concentrations are sufficiently high. Uranium phosphates are less soluble than schoepite, especially at low pH. The uranium phosphate solids that might form include uranium hydrogen phosphate [$UO_2HPO_4 \cdot 3H_2O_{(s)}$], chernikovite [$H_3O(UO_2)(PO_4) \bullet 3H_2O_{(s)}$], uranyl orthophosphate [$(UO_2)_3(PO_4)_2 \cdot 4H_2O_{(s)}$], autunite [$Ca(UO_2)_2(PO_4)_2 \cdot 11H_2O_{(s)}$], and sodium meta-autunite [$Na_2(UO_2PO_4)_2 \cdot xH_2O_{(s)}$] [10, 11].

The speciation and mobility of U(VI) in the subsurface are influenced by the presence of iron(III) oxyhydroxides and other minerals. Iron oxyhydroxides are strong adsorbents for heavy metals because of their reactive surfaces and high specific surface areas [12, 13]. Goethite is a common iron oxyhydroxide in soil and groundwater. Goethite and other iron oxyhydroxides have a high binding affinity for UO_2^{2+} [10, 14-16], and U(VI) adsorption to iron oxides retards transport [17]. However, at higher pH values and in the presence of inorganic carbon, the formation of stable U(VI)-carbonato complexes limits U(VI) adsorption to iron oxyhydroxides [18-21].

2.1.1. Phosphate addition for uranium remediation

Phosphate addition is a potential strategy for in-situ uranium immobilization. Uranium can adsorb to phosphate minerals like hydroxyapatite [$Ca_5(PO_4)_3(OH)_{(s)}$] at low uranium concentrations [22] and can precipitate as sparingly soluble uranyl phosphate solids at higher uranium concentrations [23]. Phosphate based immobilization can be particularly useful for sites with low pH, like a contaminated-site at Oak Ridge National Laboratory in Tennessee, United States [24]. In such cases, carbonate effects are less significant and adsorption to iron oxides is not sufficient to retard U transport, but uranyl phosphates can still precipitate [3]. One method of using phosphate for immobilization is in the form of hydroxyapatite that could either be mixed with soil [25] or filled in permeable reactive barriers [22, 26]. Injection of soluble forms of phosphate to treat uranium-contaminated aquifers is another approach to in-situ immobilization. Biologically-mediated release of orthophosphate from a soluble organophosphate compound resulted in precipitation of uranium as chernikovite [27, 28]. Uranium remediation by injecting soluble phosphates is being tested in field trials at the U.S. Department of Energy's (DOE) Hanford site [29-33]. Related bench-scale experiments revealed the likely precipitation of autunite minerals ($X_{3-n}^{(n)+}[(UO_2)(PO_4)]_2 \bullet xH_2O$) in sediments amended with phosphates. Recent experiments established the low solubility and slow kinetics of autunite dissolution [34, 35]. However, the addition of soluble phosphate forms to immobilize U has potential challenges. Soluble phosphates may have to be injected as polyphosphates since monophosphates can precipitate other cationic phosphate minerals (e.g. apatite and other calcium phosphates) and decrease the hydraulic conductivity of the sediments [36]. Low

solubility uranyl phosphates, like sodium meta-autunite, may also form stable colloids at neutral-alkaline conditions that can enhance U transport [37].

Evidence for the potential long-term stability of any U(VI)-phosphates precipitated as part of a remediation strategy is provided by their occurrence as the dominant U solid phases in several natural and contaminated environments. Natural U deposits containing barium uranyl phosphates at the Coles Hill site in south central Virginia were estimated to have been stable for the last 150,000 years [38]. Field investigations at the Koongarra uranium ore deposit in Australia revealed stable nanocrystals of uranium phosphates co-occurring with iron oxyhydroxides [39]. Contaminated soils at the Fernald Environmental Management Project (FEMP) in Ohio [40, 41] and at the Oak Ridge National Lab [42] contained autunite-like uranyl phosphate phases. A study of sediments beneath former process ponds at the Hanford site (Washington, U.S.A.) found that U primarily existed as meta-torbernite [$Cu(UO_2PO_4)_2 \cdot 8H_2O_{(s)}$] in the intermediate vadose zone [43].

Uranium immobilization with phosphate can be influenced by iron oxyhydroxides through mechanisms of adsorption, heterogeneous nucleation and possibly co-precipitation. Phosphates may enhance U(VI) adsorption to Fe(III) oxides by the formation of uranyl-phosphate-Fe(III) oxide ternary surface complexes [44, 45]. Investigations of U(VI) sorption to subsurface media from DOE waste sites revealed the presence of inner-sphere uranyl phosphate ternary surface complexes [46]. U(VI)-phosphate-Fe(III) oxide interactions may be preceded or accompanied by phosphate adsorption as inner-sphere complexes on the surface of iron oxyhydroxides; the extent of phosphate adsorption decreases with increasing pH [47, 48]. At Koongarra (Australia),

uranium uptake was considered to be initiated by adsorption onto ferrihydrite, and to subsequently be dominated by formation of U, P, and Mg or Cu-containing nanocrystals during transformation of ferrihydrite to goethite and hematite [49, 50]. Uranium co-precipitation with iron oxides was observed with incorporation of a uranate species (U^{6+}) in the hematite structure [51]. Under elevated U(VI) concentrations heterogeneous nucleation of uranium oxide hydrates may occur on iron oxyhydroxide surfaces. Dissolution rates of such U(VI) precipitates may ultimately control dissolved uranium concentrations [52]. While multiple mechanisms of U immobilization by reaction with iron oxyhydroxides and phosphate are possible, a systematic study of the effects of solution composition and reaction time on the dominant uranium immobilization mechanism is lacking.

The objective of the research presented here was to quantify the effects of geochemical conditions and reaction time on uranium immobilization mechanisms in the presence of goethite and phosphate. Particular emphasis was placed on distinguishing adsorption from precipitation pathways. Identifying the mechanisms and products of phosphate-induced immobilization can aid in designing remediation strategies and predicting uranium transport in subsurface environments.

2.2. Materials and methods

2.2.1. Materials

Goethite was synthesized using an established method [12]. Ferrihydrite was first precipitated by adding 180 mL of 5 M KOH to 100 mL of 1 M $Fe(NO_3)_3$ in a 2 L high density polyethylene (HDPE) bottle. The resulting black-brown precipitate was diluted

to 2 L using ultrapure (resistivity > 18.2 MΩ-cm) water, and the diluted suspension was heated at 70º C for 60 h to form an ochre-colored precipitate. Thereafter, it was cooled at room temperature and dialyzed thoroughly to remove excess dissolved ions. The synthesized iron oxyhydroxide was confirmed to be goethite from the X-ray diffraction (XRD) pattern of the freeze-dried powder. Scanning electron microscopy (SEM) revealed the characteristic needle shaped morphology of the particles. The N_2-BET adsorption measurement yielded a specific surface area of 39.9 m^2/g, which is consistent with that of goethite used in previous studies [48, 52]. Goethite was maintained in a 2.97 ± 0.28 g/L suspension prior to its use in reactors; the concentration of this stock suspension was determined gravimetrically.

A 1 M $UO_2(NO_3)_2$ solution was prepared in ultrapure water with small additions of concentrated HNO_3. Phosphate was added as $Na_2HPO_4 \cdot 7H_2O$. The chemicals used were all ACS grade or better. Trace metal grade HNO_3 and 1 M NaOH were used to adjust the pH of the reactors. The ionic strength was fixed at 0.01 M by addition of $NaNO_3$.

2.2.2. Analysis Methods

2.2.2.1. Dissolved phase analysis

Dissolved U, P and Fe were measured using inductively coupled plasma-mass spectrometry (ICP-MS, Agilent Technologies 7500ce). Thallium was used as an internal standard for U, while Y or Sc was used for Fe and P. Calibration standards were made from certified stock calibration standards (SPEX). All standards and samples were analyzed in a 1% HNO_3 matrix. A 7 to 10 point weighted calibration curve was used.

Check standards were run every 10 to 12 samples, and a full calibration was done every 20-25 samples or whenever the check standard was not within 5% of the expected value. The method detection limits for U and P were 0.005 ppb and 0.8 ppb, respectively. Sample pH was measured using a glass electrode and a pH meter (Accumet Research).

2.2.2.2. Solid phase analysis

Solids were characterized using XRD, SEM, and surface area analysis. XRD was performed on a Rigaku Geigerflex D-MAX/A diffractometer using Cu-K_α radiation at a power of 35 kV and 35 mA. The diffractometer uses a vertical goniometer and a thallium-doped sodium iodide scintillation counter. It has a fixed sample holder that accepts horizontal mounts of powders and dried materials contained on filter membranes. The diffractometer is controlled by PC-based Datascan software by Materials Data, Inc. (MDI). MDI's Jade software was used to analyze mineral diffraction data with reference to certified powder diffraction files (PDFs) contained in the International Centre for Diffraction Data (ICDD) PDF-4+ database [53]. A full set of PDF patterns for known uranyl phosphates was included. SEM was performed on a Hitachi model S-4500 field emission scanning electron microscope that has a NORAN Instruments energy dispersive X-ray spectroscopy (EDX) spot elemental analysis system, a backscatter detector and mechanical straining stage. When required, images were obtained after gold-coating of the sample. The specific surface area (m^2/g) of freeze-dried goethite was determined by multipoint BET N_2 adsorption with an Autosorb-1-C (Quantachrome, USA) instrument using a 9 mm cell. The solid was degassed overnight before nitrogen adsorption measurements were performed.

2.2.3. Equilibrium speciation calculations

Equilibrium speciation for dissolved and precipitated uranium and phosphate in the absence of goethite was predicted based on the latest available thermodynamic data. By using a modified form of an existing surface complexation model [45], adsorbed uranium and phosphate speciation was also predicted for conditions in the presence of goethite. Calculations were performed using MINEQL^{+} [54]. The dissolved species relevant for the U(VI)-phosphate-Fe(III)oxide system are UO_2^{2+} complexes with hydroxide, phosphate, carbonate and nitrate, and phosphate and carbonate acid-base forms. These species along with their reactions and formation constants (logK) are listed in Table A of the appendix. The dissolved species may form surface complexes with goethite and, as discussed later, they may precipitate as solids if the dissolved concentrations reach supersaturated conditions. Potentially relevant solids include meta-schoepite, chernikovite, sodium meta-autunite, and uranyl orthophosphate phases. These solids with their reactions and solubility products ($logK_{sp}$) are listed in Table B of the appendix.

2.2.3.1. Selection of thermodynamic data

Aqueous reactions and logK values listed in Table A are from the latest critically reviewed thermodynamic database for uranium [11]. The $logK_{sp}$ values of several of the relevant uranium-containing minerals were included from recent reviews of past solubility studies [55-57]. These reviews laid out criteria for inclusion of reliable $logK_{sp}$ or standard-state Gibbs free energy of formation data of these minerals: a) solid phase characterization before and after the experiment to ensure stability of the mineral phase

under study; b) attainment of equilibrium from both undersaturated and supersaturated states, and c) measurement of pH and all dissolved cations at equilibrium conditions. To ensure an internally consistent database for speciation calculations in this work, $\log K_{sp}$ values of solids from studies that were consistent with the criteria of Gorman-Lewis et al. [55] and which used the database of Guillaumont et al. [11] for their aqueous uranium and phosphate speciation calculations were included. The selection of the $\log K_{sp}$ values for relevant solids (Table B) is summarized below.

$\text{Log}K_{sp}$ for metaschoepite was included from recent measurements of solubility of uranyl oxide hydrate phases by Gorman-Lewis et al. [56]. This value (5.6) is significantly different from the one (4.81) selected by Grenthe et al. [58] and retained by Guillaumont et al. [11]. For chernikovite, $H_3O(UO_2)(PO_4)\cdot 3H_2O_{(s)}$, a $\log K_{sp}$ value of −24.2 was included from Grenthe et al. [58], as the Guillaumont et al. review did not make any corrections to it. A recent solubility and calorimetry study for uranyl hydrogen phosphate, $UO_2HPO_4\cdot 3H_2O_{(s)}$, a phase similar to chernikovite but with one less water of hydration, was also included [57]. The reported $\log K_{sp}$ value of −25.52 is about an order of magnitude lower than that for chernikovite. For sodium meta-autunite, $NaUO_2PO_4\cdot xH_2O_{(s)}$, the solubility product reported by Felmy et al. [59] confirmed the value reported by Grenthe et al. [58]. The present study includes the $\log K_{sp}$ (−49.36) for uranyl orthophosphate, $(UO_2)_3(PO_4)_2\cdot 4H_2O_{(s)}$, reported by Gorman-Lewis et al. [57] to preserve the consistency of the thermodynamic database. This value agrees well with that included in the Grenthe et al. database. A recent study determined the $\log K_{sp}$ to be −49.08 by performing experiments over a broader range of phosphate concentrations and pH values than previously studied [60]. However, the value was obtained by using a

different logK (11.01) of the $UO_2PO_4^-$ aqueous species than that included in the Guillaumont et al. (13.23) database. Since the determination of the $logK_{sp}$ will be dependent on the logK values included for the aqueous speciation reactions, both the $logK_{sp}$ as well as the logK suggested by Rai et al. were not included in the present study.

2.2.3.2. Surface complexation modeling

Equilibrium speciation in the presence of goethite was predicted using a modified version of a surface complexation model developed by Cheng et al. (2004). The model considers acid-base reactions on the goethite surface, three monodentate phosphate adsorption reactions, one bidentate uranyl adsorption reaction, and a ternary uranyl-phosphate-goethite surface complexation reaction. The surface complexation reactions and their equilibrium constants ($logK_{int}$) are listed in Table 2.1. Speciation calculations used these surface reactions together with the aqueous complexation and acid-base reactions and the precipitation reactions just discussed. Electrostatic interactions were calculated using the constant capacitance model with a specific capacitance of 1.28 F/m^2. This capacitance value was chosen to be consistent with the past surface complexation models integrated into the current modeling framework.

The original model was developed from an experimental study of uranium adsorption to goethite-coated sand in the presence of phosphate for lower total uranium (TOTU) ($\leq$ 5 μM) and similar total phosphate (TOTP) (50 – 200 μM) concentrations as compared to this work. The model included uranium and phosphate aqueous complexation reactions from Grenthe et al. [58] and surface acid-base and phosphate complexation reactions and equilibrium constants from previous studies [48, 61]. Cheng

et al. first estimated the goethite surface site density from their uranium-free phosphate adsorption data and then determined constants for uranyl surface complexes on goethite in the absence ($\equiv FeO_2UO_2$) and presence ($\equiv FePO_4UO_2$) of phosphate. Details of the surface complexation models developed by Cheng et al. [45], Nilsson et al [48], and Lövgren et al.[61], hereafter referred to as the Cheng, Nilsson and Lövgren models, respectively, can be found in Appendix 2-B. Cheng et al. considered their experimental conditions to be undersaturated with respect to the formation of any uranium-containing solids and consequently did not include any dissolution-precipitation reactions in their model optimization.

Table 2.1. Reactions included in the surface complexation model at 298 K and I = 0 M.

Model Parameters	
Site density, N_s (sites/ nm^2)	1.68
Specific surface area of goethite, A_s (m^2/g)	39.9
Reaction	**$LogK_{int}$**
$\equiv FeOH + H^+ = \equiv FeOH_2^+$	7.58
$\equiv FeOH = \equiv FeO^- + H^+$	-9.62
$\equiv FeOH + 3H^+ + PO_4^{3-} = \equiv FePO_4H_2 + H_2O$	32.27
$\equiv FeOH + 2H^+ + PO_4^{3-} = \equiv FePO_4H^- + H_2O$	26.83
$\equiv FeOH + H^+ + PO_4^{3-} = \equiv FePO_4^{2-} + H_2O$	19.64
$\equiv Fe(OH)_2 + UO_2^{2+} = \equiv FeO_2UO_2 + 2H^+$	-4.36
$\equiv FeOH + UO_2^{2+} + H^+ + PO_4^{3-} = \equiv FePO_4UO_2 + H_2O$	30.49

Modifications to the Cheng model were made to extend its applicability to a wider range of uranium and phosphate concentrations and to improve its integration of equilibrium constants from previous studies. The modifications were systematically

applied to the original Cheng model as indicated in Fig. 2.1. A detailed description of these modifications is available in Appendix 2-B. The original constant capacitance model was preserved and changes were only made to the surface site density and $\log K_{int}$ values based on the following considerations. First, precipitation of uranium and phosphate as well as adsorption to goethite was considered in the optimization of the model. The relevant uranium-containing solids and their $\log K_{sp}$ values were included from subsequent studies as previously discussed [56, 57, 59]. Second, logK values for aqueous uranium and phosphate complexes were updated using the latest thermodynamic review for uranium [11]. Third, using these updated thermodynamic data, new $\log K_{int}$ values were obtained by optimizing the model fit to the original adsorption data from Nilsson et al. and Cheng et al. Fourth, corrections were made whenever $\log K_{int}$ values derived from one experimental study were included in a model describing another experimental study. These corrections accounted for differences in specific surface areas (A_s) and surface site densities (N_s) of sorbents used in the two studies. These corrections are based on a method developed by Sverjensky [62], hereafter called the Sverjensky correction, that uses a different standard state for the activities of sorbent sites and surface species (unit activity on completely unsaturated and saturated surfaces, respectively) than the 1 M standard state used for dissolved species.

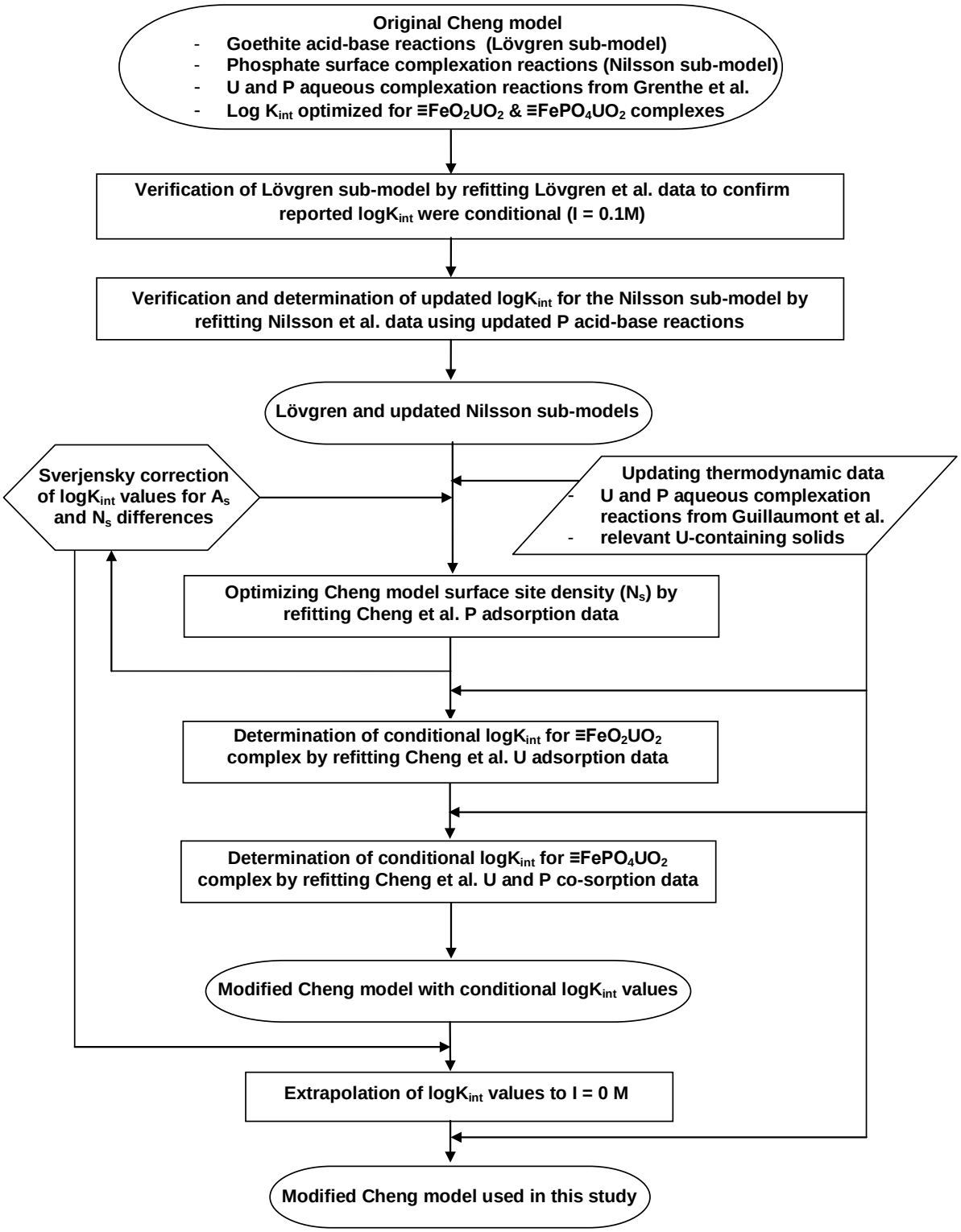

Fig. 2.1. Sequential modifications to the original Cheng model for U(VI) and phosphate adsorption to goethite.

Following from these definitions, equilibrium constants ($\log K^{\theta}$) that are dependent only on the choice of sorbent and independent of its physical characteristics are calculated. $\log K^{\theta}$ can be related to the commonly used $\log K_{int}$ (based on the 1 M standard state for surface species) for mononuclear surface complexation reactions (eq. 1):

$$K^{\theta} = K_{\text{int}}\left(\frac{N_s A_s}{N^* A^*}\right) \quad (1)$$

where, N^* and A^* are arbitrarily chosen values (10 sites/nm^2 and 10 m^2/g respectively) for a hypothetical standard surface, whose values do not affect the correction process. For performing speciation calculations using programs such as MINEQL$^+$, that are based on the commonly used 1 M standard state for surface species, $\log K_{int}$ values, as opposed to $\log K^{\theta}$, need to be entered. From eq. 1, the K_{int} values for the modified model ($K_{int,2}$) can be related to the K_{int} values of the original model ($K_{int,1}$) through eq. 2,

$$K_{\text{int},2} = K_{\text{int},1} \cdot \frac{N_{s,1} A_{s,1}}{N_{s,2} A_{s,2}} \quad (2)$$

where $N_{s,1}$ and $N_{s,2}$ are the site densities and $A_{s,1}$ and $A_{s,2}$ the specific surface areas of the sorbents used in the two studies.

Application of the revised model The $\log K_{int}$ values obtained after modifications to the model by Cheng et al. were adjusted by the Sverjensky correction before being applied to the present work. Conditional $\log K_{int}$ values (I = 0.1 M) were extrapolated to the true $\log K_{int}$ values (I = 0 M) using the Davies equation (Table 2.1). All formation constants for dissolved, adsorbed and precipitated species were entered in MINEQL$^+$ at I = 0 M. The software adjusts the activity coefficients of these species for the individual ionic

strength using the Davies equation. Using the assumed site density (1.68 sites/nm^2), and measured specific surface area (39.9 m^2/g) and concentration of goethite in each reactor (0.59 ± 0.05 g/L), the total molar concentration of surface sites was estimated to be 65.7 ± 5.6 μM. This estimate was used as an input to surface complexation modeling calculations. The system was considered to be in equilibrium with the atmospheric pCO_2 of $10^{-3.5}$ atm.

2.2.4. Batch Experiments

Batch experiments were performed at room temperature (20 ± 2ºC) to study the effect of TOTP, TOTU, presence and absence of goethite, and reaction time on U(VI) immobilization mechanisms at pH 4 (Table 2.2). The value of pH 4 was chosen for several reasons: (1) some uranium-contaminated sites have low pH because of acidic uranium waste disposal [24, 46, 63]; (2) carbonate effects are minimized at low pH; (3) previous work suggested that increased uranium uptake in the presence of phosphate at pH 4 was via formation of a $\equiv FePO_4UO_2$ ternary surface complex [44, 45] and investigating this hypothesis was one of the goals of the present study. Five TOTU levels were combined with two TOTP levels and studied both in the presence and absence of goethite. The TOTP concentrations were within the range used by other workers and are relevant for phosphate injection-based remediation strategies [44, 45], although they are higher than most groundwater concentrations, which are typically less than 10 μM [3]. Control experiments having either no phosphate or no uranium in the presence and absence of goethite were also performed. In addition to providing information on adsorption of one adsorbate at a time, these controls were also used to account for

possible sorption to reactor walls. In total 120 experimental and 84 control conditions were studied. To account for the variability within a condition, triplicate and duplicate runs were carried out for the test reactors and the controls, respectively. Replicates also provided material for solid phase characterization. For studying the effect of reaction time on uranium immobilization, the same reactors were sampled at different times.

Required volumes of uranium and phosphate stock solutions with known concentrations were added simultaneously to 125 mL HDPE bottles. The bottles previously contained $NaNO_3$ solution at pH 4 either with or without 0.59 g/L goethite. The reactors were set up such that the total solution or suspension volume was fixed at 100 mL and the ionic strength at 0.01 M. All reactors were continuously shaken at 100 rpm on a rotatory shaker at room temperature in the dark except during sampling. For each sample, 10 mL of reactor suspension were filtered through a 0.2 µm polycarbonate filter. The filtrate was acidified using 100 µL of concentrated HNO_3 and analyzed for aqueous concentrations of U and P using ICP-MS. The pH of the first of the replicate reactors for each condition was measured. The solid-loaded filter membranes were dried at 40ºC and stored prior to SEM and XRD characterization of the solids.

Table 2.2. Levels of different variables for batch experiments performed at pH 4

<table>
<tr><th>Levels of TOTU (µM)</th><th>Levels of TOTP (µM)</th><th>Goethite (g/L)</th><th>Time</th></tr>
<tr><td rowspan="5">a) 1
b) 5
c) 10
d) 50
e) 100</td><td rowspan="2">1) 15
2) 130</td><td>0.59</td><td rowspan="6">1 day
8 days
1 month
3 months
6 months
1 year</td></tr>
<tr><td>0</td></tr>
<tr><td rowspan="2">0</td><td>0.59</td></tr>
<tr><td>0</td></tr>
<tr><td rowspan="2">0</td><td rowspan="2">1) 15
2) 130</td><td>0.59</td></tr>
<tr><td>0</td></tr>
</table>

An additional batch experiment was performed to generate sufficient U(VI)-phosphate precipitate for a more thorough XRD characterization and to gain information on precipitation kinetics. A 900 mL volume at pH 4 with 100 µM TOTU and 105 µM TOTP, which was similar to the highest TOTP in the other experiments, was prepared and completely mixed. Solids were collected on a polycarbonate filter after 3 min, 13 h, and 37 h of reaction time. To overcome the effect of preferred orientation on filter membranes, solids at the end of 37 h were also collected without using a filter membrane and freeze-dried. All solids were analyzed using XRD.

2.3. Results and discussion

2.3.1. Predicted equilibrium speciation of uranium and phosphate

Predicted equilibrium speciation based on the current understanding of the geochemistry of the system serves as a benchmark for experimental observations at pH 4. Total dissolved, precipitated, and adsorbed uranium and phosphate concentrations and dominant species at equilibrium for a range of pH conditions were calculated for all TOTU and TOTP combinations studied in the batch experiments. Results of calculations for the condition with TOTU = 100 µM and TOTP = 130 µM in the absence and presence of 0.59 g/L goethite are shown in Fig. 2.2. This condition represents the highest TOTU and TOTP concentrations studied. In the presence of goethite, as discussed in section 2.3.2, the total molar concentration of surface sites was estimated to be 65.7 ± 5.6 µM.

The total dissolved uranium (U_{diss}) concentrations predicted in the presence of goethite (Fig. 2.2b) are similar to those in its absence (Fig. 2.2a) for all pH conditions. The corresponding total dissolved phosphate (P_{diss}) concentrations are slightly higher

without goethite (Figs. 2.2d and 2.2c). Different uptake mechanisms dominate in the presence and absence of goethite. For goethite-free conditions, precipitation of uranium phosphates lowers the U_{diss} and P_{diss} concentrations across the pH range 2.5 – 8.7. In the presence of goethite, U(VI) and phosphate uptake occurs by both precipitation and adsorption onto goethite.

Different aqueous species are dominant in the absence and presence of goethite (Fig. 2.2). For goethite-free conditions, UO_2^{2+}, $H_2PO_4^-$, and uranyl-phosphato dissolved complexes are dominant below pH 7; above pH 7, uranyl-carbonato complexes and HPO_4^{2-} gain predominance. In the presence of goethite, however, uranyl-phosphato complexes are not significant as most phosphate is adsorbed onto goethite.

Surface complexation modeling predicts that the dominant form of adsorbed uranium and phosphate between pH ~3.4 – 5.7 is the ternary surface complex ($\equiv FePO_4UO_2$), which continues to be a significant species until pH 8.6 (Fig. 2.2b). U(VI) adsorption in the form of the bidentate mono-nuclear surface complex ($\equiv FeO_2UO_2$) is not significant across the pH range. Significant phosphate adsorption also occurs as $\equiv FePO_4H_2$ ($pH \leq 3.3$) and $\equiv FePO_4^{2-}$ ($pH \geq 8.6$), as shown in Fig. 2.2d.

Predicted precipitation of U(VI)-phosphates varies with the presence or absence of goethite as well as the pH. In the absence of goethite, uranium hydrogen phosphate [$UO_2HPO_4 \cdot 3H_2O_{(s)}$] and uranyl orthophosphate [$(UO_2)_3(PO_4)_2 \cdot 4H_2O_{(s)}$] are expected to form at low pH (2.5 – 3.4 and 3.3 – 4.3, respectively); for higher pH (4.2 – 8.7), sodium meta-autunite [$Na_2(UO_2PO_4)_2 \cdot xH_2O_{(s)}$] will be the dominant phase (Fig. 2.2a). In the presence of goethite, these three solid phases are still expected to form, but over a slightly

narrower pH range (2.7 – 8.6) and in lower amounts due to significant adsorption of U(VI) and phosphate (Fig. 2.2b).

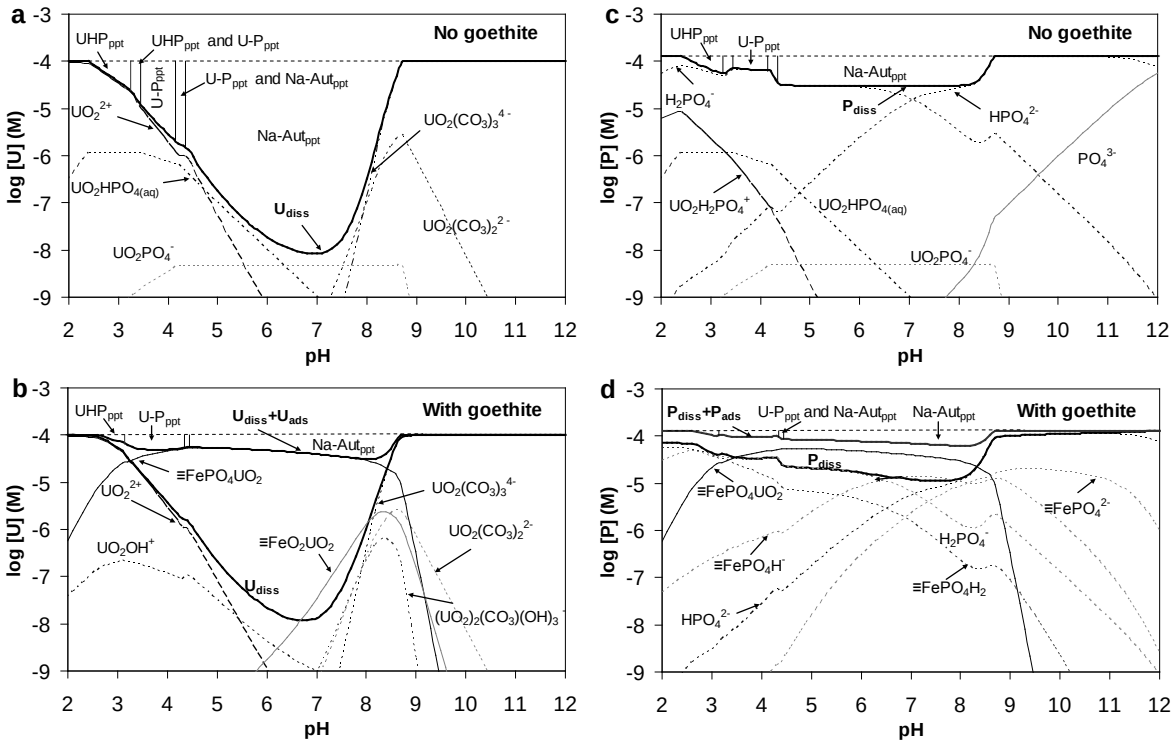

Fig. 2.2. Predicted dissolved concentrations of uranium and phosphate in an open system with TOTU = 100 µM, TOTP = 130 µM, and TOTNa = 0.01 M in the absence (a, c) and presence (b, d) of 0.59 g/L goethite; the ranges for predicted solids and predominant dissolved and adsorbed species are shown. UHP$_{ppt}$, U-P$_{ppt}$, and Na-Aut$_{ppt}$ refer to uranium hydrogen phosphate [$UO_2HPO_4 \cdot 3H_2O_{(s)}$], uranyl orthophosphate [$(UO_2)_3(PO_4)_2 \cdot 4H_2O_{(s)}$], and sodium meta-autunite [$Na_2(UO_2PO_4)_2 \cdot xH_2O_{(s)}$], respectively.

The dominant solid-associated forms at pH 4 depend on the TOTU and TOTP concentrations relative to the goethite present in the system. For high TOTP (130 µM), adsorption of uranium as the ternary surface complex, ≡$FePO_4UO_2$, is expected to be the dominant immobilized U(VI) form (> 85 %) at low to intermediate TOTU (< 50 µM) conditions (Fig. 2.3a). Sorption of phosphate onto goethite will occur predominantly as ≡$FePO_4H_2$ and, to a lesser extent, by the ternary surface complex. Significant phosphate

adsorption is expected to saturate the surface (~66 µM) and remain invariant (at ~47% TOTP) with increasing TOTU concentrations. Formation of the uranyl orthophosphate precipitate becomes increasingly favorable with increasing TOTU until at ~100 µM TOTU, precipitated U(VI) is expected to be comparable to adsorbed U(VI).

For low TOTP (15 µM), U(VI) and phosphate are not expected to form any precipitates for any of the TOTU concentrations studied (Fig. 2.3b). Almost complete adsorption of phosphate is expected. Adsorbed phosphate will be present as the monodentate surface complex $\equiv FePO_4H^-$ for low TOTU concentrations ($\leq$ 10 µM) and as the ternary surface complex at higher TOTU concentrations. In contrast, the dominant form of U(VI) at low TOTU concentrations will be the ternary surface complex. With increasing TOTU concentrations, the formation of the ternary surface complex will be limited by the availability of phosphate. U_{diss} concentrations will then increase because the binary surface complex is not predicted to form to an appreciable extent.

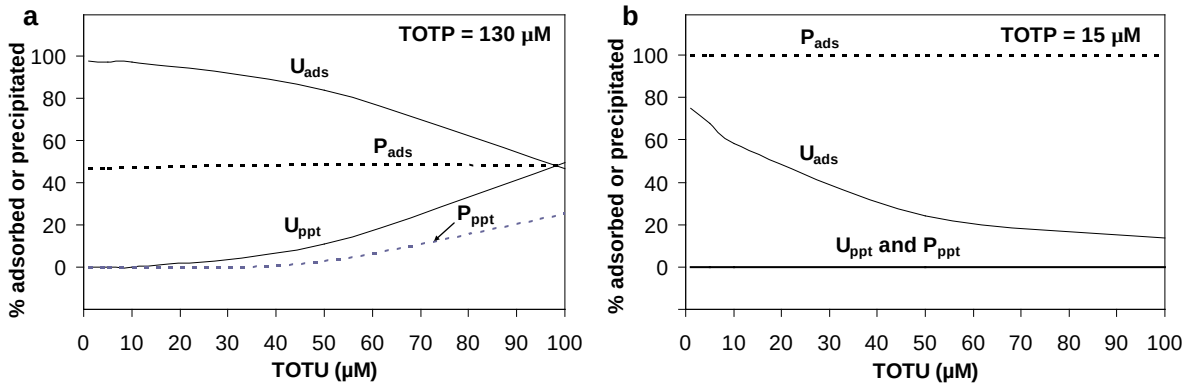

Fig. 2.3. Predicted total adsorbed and precipitated uranium and phosphate at pH 4 with (a) 130 µM TOTP and (b) 15 µM TOTP in the presence of 0.59 g/L goethite; subscripts $_{ppt}$ and $_{ads}$ refer to precipitated and adsorbed forms, respectively. The ternary surface complex ($\equiv FePO_4UO_2$) and uranyl orthophosphate [$(UO_2)_3(PO_4)_2 \cdot 4H_2O_{(s)}$] are the dominant solid associated forms of uranium.

2.3.2. Precipitation in the absence of goethite

Experimental evidence for precipitation was obtained from measurements of the U_{diss} and P_{diss} concentrations at different reaction times in the absence of goethite (Figs. 2.4 and 2.5, respectively). These figures also show data collected in the presence of goethite, which will be discussed in the next section. The differences between dissolved and total U(VI) and phosphate were caused by uranium phosphate precipitation for most goethite-free conditions. For a small number of conditions (all TOTP with 1 μM TOTU (Fig. 2.4a) and low TOTP (≤ 15 μM) with 5 μM TOTU (Fig. 2.4b)), the difference between the total and dissolved concentrations was probably caused by adsorption to the reactor walls. Sorption to reactor walls was < 10% for the 10 μM TOTU and was insignificant for higher TOTU (≥ 50 μM) concentrations.

Uranium phosphate precipitation rates depended on the TOTU and TOTP concentrations. For the low TOTP level (15 μM) and 10 μM TOTU, the formation of a uranium-containing precipitate lowered U_{diss} (Fig. 2.4c) and P_{diss} (Fig. 2.5a) concentrations only after a month; for the two highest TOTU concentrations (50 and 100 μM), the rate of precipitation of uranium phosphates was faster with increasing TOTU (between 1 to 8 days for 50 μM TOTU and < 1 day for 100 μM TOTU). For the high TOTP level (130 μM), precipitation of a uranium phosphate was rapid and significant; U(VI) uptake was ≥ 90% for 5 – 100 μM TOTU conditions within 1 day (Fig. 2.4). The measured P_{diss} concentrations after 1 day decreased with increasing TOTU as conditions became progressively more favorable for the formation of uranium phosphates (Fig. 2.5b).

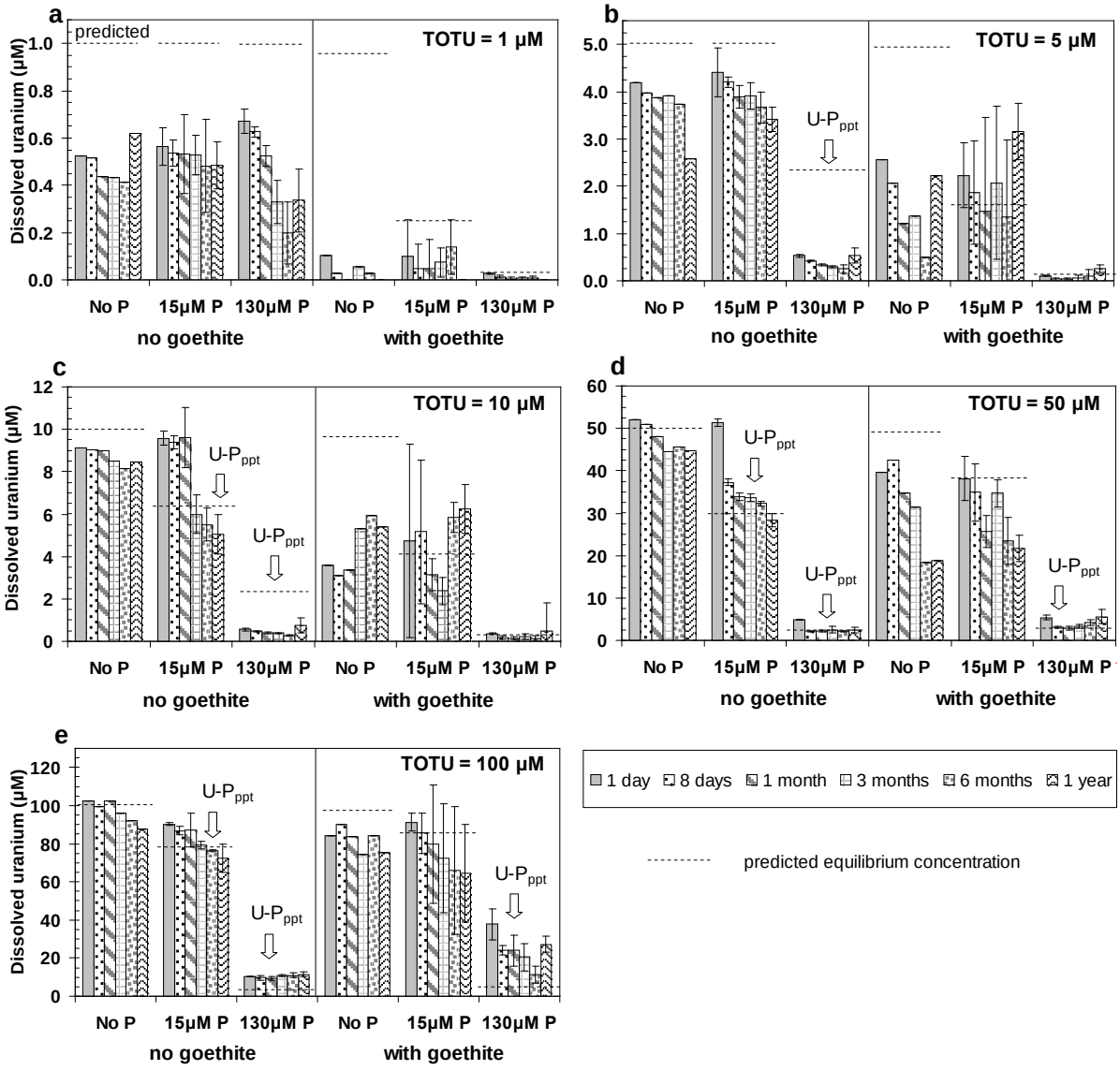

Fig. 2.4. Dissolved uranium concentrations for increasing phosphate levels for five different TOTU conditions in the absence and presence of goethite. U-P_{ppt} refers to uranyl orthophosphate, $(UO_2)_3(PO_4)_2 \cdot 4H_2O$, when predicted to form at given conditions. Vertical bars correspond to mean concentrations of triplicate reactors measured at different times and error bars represent 95% confidence intervals of the means. Error bars are not shown for duplicate control reactors; concentrations in duplicates were generally within 30% of each other. Note the different scales on the ordinate.

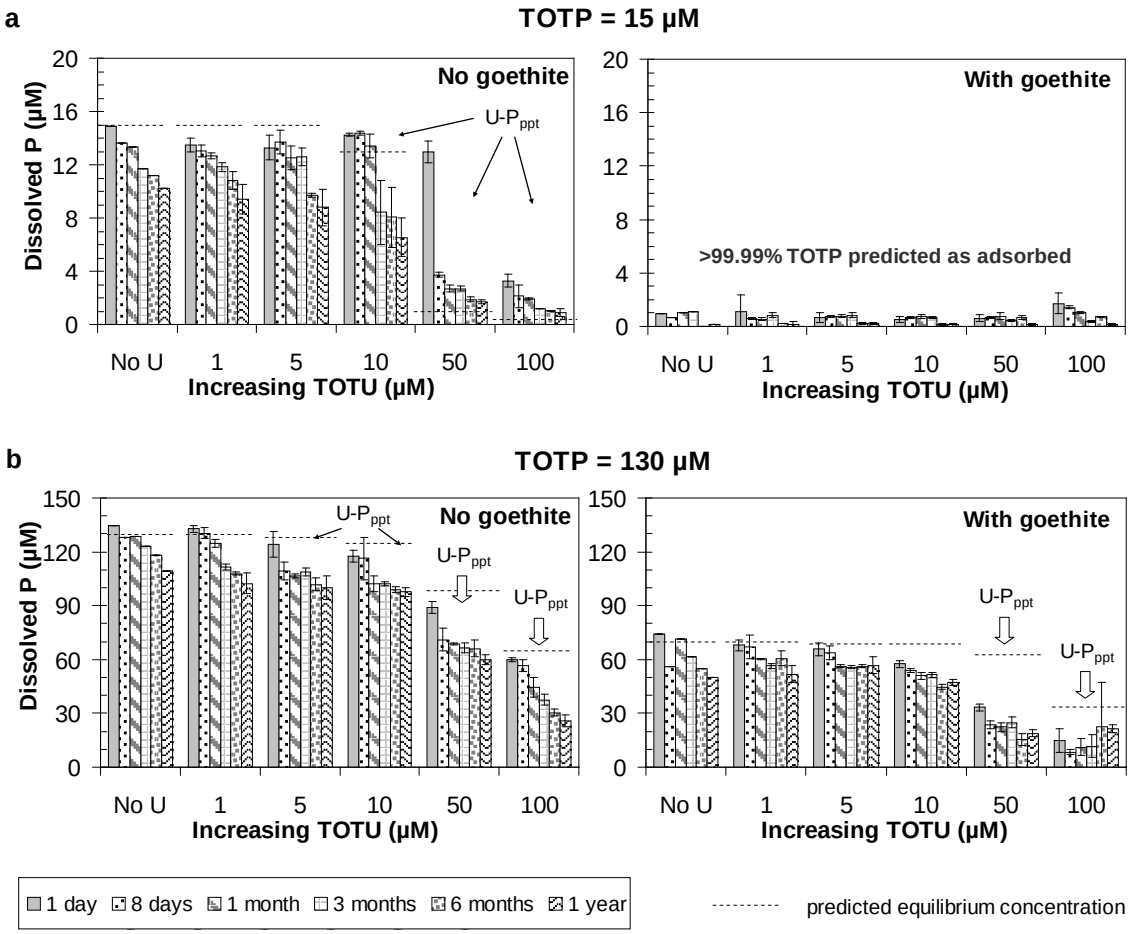

Fig. 2.5. Dissolved phosphate concentrations for increasing total uranium for two total phosphate levels: a) 15 µM and b) 130 µM. U-P_{ppt} refers to predicted formation of uranyl orthophosphate, $(UO_2)_3(PO_4)_2 \cdot 4H_2O$. Vertical bars correspond to mean concentrations of triplicate reactors measured at different times and error bars represent 95% confidence intervals of the means. Error bars are not shown for duplicate control reactors; concentrations in duplicates were generally within 30% of each other. Note the different scales on the ordinate.

Direct evidence for uranium phosphate precipitation in the absence of goethite was obtained from SEM images of solids retained on the filter membranes after sampling (Figs. 2.6a-c). The morphology of particles varied with the phosphate concentration. Particles from the low TOTP conditions were smaller (~2-3 µm) and irregular in shape (Fig. 2.6b) as compared to the particles from high TOTP conditions that were larger (~7-

8 µm) and exhibited crystal twinning (Fig. 2.6c). While the identity of the solids formed at the low TOTP condition could not be determined due to insufficient mass, particles for the high TOTP conditions resemble synthetic chernikovite [$H_3O(UO_2)(PO_4)\bullet 3H_2O_{(s)}$] crystals [64, 65]. EDX analysis confirmed the presence of U and P. Sodium was not detected, which ruled out the formation of sodium meta-autunite [$Na_2(UO_2PO_4)_2 \cdot xH_2O_{(s)}$]. However, the precipitated phase could also be uranyl orthophosphate [$(UO_2)_3(PO_4)_2 \cdot 4H_2O_{(s)}$], which was predicted to form under these conditions.

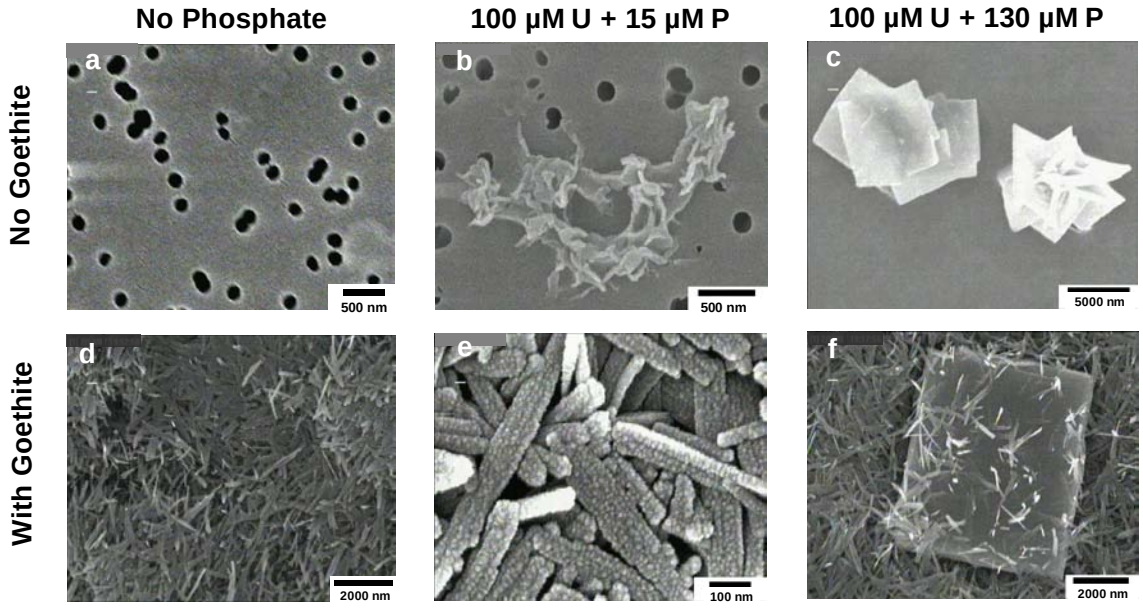

Fig. 2.6. Electron micrographs of solid residues collected on 0.2 µm filter membranes for 100 µM total uranium and total phosphate conditions of 0, 15, and 130 µM after 1 day of reaction. Images on the left are of a filter membrane ('No Phosphate' 'No Goethite') and of goethite on a filter ('No Phosphate' 'With Goethite') respectively. Note the different scales of the images.

To identify the mineral phases under different conditions, solids collected on filter membranes were also analyzed by XRD. However, the loss of several reflections from

the diffraction patterns due to preferred orientation of solids on the filter membranes rendered identification inconclusive. Solids from a separate batch experiment with a larger volume were used to generate randomly oriented particles and to study precipitation kinetics. Time-dependent XRD patterns are shown in Fig. 2.7. The diffraction pattern of the material not collected on a filter membrane indicates formation of chernikovite. Rapid nucleation of chernikovite occurred within 3 min of mixing U(VI) and phosphate. For the 37 h sample, preferred orientation of solids on the filter resulted in the loss of all but four reflections in the diffraction pattern, and a new peak that could not be identified also appeared at 12.8° 2θ. The identifiable peaks were consistent with those from the year-long experiment (Fig. 2.7), which confirmed that the same phase was replicated in this short experiment.

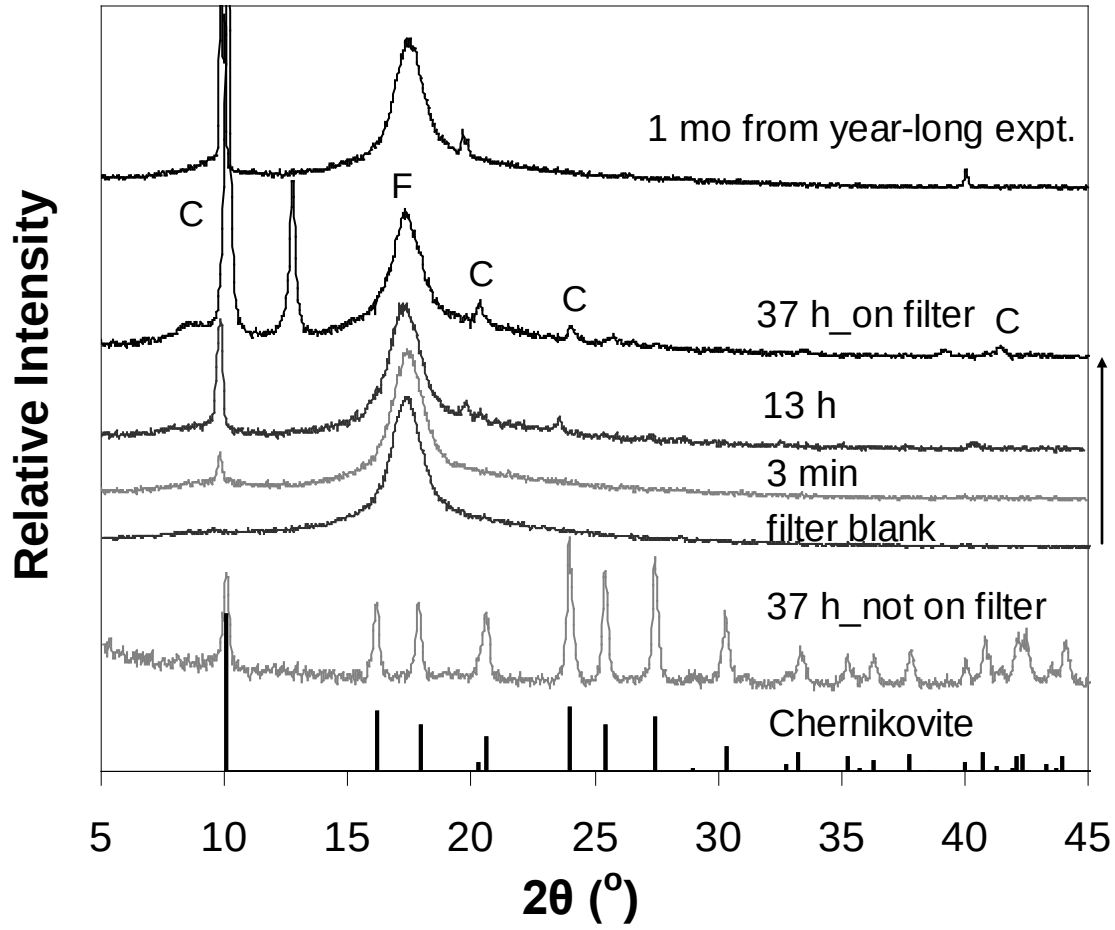

Fig. 2.7. X-ray diffraction patterns of early uranium phosphate precipitates for 100 µM TOTU and 105 µM TOTP. Reference pattern of chernikovite, PDF# 01-075-1106, is shown for comparison. Peaks corresponding to chernikovite and the polycarbonate filter blank are labeled as C and F respectively. Patterns corresponding to 37 h show the effect of preferred orientation on the filter membrane. Also shown is the 1 mo pattern from the year-long experiment with 100 µM TOTU and 130 µM TOTP. Intensities are normalized by the broad peak corresponding to the filter.

Formation of chernikovite was also supported by the U/P molar uptake ratios calculated from the measured dissolved concentrations recorded during the year-long experiment. The uptake ratios for high TOTU (50 µM and 100 µM) after 1 day were 1.0 and 1.2 respectively (Fig. 2.8c), similar to the uptake ratio of 1.0 if chernikovite were to have formed.

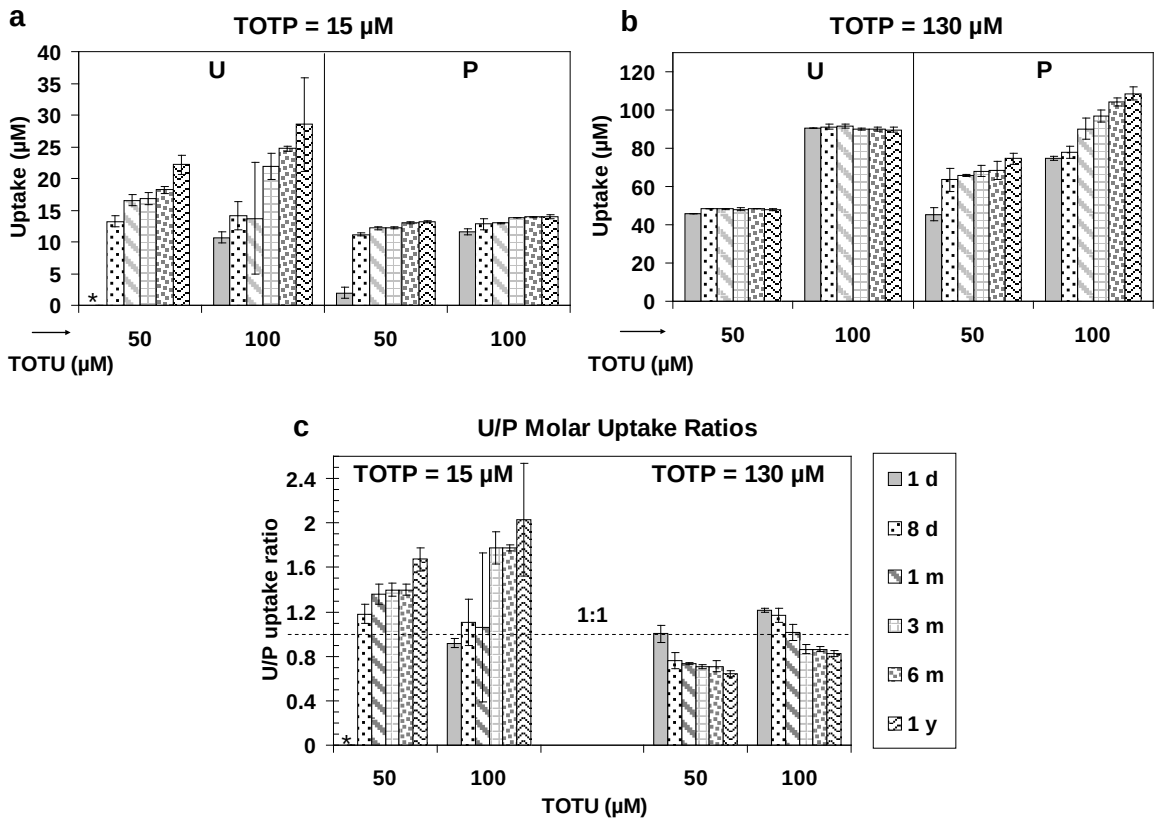

Fig. 2.8. Molar uptake of uranium and phosphate for a) 15 and b) 130 µM TOTP with increasing high TOTU conditions and c) calculated ratios at different reaction times in the absence of goethite. Molar uptake at specific reaction times was defined as the difference between the measured dissolved (Figs. 2.4d-e and 2.5a-b) and the total concentrations. No U uptake was observed for 15 µM TOTP and 50 µM TOTU after 1 d (*).

Comparison of experimental results with thermodynamic predictions Evidence for precipitation of uranium phosphates was found for all conditions for which precipitation was predicted in section 3.1. However, the phase that precipitated initially was chernikovite and not the predicted uranyl orthophosphate. Measured U_{diss} and P_{diss} concentrations immediately after precipitation were generally not consistent with those predicted for the equilibrium solubility of uranyl orthophosphate. For the high TOTP (≥ 130 µM) and high TOTU (50 µM) conditions, U_{diss} concentrations were underpredicted while P_{diss} concentrations were overpredicted by uranyl orthophosphate

solubility (Figs. 2.4d-e and 2.5b). Saturation indices [$\log(Q/K_{sp})$] with respect to the chernikovite-like uranium hydrogen phosphate [$UO_2HPO_4 \cdot 3H_2O_{(s)}$] are quite close to 0 (-0.14 and -0.2 for 50 µM and 100 µM TOTU conditions, respectively), which is consistent with the formation of chernikovite as the dominant initial U(VI) uptake mechanism at pH 4.

The initially precipitated chernikovite may transform with time into other uranium phosphate solids. For the low TOTP (15 µM) and high TOTU (50 – 100 µM) conditions, measured U_{diss} and P_{diss} concentrations decreased gradually until the predicted solubility of uranyl orthophosphate was reached after about 1 year (Figs. 2.4d-e, 2.5a). However, for the high TOTP conditions, measured U_{diss} and P_{diss} values were very different from equilibrium predictions (Figs. 2.4 and 2.5b). These differences could be caused by: a) formation of a uranium phosphate phase different from uranyl orthophosphate; b) inaccurate solubility products for the uranium phosphate solids considered in the model calculations; or c) the kinetics of formation of uranium phosphate solids playing a greater role than thermodynamic equilibrium. The metastability of uranium phosphate precipitates is discussed further in section 3.4.

2.3.3. Mechanisms for uranium and phosphate uptake in the presence of goethite

With an understanding of the conditions favoring U precipitation and of the identity of precipitated forms in the absence of goethite, the effect of goethite on the dominant U(VI) and phosphate uptake mechanisms is examined. In the presence of goethite, uptake occurred by one or more of the following mechanisms: adsorption, precipitation following homogeneous nucleation, and precipitation following heterogeneous

nucleation. The dominance of these mechanisms was dependent on the TOTU and TOTP concentrations relative to the amount of goethite in the system. The dominant mechanism for a given condition was stable over the year-long reaction.

2.3.3.1. Adsorption

Adsorption was the dominant uptake mechanism for all conditions except for the conditions of high TOTU (50 and 100 μM) with high TOTP (130 μM). Even for these exceptional cases, adsorption could be a significant secondary mechanism. Interpreting the effect of phosphate on U(VI) adsorption to goethite was complemented by single adsorbate studies.

U adsorption on goethite in the absence of phosphate. Goethite facilitated U(VI) uptake for all TOTU conditions investigated at pH 4 (Figs. 2.4a-e). The fraction of U(VI) adsorbed decreased with increasing TOTU levels. Predicted U_{diss} concentrations (shown as horizontal lines in Fig. 2.4) were significantly higher than measured concentrations for all TOTU conditions. Although sorption to reactor walls was a significant factor for low to intermediate TOTU (1 - 10 μM) conditions as discussed in section 3.2, it could not explain the differences between measured and predicted concentrations. A more significant factor was probably the underprediction of the adsorption affinity ($logK_{int}$) of U(VI) on goethite as $\equiv FeO_2UO_2$. In addition to the modified Cheng model underpredicting adsorption in the present study, the original model of Cheng et al. also underpredicted their original data at pH 4. Only ~20 μM of U(VI) uptake occurred at the

100 µM TOTU condition, suggesting that U(VI) adsorption was not limited by the availability of surface sites (66 µM TOT≡FeOH estimated).

Phosphate adsorption on goethite in the absence of uranium. Favorable and rapid phosphate uptake occurred for both levels of TOTP investigated. For the 15 µM TOTP condition, almost all phosphate (> 90% of TOTP) adsorbed onto goethite within a day of reaction (Fig. 2.5a). Increasing the TOTP to 130 µM resulted in ~50% phosphate uptake, which was close to saturating the capacity of the goethite surface (Fig. 2.5b). The model predictions of P_{diss} concentrations matched the measured values well at both TOTP levels.

U adsorption on goethite in the presence of phosphate. Phosphate did not affect U(VI) uptake on goethite at low TOTP (15 µM) conditions. Measured U_{diss} concentrations in the presence of phosphate were not significantly different from in its absence (Figs. 2.4a-e). Likewise, there was almost no effect of increasing TOTU concentrations on phosphate adsorption (Fig. 2.5a). Overall, the data suggest that the observed uptake of <20 µM of U(VI) and ~14 µM of phosphate on goethite occurred without any competition for the total available adsorption sites (66 µM). Instead of forming the predicted ternary surface complex $\equiv FePO_4UO_2$, U(VI) and phosphate may adsorb to goethite independently of each other at low TOTP conditions. If the ternary surface complex had formed, then U(VI) uptake should have been significantly enhanced relative to phosphate-free conditions. The close agreement between observed and predicted concentrations despite no evidence for the formation of the ternary surface

complex indicates that the $\log K_{int}$ for the ternary surface complex may be too high and that of the binary complex may be too low.

Unlike for the low TOTP conditions, U(VI) uptake was significantly enhanced at high TOTP (130 µM) conditions (Fig. 2.4). The corresponding phosphate uptake also showed an upward trend with increasing TOTU levels (Fig. 2.5b). Depending on the relative amounts of TOTP, TOTU, and surface sites (23.5 m^2/L for 66 µM TOT ≡FeOH), this simultaneous U(VI) and phosphate uptake could be indicative of either formation of a ternary surface complex or precipitation of a uranium phosphate. For the low to intermediate TOTU (1 - 10 µM) concentrations, the dominant U(VI) uptake mechanism appears to be adsorption by the formation of the ternary surface complex. For these conditions the predicted U_{diss} and P_{diss} concentrations match the observed ones (Figs. 2.4a-c and 2.5b) and XRD and SEM provided no direct evidence of precipitation. As opposed to the low TOTP conditions, U(VI) and phosphate compete for the available adsorption sites (66 µM). Observed phosphate uptake of 60 - 70 µM was similar to that observed in U-free experiments, which suggests that phosphate adsorption accounted for almost all of the surface monolayer. The majority of the adsorbed phosphate is likely to be independent of U(VI), such as in the form of the mononuclear binary surface complex $\equiv FePO_4H_2$ that was predicted by the model. With increasing TOTU concentrations from 0 - 10 µM, formation of the ternary surface complex, $\equiv FePO_4UO_2$, could explain significant U(VI) uptake with almost no change in phosphate uptake. This conclusion is also supported by a previous study that found that adsorption isotherms of U(VI) were the same when phosphate was either pre-adsorbed to goethite or added simultaneously with uranium [66]. Once the goethite surface coverage is exhausted by the formation of

$\equiv FePO_4H_2$ and $\equiv FePO_4UO_2$ complexes, U_{diss} and P_{diss} concentrations at equilibrium could become supersaturated with respect to a uranium phosphate solid for higher TOTU ($\geq$50 µM) concentrations.

Phosphate-enhanced cation uptake on iron oxide surfaces has previously been reported and explained by different mechanisms. An increase in lead uptake on goethite in the presence of phosphate could be explained solely by surface charge effects and not to precipitation or formation of any ternary surface complex [67]. On the other hand, simultaneous U(VI) and phosphate uptake on goethite-coated sand for 5 µM TOTU with 100 and 200 µM TOTP [45] and on ferrihydrite for 1 and 100 µM TOTU with 100 µM TOTP [44] were modeled by the formation of a ternary surface complex, $\equiv FePO_4UO_2$. Refitting of the data of Cheng et al. without including the ternary surface complex yielded poor results (see Table 2-B10). Likewise, results from the low TOTP conditions in our study suggest that alteration of surface charge by adsorbed phosphate is not sufficient to enhance U(VI) uptake. The availability of less goethite surface area in this study as compared to the studies of Cheng et al. and Payne et al. resulted in significant concentrations of dissolved as well as adsorbed phosphate at equilibrium. Consequently, both the formation of the ternary surface complex at low to intermediate TOTU and precipitation of uranium phosphates at high TOTU were facilitated.

2.3.3.2. Precipitation by homogeneous nucleation

Indirect evidence for uranium phosphate precipitation was obtained from measured U_{diss} and P_{diss} concentrations for the high TOTP (130 µM) and high TOTU (50 and 100 µM) conditions (Figs. 2.4d,e and 2.5b). Simultaneous 1:1 U:P molar uptake (~45 µM for 50

μM TOTU and ~60 μM for 100 μM TOTU conditions) after 1 day in the presence of goethite was similar to the corresponding U:P uptake in the absence of goethite (section 3.2), which suggests precipitation of chernikovite. Furthermore, the presence of goethite actually prevented the precipitation of as much uranium as in the absence of goethite; for 50 and 100 μM TOTU conditions U_{diss} concentrations increased by ~2.5 μM and ~15 μM, respectively, in the presence of goethite (Figs. 2.4d,e). Goethite acted as a sink for phosphate (Fig. 2.5b), which limited the concentration of dissolved phosphate and caused a higher U_{diss} concentration in equilibrium with chernikovite than would be present at a higher P_{diss} concentration.

Direct evidence for homogenous nucleation and precipitation of chernikovite was obtained from XRD and SEM. For the 50 and 100 μM TOTU conditions, the prominent XRD peaks in the presence of goethite that are attributed to chernikovite (Figs. 2.9b and 2.9d) match well with those when goethite was not present (Figs. 2.9a and 2.9c). The SEM image for the 100 μM TOTU condition (Fig. 2.6f) resembles the image of chernikovite in the absence of goethite (Fig. 2.6c). The presence of goethite seems to have prevented the intergrowth of crystals that was earlier observed (Fig. 2.6c), but the goethite did not affect the chernikovite crystal size.

2.3.3.3. Precipitation by heterogeneous nucleation

U(VI) uptake was predominantly by adsorption for the low TOTP (≤ 15 μM) conditions as discussed in section *3.3.1*. A notable exception was observed for the highest TOTU (100 μM) concentration. For this TOTU and TOTP combination, precipitation of uranium phosphate was predicted only in the absence of goethite, but it was also

observed in the presence of goethite. Indirect evidence for precipitation was provided by a gradual decrease in U_{diss} and P_{diss} concentrations with time similar to the trend observed for uranium phosphate precipitation in the absence of goethite. Direct observation of precipitated solids was obtained by SEM (Fig. 2.6e). The goethite surface was covered with a bead-like structure, which indicated the possibility of nucleation of solids on its surface. Furthermore, the precipitates that heterogeneously nucleated on the goethite surface were much smaller than those that homogeneously precipitated in the absence of goethite (Fig. 2.6e). EDX analysis confirmed the presence of U and P in the precipitates on the goethite surface. However, due to the limited mass of precipitate, identification of the phase by XRD was not successful.

2.3.4. Metastability of uranium phosphates

Transformation of the initially precipitated uranium phosphate phase with time can be inferred from the measured U_{diss} and P_{diss} concentrations presented in section 3.2. In the absence of goethite, a time-dependent decrease in these concentrations occurred after nucleation for the low TOTP (15 μM) conditions (Figs. 2.4 and 2.5a). For the high TOTP (130 μM) conditions, however, U_{diss} concentrations were relatively stable over time, but the corresponding P_{diss} concentrations decreased gradually for all TOTU levels (Fig. 2.5b). This variability in U(VI) and phosphate uptake with time indicates the meta-stable nature of uranium phosphates.

Metastability of uranium phosphates in the absence of goethite was investigated in detail for the two levels of TOTP and high TOTU (50 μM) by examining the variation of the U/P molar uptake ratios (Fig. 2.8). The initial U/P uptake ratio (just after

nucleation) for each of the TOTP conditions was ~0.9 - 1.2 suggesting a 1:1 stoichiometry in the formation of uranyl phosphates such as chernikovite [$UO_2HPO_4 \cdot 4H_2O_{(s)}$]. The formation of chernikovite was also confirmed by SEM (Fig. 2.6c) and XRD (Fig. 2.7) as discussed earlier. With time chernikovite transformed into another phase whose U:P molar composition may have been affected by the TOTU:TOTP in the system. For the low TOTP (15 µM) level the U/P uptake ratios after nucleation increased gradually with reaction time, whereas for the high TOTP level (130 µM) they decreased with reaction time (Fig. 2.8c).

For the 50 µM TOTU condition with low TOTP (when TOTU is in excess of TOTP), the molar U/P ratio increased from ~1.2 after 8 days to ~1.7 after 1 year of reaction time. Likewise for the 100 µM TOTU, the U/P ratio increased steadily to ~2.0 after 1 year of reaction time from an initial value of ~0.9 after 1 day. Dissolved phosphate uptake after nucleation for both levels of TOTU was > 80 % of TOTP and did not significantly increase with time. It appears that U(VI) was preferentially taken up as adsorbed or precipitated uranium that may have transformed chernikovite into a new phase with U/P > 1, such as $(UO_2)_3(PO_4)_2 \cdot xH_2O$.

The effect of TOTU:TOTP on the formation of meta-stable precipitates can also be seen for the high TOTP (130 µM) level where TOTP is in excess of TOTU. Dissolved uranium uptake was ≥ 90% of TOTU for both TOTU conditions and remained invariant over the 1 year period (Fig. 2.8b). However, the corresponding phosphate uptake increased from ~35% to ~57% for 50 µM TOTU and from ~57% to ~84% for 100 µM TOTU over the same period. The continuing phosphate uptake with time suggested that either phosphate adsorbed to the chernikovite particles or that a new phase with U/P < 1,

such as $UO_2(H_2PO_4)_2 \cdot xH_2O$ formed (Fig. 2.8c). Complete dissolution of 14-month aged uranium phosphate solids formed under these conditions resulted in U/P molar ratios of 0.62 - 0.65 that were consistent with the calculated uptake ratios after 1 year of reaction.

Under similar TOTU: TOTP conditions, chernikovite has been a precursor in the formation of other uranium phosphate minerals. In a study involving synthesis of sodium meta-autunite by indirect precipitation, chernikovite was synthesized first [68]. In another study, uranium phosphate hydrate $[(UO_2)_3(PO_4)_2 \cdot 4H_2O_{(s)}]$ was synthesized by first precipitating uranyl hydrogen phosphate $[UO_2HPO_4 \cdot 2H_2O_{(s)}]$ at room temperature and then aging this precursor at 80°C [69].

Metastability of the initially precipitated solid in the absence of goethite was also evident from XRD. With increasing reaction time peaks corresponding to primary and higher-order reflections of the (002) plane of chernikovite intensify and shift towards higher $2\theta^o$ (smaller lattice spacings) by about 0.2-0.3^o 2θ (Fig. 2.9a,c). This shift could be due to transformation of one uranium phosphate phase to another, or it could be an effect of changes in the number or coordination of waters of hydration in the crystal structure. Because of preferred orientation of the solids on the filters, the number of prominent reflections was insufficient to definitively identify the mineral phase at each time point.

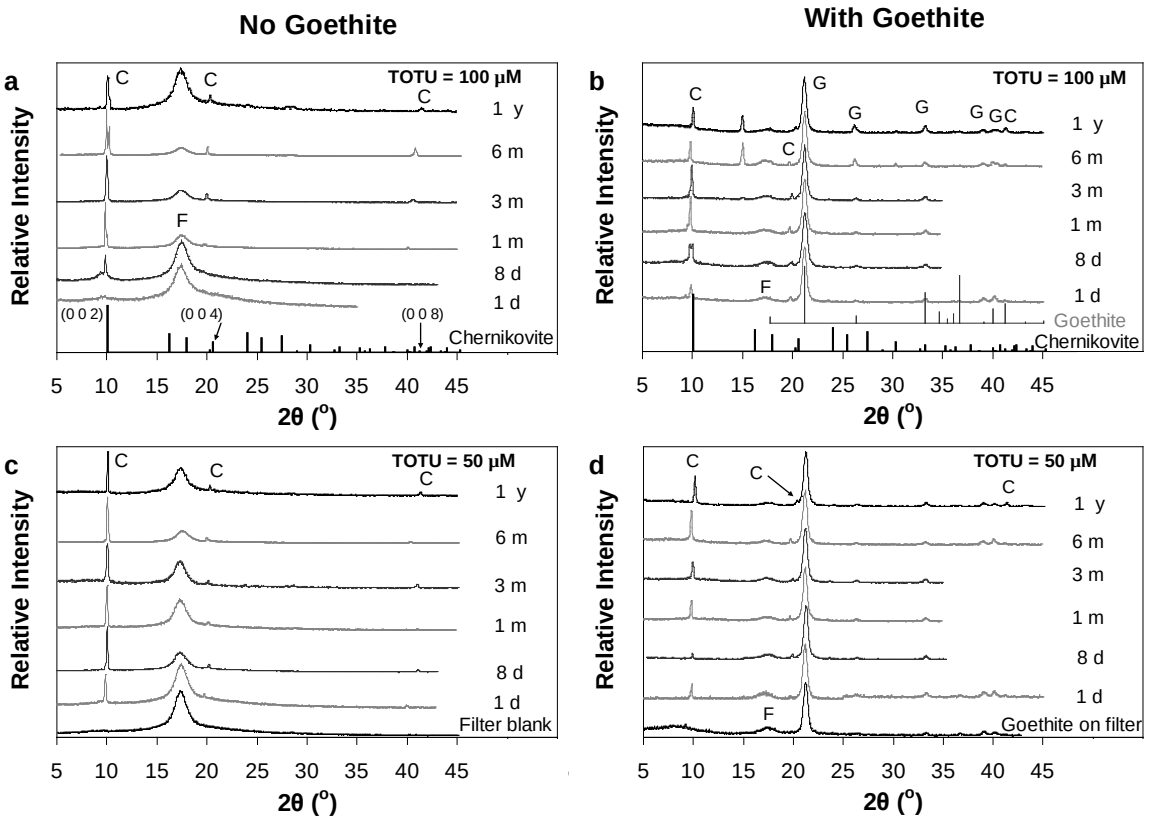

Fig. 2.9. Time-dependent X-ray diffraction patterns of solids collected from goethite-free and goethite-present reactors for TOTP = 130 µM and the two highest uranium concentrations (50 and 100 µM). Reference patterns for chernikovite [PDF# 01-075-1106 (black)] and goethite [PDF# 00-029-0713 (grey)] are shown for comparison. Peaks for goethite, the polycarbonate filter, and chernikovite are labeled as G, F, and C, respectively. Not all patterns were collected to 45°.

Metastability of heterogeneously or homogeneously nucleated uranium phosphate phases was also evident in the presence of goethite. For the 15 µM TOTP and 100 µM TOTU condition favoring heterogeneous nucleation of uranium phosphates, the gradual decrease in U_{diss} and P_{diss} concentrations (Figs. 2.4e and 2.5a) was similar in the absence and presence of goethite. This simultaneous U(VI) and phosphate uptake with time could be attributed to growth of nuclei after initial nucleation facilitated by the goethite surface (Fig. 2.6e). For the 130 µM TOTP and 50 - 100 µM TOTU conditions favoring homogenous nucleation of chernikovite, the time-dependent XRD patterns of solids (Fig.

2.9b,d) indicated a similar shift in the reflections of the (002) plane of chernikovite as observed in the absence of goethite (Fig. 2.9a,c). For the 100 µM TOTU condition, a new diffraction peak at ~15 2θº appeared after 6 months. This peak was neither observed in the absence of goethite nor was it one of the chernikovite reflections. The appearance of the unidentified peak coincided with a slight increase in corresponding P_{diss} concentration after 6 months (Fig. 2.5b) and U_{diss} concentration after 1 year (Fig. 2.4e).

2.3.5. Relevance to in-situ immobilization

The findings of this study are relevant to phosphate-based immobilization strategies for in-situ remediation of uranium-contaminated sites with mildly or strongly acidic pH. Phosphate will adsorb to any iron (oxy)hydroxides present at these sites. If sufficient phosphate to overcome the adsorptive capacity of the subsurface solids is added, then uranium phosphates can precipitate and prevent the migration of uranium out of the contaminated zones. The total phosphate concentration must be adjusted such that U(VI)-phosphate precipitation is preferential to adsorption, which in this study was between 15 µM and 130 µM depending on the total U(VI) and total sorption sites present. Based on site-specific uranium(VI) and iron (oxy)hydroxide contents, results from this study could be used to determine the critical phosphate needed to immobilize uranium as stable precipitates.

Information on immobilization mechanisms can help predict uranium transport because the long-term stability and remobilization rates may depend on the mechanism. The equilibrium model developed in this work could be useful for incorporation into reactive transport models as it encompasses a broad range of conditions over which

uranium adsorption and precipitation can occur. Although the results were obtained at pH 4, the generalized framework of the model makes it amenable to predictions of U(VI) immobilization mechanisms at higher pH as well. However, as witnessed in this study, the kinetics of formation of uranium phosphates and not equilibrium can govern the initial and final immobilized forms. Therefore, the equilibrium predictions of immobilization mechanisms should still be complemented with experimental measurements using approaches similar to those used in this study.

2.4. Conclusions

The batch experiments and associated modeling of equilibrium adsorption and precipitation provide information on the impacts of phosphate on uranium immobilization both in the presence and absence of goethite. Precipitation of uranium phosphates in the presence of goethite was the dominant mechanism at high total uranium (50 - 100 μM) and high total phosphate (130 μM) concentrations. Homogeneous nucleation of chernikovite, $H_3O(UO_2)(PO_4)\bullet 3H_2O_{(s)}$, occurred rapidly for initially supersaturated suspensions both with and without goethite, although equilibrium calculations predicted uranium orthophosphate, $(UO_2)_3(PO_4)_2 \cdot 4H_2O_{(s)}$, as the most stable phase. Adsorption was the dominant mechanism for low total phosphate conditions (≤15 μM) for most total uranium concentrations, except at 100 μM when heterogeneous nucleation of a uranium phosphate phase on the goethite surface was observed. Adsorption was also dominant at conditions when total phosphate (130 μM) was in large excess of the total uranium (1 - 10 μM). The observed simultaneous uranium and phosphate uptake could be due to the formation of a $\equiv FePO_4UO_2$ ternary surface complex. Depending on the total adsorption

sites available and total uranium concentrations, a critical phosphate concentration (between 15 - 130 µM in this study) must be met to achieve preferential uranium phosphate precipitation over adsorption. The goethite surface acts as a sink for dissolved phosphate, limiting the formation of uranium phosphates and resulting in higher dissolved U(VI) concentrations than would be attainable in goethite-free suspensions for high total uranium concentrations (50 - 100 µM). Results from goethite-free conditions indicated that U(VI)-phosphate solids nucleated rapidly and gradually transformed from chernikovite to another phase over a period of 1 year. The molar U/P uptake ratio decreased with time for conditions when total phosphate was in excess of total U(VI), which indicated preferential phosphate uptake on the initially nucleated chernikovite phase; the U/P uptake ratio increased when total U(VI) was in excess of total phosphate. Metastability of uranyl phosphates was also observed in the presence of goethite. The combination of systematic experiments that analyzed both solutions and solids with updated geochemical equilibrium models was essential to identifying the effects of geochemical composition and time on the rates and mechanisms of U(VI) removal from solution.

References

1. Riley, R. G.; Zachara, J. M. *Chemical contaminants on DOE lands and selection of contaminant mixtures for subsurface science research*; DOE/ER-0547T; U.S. Dept. of Energy, Office of Energy Research: Washington, DC, 1992, 1992.
2. U.S.DOE, *Linking legacies: connecting Cold War nuclear weapons processes to their environmental consequences*. U.S. Department of Energy, Office of Environmental Management: 1997.
3. Langmuir, D., *Aqueous environmental geochemistry*. Prentice-Hall, Inc.: Upper Saddle River, New Jersey, 1997.
4. Wu, W. M.; Carley, J.; Gentry, T.; Ginder-Vogel, M. A.; Fienen, M.; Mehlhorn, T.; Yan, H.; Caroll, S.; Pace, M. N.; Nyman, J.; Luo, J.; Gentile, M. E.; Fields, M. W.; Hickey, R. F.; Gu, B. H.; Watson, D.; Cirpka, O. A.; Zhou, J. Z.; Fendorf, S.; Kitanidis, P. K.; Jardine, P. M.; Criddle, C. S., Pilot-scale in situ bioremedation of uranium in a highly contaminated aquifer. 2. Reduction of U(VI) and geochemical control of U(VI) bioavailability. *Environmental Science & Technology* **2006,** *40*, (12), 3986-3995.
5. Anderson, R. T.; Vrionis, H. A.; Ortiz-Bernad, I.; Resch, C. T.; Long, P. E.; Dayvault, R.; Karp, K.; Marutzky, S.; Metzler, D. R.; Peacock, A.; White, D. C.; Lowe, M.; Lovley, D. R., Stimulating the in situ activity of Geobacter species to remove uranium from the groundwater of a uranium-contaminated aquifer. *Applied and Environmental Microbiology* **2003,** *69*, (10), 5884-5891.
6. Ginder-Vogel, M.; Criddle, C. S.; Fendorf, S., Thermodynamic constraints on the oxidation of biogenic UO_2 by Fe(III) (hydr)oxides. *Environmental Science & Technology* **2006,** *40*, (11), 3544-3550.
7. Gu, B. H.; Yan, H.; Zhou, P.; Watson, D. B.; Park, M.; Istok, J., Natural humics impact uranium bioreduction and oxidation. *Environmental Science & Technology* **2005,** *39*, (14), 5268-5275.
8. Zhong, L. R.; Liu, C. X.; Zachara, J. M.; Kennedy, D. W.; Szecsody, J. E.; Wood, B., Oxidative remobilization of biogenic uranium(IV) precipitates: Effects of iron(II) and pH. *Journal of Environmental Quality* **2005,** *34*, (5), 1763-1771.
9. Zhou, P.; Gu, B. H., Extraction of oxidized and reduced forms of uranium from contaminated soils: Effects of carbonate concentration and pH. *Environmental Science & Technology* **2005,** *39*, (12), 4435-4440.
10. Finch, R.; Murakami, T., Systematics and Paragenesis of Uranium Minerals. In *Uranium: mineralogy, geochemistry and the environment*, Burns, P. C.; Finch, R., Eds. Mineralogical Society of America: Washington, DC, 1999; Vol. 38, pp 91-180.
11. Guillaumont, R.; Fanghänel, T.; Fuger, J.; Grenthe, I.; Neck, V.; Palmer, D. A.; Rand, M. H., *Update on the chemical thermodynamics of uranium, neptunium, plutonium, americium and technetium*. OECD Nuclear Energy Agency (ed.), Elsevier, Amsterdam: 2003.
12. Schwertmann, U.; Cornell, R. M., *Iron Oxides in the Laboratory*. Second ed.; Wiley-VCH: New York, NY, 2000.
13. Dzombak, D. A.; Morel, F. M. M., *Surface Complexation Modeling*. Wiley-Interscience: New York, 1990.

14. Morrison, S.; Spangler, R.; Tripathi, V., Adsorption of uranium (VI) on amorphous ferric oxyhydroxide at high concentrations of dissolved carbon (IV) and sulfur (VI). *Journal of Contaminant Hydrology* **1995,** *17*, (4), 333-346.
15. Hsi, C.-K. D.; Langmuir, D., Adsorption of uranyl onto ferric oxyhydroxides: application of the surface complexation site-binding model. *Geochimica et Cosmochimica Acta* **1985,** *49*, 1931-1941.
16. Waite, T.; Davis, J.; Payne, T.; Waychunas, G.; Xu, N., Uranium (VI) adsorption to ferrihydrite: Application of a surface complexation model. *Geochimica et Cosmochimica Acta* **1994,** *58*, 5465-5478.
17. Gabriel, U.; Gaudet, J. P.; Spadini, L.; Charlet, L., Reactive transport of uranyl in a goethite column: an experimental and modelling study. *Chemical Geology* **1998,** *151*, (1-4), 107-128.
18. Wazne, M.; Korfiatis, G. P.; Meng, X. G., Carbonate effects on hexavalent uranium adsorption by iron oxyhydroxide. *Environmental Science & Technology* **2003,** *37*, (16), 3619-3624.
19. Villalobos, M.; Trotz, M. A.; Leckie, J. O., Surface complexation modeling of carbonate effects on the adsorption of Cr(VI), Pb(II), and U(VI) on goethite. *Environmental Science & Technology* **2001,** *35*, (19), 3849-3856.
20. Duff, M. C.; Amrhein, C., Uranium(VI) adsorption on goethite and soil in carbonate solutions. *Soil Science Society of America Journal* **1996,** *60*, 1393-1400.
21. Hiemstra, T.; Van Riemsdijk, W. H.; Rossberg, A.; Ulrich, K. U., A surface structural model for ferrihydrite. II. Adsorption of uranyl and carbonate. *Geochemica et Cosmochimica Acta* **2009,** *73*, 4437-4451.
22. Fuller, C. C.; Bargar, J. R.; Davis, J. A.; Piana, M. J., Mechanisms of uranium interactions with hydroxyapatite: Implications for groundwater remediation. *Environmental Science & Technology* **2002,** *36*, (2), 158-165.
23. Jeanjean, J.; Rouchaud, J.; Tran, L.; Fedoroff, M., Sorption of uranium and other heavy metals on hydroxyapatite. *Journal of Radioanalytical and Nuclear Chemistry* **1995,** *201*, (6), 529-539.
24. Brooks, S. C. *Waste characteristics of the former S-3 ponds and outline of uranium chemistry relevant to NABIR Field Research Center Studies*; ORNL/TM-2001/27; NABIR FRC: 2001.
25. Arey, J. S.; Seaman, J. C.; Bertsch, P., Immobilization of uranium in contaminated sediments by hydroxyapatite addition. *Environmental Science & Technology* **1999,** *33*, (2), 337-342.
26. Simon, F. G.; Biermann, V.; Peplinski, B., Uranium removal from groundwater using hydroxyapatite. *Applied Geochemistry* **2008,** *23*, 2137-2145.
27. Beazley, M.; Martinez, R.; Sobecky, P.; Webb, S.; Taillefert, M., Nonreductive Biomineralization of Uranium (VI) Phosphate Via Microbial Phosphatase Activity in Anaerobic Conditions. *Geomicrobiology Journal* **2009,** *26*, (7), 431-441.
28. Beazley, M. J.; Martinez, R. J.; Sobecky, P. A.; Webb, S. M.; Taillefert, M., Uranium biomineralization as a result of bacterial phosphatase activity: Insights from bacterial isolates from a contaminated subsurface. *Environmental Science & Technology* **2007,** *41*, (16), 5701-5707.

29. U.S.DOE *Limited field investigation plan for the 300 area uranium plume, 300-ff-5 operable unit, Hanford Site*; U.S. Department of Energy, Pacific Northwest National Laboratory, Richland, Washington: 2005.
30. Vermuel, V.; Fruchter, J.; Wellman, D.; Williams, B.; Williams, M., Site Characterizatio Plan: Uranium Stabilization through Polyphosphate Injection–300 Area Uranium Plume Tre Demonstration Project. In PNNL-16008, Pacific Northwest National Laboratory, Richland, Washin: 2006.
31. Wellman, D.; Fruchter, J.; Vermeul, V. *Experimental Plan: Uranium Stabilization Through Polyphosphate Injection 300 Area Uranium Plume Treatability Demonstration Project*; PNNL-16101, Pacific Northwest National Laboratory (PNNL), Richland, WA (US): 2006.
32. Wellman, D.; Fruchter, J.; Vermeul, V.; Williams, M. *Challenges Associated with Apatite Remediation of Uranium in the 300 Area Aquifer*; PNNL-17480, Pacific Northwest National Laboratory (PNNL), Richland, WA (US): 2008.
33. Wellman, D.; Pierce, E.; Richards, E.; Butler, B.; Parker, K.; Glovack, J.; Burton, S.; Baum, S.; Clayton, E.; Rodriguez, E. *Interim Report: Uranium Stabilization Through Polyphosphate Injection-300 Area Uranium Plume Treatability Demonstration Project*; PNNL-16683, Pacific Northwest National Laboratory (PNNL), Richland, WA (US), Environmental Molecular Sciences Laboratory (EMSL): 2007.
34. Wellman, D. M.; Gunderson, K. M.; Icenhower, J. P.; Forrester, S. W.; Forrester, S. W., Dissolution kinetics of synthetic and natural meta-autunite minerals, $X_{3-n}^{(n)+}[(UO_2)(PO_4)]_2 \cdot xH_2O$, under acidic conditions. *Geochemistry Geophysics Geosystems* **2007,** *8*.
35. Wellman, D. M.; Icenhower, J. P.; Gamerdinger, A. P.; Forrester, S. W., Effects of pH, temperature, and aqueous organic material on the dissolution kinetics of meta-autunite minerals, $(Na,Ca)_{2-1}[(UO_2)(PO_4)]_2 \cdot 3H_2O$. *American Mineralogist* **2006,** *91*, 143-158.
36. Wellman, D. M.; Icenhower, J. P.; Owen, A. T., Comparative analysis of soluble phosphate amendments for the remediation of heavy metal contaminants: Effect on sediment hydraulic conductivity. *Environmental Chemistry* **2006,** *3*, (3), 219-224.
37. Zheng, Z. P.; Wan, J. M.; Song, X. Y.; Tokunaga, T. K., Sodium meta-autunite colloids: Synthesis, characterization, and stability. *Colloids and Surfaces a-Physicochemical and Engineering Aspects* **2006,** *274*, (1-3), 48-55.
38. Jerden, J. L.; Sinha, A. K., Phosphate based immobilization of uranium in an oxidizing bedrock aquifer. *Applied Geochemistry* **2003,** *18*, (6), 823-843.
39. Murakami, T., Ohnuki, T., Isobe, H. and Sato, T., Mobility of uranium during weathering. *American Mineralogist* **1997,** *82*, 888-8999.
40. Morris, D. E.; Allen, P. G.; Berg, J. M.; Chisholm-Brause, C. J.; Conradson, S. D.; Donohoe, R. J.; Hess, N. J.; Musgrave, J. A.; Tait, C. D., Speciation of uranium in Fernald soils by molecular spectroscopic methods: characterization of untreated soils. *Environmental Science and Technology* **1996,** *30*, (7), 2322-2331.
41. Buck, E. C.; Brown, N. R.; Dietz, N. L., Contaminant uranium phases and leaching at the Fernald site in Ohio. *Environmental Science and Technology* **1996,** *30*, (1), 81-88.

42. Roh, Y.; Lee, S. R.; Choi, S.-K.; Elless, M. P.; Lee, S. Y., Physicochemical and mineralogical characterization of uranium-contaminated soils. *Soil and Sediment Contamination* **2000,** *9*, (5), 463-486.
43. Catalano, J. G.; McKinley, J. P.; Zachara, J. M.; Heald, S. M.; Smith, S. C.; Brown, G. E., Changes in uranium speciation through a depth sequence of contaminated Hanford sediments. *Environmental Science & Technology* **2006,** *40*, (8), 2517-2524.
44. Payne, T. E.; Davis, J. A.; Waite, T. D., Uranium adsorption on ferrihydrite - Effects of phosphate and humic acid. *Radiochimica Acta* **1996,** *74*, 239-243.
45. Cheng, T.; Barnett, M. O.; Roden, E. E.; Zhuang, J. L., Effects of phosphate on uranium(VI) adsorption to goethite-coated sand. *Environmental Science & Technology* **2004,** *38*, (22), 6059-6065.
46. Bostick, B. C.; Fendorf, S.; Barnett, M. O.; Jardine, P. M.; Brooks, S. C., Uranyl surface complexes formed on subsurface media from DOE facilities. *Soil Science Society of America Journal* **2002,** *66*, (1), 99-108.
47. Arai, Y.; Sparks, D. L., ATR-FTIR spectroscopic investigation on phosphate adsorption mechanisms at the ferrihydrite-water interface. *J. Colloid Interface Sci.* **2001,** *241*, (2), 317-326.
48. Nilsson, N.; Lovgren, L.; Sjoberg, S., Phosphate Complexation at the Surface of Goethite. *Chemical Speciation and Bioavailability* **1992,** *4*, (4), 121-130.
49. Murakami, T.; Sato, T.; Ohnuki, T.; Isobe, H., Field evidence for uranium nanocrystallization and its implications for uranium transport. *Chemical Geology* **2005,** *221*, (1-2), 117-126.
50. Sato, T.; Murakami, T.; Yanase, N.; Isobe, H.; Payne, T. E.; Airey, P. L., Iron nodules scavenging uranium from groundwater. *Environmental Science & Technology* **1997,** *31*, (10), 2854-2858.
51. Duff, M. C.; Coughlin, J. U.; Hunter, D. B., Uranium co-precipitation with iron oxide minerals. *Geochimica et Cosmochimica Acta* **2002,** *66*, (20), 3533-3547.
52. Giammar, D. E.; Hering, J. G., Time scales for sorption-desorption and surface precipitation of uranyl on goethite. *Environmental Science & Technology* **2001,** *35*, (16), 3332-3337.
53. ICDD, Powder diffraction file. In International Centre for Diffraction Data: Newtown Square, PA, 2007.
54. Schecher, W. D.; McAvoy, D. C. *MINEQL+: A chemical equilibrium modeling system, version 4.5*, Environmental Research Software: Hallowell, ME, 2002.
55. Gorman-Lewis, D.; Burns, P. C.; Fein, J. B., Review of uranyl mineral solubility measurements. *Journal of Chemical Thermodynamics* **2008,** *40*, (3), 335-352.
56. Gorman-Lewis, D.; Fein, J. B.; Burns, P. C.; Szymanowski, J. E. S.; Converse, J., Solubility measurements of the uranyl oxide hydrate phases metaschoepite, compreignacite, Na-compreignacite, becquerelite, and clarkeite. *Journal of Chemical Thermodynamics* **2008,** *40*, (6), 980-990.
57. Gorman-Lewis, D.; Shvareva, T.; Kubatko, K.; Burns, P. C.; Wellman, D. M.; Mcnamara, B.; Szymanowski, J. E. S.; Navrotsky, A.; Fein, J. B., Thermodynamic properties of autunite, uranyl hydrogen phosphate, and uranyl orthophosphate from solubility and calorimetric measurements. *Environmental Science & Technology* **2009,** *43*, (19), 7416-7422.

58. Grenthe, I.; Fuger, J.; Konings, R. J. M.; Lemire, R. J.; Mueller, A. B.; Nguyen-Trung, C.; Wanner, H., *Chemical Thermodynamics of Uranium*. Elsevier: Amsterdam, 1992.
59. Felmy, A. R.; Xia, Y. X.; Wang, Z. M., The solubility product of $NaUO_2PO_4 \cdot xH_2O$ determined in phosphate and carbonate solutions. *Radiochimica Acta* **2005,** *93*, (7), 401-408.
60. Rai, D.; Xia, Y. X.; Rao, L. F.; Hess, N. J.; Felmy, A. R.; Moore, D. A.; McCready, D. E., Solubility of $(UO_2)_3(PO_4)_2 \cdot 4H_2O$ in H^+-Na^+-OH^--$H_2PO_4^-$-$HPO4^{2-}$-PO_4^{3-}-H_2O and its comparison to the analogous PuO_2^{2+} system. *Journal of Solution Chemistry* **2005,** *34*, (4), 469-498.
61. Lövgren, L.; Sjöberg, S.; Schindler, P. W., Acid/base reactions and Al(III) complexation at the surface of goethite. *Geochimica et Cosmochimica Acta* **1990,** *54*, 1301-1306.
62. Sverjensky, D. A., Standard states for the activities of mineral surface sites and species. *Geochimica et Cosmochimica Acta* **2003,** *67*, (1), 17-28.
63. Barnett, M. O.; Jardine, P. M.; Brooks, S. C.; Selim, H. M., Adsorption and transport of uranium(VI) in subsurface media. *Soil Science Society of America Journal* **2000,** *64*, 908-917.
64. Van Haverbeke, L.; Vochten, R.; Van Springel, K., Solubility and spectrochemical characteristics of synthetic chernikovite and meta-ankoleite. *Mineralogical Magazine* **1996,** *60*, 759-766.
65. Vochten, R., Transformation of chernikovite and sodium autunite into lehnerite. *American Mineralogist* **1990,** *75*, 221-225.
66. Cheng, T.; Barnett, M. O.; Roden, E. E.; Zhuang, J. L., Effects of solid-to-solution ratio on uranium(VI) adsorption and its implications. *Environmental Science & Technology* **2006,** *40*, (10), 3243-3247.
67. Xie, L.; Giammar, D., Influence of Phosphate on Adsorption and Surface Precipitation of Lead on Iron Oxide Surfaces. *Adsorption of metals by geomedia II: variables, mechanisms, and model applications* **2008**, 349.
68. Wellman, D. M.; Catalano, J. G.; Icenhower, J. P.; Gamerdinger, A. P., Synthesis and characterization of sodium meta-autunite, $Na[UO_2PO_4] \cdot 3H_2O$. *Radiochimica Acta* **2005,** *93*, (7), 393-399.
69. Sandino, A.; Bruno, J., The solubility of $(UO_2)_3(PO_4)_2 \cdot 4H_2O_{(s)}$ and the formation of U(VI) phosphate complexes: Their influence in uranium speciation in natural waters. *Geochimica et Cosmochimica Acta* **1992,** *56*, 4135-4145.
70. Herbelin, A. L.; Westall, J. C. *FITEQL - A Computer Program for Determination of Chemical Equilibrium Constants from Experimental Data*; 99-01; Oregon State University: Corvallis, OR, 1999.
71. Schwertmann, U.; Cornell, R. M., *The Iron Oxides: Structure, Properties, Reactions, Occurrences and Uses*. Second ed.; Wiley-VCH: New York, NY, 2003.
72. Davis, J. A.; Kent, D. B., Surface complexation modeling in aqueous geochemistry. In *Mineral-Water Interface Geochemistry*, Hochella, M. F.; White, A. F., Eds. Mineralogical Society of America: Washington, DC, 1990; Vol. 23, pp 177-260.

Appendix 2-A: Relevant thermodynamic data

Table A. Relevant aqueous reactions and stability constants at 298 K and I = 0 M.

Reaction	LogK	
	Present work[a]	Cheng et al. (2004)[b]
Uranyl hydroxide complexes:		
$UO_2^{2+} + H_2O = UO_2OH^+ + H^+$	-5.25	-5.20
$UO_2^{2+} + 2H_2O = UO_2(OH)_{2(aq)} + 2H^+$	-12.15	-12.02
$UO_2^{2+} + 3H_2O = UO_2(OH)_3^- + 3H^+$	-20.25	-19.20
$UO_2^{2+} + 4H_2O = UO_2(OH)_4^{2-} + 4H^+$	-32.40	-33.00
$2UO_2^{2+} + H_2O = (UO_2)_2OH^{3+} + H^+$	-2.70	-2.70
$2UO_2^{2+} + 2H_2O = (UO_2)_2(OH)_2^{2+} + 2H^+$	-5.62	-5.62
$3UO_2^{2+} + 4H_2O = (UO_2)_3(OH)_4^{2+} + 4H^+$	-11.90	-11.90
$3UO_2^{2+} + 5H_2O = (UO_2)_3(OH)_5^+ + 5H^+$	-15.55	-15.55
$3UO_2^{2+} + 7H_2O = (UO_2)_3(OH)_7^- + 7H^+$	-32.20	-31.00
$4UO_2^{2+} + 7H_2O = (UO_2)_4(OH)_7^+ + 7H^+$	-21.90	-21.90
Uranyl phosphate complexes:		
$UO_2^{2+} + PO_4^{3-} = UO_2PO_4^-$	13.23	13.23
$UO_2^{2+} + PO_4^{3-} + H^+ = UO_2HPO_{4(aq)}$	19.59	18.32[g]
$UO_2^{2+} + PO_4^{3-} + 2H^+ = UO_2H_2PO_4^+$	22.82	20.15[g]
$UO_2^{2+} + PO_4^{3-} + 3H^+ = UO_2H_3PO_4^{2+}$	22.46	19.79[g]
$UO_2^{2+} + 2PO_4^{3-} + 4H^+ = UO_2(H_2PO_4)_{2(aq)}$	44.04	38.7[g]
$UO_2^{2+} + 2PO_4^{3-} + 5H^+ = UO_2(H_2PO_4)(H_3PO_4)^+$	45.05	39.71[g]
Uranyl carbonate complexes:		
$UO_2^{2+} + CO_3^{2-} = UO_2CO_{3(aq)}$	9.94	#
$UO_2^{2+} + 2CO_3^{2-} = UO_2(CO_3)_2^{2-}$	16.61	#
$UO_2^{2+} + 3CO_3^{2-} = UO_2(CO_3)_3^{4-}$	21.84	#
$3UO_2^{2+} + 6CO_3^{2-} = (UO_2)_3(CO_3)_6^{6-}$	54.0	#
$2UO_2^{2+} + 3H_2O + CO_3^{2-} = (UO_2)_2CO_3(OH)_3^- + 3H^+$	-0.858	#
$3UO_2^{2+} + 3H_2O + CO_3^{2-} = (UO_2)_3CO_3(OH)_3^+ + 3H^+$	0.652	#
$11UO_2^{2+} + 12H_2O + 6CO_3^{2-} = (UO_2)_{11}(CO_3)_6(OH)_{12}^{2-} + 6H^+$	36.412	#

Uranyl nitrate complex:		
$UO_2^{2+} + NO_3^- = UO_2NO_3^+$	0.3	#
Phosphate acid-base:		
$PO_4^{3-} + H^+ = HPO_4^{2-}$	12.35	11.08[g]
$PO_4^{3-} + 2H^+ = H_2PO_4^-$	19.56	17.35[g]
$PO_4^{3-} + 3H^+ = H_3PO_{4(aq)}$	21.70	19.03[g]
Carbonate acid-base:		
$CO_3^{2-} + H^+ = HCO_3^{--}$	10.327	#
$CO_3^{2-} + 2H^+ = H_2CO_3^*{}_{(aq)}$	16.68	#
$CO_3^{2-} + 2H^+ = CO_{2(g)} + H_2O$	18.152	#
Auxiliary reactions:		
$H_2O = OH^- + H^+$	-13.997[f]	-13.99
$Na^+ + CO_3^- = NaCO_3^-$	1.27[f]	#
$Na^+ + H^+ + CO_3^- = NaHCO_{3(aq)}$	10.079[f]	#

a From Guillaumont et al. [11] b From Grenthe et al. [58]
f From MINEQL$^+$ [54] database # Not considered by Cheng et al. [45]
g Phosphate acid-base data from Nilsson et al. [48] were incorrectly extrapolated to I = 0 M. The error propagated to constants for uranyl phosphate complexes when reactions were written in terms of the PO_4^{3-}.

Table B. Relevant solids and their solubility products at 298 K and I = 0 M.

Uranium and other solids #:	*Name*	$LogK_{sp}$
$UO_3{\cdot}2H_2O_{(s)} + 2H^+ = UO_2^{2+} + 3H_2O$	***Meta-schoepite***	5.6[d]
$H_3O(UO_2)(PO_4){\bullet}3H_2O_{(s)} = UO_2^{2+} + PO_4^{3-} + H^+ + 4H_2O$	***Chernikovite***	-24.20[b]
$UO_2HPO_4{\cdot}3H_2O_{(s)} = UO_2^{2+} + PO_4^{3-} + H^+ + 3H_2O$	***Uranium hydrogen phosphate***	-25.52[e]
$NaUO_2PO_4{\cdot}xH_2O_{(s)} = UO_2^{2+} + Na^+ + PO_4^{3-} + xH_2O$	***Sodium meta-autunite***	-23.64[b,c]
$UO_2(H_2PO_4)_2{\cdot}3H_2O_{(s)} = UO_2^{2+} + 2PO_4^{3-} + 4H^+ + 3H_2O$	***Uranyl phosphate hydrate***	-45.10[b]
$(UO_2)_3(PO_4)_2{\cdot}4H_2O_{(s)} = 3UO_2^{2+} + 2PO_4^{3-} + 4H_2O$	***Uranyl orthophosphate***	-49.36[b,e]
$UO_2CO_{3(s)} = UO_2^{2+} + CO_3^{2-}$	***Rutherfordine***	-14.76[a]
$Na_4UO_2(CO_3)_{3(s)} = UO_2^{2+} + 4Na^+ + 3CO_3^{2-}$		-27.18[a]
$UO_2(NO_3)_2{\cdot}6H_2O_{(s)} = UO_2^{2+} + 2NO_3^- + 6H_2O$		2.046[a]
$Na_2CO_3{\cdot}10H_2O_{(s)} = 2Na^+ + CO_3^{2-} + 10H_2O$	***Natron***	-1.311[f]

a From Guillaumont et al. [11] unless otherwise noted. b From Grenthe et al. [58]
c From Felmy et al. [59] d From Gorman-Lewis et al. [56]
e From Gorman-Lewis et al. [57] f From MINEQL$^+$ [54] database

Appendix 2-B: Modifications to the surface complexation model for U(VI)-PO_4^{3-}-Fe(III) ternary system developed by Cheng et al. [45].

(Submitted to *Geochimica et Cosmochimica Acta* as electronic annex to the main paper)

Motivation

The model of Cheng et al. was modified to predict uranium loss from solution over a broader range of uranium and phosphate concentrations. The modifications aimed at improving the integration of equilibrium constants of dissolved and surface species from previous studies and updating them as per the latest internally consistent thermodynamic database available.

Definitions

The surface complexation models developed by Cheng et al. [45], Nilsson et al. [48], and Lövgren et al.[61] will henceforth be referred to as the Cheng, Nilsson and Lövgren models, respectively. The method suggested by Sverjensky [62] to correct the $\log K_{int}$ values for differences in specific surface area and site density of a given sorbent is henceforth called the Sverjensky correction.

Overview of the original Cheng model

The surface complexation reactions and constants included in the original Cheng model are listed in Table 2-B1. Also included in the original model were aqueous uranium (U) and phosphate (P) reactions and other auxiliary reactions from the thermodynamic database compiled by Grenthe et al. [58]. These reactions and equilibrium constants are listed in Table A of the appendix to the paper. Goethite acid-base speciation reactions and constants were included from an independent study by Lövgren et al. [61]. These were conditional $\log K_{int}$ values valid at ionic strength (I) 0.1 M. Lövgren et al. had

previously estimated the surface site density of goethite (1.68 sites/ nm^2) by acid-base titration and optimized the electrostatic model at a specific capacitance value of 1.28 F/m^2. This constant capacitance model was preserved in the Cheng model. In a subsequent study by the same group [48], the constant capacitance model of Lövgren et al. was expanded to describe phosphate adsorption onto goethite by using three mononuclear phosphate surface complexation reactions listed in Table 2-B1.

Table 2-B1. Surface complexation reactions and constants at 298 K and I = 0.1 M included in the original Cheng model

Reaction	$LogK_{int,}$	Reference
Acid-base reactions on goethite surface:		
$\equiv FeOH + H^+ = \equiv FeOH_2^+$	7.47	[61]
$\equiv FeOH = \equiv FeO^- + H^+$	-9.51	
Phosphate surface complexation:		
$\equiv FeOH + 3H^+ + PO_4^{3-} = \equiv FePO_4H_2 + H_2O$	30.03	[48]
$\equiv FeOH + 2H^+ + PO_4^{3-} = \equiv FePO_4H^- + H_2O$	25.28	
$\equiv FeOH + H^+ + PO_4^{3-} = \equiv FePO_4^{2-} + H_2O$	19.51	
Uranyl surface complexation:		
$\equiv Fe(OH)_2 + UO_2^{2+} = \equiv FeO_2UO_2 + 2H^+$	-4.66	Cheng et al. [45]
Ternary surface complexation:		
$\equiv FeOH + UO_2^{2+} + H^+ + PO_4^{3-} = \equiv FePO_4UO_2 + H_2O$	27.95	Cheng et al. [45]

Cheng et al. obtained a surface site density of 3.23 sites/nm^2 by fitting their data for phosphate adsorption onto goethite-coated sand in the absence of U(VI) using the reactions in the Nilsson sub-model without modifications. Using this site density value and the goethite acid-base speciation constants derived by Lövgren et al., U(VI) adsorption to goethite-coated sand in the absence of phosphate was modeled. The conditional $logK_{int}$ value for an inner-sphere mononuclear bidentate uranyl surface

complex, $\equiv FeO_2UO_2$, listed in Table 2-B1 was calculated. Finally, data for U(VI) adsorption to goethite-coated sand in the presence of phosphate was modeled by including the Nilsson sub-model, the uranyl surface complex, and a ternary surface complex containing U(VI) and phosphate, $\equiv FePO_4UO_2$, that explained enhanced uranium uptake. A conditional $\log K_{int}$ for the ternary surface complex, listed in Table 2-B1, was determined [45].

Modifications to the Cheng model were made in a sequence of five steps as per the objectives discussed in the paper (Fig. 2.1). These are described in detail below.

Step 1: **Verification of goethite acid-base log K_{int} values obtained by Lövgren et al. [61]**

The aim of fitting these constants was to verify that the reported log K_{int} values were conditional (specific to 0.1 M ionic strength) and to check the convergence of separate fits, obtained first by using FITEQL 4.0 [70], and thereafter employing forward fits with MINEQL$^+$ [54]. This fitting approach was used for modifications to subsequent models.

Table 2-B2 lists the experimental conditions and parameters, aqueous speciation reactions and constants, and surface reactions included in the original Lövgren model. Since the data corresponded to I = 0.1 M, $\log K_w$ for water was adjusted to -13.78 using the Davies equation. Using listed parameters and $\log K_w$ as inputs, goethite protonation-deprotonation data from Lövgren et al. were modeled using FITEQL 4.0 to obtain conditional $\log K_{int}$ values. Data were entered as $-\log[H^+]$, and not as –log[59], against the corresponding total proton concentration (TOTH). Our fit results match closely with those obtained by Lövgren et al. and are *shown in italics* in Table 2-B2. True $\log K_{int}$ values were then computed using the Davies equation and entered into MINEQL$^+$ to

arrive at forward fit predictions to the data at I = 0.1 M. The Lövgren et al. data and our FITEQL 4.0 and MINEQL$^+$ fits are shown in Fig. 2-B1. The close convergence of the two fitting approaches and their excellent predictions of the Lövgren et al. data confirmed that the logK_{int} values reported by Lövgren et al. were indeed conditional to I = 0.1 M.

Table 2-B2. Lövgren surface complexation model at 298 K

Experimental and model parameters	**Lövgren model**	***Our fit, FITEQL***
Site density, N_s (sites/ nm^2)	1.68	1.68
[solids], g/L	11	11
Specific surface area of goethite, A_s (m^2/g)	39.9	39.9
$[\equiv FeOH]_t$, M	0.00122	0.00122
Aqueous reactions (I = 0.1 M):		
$H_2O = OH^- + H^+$	-13.78	-13.78
Acid-base reactions on goethite surface (I = 0.1 M) (conditional logK_{int}):		
$\equiv FeOH + H^+ = \equiv FeOH_2^+$	7.47 *(7.58 at I = 0 M)*	*7.44*
$\equiv FeOH = \equiv FeO^- + H^+$	-9.51 *(-9.62 at I = 0 M)*	*-9.57*

italicized numbers indicate modifications to the existing model or updated surface constants

Furthermore, MINEQL$^+$ requires the acid-base logK values as well as logK_{int} values to be true (I = 0 M) and not conditional constants. MINEQL$^+$ calculates activity coefficients for ionic species for the specified ionic strength using the Davies equation. After successful verification of the Lövgren model, the original logK_{int} values were retained as inputs to subsequent models (Nilsson and Cheng).

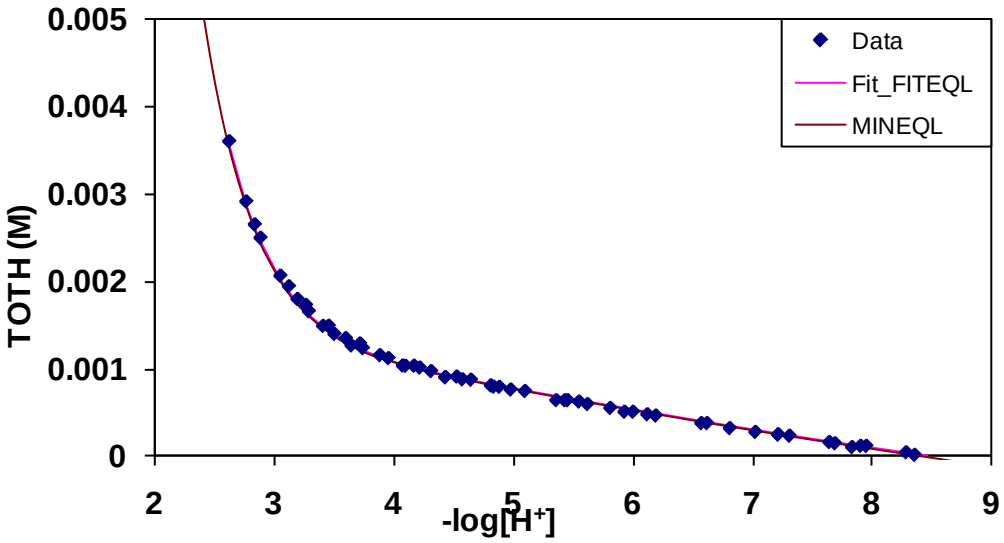

Fig. 2-B1. Goethite acid-base titration data from Lövgren et al. and our fit results

Step 2: **Determination of updated logK_{int} values for phosphate surface complexation reactions included in the Nilsson model**

Using goethite acid-base logK_{int} values from the Lövgren model and PO_4^{3-} acid-base logK values reported in Guillaumont et al. [11], phosphate adsorption data from Nilsson et al. [48] were modeled to obtain updated logK_{int} values for the three phosphate species adsorbed to the goethite surface included in the Nilsson model. This task was accomplished in two steps as outlined below:

2a) Replicating Nilsson model fits

This procedure involved using the reported PO_4^{3-} acid-base logK values from Nilsson et al. along with logK_w at I = 0.1M and fitting their data using FITEQL 4.0 and MINEQL$^+$. The surface complexation reactions and experimental parameters are listed in Table 2-B3.

LogK_{int} values for phosphate surface complexation reactions were obtained by simultaneously fitting two sets of adsorption data corresponding to two TOTP levels.

Table 2-B3. Reactions and constants in the Nilsson model at 298 K and I = 0.1 M.		
Experimental and model parameters	**Nilsson et al. reported**	***Our FITEQL fit***
Site density, N_s (sites/ nm^2)	1.68	1.68
[solids], g/L	11 (7)*	7
Specific surface area of goethite, A_s (m^2/g)	39.9	39.9
$[\equiv FeOH]_t$, M	0.0008	0.0008
Acid-base reactions on goethite surface (from Lövgren model):		
$\equiv FeOH + H^+ = \equiv FeOH_2^+$	7.47	7.47
$\equiv FeOH = \equiv FeO^- + H^+$	-9.51	-9.51
Phosphate acid-base aqueous reactions:		
$H^+ + PO_4^{3-} = HPO_4^{2-}$	11.74	11.74
$2H^+ + PO_4^{3-} = H_2PO_4^-$	18.45	18.45
$3H^+ + PO_4^{3-} = H_3PO_{4(aq)}$	20.35	20.35
Phosphate surface complexation reactions: #		
$\equiv FeOH + 3H^+ + PO_4^{3-} = \equiv FePO_4H_2 + H_2O$	31.13	*30.97*
$\equiv FeOH + 2H^+ + PO_4^{3-} = \equiv FePO_4H^- + H_2O$	26.38	*25.67*
$\equiv FeOH + H^+ + PO_4^{3-} = \equiv FePO_4^{2-} + H_2O$	20.61	*18.6*

italicized numbers indicate modifications to the existing model or updated surface constants

* Nilsson et al. [48] reported 11 g/L, but it appears that they may have actually used a lower concentration (7 g/L). They used $\log K_{int}$ values for goethite acid-base from their previous work [61] wherein site density was independently estimated to be 1.68 sites/nm^2. Lövgren et al. had used 11 g/L goethite suspension giving total surface sites concentration, $[=FeOH]_t$ = 1.2 mM. However, Nilsson et al. reported all their data relative to $[=FeOH]_t$ = 0.8 mM without independently estimating the site densities or explicitly stating the value they had used. Assuming that they kept the same site density as Lövgren et al. found, it appears that they may have used a less concentrated goethite suspension (7 g/L). This concentration was also reported in a related aluminum sorption study in the original paper [61], wherein all results were reported with respect to $[=FeOH]_t$ = 0.8 mM. Moreover, the fit became poorer when 11 g/L with a lower site density (1.1 sites/nm^2) was used.

The fitting results reported by Nilsson et al. were compared with what we achieved (in *italics*) (Table 2-B3). Nilsson et al. had obtained $\log K_{int}$ values using their surface charge (Z_b) vs $-\log[H^+]$ data from titrations with goethite and phosphate at I = 0.1 M, and they used these constants to accurately predict their phosphate adsorption data. Instead, in our fitting approach we used their adsorption data to optimize $\log K_{int}$ values. Both these approaches fit the adsorption data well. Whereas $\log K_{int}$ for the first two phosphate surface complexation reactions were similar to those in the Nilsson model, the value for the third reaction was lower by two orders of magnitude (Table 2-B3).

The data from Nilsson et al. and our FITEQL fitting results using the updated and original Nilsson $\log K_{int}$ values for the two TOTP conditions are shown in Fig. 2-B2. Fits were better for the updated $\log K_{int}$ values obtained in this work. FITEQL fits and results from MINEQL$^+$ calculations were in excellent agreement with each other (not shown).

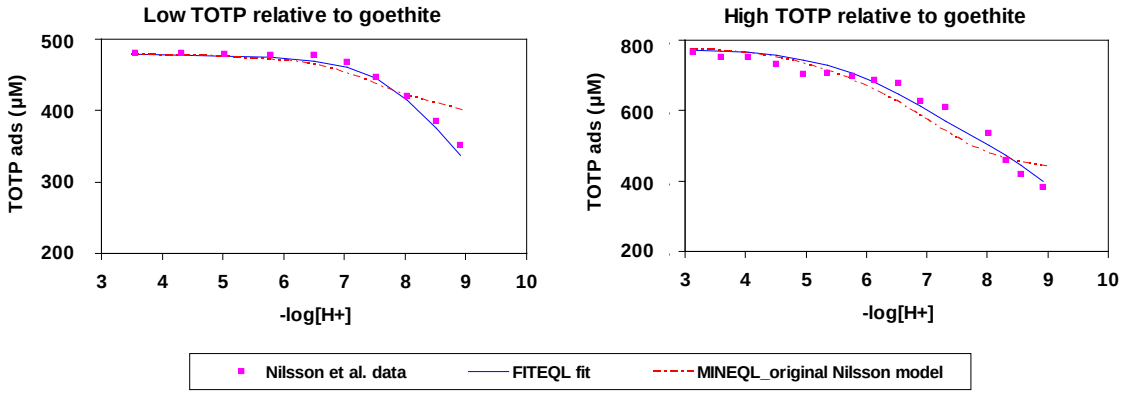

Fig. 2-B2. Phosphate adsorption to goethite data from Nilsson et al. [48] and our fit results

2b) Fitting Nilsson et al. data using phosphate acid-base reactions as reported in the Nuclear Energy Agency (NEA) database [11].

In this step, PO_4^{3-} acid-base reactions were updated based on the auxiliary data published in the most recent critical review of uranium chemical thermodynamics [11]. FITEQL and MINEQL$^+$ fits to the Nilsson et al. data, obtained as in step 2a, were in excellent agreement with each other and described the data very well (Fig. 2-B3). The $\log K_{int}$ results obtained in this step were similar to those in step 2a (Table 2-B4), since the two sets of acid-base constants themselves were not very different. Again, the $\log K_{int}$ for the surface complex, $\equiv FePO_4^{2-}$, was about two orders of magnitude lower than that reported in the Nilsson model (Table 2-B3). The updated $\log K_{int}$ values obtained in this step were subsequently used for the sake of consistency.

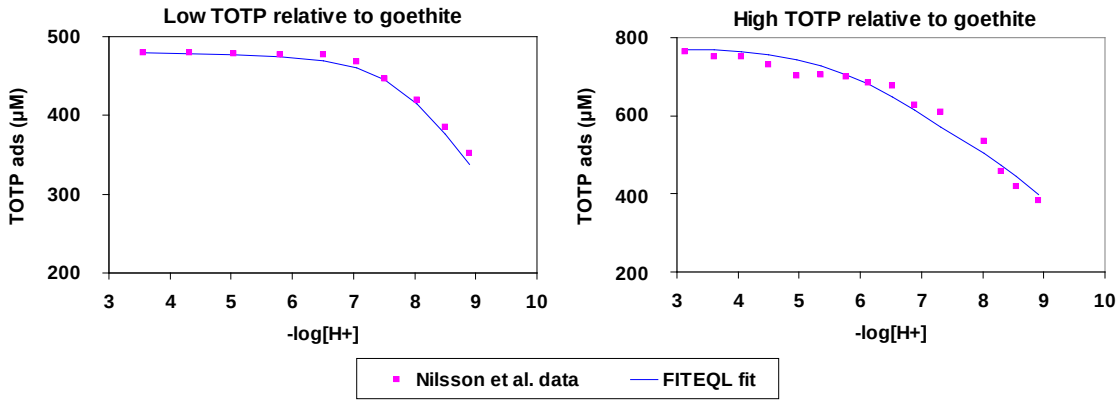

Fig. 2-B3. Nilsson et al. phosphate adsorption data and our fits results using updated PO_4^{3-} acid-base reaction constants.

Table 2-B4. Reactions and constants at 298 K and I = 0.1 M.		
Experimental and model parameters	**Nilsson et al., our fit using their PO_4^{3-} acid-base constants (step 2a)**	***Nilsson et al., our fit using NEA[a] PO_4^{3-} acid-base constants***
Site density, N_s (sites/ nm^2)	1.68	1.68
[solids], g/L	7	7
Specific surface area of goethite, A_s (m^2/g)	39.9	39.9
$[\equiv FeOH]_t$, M	0.0008	0.0008
Acid-base reactions on goethite surface (from Lövgren model):		
$\equiv FeOH + H^+ = \equiv FeOH_2^+$	7.47	7.47
$\equiv FeOH = \equiv FeO^- + H^+$	-9.51	-9.51
Phosphate acid-base aqueous reactions:		
$H^+ + PO_4^{3-} = HPO_4^{2-}$	11.74	*11.69*
$2H^+ + PO_4^{3-} = H_2PO_4^-$	18.45	*18.45*
$3H^+ + PO_4^{3-} = H_3PO_{4(aq)}$	20.35	*20.37*
Phosphate surface complexation reactions:		
$\equiv FeOH + 3H^+ + PO_4^{3-} = \equiv FePO_4H_2 + H_2O$	30.97	*30.95*
$\equiv FeOH + 2H^+ + PO_4^{3-} = \equiv FePO_4H^- + H_2O$	25.67	*25.62*
$\equiv FeOH + H^+ + PO_4^{3-} = \equiv FePO_4^{2-} + H_2O$	18.6	*18.54*

italicized numbers indicate modifications to the existing model or updated surface constants

a Nuclear Energy Agency is a specialized agency within the Organization for Economic Co-operation and Development (OECD) countries that assists in developing international cooperation for safe and eco-friendly use of nuclear energy for peaceful purposes.

Step 3: **Determination of Cheng et al. surface site density by optimization of their phosphate adsorption data using Nilsson sub-model.**

Cheng et al. modeled their phosphate adsorption to goethite-coated sand (gcs) data in the absence of uranium to obtain a surface site density (N_s) of goethite. The $\log K_{int}$ values reported by Lövgren et al. and Nilsson et al. were used as sub-models without correcting them to account for the differences in the specific surface area (A_s) and N_s of goethite used in the two studies. Data for only one TOTP and gcs condition (out of four studied) was used for fitting.

In this step, we tried to update these $\log K_{int}$ by, a) applying the Sverjensky correction to account for differences in A_s and N_s; b) updating PO_4^{3-} acid-base aqueous constants to those reported by the Guillaumont et al.; c) using all four TOTP-gcs conditions in fitting; and d) using the updated Nilsson model for describing phosphate surface complexation to goethite. The surface complexation reactions, relevant experimental and model parameters for the Nilsson model derived in step 2b, and the parameters for our fit to phosphate adsorption data from Cheng et al. are shown in Table 2-B5. Also *italicized* are final Sverjensky-corrected $\log K_{int}$ values using the N_s optimized in this step.

The main paper includes a brief description of the Sverjensky method for adjusting the $\log K_{int}$ values of a sorbent to account for differences in the A_s and N_s values for specific materials used in different studies. The following equation, reproduced from the paper, is used in subsequent modifications to the existing models.

$$K_{\text{int},2} = K_{\text{int},1} \cdot \frac{N_{s,1} A_{s,1}}{N_{s,2} A_{s,2}} \qquad (2)$$

Subscripts 1 and 2 respectively refer to the original and derived models.

Table 2-B5. Original and modified surface complexation models at 298 K at I = 0.1 M.			
Experimental and model parameters	**Original Cheng model**	**Nilsson et al. data, our fit from step 2b**	**Cheng et al. data, *our fit***
Site density, N_s (sites/ nm^2)	3.23	1.68	*Varied, final 2.31*
[solids], g/L	3.33	7	3.33, 33.3
Specific surface area of gcs, A_s (m^2/g)	1.25	NA	1.25
Specific surface area of goethite, (m^2/g)	149	39.9	*39.9, assumed for Sverjensky correction*
$[\equiv FeOH]_t$, M	$2.23\cdot10^{-5}$	$8\cdot10^{-4}$	$1.59\cdot10^{-5}$ $1.59\cdot10^{-4}$
Acid-base reactions on goethite surface:		**LogK$_{int}$**	
$\equiv FeOH + H^+ = \equiv FeOH_2^+$	7.47	7.47	*7.33*[a]
$\equiv FeOH = \equiv FeO^- + H^+$	-9.51	-9.51	*-9.65*[a]
Phosphate acid-base aqueous reactions:		**LogK**	
$H^+ + PO_4^{3-} = HPO_4^{2-}$	11.74	11.69	11.69
$2H^+ + PO_4^{3-} = H_2PO_4^-$	18.45	18.45	18.45
$3H^+ + PO_4^{3-} = H_3PO_{4(aq)}$	20.35	20.37	20.37
Phosphate surface complexation reactions:		**LogK$_{int}$**	
$\equiv FeOH + 3H^+ + PO_4^{3-} = \equiv FePO_4H_2 + H_2O$	30.03	30.95	*30.81*[a]
$\equiv FeOH + 2H^+ + PO_4^{3-} = \equiv FePO_4H^- + H_2O$	25.28	25.62	*25.48*[a]
$\equiv FeOH + H^+ + PO_4^{3-} = \equiv FePO_4^{2-} + H_2O$	19.51	18.54	*18.40*[a]

a *italicized* numbers indicate modifications to the existing model or updated surface constants after Sverjensky correction using the optimized N_s (2.31 sites/nm^2)

For Sverjensky corrections specific to the solid, A_s of goethite instead of gcs was used. Cheng et al. did not report an independent measurement of goethite A_s but indirectly estimated it to be 149 m^2/g based on dithionate extractable Fe and the measured gcs A_s (1.25 m^2/g). This estimate is unexpectedly high for goethite. Although the estimate of Cheng et al. was within the range of A_s values (80 – 150 m^2/g) reported [71]

for their goethite synthesis method (oxidation of Fe(II) at pH 6-7), the estimate depended strongly on the accuracy of the measurement of iron extracted from gcs. Fitting their data with an A_s of 149 m^2/g or 80 m^2/g resulted in poor fits. Even though the goethite synthesis method used by Nilsson et al. (and our study) was different from the method employed by Cheng et al., for consistency a value of 39.9 m^2/g was used for applying the Sverjensky correction.

Forward modeling was done using MINEQL$^+$ to fit four sets of adsorption data reported by Cheng et al. [45]. The four sets were combinations of two TOTP and two gcs concentration levels. For the choice of A_s (39.9 m^2/g), site densities were varied to arrive at the best fit with global minimum root mean squared (rms) error. The fit rms error was estimated by calculating the square root of the mean of the squares of differences between predicted and dissolved percent adsorbed values for each of the four conditions. The fitting was done iteratively. First, assuming the site density (1.68 sites/nm^2) of the updated Nilsson model derived in step 2b, the Sverjensky correction was applied to the $logK_{int}$ values from the Nilsson model to obtain Cheng et al. system-specific $logK_{int}$ values. Second, predictions relevant to all four adsorption conditions were made using MINEQL$^+$, and the error was calculated against the Cheng et al. data. Third, the fit was refined by assuming a new site density and the whole process was repeated until a satisfactory fit to the four sets of data was obtained. Model predictions corresponding to a few site density assumptions are shown in Fig. 2-B4, and the respective error calculation results are summarized in Table 2-B6. The best fit was achieved at 2.31 sites/nm^2; having the least rms error of 6.57. A value of 2.31 instead of just 2.3 was chosen as it is a recommended global optimum site density [72].

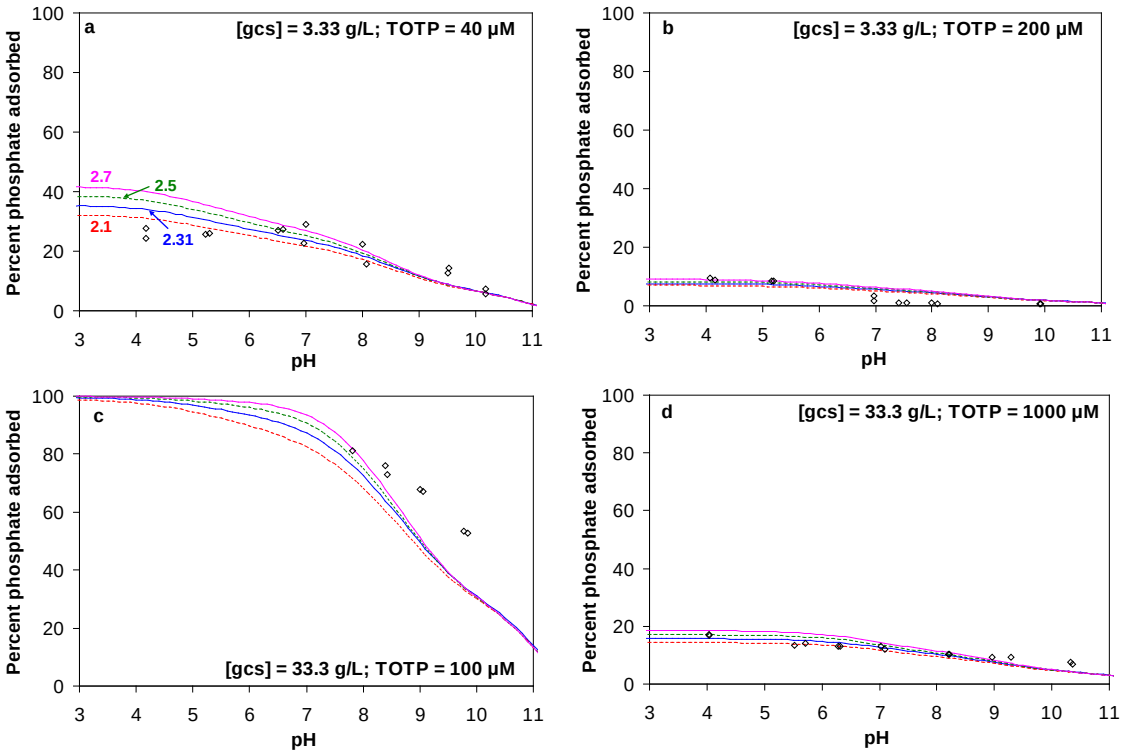

Fig. 2-B4. Fitting results at various surface site densities for Cheng phosphate adsorption in the absence of uranium data for gcs with 39.9 m^2/g surface area. Symbols represent data and various colored lines correspond to model fits with specific site densities.

Table 2-B6 Error results for various site densities and surface area values

A_s (m^2/g)	39.9	80	149
Site density, N_s	**Overall root mean squared (rms) error[a]**		
1.68			12.20
2.1	7.73		
2.31	*6.57*	8.92	11.09
2.4	7.04		
2.5	6.94		
2.7	6.93	9.16	11.37

[a] rms error = $\sqrt{\sum_{i=1}^{N}(x_m - x_p)^2 / N}$, where x_m and x_p respectively represent measured and predicted concentrations, and N is the total number of data points included in the fit (here, 47).

The best fit matched measured data quite well for most conditions, except at high pH for the high [gcs] and high TOTP condition (Fig. 2-B4c). The model predictions

could be improved by choosing different logK values for adsorbed phosphate species. However, such modification would involve significant deviation from the existing modeling framework that integrates Nilsson and Lövgren models.

Step 4: Determination of $logK_{int}$ for the formation of $\equiv FeO_2UO_2$ surface complex by fitting Cheng phosphate-free U(VI) adsorption data

Cheng et al. recorded two sets of adsorption data corresponding to two levels of gcs concentrations, with the same fixed TOTU concentration (5 μM). The Cheng model incorporated the Lövgren sub-model for goethite acid-base speciation and estimated a conditional $logK_{int}$ of -4.66 for $\equiv FeO_2UO_2$ by fitting their data at the higher gcs concentration (33.3 g/L). For the lower gcs concentration (3.33 g/L), their model overpredicted adsorption. The experimental and model parameters and the surface complexation reactions included in the fits are summarized in Table 2-B7.

Table 2-B7. Original and modified surface complexation models at 298 K at I = 0.1 M.

Experimental and model parameters	***Original Cheng model***	**Cheng U data, *our fit***
Site density, N_s (sites/ nm^2)	3.23	2.31 (from step 3)
[solids], g/L	33.3	3.33, 33.3
Specific surface area of gcs, A_s (m^2/g)	1.25	1.25
$[\equiv FeOH]_t$, M	$2.23 \cdot 10^{-4}$	$1.59 \cdot 10^{-5}$, $1.59 \cdot 10^{-4}$
Specific surface area of goethite, (m^2/g)	149	*39.9, assumed for Sverjensky correction*
Acid-base on goethite surface:	**$LogK_{int}$**	
$\equiv FeOH + H^+ = \equiv FeOH_2^+$	7.47	*7.33*[a]
$\equiv FeOH = \equiv FeO^- + H^+$	-9.51	*-9.65*[a]
Uranyl surface complexation reaction:		
$\equiv Fe(OH)_2 + UO_2^{2+} = \equiv FeO_2UO_2 + 2H^+$	-4.66	*-4.72*

\# *italicized* numbers indicate modifications to the existing model or updated surface constants

[a] from Lövgren model after Sverjensky correction

Our corrections to the Cheng et al. $\log K_{int}$ fits were threefold; 1) we used U(VI) aqueous speciation logK values from Guillaumont et al. (2003) (Table A), while Cheng et al. sourced them from Grenthe et al. (1992); 2) we corrected the estimated goethite acid-base $\log K_{int}$ values by applying the Sverjensky correction (after assuming goethite A_s as 39.9 m^2/g); 3) we used the updated site density of 2.31 sites/nm^2.

MINEQL$^+$ was used to forward fit the U(VI) adsorption data of Cheng et al. The data and model suggest a primarily carbonate-free system. Our model calculations initially included U(VI)-carbonate complexes, but the resulting fits were poorer than without them. Therefore, fitting was performed for a closed system with no dissolved carbonate. Unlike in the original work, data corresponding to both concentrations of gcs were used for fitting to extend the model to a broader range of TOTU/TOT≡FeOH ratios. The best fit corresponds to a true $\log K_{int}$ of -4.5, i.e. a conditional $\log K_{int}$ of -4.72 (at I = 0.1 M) (Fig. 2-B5). It has the least rms error (Table 2-B8). Since the number of data points at low [gcs] was higher than those at high [gcs], the final fit predicts U(VI) adsorption at lower [gcs] quite well but underpredicts adsorption for higher [gcs]. The inability of the model to accurately predict data at both [gcs] suggests that there could be two types of binding sites present on the goethite surface. However, we have preserved the single site binding Cheng model for consistency.

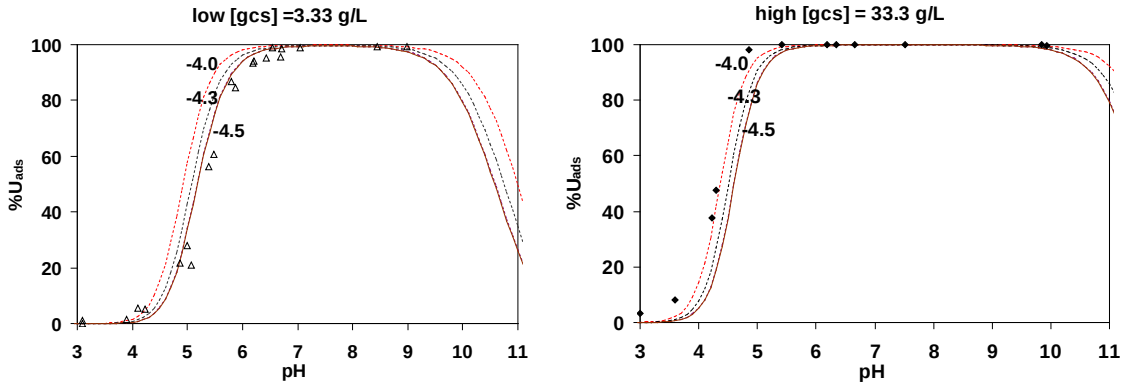

log K_{int} value of -4.5 at I = 0 M corresponds to -4.72 at I = 0.1 M

Fig. 2-B5 Fitting results for U(VI) adsorption data in the absence of phosphate. Site density of 2.31 sites/nm^2 estimated in step 3 was used. Symbols represent data and various colored lines correspond to model fits with specific site densities.

Table 2-B8 Rms error results for different logK_{int} values in fitting adsorbed U(VI) data

logK_{int}	-4	-4.3	-4.4	*-4.5*	-4.52	-4.55	-4.6
U Fit error sum	13.40	9.88	9.73	*9.48*	9.49	9.52	9.64

Note: The total number of data points included in the optimization was 33.

Step 5: **Determination of logK_{int} values for the formation of the ≡$FePO_4UO_2$ surface complex.**

Cheng et al. extended the U(VI) adsorption model discussed in step 4 to conditions in the presence of phosphate by including the Nilsson model as a sub-model. LogK_{int} values obtained earlier by Lövgren et al., Nilsson et al., and Cheng et al. for goethite acid-base speciation, phosphate surface complexation, and uranyl binary surface complexation reactions, respectively, were included without any modifications. A ternary surface complex, ≡$FePO_4UO_2$, was added to their model to account for the effect of phosphate on U(VI) adsorption to goethite. Uranium and phosphate adsorption data were collected for four combinations of [gcs] and TOTP at a fixed TOTU (5 μM)

concentration. Cheng et al. obtained $\log K_{int}$ values for the ternary surface complex by fitting U(VI) adsorption data to only one of these four sets of conditions, i.e. for TOTP = 100 μM and [gcs] = 33.3 g/L. U(VI) adsorption data for the other three sets of conditions and phosphate co-sorption data for all the four conditions were not included in this fitting procedure. The parameters, surface complexation reactions and constants included in the original and modified Cheng models are summarized in Table 2-B9.

Table 2-B9. Original and updated Cheng model parameters, reactions and constants at 298 K for I = 0.1 M

Experimental and model parameters	**Original Cheng model**	**Cheng U(VI) & PO_4 data, *our fit***
Site density, N_s (sites/ nm^2) [gcs], g/L Specific surface area of gcs, A_s (m^2/g) $[\equiv FeOH]_t$, M Specific surface area of goethite, (m^2/g)	3.23 33.3 1.25 $2.23\cdot10^{-4}$ 149	*2.31* 3.33, 33.3 1.25 $1.59\cdot10^{-5}$, $1.59\cdot10^{-4}$ 39.9, assumed for Sverjensky correction
Reaction	**$\log K_{int}$**	
Acid-base reactions on goethite surface:		
$\equiv FeOH + H^+ = \equiv FeOH_2^+$	7.47	*7.33*[a]
$\equiv FeOH = \equiv FeO^- + H^+$	-9.51	*-9.65*[a]
Phosphate surface complexation:		
$\equiv FeOH + 3H^+ + PO_4^{3-} = \equiv FePO_4H_2 + H_2O$	30.03	*30.81*[b]
$\equiv FeOH + 2H^+ + PO_4^{3-} = \equiv FePO_4H^- + H_2O$	25.28	*25.48*[b]
$\equiv FeOH + H^+ + PO_4^{3-} = \equiv FePO_4^{2-} + H_2O$	19.51	*18.40*[b]
Uranyl surface complexation:		
$\equiv Fe(OH)_2 + UO_2^{2+} = \equiv FeO_2UO_2 + 2H^+$	-4.66	*-4.72*
Ternary surface complexation:		
$\equiv FeOH + UO_2^{2+} + H^+ + PO_4^{3-} = \equiv FePO_4UO_2 + H_2O$	27.95	*28.81*

\# *italicized* numbers indicate modifications to the existing model or updated surface constants
a from Lövgren model after Sverjensky correction
b from updated Nilsson model after Sverjensky correction

Our modifications to the Cheng model were as follows: 1) we used logK values for aqueous uranium and phosphate species from the Guillaumont et al. review (Table A); 2) we included relevant uranium-containing solids (Table B) while optimizing the surface complexation model, because some conditions studied by Cheng et al. could have been supersaturated with respect to sodium meta-autunite; 3) we integrated the $logK_{int}$ for goethite acid-base and phosphate surface complexation reactions from Lövgren and Nilsson models, respectively, after Sverjensky correction; 4) we used a surface site density (2.31 sites/nm^2) from step 3 and $logK_{int}$ (-4.72 at I = 0.1 M) for $\equiv FeO_2UO_2$ formation from step 4; 5) we simultaneously modeled U(VI) and phosphate adsorption data corresponding to all four sets of TOTP-[gcs] conditions.

Forward fitting of data in $MINEQL^+$ involved the assumption of a $logK_{int}$ for the ternary surface complex, $\equiv FePO_4UO_2$, and calculation of the global rms errors between model predictions and observed data. Error estimates for some of the assumed $logK_{int}$ values are listed in Table 2-B10. The best fit was achieved for $logK_{int}$ of 30.35 at I =0 M (conditional $logK_{int}$ of 28.81 at I =0.1 M). Model calculations excluding the ternary surface complex were also tried, but they resulted in poor fits. U(VI) and phosphate uptake data and best fit results are shown in Fig. 2-B6.

Table 2-B10. Rms error results for different $logK_{int}$ values used for fitting adsorbed U(VI) data

$logK_{int}$	31	30.4	30.36	30.35	30.33	30	No ternary complex
U Fit error sum	15.36	11.82	11.805	*11.804*	11.808	12.94	29.51
P Fit error sum	6.27	6.42	6.428	*6.425*	6.423	6.45	6.78
Overall error sum	16.59	13.46	13.442	*13.440*	13.442	14.46	30.28

Note: The total number of data points included in the optimization was 59.

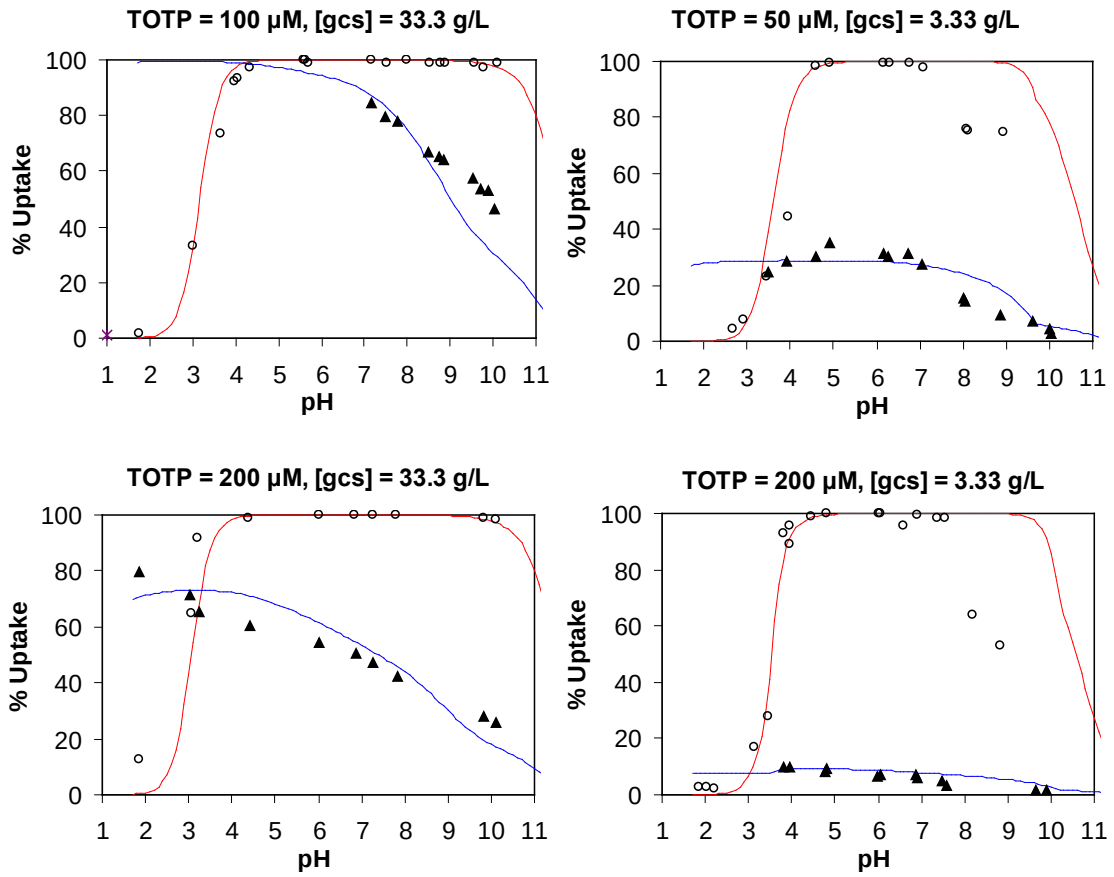

log K_{int} value of 30.35 for modified Cheng model at I = 0 M corresponds to 28.81 at I = 0.1 M

Fig. 2-B6. Best fit results for Cheng et al. U(VI) and phosphate adsorption data at 5 µM TOTU to obtain log K_{int} for the species, ≡$FePO_4UO_2$. Open and closed symbols represent U(VI) and phosphate uptake, respectively. The red and blue lines correspond to U(VI) and phosphate model fits, respectively.

The modified Cheng model provides a good fit to U(VI) and phosphate uptake data for most conditions, except for U uptake at high pH and low [gcs] = 3.33 g/L where favorable uranyl carbonate aqueous complexation may have limited uranium uptake. The quality of these fits is similar to those obtained by Cheng et al. [45] for their original model. Hence, this model was used to predict dissolved, adsorbed, and precipitated uranium and phosphate speciation for the range of conditions studied in our experimental work. To be able to predict equilibrium speciation for our conditions, logK_{int} values from the modified Cheng model (at I = 0.1 M) were first adjusted for differences in sorbent

properties using the Sverjensky correction (eq. 2) and later corrected for ionic strength differences using the Davies equation. We chose the site density from Lövgren et al. (1.68 sites/nm^2) since our goethite synthesis method and the measured A_s value (39.9 m^2/g) were the same as reported by Lövgren et al. (and Nilsson et al.) but different from that of Cheng et al. Moreover, the goethite surface site density was independently calculated by Lövgren et al. from a surface protonation-deprotonation study unlike the site density obtained for the modified Cheng model (2.31 sites/nm^2). A brief comparative summary of the original and modified Cheng models with that used in the present work is provided in Table 2-B11.

Table 2-B11. Cheng surface complexation model and reactions at 298 K.

Experimental and model parameters	**Original model**	**Modified model**	**Present Work**
Site density, N_s (sites/ nm^2)	3.23	2.31	1.68
Specific surface area of goethite, A_s (m^2/g)	149	39.9	39.9
Reaction	**I = 0.1 M**		**I = 0 M**
	$LogK_{int}$		
$\equiv FeOH + H^+ = \equiv FeOH_2^+$	7.47	7.33	7.58
$\equiv FeOH = \equiv FeO^- + H^+$	-9.51	-9.65	-9.62
$\equiv FeOH + 3H^+ + PO_4^{3-} = \equiv FePO_4H_2 + H_2O$	30.03	30.81	32.27
$\equiv FeOH + 2H^+ + PO_4^{3-} = \equiv FePO_4H^- + H_2O$	25.28	25.48	26.83
$\equiv FeOH + H^+ + PO_4^{3-} = \equiv FePO_4^{2-} + H_2O$	19.51	18.40	19.64
$\equiv Fe(OH)_2 + UO_2^{2+} = \equiv FeO_2UO_2 + 2H^+$	-4.66	-4.72	-4.36
$\equiv FeOH + UO_2^{2+} + H^+ + PO_4^{3-} = \equiv FePO_4UO_2 + H_2O$	27.95	28.81	30.49
Phosphate acid-base aqueous reactions	**LogK**		
$H^+ + PO_4^{3-} = HPO_4^{2-}$	11.74	11.69	12.35
$2H^+ + PO_4^{3-} = H_2PO_4^-$	18.45	18.45	19.56
$3H^+ + PO_4^{3-} = H_3PO_{4(aq)}$	20.35	20.37	21.70

Chapter 3 Molecular-scale structure of uranium(VI) immobilized with goethite and phosphate

3.1. Introduction

Past mining, processing, and waste disposal activities have left a legacy of uranium-contaminated soil and groundwater. Phosphate addition to subsurface environments can potentially immobilize U(VI) in-situ through interactions with uranium at mineral-water interfaces. Phosphate-enhanced metal uptake on mineral surfaces has been studied previously. Lead uptake on goethite was enhanced due to alterations to the surface charge caused by favorable phosphate adsorption [1]. In a field experiment at a contaminated site in Florida, phosphate promoted the immobilization of lead, zinc and copper [2]. Phosphate-containing fertilizers decreased the leachability of cadmium from contaminated soils and promoted more stable forms of cadmium that were bound to manganese and iron oxides [3]. The use of the phosphate mineral apatite to remediate heavy metal contamination by enhancing adsorption or by inducing precipitation of metal phosphates is well demonstrated [4, 5].

The presence of phosphate can also affect U(VI) interactions with subsurface minerals and iron oxyhydroxides. Dominance of inner-sphere uranyl phosphate ternary surface complexes on subsurface media from DOE waste sites was suggested [6]. Enhanced uptake of U(VI) on Fe(III) oxides in bench-scale studies was considered to be facilitated by the formation of uranyl-phosphate-Fe(III) oxide ternary surface complexes

[7-9] when conditions were undersaturated with respect to uranium phosphate precipitation. However, spectroscopic evidence for the structure of this ternary surface complex has not yet been reported.

At higher U concentrations formation of uranium phosphate solids in the presence of minerals may be important. At Koongarra (Australia) uranium uptake was considered to be initiated by adsorption onto ferrihydrite, and to subsequently be dominated by formation of U, P, and Mg or Cu-containing nanocrystals during transformation of ferrihydrite to goethite and hematite [10, 11]. Stability of the natural U deposits containing barium uranyl phosphates at the Coles Hill site in south central Virginia was estimated to be 150,000 years [12]. Autunite-like uranyl phosphate phases were found in the contaminated soils at the Fernald Environmental Management Project (FEMP) in Ohio [13, 14] and at the Oak Ridge National Lab [15]. U primarily existed as meta-torbernite [$Cu(UO_2PO_4)_2 \cdot 8H_2O_{(s)}$] in the intermediate vadose zone beneath former process ponds at the Hanford site (Washington, U.S.A.) [16-19].

Information on the coordination environment of uranium will be helpful in identifying U(VI) uptake mechanisms in the presence of phosphate and iron oxyhydroxides. Several past studies have probed the molecular-scale information on individual component interactions of the U(VI)-phosphate-iron oxide system- U(VI) adsorption to iron oxides, phosphate adsorption to iron oxides, structures of uranium phosphate precipitates. In the absence of phosphate, uranium uptake at low pH on ferrihydrite [20, 21], hematite [22] and goethite [23] was facilitated by the formation of a favorable bidentate edge-sharing surface complex (U-Fe distance ~ 3.45 Å in

≡$Fe(OH)_2UO_2$). For carbonate-free conditions, a recent study on U(VI) complexation on goethite proposed the existence of a bidentate corner-sharing surface complex, $(\equiv FeOH)_2UO_2(H_2O)_3$ (U-Fe distance ~ 4.1 Å), that is expected to dominate U(VI) sorption on goethite, with the edge-sharing complex being a minor form of adsorbed U(VI) [24]. The predominance of the corner-sharing complex was supported by the abundancy of surface sites provided by the dominant [25] surface of goethite. In the presence of carbonate, uranium carbonate surface complexes have been proposed, although their existence for pH range 4-7 is being debated. The spectroscopic evidence for the existence of a uranyl carbonate surface complex is commonly attributed to an observed peak at ~2.4 Å (uncorrected for phase shift) in the Fourier-transforms of the U L_{III}-edge extended X-ray absorption fine-structure (EXAFS) spectra of adsorbed uranium. While many past spectroscopic studies on hematite [22, 26], Wyoming montmorillonite [27], and goethite [24] have attributed this peak to U-C scattering from a uranyl carbonate surface complex, several other studies on ferrihydrite [20, 28] and on schwertmannite and goethite [29] have found that this peak was also present in spectra from samples prepared in a carbonate-free atmosphere. A recent study using advanced EXAFS iterative transformation factor analysis for a range of pH and pCO_2 conditions indicated that uranium carbonate surface complexes on ferrihydrite were dominant only at high pH and high pCO_2 levels [30].

The favorable phosphate adsorption to iron oxyhydroxide surfaces as inner-sphere complexes could impact U(VI)-phosphate-Fe(III) oxide interactions. Information on the structure of adsorbed phosphate on iron oxides was reported using attenuated total

reflectance-Fourier transform infrared (ATR-FTIR) spectroscopy. For goethite, both the protonated, bidentate binuclear, $(\equiv FeO)_2(OH)PO$ and nonprotonated, bidentate binuclear, $(\equiv FeO)_2PO_2$, inner sphere complexes dominated at low pH (4.5), and the nonprotonated species dominated at high pH $\geq$ 7.5 [31]. For ferrihydrite, only the nonprotonated species was dominant at high pH [31, 32]. It is also suggested that phosphate adsorption will ultimately lead to surface precipitation of an iron phosphate phase on the iron oxide surface at phosphate concentrations much lower than calculated for equilibrium with goethite and iron phosphate [33, 34].

Macroscopic results from batch studies presented in Chapter 2 suggested an enhanced uptake of uranium on goethite at high phosphate concentrations by mechanisms that depend on the total uranium concentration. For high uranium concentrations, the precipitation of chernikovite, $H_3O(UO_2)(PO_4)\bullet 3H_2O_{(s)}$, was indicated by X-ray diffraction, scanning electron microscopy, and changes in dissolved uranium and phosphate concentrations. For low to intermediate total uranium concentrations, however, the immobilization mechanism could not be determined using available techniques. The objective of this study was to identify the immobilization mechanisms of uranium at the molecular-scale in the absence and presence of phosphate, and as a function of pH using X-ray absorption fine-structure (XAFS) spectroscopy. In preparation for XAFS analysis, goethite suspensions were equilibrated with U(VI) in the presence and absence of phosphate over a pH range of 4-7, which is an environmentally relevant range over which U(VI)-carbonate complexes are not significant. The determination of the U(VI) coordination environment by XAFS spectroscopy can enable

distinctions between formation of ternary surface complexes and precipitation of poorly-crystalline U(VI)-phosphates.

3.2. Materials and methods

3.2.1. Materials

Goethite was prepared by aging ferrihydrite that was initially precipitated using an established method [35]. Details of goethite synthesis and characterization are provided in Chapter 2. The specific surface area of goethite was measured to be 39.9 m^2/g. Goethite was maintained as a 2.97 g/L stock suspension prior to its use in batch reactors at a diluted concentration of 0.59 g/L.

All chemicals used were ACS grade or better. Ultrapure (resistivity > 18.2 MΩ-cm) water was used for preparing stock solutions and dilutions. Uranium and phosphate were respectively added from stock solutions of 1 M $UO_2(NO_3)_2$ and 0.01 M $Na_2HPO_4 \cdot 7H_2O$. Buffer concentrations of 0.5 mM MES (morpholino ethanesulfonic acid) and 0.5 mM HEPES (hydroxyethyl piperazineethanesulfonic acid) were used to fix the pH at 6 and 7 respectively, while no buffer was used at pH 4. Adjustments to system pH were made using trace metal grade HNO_3 and 1 M NaOH. $NaHCO_3$ was added at pH 6 ($10^{-4.79}$ M) and pH 7 ($10^{-4.19}$ M) to achieve faster equilibration with atmospheric CO_2 (pCO_2. = $10^{-3.44}$ atm). $NaNO_3$ was used to fix the ionic strength at 0.01 M.

3.2.2. Batch Experiments

Batch studies presented in Chapter 2 suggested a phosphate-enhanced uptake of uranium at pH 4 by mechanisms that depended on the total uranium concentration. While

precipitation of chernikovite, $H_3O(UO_2)(PO_4)\cdot 3H_2O_{(s)}$, was dominant for high TOTU concentrations, direct evidence for the formation of a U(VI)-phosphate-iron oxide ternary surface complex for low to intermediate TOTU concentrations (1 – 10 µM) could not be determined using available techniques. Consequently, XAFS spectroscopy was used to investigate the changes in U(VI) coordination environment with TOTU concentrations. U(VI)-equilibrated goethite suspensions from pH 4 experiments for a range of uranium concentrations were collected (Table 3.1)

Apart from microscopic investigations at pH 4, additional batch experiments were performed for 10 µM TOTU concentrations at pH 6 and 7. The 10 µM TOTU concentration was chosen because it marked a transition in uptake mechanism at pH 4 from U(VI) adsorption to U(VI) precipitation in the presence of phosphate. The effect of pH and reaction time was investigated by following an experimental procedure identical to the pH 4 experiments (details in section 2.2.4). The total phosphate concentrations (101 µM) for pH 6 and 7 experiments were similar to the concentrations (130 µM) used for the pH 4 experiments; fresh stock solutions were prepared for the two set of experiments and the pH 4 stock likely was contaminated with phosphate from glassware. Experiments having either no phosphate or no uranium in the presence and absence of goethite were also performed. In total, 36 conditions were studied at pH 6 and 7 (Table 3.1). Reactors were periodically sampled to analyze dissolved U and P concentrations and to characterize solids by SEM and XRD. The samples after 1 y were collected for XAFS analysis.

Sample preparation for XAFS. U(VI)-equilibrated goethite suspensions from pH 4-7 batch experiments were centrifuged at 11,000 rpm for 20 min. The resulting wet pastes were loaded into plexiglass sample holders. Each sample holder (1 inch by 2 inches) had a well for holding the sample of 0.038 mL (1.5 mm x 5 mm x 5mm). The samples were sealed into the sample holder wells by wrapping with two layers of Kapton tape. The sealed sample holders were further contained within heat-sealed plastic bags before being used for XAFS measurements. Additionally, uranyl nitrate and uranyl phosphate (from pH 4 experiments in the absence of goethite) standards were analyzed by XAFS. Since these solids contained concentrated uranium, ~15 mg of uranium-containing mineral was mixed with ~85 mg of boron nitride to provide appropriate total uranium concentrations for XAFS.

Table 3.1. Experimental conditions in the absence and presence of 0.59 g/L goethite

pH	TOTU (μM)	TOTP (μM)	Reaction Time
4[a]	1, 5, 10, 50, 100	130	1 d 8 d 1 mo 3 mo 6 mo 1 y
	1, 10, 50, 100	0	
	0	130	
6	10	101	
	10	0	
	0	101	
7	10	101	
	10	0	
	0	101	

[a] conditions investigated as part of the experimental study presented in Chapter 2

3.2.3. Analysis

Dissolved U and P concentrations were measured using ICP-MS (Agilent 7500ce) with method detection limits of 0.005 ppb and 0.8 ppb, respectively. Details on sample preparation and analysis were discussed in Chapter 2. Sample pH was recorded using an Accumet Research glass electrode and pH meter. Residual solids collected on filter membranes and solids resulting from centrifugation at 11000 rpm for 20 min were analyzed by XRD (Rigaku Geigerflex D-MAX/A) using Cu-K_α radiation. Scanning electron microscopy was performed using a JEOL 7001LVF SEM.

Structural Analysis. Molecular-scale information on the dominant U(VI) uptake mechanisms was obtained by using XAFS spectroscopy. XAFS is an element-specific spectroscopic technique used to investigate the molecular-scale physical and chemical structure of matter. Incident X-rays at energies near and above the binding energy of core electronic levels of a particular element are absorbed based on the element's specific coordination environment and oxidation state. The absorption at energies above the threshold is modulated by scattering from the atoms surrounding the absorbing atom and constitutes the XAFS [36]. An XAFS spectrum comprises two portions: i) the region typically within 30 eV of the main absorption edge called X-ray absorption near-edge structure (XANES); ii) the fine-structure beyond the main absorption edge region called the EXAFS. While XANES is particularly sensitive to the oxidation state and coordination chemistry of the selected element, EXAFS is helpful in determining the identity, distance, and number of neighboring atoms. Because of attenuation of low-

energy X-rays by air, most XAFS studies of environmental samples have focused on elements heavier than Ca. These X-ray absorption measurements require intense and energy-tunable sources of X-rays that are provided by a synchrotron [36].

Uranium L_{III}-edge XAFS spectra were collected at room temperature on beamlines 12-BM-B and 20-BM-B at the Advanced Photon Source at Argonne National Laboratory. Both beamlines were equipped with Si(111) double-crystal monochromators. A brief schematic of the set-up for collecting XAFS spectra is shown in Figure 3.1. The monochromators were calibrated using a Y metal foil that was mounted between two N_2-filled ionization chambers downstream of the sample; the first inflection point in the Y K-edge was set to 17038 eV. Spectra were collected in two detection modes - fluorescence and transmission. Typically, concentrated samples are analyzed in the transmission mode and dilute samples are analyzed in the fluorescence mode. In the fluorescence mode, the sample was placed at 45° to the incident beam. Fluorescence signals from goethite-associated uranyl samples were collected using a 12-element solid-state Ge detector. In the transmission mode, the sample was placed at 90° to the incident beam. The intensities of the incident and transmitted beams were recorded by the ionization chambers. Spectra for the uranium phosphate solids formed in the absence of goethite were collected in transmission.

XAFS data were background-subtracted, splined, k^3-weighted and processed using the Athena [37] and SIXPack [38] interfaces to the IFEFFIT XAFS analysis package [39]. Structural fitting of the XAFS spectra of uranyl-sorbed goethite was done using FEFF 8.2 [40] generated phase-shift and backscattering amplitude functions from

the crystal structures of soddyite ($(UO_2)_2SiO_4 \cdot 2H_2O$) [41] and of metatorbernite ($Cu(UO_2PO_4)_2 \cdot 8H_2O$) [42] with Fe substituted for Cu. Spectra of the uranium phosphate solids were fit using FEFF 7.02 [40] generated functions from the sodium-meta autunite ($Na[(UO_2)(PO_4)](H_2O)_3$) structure [43]. All fits included the three multiple scattering paths involving the axial oxygen atoms of the uranyl cation. For linear combination fitting the unknown and the end member XAFS spectra were background-subtracted, splined and processed in an identical manner (k = 1 to 12.8 $Å^{-1}$, R_{bkg} = 0.8, same E_0). When optimizing the fits to the data, the edge energy was not allowed to float.

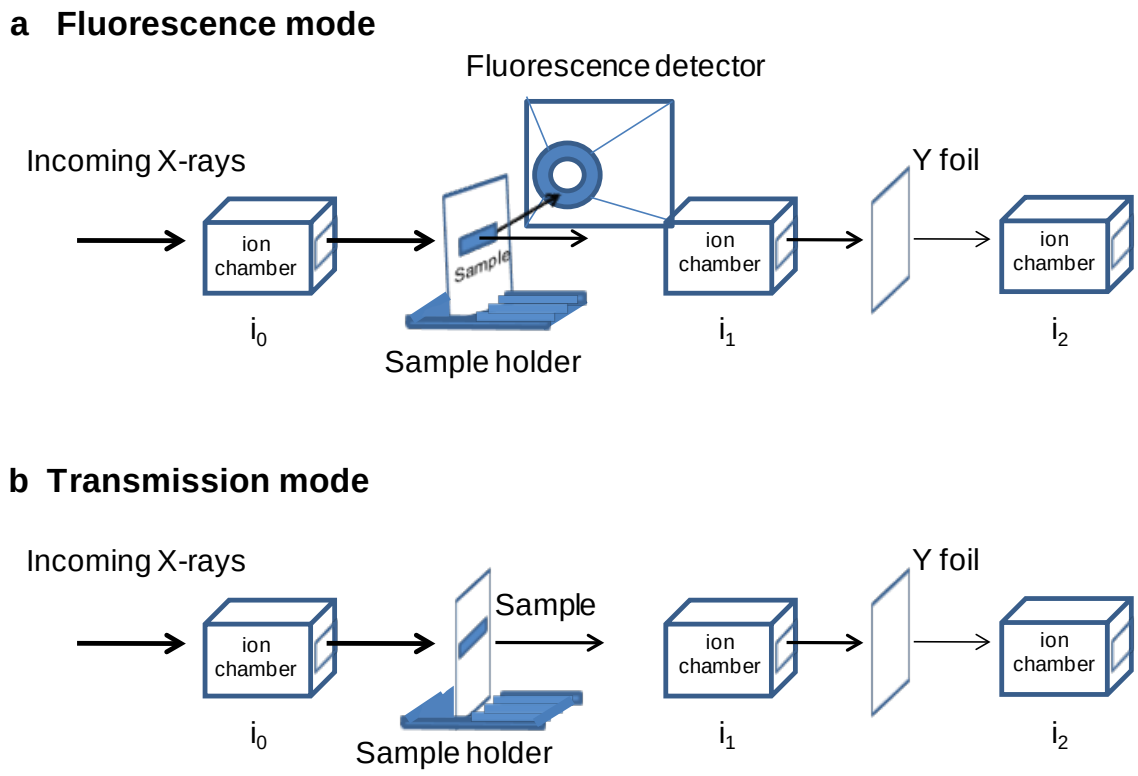

Figure 3.1. Experimental set-ups for collecting XAFS spectra in a) fluorescence and b) transmission modes. Sample is mounted on the sample holder.

3.2.4. Equilibrium speciation calculations

Dissolved U(VI) and phosphate concentrations were predicted using the speciation model presented and discussed in detail in Chapter 2. Briefly, the model included uranium and phosphate aqueous speciation (complexation, deprotonation) reactions, dissolution-precipitation reactions, and surface complexation reactions to account for adsorption. The best available thermodynamic data and past surface complexation models were integrated to form an internally consistent framework.

3.3. Results and discussion

The equilibrium predictions and macroscopic observations for pH 4, 6 and 7 for the 10 μM TOTU concentration are discussed in sections 3.3.1. and 3.3.2. Samples taken for these pH conditions were used for molecular-scale characterization and discussed in section 3.3.3. Besides these results, section 3.3.3 also contains molecular-scale characterization results for other TOTU conditions investigated at pH 4 (macroscopic observations already presented in Chapter 2).

3.3.1. Precipitation in the absence of goethite

The time-dependent decrease in measured dissolved uranium (U_{diss}) and phosphate (P_{diss}) concentrations indicated precipitation of uranium-containing solids for different conditions (Figures 3.2a-c). In the absence of phosphate, significant U(VI) uptake occurred at pH 6 (~90% of TOTU) and 7 (~97% of TOTU) after 1 y of reaction, but no uptake was recorded at pH 4 (Figure 3.2a). This uptake indicated meta-schoepite

precipitation, although the conditions were undersaturated with respect to its formation. The K_{sp} of meta-schoepite was the same as used in the equilibrium speciation model in Chapter 2.

In the presence of phosphate, uranium phosphate precipitation was observed for all three pH conditions. Measured U_{diss} concentrations indicated U(VI) uptake of ~95%, ~98% and ~78% of TOTU for pH 4, 6 and 7, respectively within 1 d of reaction, while the corresponding phosphate uptake was ~12% of TOTP for pH 4 and 6 and ~8% of TOTP for pH 7. For pH 6 and 7 conditions, the U_{diss} concentrations decreased subsequently and approached the predicted equilibrium concentrations resulting in an uptake of > 99.5% TOTU after 1 y (Figure 3.2b). Uranium phosphate precipitation at the circum-neutral pH conditions was slightly higher than at pH 4.

3.3.2. Uptake in the presence of goethite

3.3.2.1. Adsorption in the absence of phosphate

U(VI) adsorption to goethite increased with pH (Figure 3.2d). Uptake increased from ~46% of TOTU at pH 4 to > 99.9% of TOTU as the decreasing surface charge at higher pH conditions made adsorption increasingly favorable. The equilibrium speciation model developed previously [9] underpredicted adsorption; the degree of underprediction increased at higher pH conditions.

3.3.2.2. Adsorption and precipitation in the presence of phosphate

The presence of phosphate enhanced U(VI) uptake on goethite from ~46% of TOTU to ~95% of TOTU at pH 4, while uptake for the higher pH conditions was about the same as

in the absence of phosphate (Figure 3.2e). While adsorption was the dominant U(VI) uptake mechanism at pH 4, U(VI)-phosphate precipitation was dominant at circumneutral pH (6-7) from SEM (data not shown). At pH 4, the enhanced U(VI) uptake probably occurred due to phosphate- induced formation of uranyl-phosphate-Fe(III) oxide ternary surface complexes [7-9].

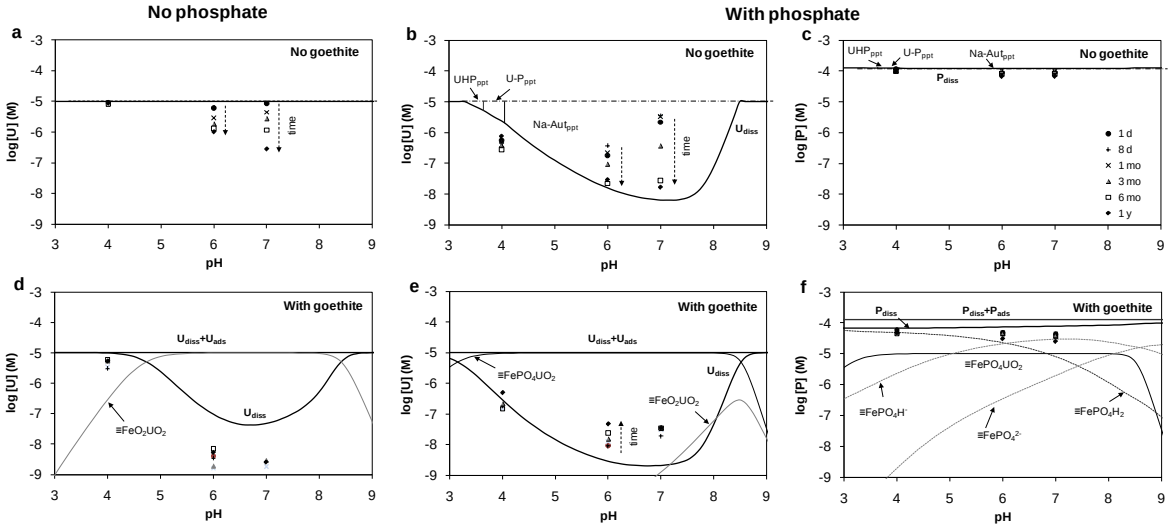

Figure 3.2. Predicted and measured dissolved uranium (a, b, d, e) and phosphate (c, f) concentrations in the absence (a, b, c) and presence (d, e, f) of 0.59 g/L goethite. Conditions in the absence (a, d) of phosphate are distinguished from those in phosphate's presence (b, c, e, f). The symbols represent data from 1d to 1y and lines depict equilibrium predictions for an open system containing TOTU = 10 µM, TOTP = 130 µM, and TOTNa = 0.01 M. Time-dependent trends in data are indicated with arrows. The ranges for predicted solids and predominant adsorbed species are shown. UHP_{ppt}, $U\text{-}P_{ppt}$, and $Na\text{-}Aut_{ppt}$ refer to uranium hydrogen phosphate [$UO_2HPO_4 \cdot 3H_2O_{(s)}$], uranyl orthophosphate [$(UO_2)_3(PO_4)_2 \cdot 4H_2O_{(s)}$], and sodium meta-autunite [$Na_2(UO_2PO_4)_2 \cdot xH_2O_{(s)}$], respectively.

Although the measured dissolved U concentrations in the presence and absence of goethite for pH 6 and 7 were about the same, the mechanisms of uptake were different. Direct evidence for these mechanisms was obtained from XAFS.

3.3.3. U(VI) uptake mechanisms at the molecular-scale

Results from EXAFS analysis of goethite-associated uranium samples from the batch experiments for the TOTU and TOTP conditions investigated at pH 4 (Chapter 2) and for the 10 µM TOTU and ~100 µM TOTP condition at pHs 6 and 7 are presented here. To investigate the effect of phosphate on U(VI) coordination environment, the structures of end members - a) adsorbed U(VI) in the absence of phosphate, and b) precipitated U(VI)-phosphate - were analyzed. Results from shell-by-shell fitting of the Fourier-transformed EXAFS spectra for these end members are discussed first. Next, relative percentages of the two end members in unresolved EXAFS spectra from U(VI) uptake in the presence of phosphate using linear-combination fitting analysis are presented. Finally, a structural model for the U(VI)-phosphate-iron oxide ternary surface complex is proposed.

3.3.3.1. U(VI) adsorption in the absence of phosphate

U(VI) probably adsorbed to the goethite surface by forming bidentate edge-sharing and corner-sharing inner-sphere binary surface complexes (Figure 3.3). EXAFS spectra and the corresponding Fourier-transforms for uranyl sorbed goethite samples for different TOTU concentrations at pH 4 and for the 10 µM TOTU concentration at pHs 6 and 7 are shown in Figure 3.4. U(VI) adsorption to goethite for low to circum-neutral pH (4-7) conditions was modeled by using a structural model that included a single axial oxygen shell (U-O_{ax}) at ~1.78 Å, a split equatorial oxygen shell at ~2.3 (U-O_{eq1}) and ~2.5 Å (U-O_{eq2}) commonly observed for inner-sphere U(VI) surface species, the three multiple scattering paths associated with U-O_{ax}, and two iron shells at ~3.48 Å (U-Fe_1) and ~4.0-

4.3 Å ($U\text{-}Fe_2$) (Table 3.2). A single iron shell could not completely reproduce the two Fourier transform features at ~3 Å and between ~3.5-4.0 Å (uncorrected for phase shift), except for the lowest uranium loading (1 μmolU/g) where the low signal-to-noise ratio limited the structural fitting to k = 10.5 $Å^{-1}$ (Figure 3.4 line a).

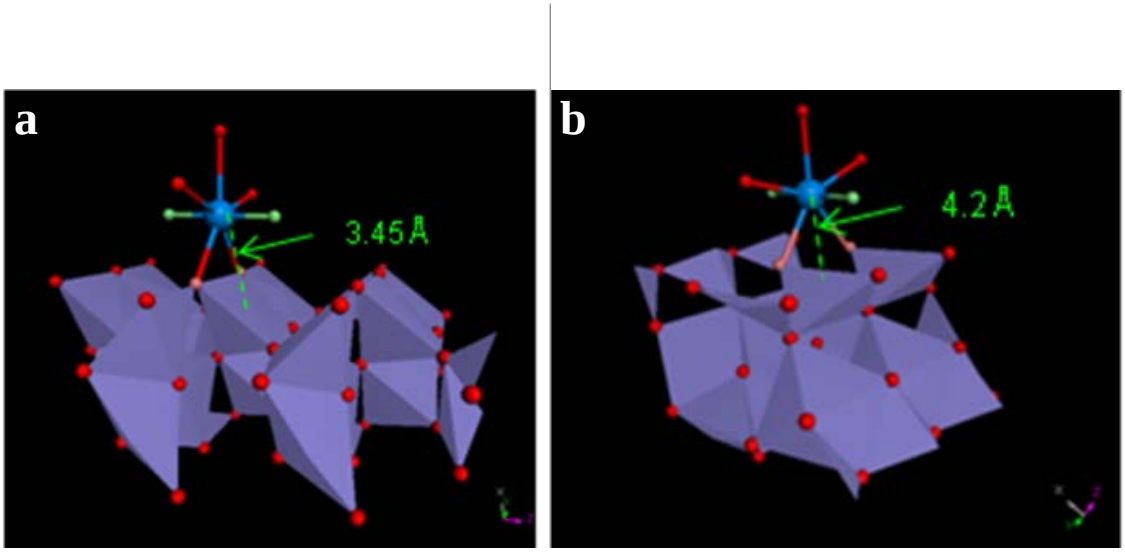

Figure 3.3. Adsorption of uranyl to the goethite surface by a) bidentate edge-sharing and b) bidentate corner-sharing binary surface complexes. The uranyl molecule is depicted with two axially bonded O atoms (parallel to the surface) and five equatorial O atoms (perpendicular to the surface) bonded to the central U atom.

Past studies of U(VI) adsorption on iron oxide surfaces have attributed the ~3 Å Fourier transform feature to either multiple scattering related to the $U\text{-}O_{ax}$ shell entirely [24] or to $U\text{-}O_{ax}$ multiple scattering and a monodentate edge-sharing (E2) inner-sphere complex [20, 22, 30]. For the spectra analyzed in this study, both the $U\text{-}O_{ax}$ multiple scattering and the E2 complex were needed to fit this feature. In order to fit the ~3.5 Å feature, our model also included a bidentate corner-sharing (C2) binary surface complex proposed recently [24]. Due to the elongated needle-shaped structure of goethite, sites

favoring the formation of the C2 complex are more abundant than the edge-sites, which could explain the high sorption capacity of goethite. The effect of carbonate on U(VI) adsorption was accounted for by a U(VI)-CO_3 ternary surface complex by some studies in the past even at low pH [22, 27]. However, in a recent study of uranyl adsorption to ferrihydrite, Rossberg et al. studied a range of pH and pCO_2 conditions and used Iterative Transformation Factor Analysis of EXAFS spectra to show that monodentate uranyl triscarbonato surface complexes are significant only at high pH and elevated pCO_2 levels [30]. In our model, no U-C paths were included because, for the pH and pCO_2 conditions investigated, uranyl carbonate surface complexes were not expected to be significant [30].

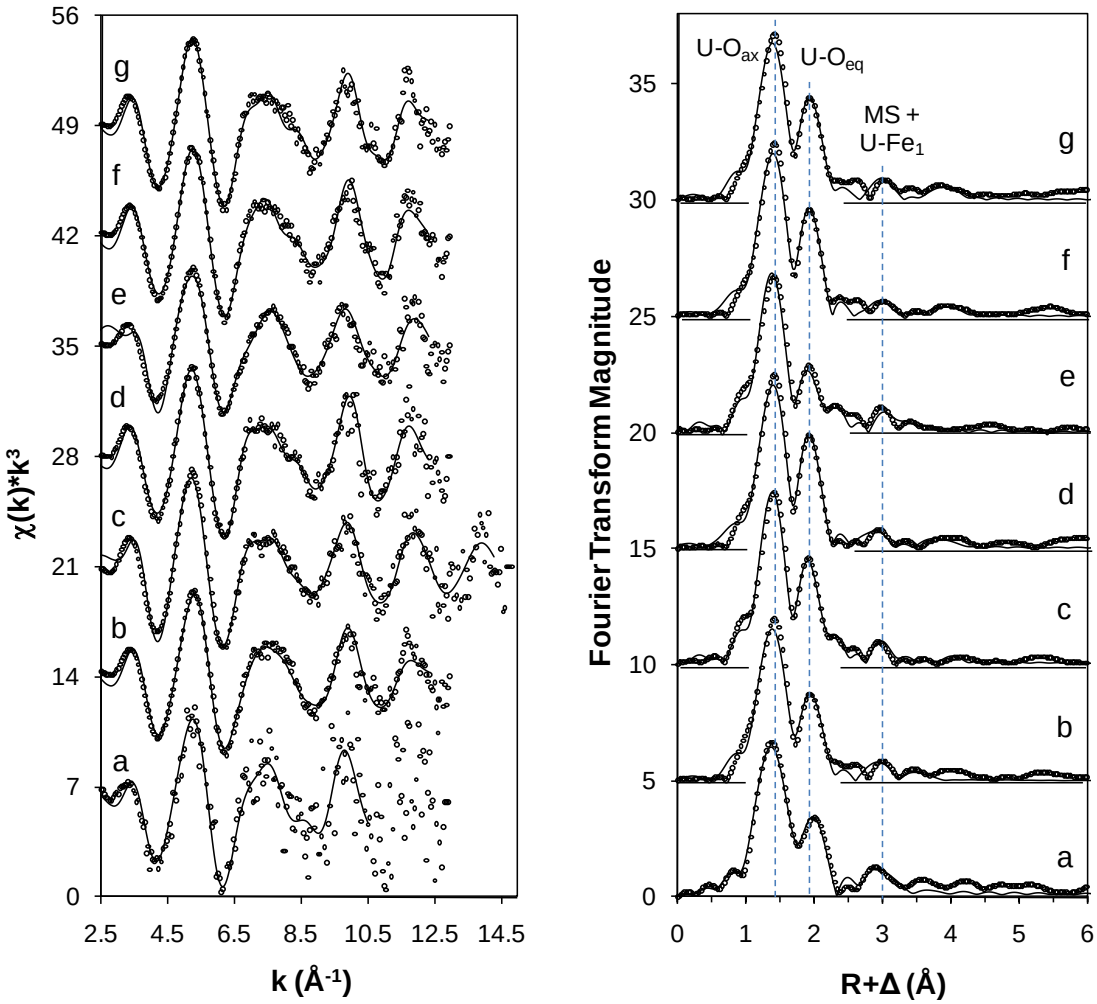

Figure 3.4. U L_{III}-edge EXAFS spectra (left) and Fourier transforms (right) of uranyl-sorbed goethite samples for different pH, TOTU, and surface coverages: a) pH4_1µM TOTU_1 µmolU/g; b) pH4_10µM TOTU_8 µmolU/g; c) pH4_50µM TOTU_18 µmolU/g; d) pH4_50µM TOTU_54 µmolU/g; e) pH4_100µM TOTU_43 µmol U/g; f) pH6_10µM TOTU_17µmolU/g; g) pH7_10µM TOTU_17µmolU/g. Dots represent data and lines represent the least-squares fits to the data. Samples c and d were recorded after 1 d and 1 y of reaction time, respectively. Vertical dotted lines indicate shells from the nearest neighbors and multiple scattering (MS) from the axially-coordinated oxygen atoms of U.

Table 3.2. EXAFS fitting results for U(VI) adsorption to goethite

Sample		U-O_{ax}	U-O_{eq1}	U-O_{eq2}	U-Fe_1	U-Fe_2	ΔE_0 (eV)[e]	χ_r^2 [f]	R-factor [g]
a) pH 4_1 µmol U/g	N[a]	2[d]	1.6(8)	3.3(8)	0.8(4)		11(3)	1.9	0.021
1 µM TOTU	R (Å)[b]	1.79(1)	2.24(5)	2.40(3)	3.45(3)				
	σ^2 (Å^2)[c]	0.0021(7)	0.005[d]	0.005[d]	0.005[d]				
b) pH 4_8 µmol U/g	N[a]	2[d]	2.2(8)	4(1)	0.5(6)	0.6(1.1)	9(3)	35.08	0.036
10 µM TOTU	R (Å)[b]	1.77(1)	2.19(3)	2.38(2)	3.40(7)	4.0(1)			
	σ^2 (Å^2)[c]	0.0033(8)	0.006(3)	0.006	0.008[d]	0.008[d]			
c) pH 4_18 µmol U/g	N[a]	2[d]	2.8(8)	2.1(5)	0.3(2)	0.5(5)	16(1)	3.56	0.027
50 µM TOTU_1d	R (Å)[b]	1.800(5)	2.35(2)	2.49(3)	3.42(4)	4.34(5)			
	σ^2 (Å^2)[c]	0.0022(3)	0.005(3)	0.005	0.004[d]	0.004[d]			
d) pH 4_54 µmol U/g	N[a]	2[d]	2.1(6)	4.9(9)	0.6(4)	1.1(9)	7(2)	7.97	0.015
50 µM TOTU_1y	R (Å)[b]	1.772(7)	2.17(2)	2.37(1)	3.36(4)	4.27(5)			
	σ^2 (Å^2)[c]	0.0028(5)	0.005(2)	0.005	0.008[d]	0.008[d]			
e) pH 4_43 µmol U/g	N[a]	2[d]	1.9(6)	1.6(7)	0.3(6)	0.5(9)	17.6(2)	23.72	0.041
100 µM TOTU	R (Å)[b]	1.802(5)	2.36(3)	2.53(4)	3.5(1)	4.1(1)			
	σ^2 (Å^2)[c]	0.0028(6)	0.005(2)	0.005	0.008[d]	0.008[d]			
f) pH 6_17 µmol U/g	N[a]	2[d]	2.1(7)	5(1)	0.1(3)	0.6(6)	8(3)	27.41	0.025
10 µM TOTU	R (Å)[b]	1.771(9)	2.17(2)	2.36(2)	3.4(1)	4.32(6)			
	σ^2 (Å^2)[c]	0.0028(6)	0.005(2)	0.005	0.004[d]	0.004[d]			
g) pH 7_17 µmol U/g	N[a]	2[d]	1.8(8)	5(2)	0.3(3)	0.8(7)	10(3)	28.85	0.034
10 µM TOTU	R (Å)[b]	1.78(1)	2.20(4)	2.39(2)	3.44(6)	4.30(5)			
	σ^2 (Å^2)[c]	0.0029(7)	0.006(3)	0.006	0.004[d]	0.004[d]			

Note: The estimated standard deviations are listed in parentheses, representing errors in the last digit; the amplitude damping factor, $S_o^2 = 1$, was used for all fits.

[a] coordination number; [b] interatomic distance; [c] Debye-Waller factor; [d] values fixed during fitting; [e] difference in threshold Fermi level between data and theory; [f] reduced χ^2, and [g] R-factor, as goodness of fit parameters.

Although the Fourier-transforms corresponding to higher uranium loadings (> 1 μmolU/g) were successfully reproduced with two iron shells, the second iron shell distance for different U loadings varied (U-Fe_2 ~4.0-4.3 Å). This variability could be an indication of the noise in spectra collected upto k = 13 $Å^{-1}$. For the one spectrum collected until k = 15 $Å^{-1}$ (Figure 3.4 line c) the fit was better than others (lowest χ_r^2 and low R-factor). However, a better signal-to-noise ratio may be needed to resolve the second Fe shell consistently for all the samples [24]. Furthermore, the U-O_{eq1} distances for some uranyl-sorbed samples were too short (Table 3.2 b,d,f,g) as compared to what is typically reported (2.25 - 2.35 Å). Further analysis would be required to refine these fits. Some of these refinements may involve: (i) increasing the lower limit of the k-range for fitting (from 2.5 to 3.5 $Å^{-1}$); (ii) using the phase-shift and backscattering amplitude functions from the crystal structures of Fe-substituted metatorbernite instead of soddyite that may result in a more uniform ΔE_0 fit for the different samples.

3.3.3.2. U(VI)-phosphate precipitation in the absence of goethite

Phosphate enhanced U(VI) uptake in the absence of goethite at pH 4 due to chernikovite ($H_3O(UO_2)(PO_4)\cdot 3H_2O_{(s)}$) precipitation for intermediate (10 μM) to high (100 μM) TOTU concentrations (Chapter 2). Solid residues from the 100 μM TOTU experiment were analyzed by XAFS (Figure 3.5). The formation of a meta-autunite (in chernikovite) confirmed previously by XRD and SEM (Chapter 2) was also observed by XAFS; the experimental spectrum was successfully fit (Table 3.3) to the sodium meta-autunite structure [43]. The meta-autunites are sheets of coordinated uranium and phosphate polyhedra with a cation in their interlayers [44]. Since XAFS cannot be used to distinguish the interlayer cations in these structures sodium meta-autunite ($Na[(UO_2)(PO_4)](H_2O)_3$) is indistinguishable from chernikovite (H_3O^+ is the interlayer

cation in $H_3O(UO_2)(PO_4)\cdot 3H_2O_{(s)}$) by this technique. This spectrum was subsequently used as an end member for the linear combination fitting of spectra of samples with uranium immobilized by unknown mechanisms (next section).

U(VI)-phosphate precipitation was also found for pH 6 and 7 conditions and confirmed by SEM and XRD (data not shown).

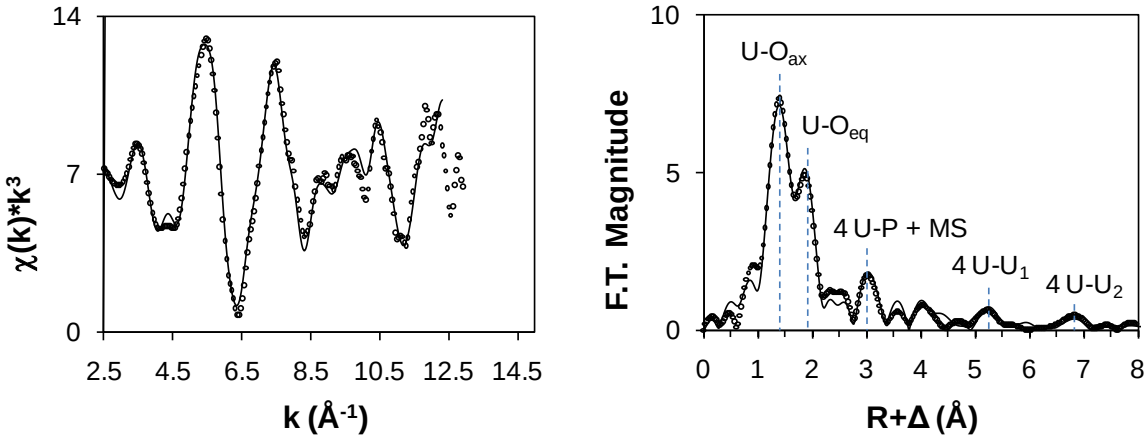

Figure 3.5. U L_{III}-edge EXAFS spectra (left) and Fourier transforms (right) of the uranium phosphate solids collected from the 100 µM TOTU condition at pH 4 after 1 y of reaction time. The spectrum was fitted to the sodium meta-autunite structure. Dots represent data and lines represent the least-squares fits to the data. Vertical dotted lines indicate shells from the nearest neighbors and multiple scattering (MS) from the U-P and U-O_{ax} shells. Multiple scattering from U-O_{eq} was responsible for the ~4 Å peak shown in the Fourier transform.

Table 3.3. EXAFS fitting results for U(VI)-phosphate formation in the absence of goethite

Sample		**U-O_{ax}**	**U-O_{eq1}**	**U-P**	**U-U_1**	**U-U_2**	**ΔE_0 (eV)[e]**	**χ_r^2 [f]**	**R-factor [g]**
Chernikovite	N[a]	2[d]	4.5(3)	4[d]	4[d]	4[d]	5.4(8)	56.93	0.0156
pH 4	R (Å)[b]	1.775(4)	2.281(5)	3.64(1)	5.28(2)	6.84(5)			
100 µM TOTU	σ^2 (Å^2)[c]	0.0023(3)	0.0048(7)	0.003(1)	0.010(2)	0.010			

Note: The estimated standard deviations are listed in parentheses, representing errors in the last digit; the amplitude a coordination number; b interatomic distance; c Debye-Waller factor; d values fixed during fitting; e difference in threshold Fermi level between data and theory; damping factor, $S_o^2 = 1$, was used for all fits. f reduced χ^2, and g R-factor, as goodness of fit parameters.

3.3.3.3. Phosphate-induced U(VI) uptake in the presence of goethite

Adsorption of U(VI) on goethite was the dominant mechanism for U(VI) uptake in the presence of phosphate at pH 4 for the low TOTU concentrations, while U(VI) uptake for the high TOTU concentrations was predominantly by precipitation of chernikovite (Chapter 2). In order to quantify the relative amounts of adsorbed and precipitated U(VI) for different TOTU concentrations and pH values, the EXAFS spectra corresponding to these uranium-associated goethite samples were reproduced by linear combination (LC) fitting of end member spectra (sodium meta-autunite spectrum and phosphate-free uranyl-sorbed goethite) resolved in previous sections (Figure 3.6).

Results for pH 4 indicate the presence of U(VI) in both adsorbed and precipitated forms, with the percentage of precipitated U(VI) typically increasing with TOTU. At low TOTU conditions ($\leq$5 μM), uranium was predominantly present in an adsorbed form. With increasing TOTU, the percentages of precipitated U increased from ~ 17-20 % for $\leq$5 μM TOTU to ~ 31 % for 10 μM TOTU to ~ 66 % for 50 μM TOTU (Figure 3.6 lines a-d). However, with a further increase in TOTU concentration to 100 μM, the percentage of precipitated U decreased to ~ 27 % (Figure 3.6 line e) because precipitation was limited by the availability of dissolved phosphate. Furthermore, with an increase in pH to 6 or 7 at a fixed TOTU (10 μM) concentration the predominant mechanism changed from adsorption (69 %) to precipitation (72-75 %, Figure 3.6 lines f,g). The spectra for conditions with 66-75 % precipitation (Figure 3.6 lines d,f,g) closely resemble the meta-autunite end member spectrum just resolved.

LC fitting results qualitatively agree with macroscopic uptake results for the high TOTU concentrations at pH 4 and for the circumneutral pH conditions where U(VI)-phosphate precipitation dominated (Chapter 2 and section 3.3.2.2, respectively). For the low to

intermediate TOTU (≤10 μM) concentrations, however, no evidence for precipitation was found at pH 4 from XRD and SEM. XAFS is a probe of short-range order. The fact that ~17-30 % of the meta-autunite end member was needed to fit the unknown spectra indicates that a phosphate shell in the coordination environment of uranium was required to reproduce the observed backscattering. These results indirectly point to the possibility of a ternary surface complex involving uranium, phosphate and iron. The structure of this ternary surface complex is explored further in the next section.

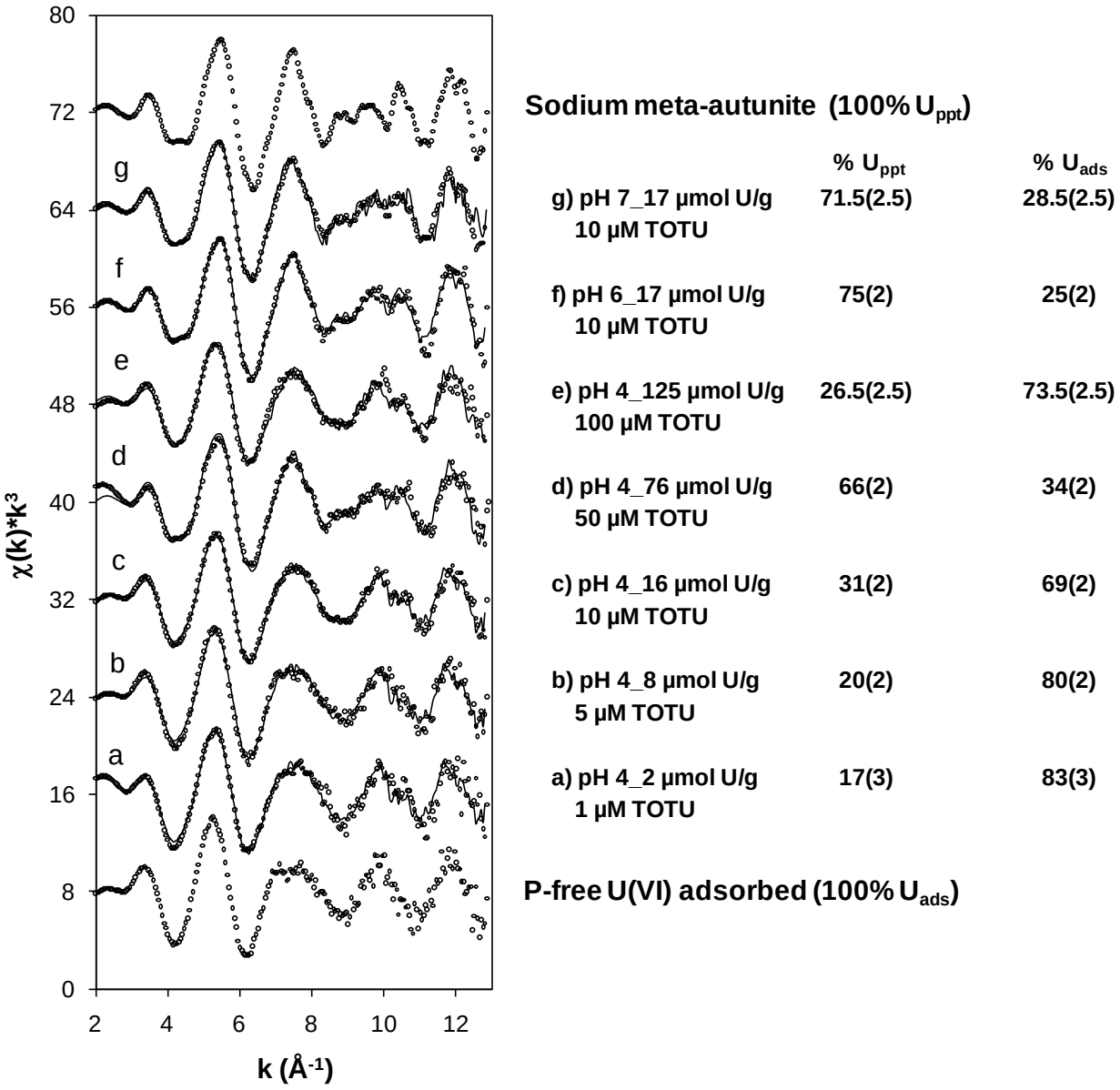

Figure 3.6. Two-component linear combination fits (solid lines) to the EXAFS spectra of goethite-associated U(VI) samples. The end members are shown at the top and bottom of the figure. Also shown are the percentages of adsorbed and precipitated uranium. The P-free end member shown is a representative spectrum of U(VI) adsorbed to goethite corresponding to 50 µM TOTU. While fitting, the spectrum for adsorbed U(VI) for each TOTU condition and pH was chosen as the end member. The estimated standard deviations are listed in parentheses, representing errors in the last digit.

3.3.3.4. Structure of the U(VI)-phosphate-iron oxide ternary surface complex

Although formation of a ternary surface complex was believed to cause the simultaneous uptake of U(VI) and phosphate on iron oxide surfaces for undersaturated conditions [6-9] spectroscopic evidence of its structure has been lacking. The EXAFS spectra and their Fourier-transforms from the uranyl-sorbed goethite samples in the presence of phosphate at pH 4 for the the low to intermediate TOTU concentrations discussed previously were fit over a k range of ~ 2.5-12.3 $Å^{-1}$ and R range of 1-4.5 Å (Figure 3.7). The best fits were achieved from a starting structural model that included a single axial oxygen shell ($U\text{-}O_{ax}$) at ~1.78 Å, a split equatorial oxygen shell at ~2.3 ($U\text{-}O_{eq1}$) and ~2.5 Å ($U\text{-}O_{eq2}$), the three multiple scattering paths associated with $U\text{-}O_{ax}$, a single phosphorus shell at ~3.6 Å (U-P) and a single iron shell at ~4.3 Å (U-Fe) (Table 3.4).

The model was developed progressively. Multiple scattering from the $U\text{-}O_{ax}$ shell alone could not completely reproduce the feature at ~3 Å in the Fourier transform (uncorrected for phase shift). Likewise, the model used to fit the phosphate-free adsorbed U(VI) spectra described earlier could also not explain the ~3 Å feature completely (the amplitude in the presence of phosphate was higher), although it could explain the ~4 Å feature with a single iron shell at ~4.3 Å. When the iron shells were excluded from the starting structural model and instead a phosphorus shell (U-P) was included, then the ~3 Å feature could be modeled. The U-P distance resulting from this fit (~3.6 Å) was similar to the U-P distance in uranyl phosphate minerals such as chernikovite (Table 3.3). Furthermore, by including an Fe shell at U-Fe distances comparable to the C2 surface complexes fit in the absence of phosphate, a fit of the ~4 Å feature could also be achieved. The variability seen in fitting the $U\text{-}Fe_2$ distances for the different surface loadings in the absence of phosphate could also be seen for the U-Fe distances for the ternary surface complex model (Figure 3.7). Nonetheless, the Fourier-transform feature

at ~4 Å appears to be real and the variable U-Fe shell distances could be constrained further by improved analysis on a less noisy data.

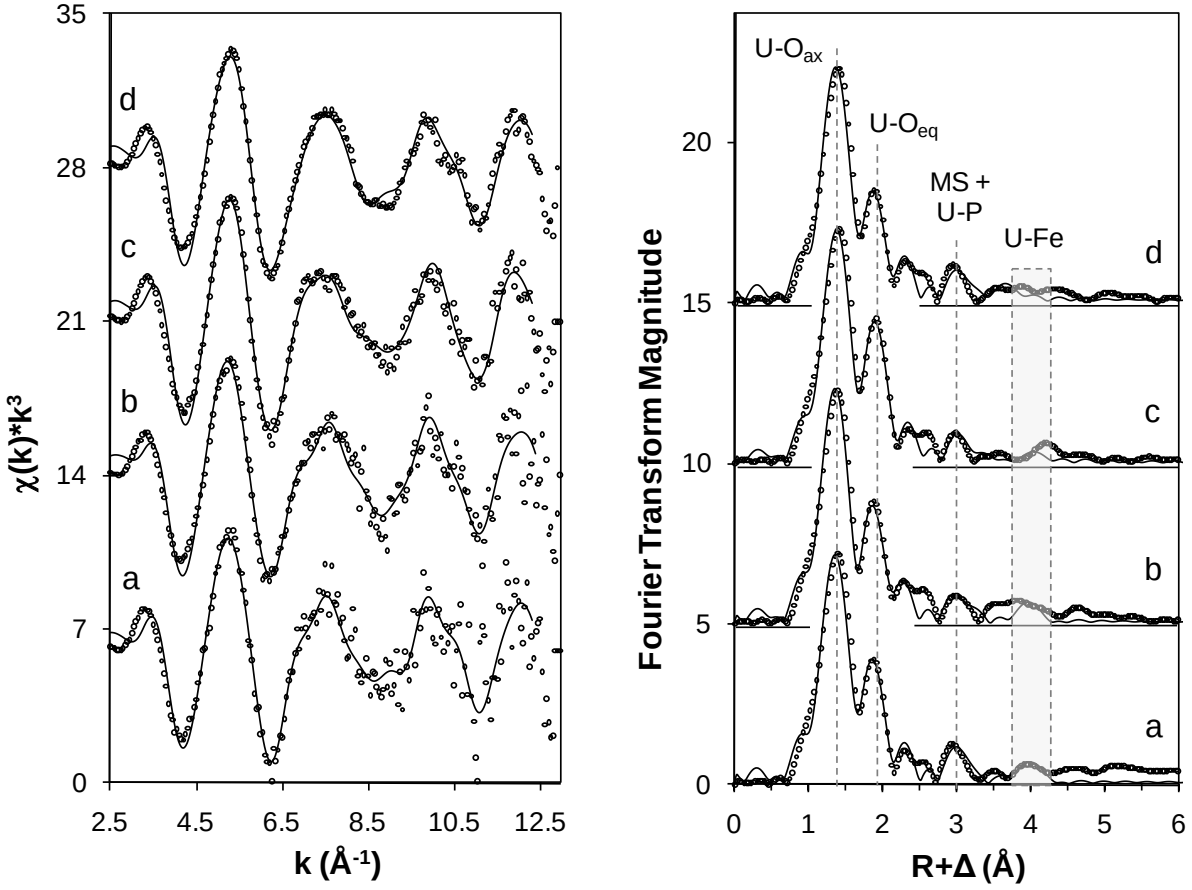

Figure 3.7. U L_{III}-edge EXAFS spectra (left) and Fourier transforms (right) of uranyl-sorbed goethite samples in the presence of phosphate for different pH, TOTU, and surface coverages: a) pH4_1µMTOTU_2µmol U/g_1d; b) pH4_10µMTOTU_2µmolU/g_1y; c) pH4_5µMTOTU_8µmolU/g; d) pH4_10µM TOTU_16µmolU/g. Dots represent data and lines represent the least-squares fits to the data. Samples a and b were recorded after 1 d and 1 y of reaction time, respectively. Vertical dotted lines indicate shells from the nearest neighbors and multiple scattering (MS) from the axially-coordinated oxygen atoms of U.

These results suggest that for the undersaturated conditions, uranium has both iron and phosphate as its neighbors. This could mean that UO_2^{2+} is bridging phosphate and the goethite surface on double-corner sites (that favored the C2 complex in the absence of phosphate). Hence, the structure of the ternary surface complex could be written as $(\equiv FeO)_2UO_2PO_4$ (Figure 3.8).

Table 3.4. EXAFS fitting results for U(VI)-sorbed spectra in the presence of phosphate

Sample		$U\text{-}O_{ax}$	$U\text{-}O_{eq1}$	$U\text{-}O_{eq2}$	U-P	U-Fe	ΔE_0 (eV)[e]	χ_r^2 [f]	R-factor[g]
a) pH 4_2 µmol U/g	N[a]	2[d]	3.1(4)	1.4(5)	0.6(4)	1.0(7)	14(2)	43.33	0.0249
1 µM TOTU_1d	R (Å)[b]	1.780(7)	2.33(2)	2.51(4)	3.60(4)	4.38(4)			
	σ^2 (Å^2)[c]	0.0027(5)	0.005[d]	0.005	0.002[d]	0.005[d]			
b) pH 4_2 µmol U/g	N[a]	2[d]	2.7(5)	1.7(6)	0.3(5)	1.0(9)	15(2)	7.42	0.0405
1 µM TOTU_1y	R (Å)[b]	1.780(8)	2.34(2)	2.51(4)	3.61(9)	4.34(5)			
	σ^2 (Å^2)[c]	0.0025(6)	0.005[d]	0.005	0.002[d]	0.006[d]			
c) pH 4_8 µmol U/g	N[a]	2[d]	3.3(5)	1.2(5)	0.2(5)	0.4(6)	17(2)	16.34	0.0320
5 µM TOTU	R (Å)[b]	1.792(8)	2.36(2)	2.53(6)	3.6(1)	4.32(9)			
	σ^2 (Å^2)[c]	0.0027(6)	0.005[d]	0.005	0.002[d]	0.004[d]			
d) pH 4_16 µmol U/g	N[a]	2[d]	2.8(4)	1.6(5)	0.4(4)	0.4(6)	16.0(2)	92.03	0.0331
10 µM TOTU	R (Å)[b]	1.788(5)	2.33(1)	2.51(3)	3.62(7)	4.09(8)			
	σ^2 (Å^2)[c]	0.0024(5)	0.005[d]	0.005	0.002[d]	0.005[d]			

Note: The estimated standard deviations are listed in parentheses, representing errors in the last digit; the amplitude damping factor, $S_o^2 = 1$, was used for all fits.
a coordination number; b interatomic distance; c Debye-Waller factor; d values fixed during fitting; e difference in threshold Fermi level between data and theory; f reduced χ^2, and g R-factor, as goodness of fit parameters.

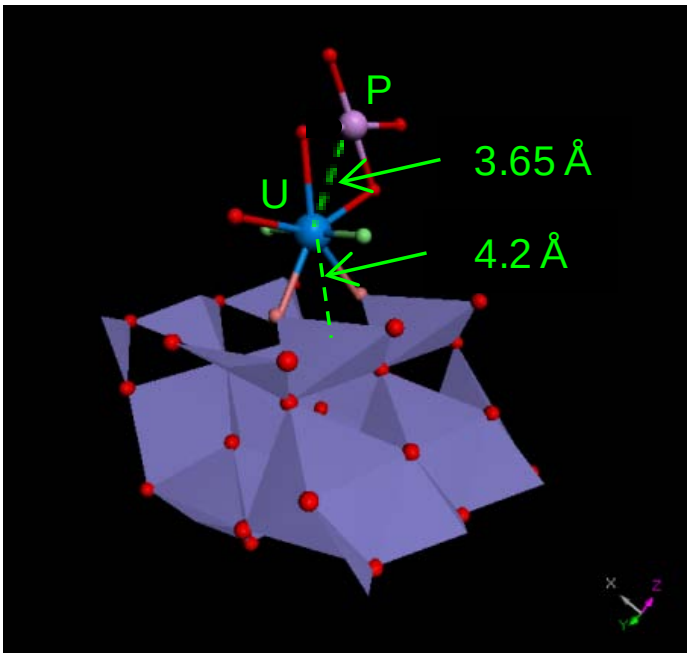

Figure 3.8. Structure of the uranyl-phosphate-iron oxide ternary surface complex. The uranyl molecule bridges phosphate and the goethite surface on double-corner sharing adsorption sites. The uranyl molecule is depicted with two axially bonded O atoms (parallel to the surface) and five equatorial O atoms (perpendicular to the surface) bonded to the central U atom.

3.4. Environmental implications

U(VI) uptake in the presence of phosphate was enhanced at high uranium concentrations and at high pH conditions due to precipitation of meta-autunite. Based on site-specific geochemistry the concentration of injectible phosphate could be altered to achieve sufficient U(VI) precipitation.

Immobilization mechanisms can significantly affect the transport and long-term stability of uranium in contaminated environments. Knowledge of molecular-scale processes provides insights into the dominant immobilization mechanisms that ultimately govern macroscopic field-scale transport rates. This study provides spectroscopic information on the structure of a U(VI)-phosphate-Fe(III) oxide ternary surface complex. This information could be integrated into the surface complexation models that described U(VI)-phosphate-iron oxide interactions. Integration of mechanistic studies with transport experiments will enable us to relate

macroscopic uptake rates to molecular-scale changes in the coordination environment of uranium. The results will contribute to the basis for including specific mechanisms in reactive transport models used for predicting the fate and transport of uranium.

3.5. Conclusions

For a fixed total uranium concentration (10 µM), U(VI) uptake in the presence of phosphate occurred by adsorption at pH 4 and by precipitation at pH 6-7 indicating that uranium phosphate precipitation was more favorable at circumneutral pH than at low pHs. EXAFS analysis revealed that the structure of precipitated U(VI) resembled the structure of the meta-autunite group of solids. In the absence of phosphate, EXAFS spectra of adsorbed U(VI) for low to circum-neutral pH (4-7) conditions indicated the presence of bidentate edge-sharing, $\equiv Fe(OH)_2UO_2$, and bidentate corner-sharing $(\equiv FeOH)_2UO_2$, surface complexes at respective coordination distances of ~3.48 Å (U-Fe_1) and ~4.0-4.3 Å (U-Fe_2). For goethite-associated U(VI) EXAFS spectra in the presence of phosphate; first, the relative amounts of precipitated and adsorbed U(VI) were quantified using linear combinations of the precipitated U(VI) and phosphate-free adsorbed U(VI) end member spectra that also provided indirect evidence for the formation of ternary surface complex involving uranium, phosphate and iron; second, a structural model for the ternary surface complex was proposed that included besides the axial and equatorial oxygens, a single phosphate shell at ~3.6 Å (U-P) and a single iron shell at ~4.3 Å (U-Fe), instead of the two Fe shells resolved previously in the absence of phosphate. Since uranium had both iron and phosphate as its neighbors the structure of the ternary surface complex could be written as $(\equiv FeO)_2UO_2PO_4$.

References

1. Xie, L.; Giammar, D., Influence of Phosphate on Adsorption and Surface Precipitation of Lead on Iron Oxide Surfaces. *Adsorption of metals by geomedia II: variables, mechanisms, and model applications* **2008**, 349.
2. Cao, R.; Ma, L.; Chen, M.; Singh, S.; Harris, W., Phosphate-induced metal immobilization in a contaminated site. *Environmental Pollution* **2003,** *122*, (1), 19-28.
3. Thawornchaisit, U.; Polprasert, C., Evaluation of phosphate fertilizers for the stabilization of cadmium in highly contaminated soils. *Journal of hazardous materials* **2009,** *165*, (1-3), 1109-1113.
4. Nzihou, A.; Sharrock, P., Role of Phosphate in the Remediation and Reuse of Heavy Metal Polluted Wastes and Sites. *Waste and Biomass Valorization*, 1-12.
5. Giammar, D.; Xie, L.; Pasteris, J., Immobilization of lead with nanocrystalline carbonated apatite present in fish bone. *Environmental Engineering Science* **2008,** *25*, (5), 725-736.
6. Bostick, B. C.; Fendorf, S.; Barnett, M. O.; Jardine, P. M.; Brooks, S. C., Uranyl surface complexes formed on subsurface media from DOE facilities. *Soil Science Society of America Journal* **2002,** *66*, (1), 99-108.
7. Cheng, T.; Barnett, M. O.; Roden, E. E.; Zhuang, J. L., Effects of phosphate on uranium(VI) adsorption to goethite-coated sand. *Environmental Science & Technology* **2004,** *38*, (22), 6059-6065.
8. Payne, T. E.; Davis, J. A.; Waite, T. D., Uranium adsorption on ferrihydrite - Effects of phosphate and humic acid. *Radiochimica Acta* **1996,** *74*, 239-243.
9. Singh, A.; Ulrich, K.-U.; Giammar, D. E., Impact of phosphate on U(VI) immobilization in the presence of goethite. *Geochimica et Cosmochimica Acta* **2010 (submitted)**.
10. Murakami, T.; Sato, T.; Ohnuki, T.; Isobe, H., Field evidence for uranium nanocrystallization and its implications for uranium transport. *Chemical Geology* **2005,** *221*, (1-2), 117-126.
11. Sato, T.; Murakami, T.; Yanase, N.; Isobe, H.; Payne, T. E.; Airey, P. L., Iron nodules scavenging uranium from groundwater. *Environmental Science & Technology* **1997,** *31*, (10), 2854-2858.
12. Jerden, J. L.; Sinha, A. K., Phosphate based immobilization of uranium in an oxidizing bedrock aquifer. *Applied Geochemistry* **2003,** *18*, (6), 823-843.
13. Morris, D. E.; Allen, P. G.; Berg, J. M.; Chisholm-Brause, C. J.; Conradson, S. D.; Donohoe, R. J.; Hess, N. J.; Musgrave, J. A.; Tait, C. D., Speciation of uranium in Fernald soils by molecular spectroscopic methods: characterization of untreated soils. *Environmental Science and Technology* **1996,** *30*, (7), 2322-2331.
14. Buck, E. C.; Brown, N. R.; Dietz, N. L., Contaminant uranium phases and leaching at the Fernald site in Ohio. *Environmental Science and Technology* **1996,** *30*, (1), 81-88.
15. Roh, Y.; Lee, S. R.; Choi, S.-K.; Elless, M. P.; Lee, S. Y., Physicochemical and mineralogical characterization of uranium-contaminated soils. *Soil and Sediment Contamination* **2000,** *9*, (5), 463-486.
16. Catalano, J. G.; McKinley, J. P.; Zachara, J. M.; Heald, S. M.; Smith, S. C.; Brown, G. E., Changes in uranium speciation through a depth sequence of contaminated Hanford sediments. *Environmental Science & Technology* **2006,** *40*, (8), 2517-2524.

17. Singer, D. M.; Zachara, J. M.; Brown, G. E., Uranium Speciation As a Function of Depth in Contaminated Hanford Sediments - A Micro-XRF, Micro-XRD, and Micro- And Bulk-XAFS Study. *Environmental Science & Technology* **2009,** *43*, (3), 630-636.
18. Arai, Y.; Marcus, M. K.; Tamura, N.; Davis, J. A.; Zachara, J. M., Spectroscopic evidence for uranium bearing precipitates in vadose zone sediments at the Hanford 300-area site. *Environmental Science & Technology* **2007,** *41*, (13), 4633-4639.
19. Stubbs, J.; Veblen, L.; Elbert, D.; Zachara, J.; Davis, J.; Veblen, D., Newly recognized hosts for uranium in the Hanford Site vadose zone. *Geochimica Et Cosmochimica Acta* **2009,** *73*, (6), 1563-1576.
20. Waite, T.; Davis, J.; Payne, T.; Waychunas, G.; Xu, N., Uranium (VI) adsorption to ferrihydrite: Application of a surface complexation model. *Geochimica et Cosmochimica Acta* **1994,** *58*, (24), 5465-5478.
21. Ulrich, K.; Rossberg, A.; Foerstendorf, H.; Zänker, H.; Scheinost, A., Molecular characterization of uranium (VI) sorption complexes on iron (III)-rich acid mine water colloids. *Geochimica et Cosmochimica Acta* **2006,** *70*, (22), 5469-5487.
22. Bargar, J.; Reitmeyer, R.; Davis, J., Spectroscopic Confirmation of Uranium (VI)-Carbonato Adsorption Complexes on Hematite. *Environ. Sci. Technol* **1999,** *33*, (14), 2481-2484.
23. Moyes, L.; Parkman, R.; Charnock, J.; Vaughan, D.; Livens, F.; Hughes, C.; Braithwaite, A., Uranium uptake from aqueous solution by interaction with goethite, lepidocrocite, muscovite, and mackinawite: An X-ray absorption spectroscopy study. *Environ. Sci. Technol* **2000,** *34*, (6), 1062-1068.
24. Sherman, D.; Peacock, C.; Hubbard, C., Surface complexation of U (VI) on goethite ([alpha]-FeOOH). *Geochimica et Cosmochimica Acta* **2008,** *72*, (2), 298-310.
25. Abd El-Naby, H. H.; Dawood, Y. H., Natural attenuation of uranium and formation of autunite at the expense of apatite within an oxidizing environment, south Eastern Desert of Egypt. *Applied Geochemistry* **2008,** *23*, (12), 3741-3755.
26. Bargar, J.; Reitmeyer, R.; Lenhart, J.; Davis, J., Characterization of U (VI)-carbonato ternary complexes on hematite: EXAFS and electrophoretic mobility measurements. *Geochimica et Cosmochimica Acta* **2000,** *64*, (16), 2737-2749.
27. Catalano, J.; Brown, G., Uranyl adsorption onto montmorillonite: Evaluation of binding sites and carbonate complexation. *Geochimica et Cosmochimica Acta* **2005,** *69*, (12), 2995-3005.
28. Reich, T.; Moll, H.; Arnold, T.; Denecke, M.; Hennig, C.; Geipel, G.; Bernhard, G.; Nitsche, H.; Allen, P.; Bucher, J., An EXAFS study of uranium (VI) sorption onto silica gel and ferrihydrite. *Journal of Electron Spectroscopy and Related Phenomena* **1998,** *96*, (1-3), 237-243.
29. Walter, M.; Arnold, T.; Reich, T.; Bernhard, G., Sorption of Uranium (VI) onto Ferric Oxides in Sulfate-Rich Acid Waters. *Environ. Sci. Technol* **2003,** *37*, (13), 2898-2904.
30. Rossberg, A.; Ulrich, K.; Weiss, S.; Tsushima, S.; Hiemstra, T.; Scheinost, A., Identification of Uranyl Surface Complexes on Ferrihydrite: Advanced EXAFS Data Analysis and CD-MUSIC Modeling. *Environ. Sci. Technol* **2009,** *43*, (5), 1400-1406.
31. Luengo, C.; Brigante, M.; Antelo, J.; Avena, M., Kinetics of phosphate adsorption on goethite: Comparing batch adsorption and ATR-IR measurements. *Journal of Colloid and Interface Science* **2006,** *300*, (2), 511-518.
32. Arai, Y.; Sparks, D. L., ATR-FTIR spectroscopic investigation on phosphate adsorption mechanisms at the ferrihydrite-water interface. *Journal of Colloid and Interface Science* **2001,** *241*, (2), 317-326.

33. Ler, A.; Stanforth, R., Evidence for surface precipitation of phosphate on goethite. *Environmental Science & Technology* **2003,** *37*, (12), 2694-2700.
34. Li, L.; Stanforth, R., Distinguishing Adsorption and Surface Precipitation of Phosphate on Goethite ([alpha]-FeOOH). *Journal of colloid and interface science* **2000,** *230*, (1), 12-21.
35. Schwertmann, U.; Cornell, R. M., *The Iron Oxides: Structure, Properties, Reactions, Occurrences and Uses*. Second ed.; Wiley-VCH: New York, NY, 2003.
36. Newville, M., Fundamentals of XAFS. In Revision 1.8 ed.; Consortium for Advanced Radiation Sources University of Chicago, Chicago, IL, 2008.
37. Ravel, B.; Newville, M., ATHENA, ARTEMIS, HEPHAESTUS: data analysis for X-ray absorption spectroscopy using IFEFFIT. *Journal of Synchrotron Radiation* **2005,** *12*, (4), 537-541.
38. Webb, S., SIXPACK: a graphical user interface for XAS analysis using IFEFFIT. *Physica Scripta* **2005,** *115*, 1011–1014.
39. Newville, M., IFEFFIT: interactive XAFS analysis and FEFF fitting. *Journal of Synchrotron Radiation* **2001,** *8*, (2), 322-324.
40. Ankudinov, A.; Bouldin, C.; Rehr, J.; Sims, J.; Hung, H., Parallel calculation of electron multiple scattering using Lanczos algorithms. *Physical Review B* **2002,** *65*, (10), 104107.
41. Demartin, F.; Gramaccioli, C.; Pilati, T., The importance of accurate crystal structure determination of uranium minerals. II. Soddyite (UO2) 2 (SiO4). 2H2O. *Acta Crystallographica Section C: Crystal Structure Communications* **1992,** *48*, (1), 1-4.
42. Locock, A.; Burns, P., Crystal structures and synthesis of the copper-dominant members of the autunite and meta-autunite groups: torbernite, zeunerite, metatorbernite and metazeunerite. *Canadian Mineralogist* **2003,** *41*, (2), 489.
43. Locock, A.; Burns, P.; Duke, M.; Flynn, T., Monovalent cations in structures of the meta-autunite group. *Canadian Mineralogist* **2004,** *42*, (4), 973.
44. Finch, R.; Murakami, T., Systematics and Paragenesis of Uranium Minerals. In *Uranium: mineralogy, geochemistry and the environment*, Burns, P. C.; Finch, R., Eds. Mineralogical Society of America: Washington, DC, 1999; Vol. 38, pp 91-180.

Chapter 4 Effect of phosphate on uranium(VI) uptake and remobilization under flow conditions in the presence of goethite

4.1. Introduction

Uranium (U) contamination of soils and groundwater is a serious environmental concern. Of the strategies proposed to remediate U-contaminated sites, *in-situ* injection of soluble phosphate-containing compounds to the subsurface to precipitate insoluble uranium phosphate solids is one of the most promising [1-4]. Precipitation of U(VI) phosphates is especially attractive when sustaining reducing conditions to immobilize U as $U(IV)O_2$ is not feasible. Phosphates could also enhance U(VI) uptake by minerals such as iron oxides that are present in subsurface environments [5-7]. Uranium and phosphate interactions can be affected by mineral surfaces.

Phosphate-enhancement of U(VI) uptake in the presence of iron oxides has been reported in past equilibration studies. Uptake was probably enhanced by the formation of a ternary surface complex on the iron oxide surface at undersaturated conditions [5-7] and by the precipitation of chernikovite ($UO_2HPO_4 \cdot 4H_2O_{(s)}$) at higher TOTU and TOTP conditions [7]. Investigations of U(VI) uptake in the presence of phosphate and goethite under flow conditions can provide information about the rates of uptake reactions. These uptake rates can be combined with equilibrium calculations to help determine the predominant immobilization mechanism. Information about the relative kinetics of uptake mechanisms will also determine whether U(VI) fate is controlled by chemical reaction or by transport. The timescale of reactive controls can be compared to the

timescale for transport governed by typical groundwater velocities ranging from 0.012-1.1 m/d [8]. Besides knowledge of the uptake rates it is also important to quantify the rate of U(VI) remobilization when conditions change, such as will occur following the period of phosphate injection for a phosphate-based remediation strategy. By relating the dominant U(VI) uptake mechanism to its remobilization the long-term stability of immobilized uranium can be quantified.

The objectives of this study were to quantify the rates of U(VI) and phosphate uptake and remobilization in the absence and presence of goethite and to relate those rates to specific uptake and remobilization mechanisms. Continuous-flow stirred tank reactor (CFSTR) experiments were conducted under conditions supersaturated and undersaturated with respect to chernikovite. Uptake through a U(VI) adsorption pathway was distinguished from a chernikovite precipitation pathway by probing the coordination environment of immobilized U(VI) using XAFS. The U(VI) uptake rates were quantified using CFSTR modeling and related to U(VI) remobilization.

4.2. Materials and methods

4.2.1. Materials

All chemicals used were ACS grade or better. Ultrapure (resistivity > 18.2 MΩ-cm) water was used for preparing stock solutions and dilutions. Goethite was synthesized by initial precipitation of ferrihydrite followed by aging using the method outlined in Schwertmann and Cornell [9]. Details about the preparation and characterization of goethite have been described previously [7]. Goethite was kept as a 2.97 g/L stock suspension prior to use. Its specific surface area was determined to be 39.9 m^2/g.

Uranium was added as $UO_2(NO_3)_2$ and phosphate was added as $Na_2HPO_4 \cdot 7H_2O$. The pH of the system was adjusted to 4 using trace metal grade HNO_3 and NaOH. The ionic strength was fixed at 0.01 M by adding $NaNO_3$.

4.2.2. Continuous-flow stirred tank reactor (CFSTR) experiments

The CFSTR experimental set-up was chosen due to their ease for obtaining information on U and phosphate uptake rates and to the flexibility of simultaneously contacting uranium and phosphate in the reactor. The CFSTRs have cylindrical tanks of 84 mL volume (V) that were preloaded with 0.59 g/L goethite suspensions at pH 4 and 0.01 M ionic strength (Figure 4.1). Each reactor was magnetically stirred and was capped with a 0.2 μm polycarbonate filter to keep the reactor solids from escaping. Two influent solutions were simultaneously introduced into the reactor at a flow rate of 0.2 mL/min, resulting in an effluent flow rate (Q) of 0.4 mL/min. All influent solutions were at pH 4 and at the same ionic strength (0.01 M). Effluent from each reactor was collected using a fraction collector. For each reactor, uranium uptake was investigated first during the uptake period. Thereafter, the immobilized uranium was subjected to elution during the remobilization period.

For the uptake period, one of the two influent solutions contained dissolved uranium and the other contained dissolved phosphate (Figure 4.2). The uranium and phosphate input streams were isolated from each other prior to introduction to avoid any precipitation of uranyl phosphates in the influent lines. The uptake period was run for 2.5 residence times ($t_R = V/Q$). At the end of the uptake period both influent streams were changed to U-free and phosphate-free solutions, which marked the beginning of the

remobilization period. As opposed to the uptake period, the remobilization period was run for ~6 t_R. The flow rate and the total residence times for each period were chosen to minimize the gradual decrease in the concentration of freely suspended goethite due to goethite deposition on the filter membrane.

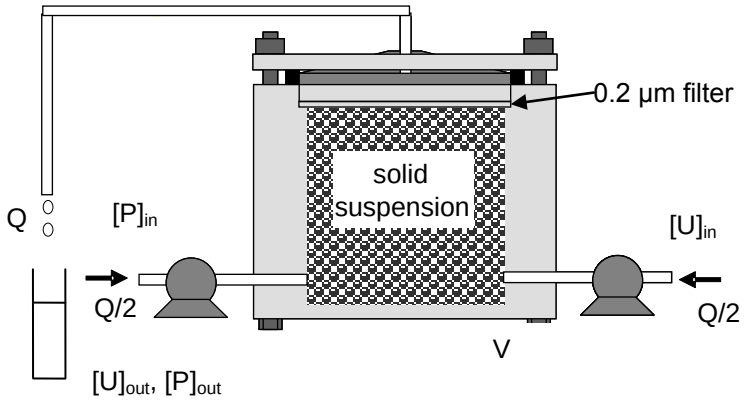

Figure 4.1. Continuous-flow stirred tank reactor (CFSTR) having multiple feed ports

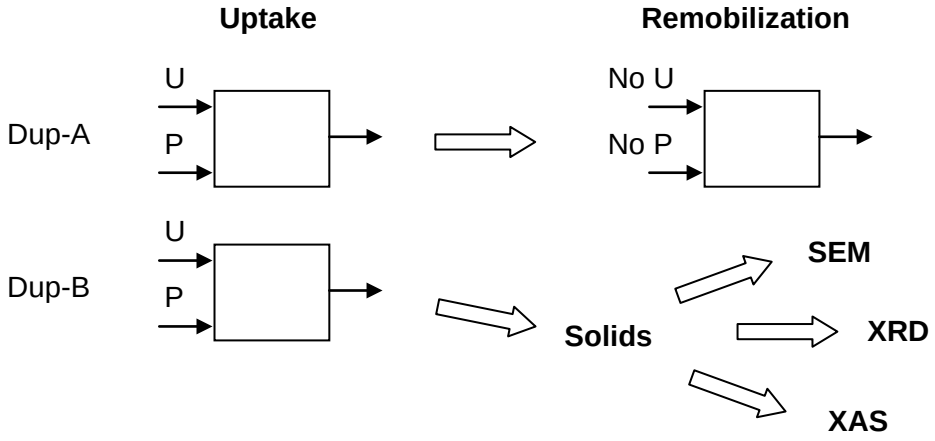

Figure 4.2. Uptake and remobilization periods for each CFSTR condition

Effluent U, P and Fe concentrations were measured with ICP-MS in small aliquots collected at regular time intervals. Concentrations of U and P provided information for determining uptake and remobilization rates, and Fe was monitored to

check if any goethite particles were leaking out of the reactor. Phosphate-free controls when no phosphate was introduced in the influent solutions were also performed. Procedural blanks were performed for supersaturated conditions that did not have goethite in the reactor but did have inlet uranium and phosphate solutions. Pb was used as a conservative tracer in previous studies in this lab to assess the mixing and ideality of CFSTR behavior. The measured effluent Pb concentrations matched closely with concentrations estimated using mass balance equations for an ideal CFSTR. Table 4.1 contains a matrix of the conditions that were studied at pH 4. Using the results from batch studies (Chapter 2) the concentrations of uranium and phosphate were chosen to have one condition favoring chernikovite precipitation and another that was undersaturated with respect to chernikovite and favored U-P-Fe ternary surface complex formation. The uptake experiments were run in duplicate. One of the duplicates was used for the remobilization period. The goethite suspension from the other replicate was centrifuged after the uptake period, and the resulting wet paste was saved for solid phase characterization.

Pastes were characterized using scanning electron microscopy (SEM), X-ray diffraction (XRD) and X-ray absorption fine-structure spectroscopy (XAFS) to determine the nature of U association with the solid phases. For the XAFS analysis, the condensed uranium-associated goethite wet pastes were loaded into 38 μL plexiglass sample holders, sealed with two layers of Kapton® tape and heat-sealed in a polyethylene bag. The remaining wet pastes were allowed to dry for the SEM and XRD analyses.

Table 4.1. Experimental conditions for CFSTR study at pH 4

Conditions[a]	TOTU (μM)	$TOTPO_4$ (μM)	Goethite (g/L)	Reactors	t_R
Undersaturated[a]					
Uptake in the absence of phosphate	1	0	0.59	2	2.5
Remobilization	0	0	0.59	1	6
Uptake in the presence of phosphate	1	100	0.59	2	2.5
Remobilization	0	0	0.59	1	6
Uptake in the absence of phosphate	100	0	0.59	2	2.5
Remobilization	0	0	0.59	1	6
Supersaturated[a]					
Uptake in the absence of goethite	100	100	0	2	2.5
Remobilization	0	0	0	1	6
Uptake in the presence of goethite	100	100	0.59	2	2.5
Remobilization	0	0	0.59	1	6

[a] with respect to chernikovite ($UO_2HPO_4 \cdot 4H_2O_{(s)}$)

4.2.3. Analysis

Dissolved U, P, and Fe concentrations were measured in a 1% HNO_3 matrix using ICP-MS (Agilent 7500ce) with method detection limits of 0.005 ppb, 0.8 ppb, and 1 ppb, respectively. Sample pH was measured using an Accumet Research glass electrode and pH meter. Residual solids from centrifuged pastes and those collected on filter membranes capping the reactors were analyzed by XRD (Rigaku Geigerflex D-MAX/A) using Cu-K_α radiation. Microscopy on these solids was performed using a JEOL 7001LVF SEM.

U L_{III}-edge XAFS spectra were collected at beamline 20-BM-B at the Advanced

Photon Source at Argonne National Laboratory. This beamline is equipped with a Si(111) double-crystal monochromator. The monochromator was calibrated using a Y metal foil that was mounted between two ionization chambers downstream of the sample; the first inflection point in the Y K-edge was set to 17038 eV. Fluorescence signals were collected using a 12-element solid-state Ge detector.

XAFS data were background-subtracted, splined, and processed using the Athena [10] and SIXPack [11] interfaces to the IFEFFIT XAFS analysis package [12]. Structural fitting of the XAFS spectra of uranyl-sorbed goethite was done using FEFF 8.2 [13] generated phase-shift and backscattering amplitude functions from the crystal structures of soddyite ($(UO_2)_2SiO_4 \cdot 2H_2O$) [14] and of metatorbernite ($Cu(UO_2PO_4)_2 \cdot 8H_2O$) [15] with Fe substituted for Cu. Spectra of the uranium phosphate solids were fit using FEFF 7.02 [13] generated functions from the sodium-meta autunite ($Na[(UO_2)(PO_4)](H_2O)_3$) structure [16]. All fits included the three multiple scattering paths involving the axial oxygen atoms of the uranyl cation.

4.2.4. Uptake rate calculations

U(VI) and phosphate uptake rates in the CFSTRs were calculated by performing U and phosphate mass balances on the reactor for each of the conditions and optimizing the rate constants to achieve the best model fit to the observed data.

4.2.4.1. Uranium uptake in the absence of phosphate

The experiment on U(VI) uptake by goethite in the absence of phosphate was modeled to obtain a rate constant (γ_U, min^{-1}) for the formation of the binary surface complex

≡FeO_2UO_2. Data for the low TOTU (1 µM) and high TOTU (100 µM) conditions were optimized to get the best fit γ_U for each TOTU condition, and the constants were then compared. Using the general mass balance (eq 1), uranium liquid-phase (LMB) and solid-phase mass balances (SMB) on the CFSTR resulted in eqs. 2 and 3.

$$Rate\ \ mass_{in} - Rate\ mass_{out} + Rate\ mass_{generated} - Rate\ mass_{lost} = Rate\ mass_{accumulated} \quad (1)$$

Uranium LMB:
$$\frac{Q}{2}U_{in} - QU_{eff} - VC_g\frac{dU_s}{dt} = V\frac{dU_{eff}}{dt} \quad (2)$$

Uranium SMB:
$$\frac{dU_s}{dt} = \gamma_U\left(U_s^{\ *} - U_s\right) = \gamma_U\left(\frac{3U_{eff}}{1+0.11U_{eff}} - U_s\right) \quad (3)$$

where Q is in L/min; V is in L; C_g is the goethite concentration in the reactor (g/L); U_{in} (constant, 2*TOTU) and U_{eff} are the respective dissolved uranium concentrations (µM) in the influent and effluent streams; U_s is the adsorbed uranium concentration (µmol/g) and U_s^* is the predicted equilibrium adsorbed uranium concentration at any time. The $\gamma_U\left(U_s^{\ *} - U_s\right)$ term is used to account for adsorption and desorption. U_s^* is expressed in terms of U_{eff} based on a Langmuir isotherm description of adsorption equilibrium. The isotherm parameters were independently achieved for pH 4 using batch adsorption data (Chapter 2), and the approach is described in detail in Appendix 4-A.

U(VI) uptake due to adsorption on goethite is given by the $-VC_g\frac{dU_s}{dt}$ term, which is then related to the distance from equilibrium term, $\gamma_U\left(U_s^{\ *} - U_s\right)$. Eqs. 2 and 3 were solved simultaneously by numerical integration (details in Appendix 4-B) using the initial condition: $U_{eff} = U_s = 0$.

4.2.4.2. Uranium uptake in the presence of phosphate

The effect of phosphate on U(VI) uptake on goethite was investigated for conditions undersaturated with respect to chernikovite. For supersaturated conditions, this effect was examined in the absence and presence of goethite.

Undersaturated conditions. For conditions undersaturated with respect to chernikovite, uranium and phosphate liquid-phase (LMB) and solid-phase mass balances (SMB) are given by eqs. 4-7. The uptake of U and phosphate is controlled by adsorption. In these equations γ_{UP} is the rate of adsorption of U and phosphate due to the formation of the ternary surface complex, $\equiv FePO_4UO_2$, and γ_P is the rate of adsorption of phosphate when the binary surface complex, $\equiv FePO_4H_2$, forms. Although U(VI) can also be taken up as the binary surface complex, $\equiv FeO_2UO_2$, it was not considered since the simultaneous U(VI) and phosphate uptake in macroscopic studies (Chapter 2) and the molecular-scale coordination environment of adsorbed uranium (Chapter 3) indicated the dominance of a ternary surface complex.

Uranium LMB:
$$\frac{Q}{2}U_{in} - QU_{eff} - VC_g\frac{dU_s}{dt} = V\frac{dU_{eff}}{dt} \quad (4)$$

Uranium SMB:
$$\frac{dU_s}{dt} = \gamma_{UP}\left(U_s^{\,*} - U_s\right) = \gamma_{UP}\left(\frac{65U_{eff}}{1+0.56U_{eff}} - U_s\right) \quad (5)$$

Phosphate LMB:
$$\frac{Q}{2}P_{in} - QP_{eff} - VC_g\frac{dU_s}{dt} - VC_g\frac{dP_s}{dt} = V\frac{dP_{eff}}{dt} \quad (6)$$

Phosphate SMB:

$$\frac{dP_s}{dt} = \gamma_P\left(P_s^{\,*} - P_s\right) + \gamma_{UP}\left(U_s^{\,*} - U_s\right) = \gamma_P\left(\frac{81.6P_{eff}}{1+0.79P_{eff}} - P_s\right) + \gamma_{UP}\left(\frac{65U_{eff}}{1+0.56U_{eff}} - U_s\right) \quad (7)$$

where P_{in} (constant, 2*$TOTPO_4$) and P_{eff} are the respective dissolved phosphate concentrations (μM) in the influent and effluent streams; P_s and P_s^* are the adsorbed phosphate concentrations (μmol/g) at any time and at equilibrium, respectively. Similar to eq. 2, U_s^* for this case is related to U_{eff} by a Langmuir fit to batch U adsorption data (Chapter 2) in the presence of phosphate at comparable $TOTPO_4$ conditions to those in the CFSTR experiments. Phosphate uptake has two terms: adsorption through the formation of the ternary surface complex, described by γ_{UP}, and adsorption as a binary surface complex. Both U and phosphate Langmuir isotherm fits utilize actual data supplemented with virtual data points generated using a surface complexation model [7]; the details of the Langmuir isotherm fits are provided in the Appendix 4-A. Eqs. 4-7 were solved simultaneously by numerical integration (details in Appendix 4-B) using the initial conditions: $U_{eff} = U_s = P_{eff} = P_s = 0$.

Supersaturated conditions in the absence of goethite. The high TOTU (100 μM) and high TOTP (100 μM) conditions at pH 4 were supersaturated with respect to chernikovite. The uptake period from the CFSTR experiments was used to estimate the critical supersaturation ratio for nucleation (Ω*) and the precipitation rate constant (k_p, μmol/m^2.min) for chernikovite. The remobilization period was then used to estimate chernikovite dissolution rate constant (k_d, μmol/m^2.min).

Uranium LMB: $$\frac{Q}{2}U_{in} - QU_{eff} - k_p SSA\, C_{Ch}\, V\, f(\Delta G) = V\frac{dU_{eff}}{dt} \quad (8)$$

Phosphate LMB: $$\frac{Q}{2}P_{in} - QP_{eff} - k_p SSA\, C_{Ch}\, V\, f(\Delta G) = V\frac{dP_{eff}}{dt} \quad (9)$$

SMB: $$k_p 10^{-6} SSA\ C_{Ch}\ V\ f(\Delta G)\ MW = V\frac{dC_{Ch}}{dt} \quad (10)$$

At t = 0, $U_{eff} = P_{eff} = C_{Ch} = 0$ (11)

where the $-k_p SSA\ C_{Ch}\ V\ f(\Delta G)$ term accounts for U(VI) and phosphate uptake due to precipitation of chernikovite; C_{Ch} and SSA respectively refer to the concentration (g/L) and specific surface area (m^2/g) of chernikovite at any time, and MW is the molecular weight of chernikovite (g/mol). The factor 10^{-6} in eq 10 is included to convert µmol to mol for use of MW in g/mol. Assuming the solubility product (K_{sp}) of chernikovite ($UO_2HPO_4 \cdot 4H_2O_{(s)}$) to be the same as the K_{sp} of uranium hydrogen phosphate ($UO_2HPO_4 \cdot 3H_2O_{(s)}$) used in Chapter 2, the following equilibrium relation was used to define the distance to equilibrium term, f(ΔG), (eq 13).

$$UO_2HPO_4 \cdot 3H_2O_{(s)} = UO_2^{2+} + PO_4^{3-} + H^+ + 3H_2O \qquad K_{sp} = 10^{-25.52} \quad (12)$$

$$f(\Delta G) = \left(\frac{IAP}{K_{sp}} - 1\right) = \left(\frac{\{UO_2^{2+}\}\{PO_4^{3-}\}\{H^+\}}{K_{sp}} - 1\right) \quad (13)$$

where IAP is the ion activity product determined using reaction 12. The expression for f(ΔG) follows from the generic relation: $f(\Delta G) = (e^{\Delta G / RT} - 1)^{\Omega}$, where Ω is an empirical parameter (here, set to 1). To compute the f(ΔG) term, $\{UO_2^{2+}\}$ and $\{PO_4^{3-}\}$ were needed. However, U_{eff} and P_{eff} were measured. Using uranium and phosphate aqueous complexation reactions, U_{eff} and P_{eff} were written in terms of the dominant U(VI) and phosphate complexes at pH 4, respectively (eqs. 14 and 15a).

$U_{eff} = [UO_2^{2+}] + UO_2\text{-OH complexes} + UO_2\text{-}PO_4 \text{ complexes} \approx 0.85\ [UO_2^{2+}]$ (14)

$P_{eff} = PO_4 \text{ acid-base complexes} + UO_2\text{-}PO_4 \text{ complexes} \approx 0.9\ [H_2PO_4^-]$ (15a)

Now, $H_2PO_4^-$ can be written in terms of PO_4^{3-} by using the phosphate acid-base reaction $PO_4^{3-} + 2H^+ = H_2PO_4^-$ ($K_2 = 10^{19.56}$) as,

$$\{H_2PO_4^-\} = K_2 \{PO_4^{3-}\}\{H^+\}^2, \quad (15b)$$

The activities of the ionic species in eq. 13 were written in terms of their concentrations by calculating the activity coefficient (γ) values of these species for I = 0.01 M using the Davies equation. While γ = 0.9 for H^+ and $H_2PO_4^-$, γ = 0.66 for UO_2^{2+}. By combining these γ values with eqs. 14 and 15b, eq 13 can be written as:

$$f(\Delta G) = \left(\frac{0.66\ U_{eff} P_{eff}}{(0.85)(0.9)K_2 K_{sp}[H^+]} - 1\right) \quad (16)$$

After expressing f(ΔG) in terms of U_{eff} and P_{eff}, a relationship between C_{Ch} and SSA was needed because both change quickly after nucleation. Therefore, it was assumed that as U and phosphate streams were introduced into the CFSTR the saturation ratio ($\Omega = IAP/K_{sp}$) increased with time until a critical supersaturation, Ω*, was reached. Once this point was reached, the model assumed that all particles (N_p) nucleated at once and formed critical sized nuclei. Thereafter, these particles grew along their characteristic length, L, resulting in chernikovite precipitation. No new particles formed after nucleation.

The chernikovite particles collected on the filter membrane at the end of the uptake period (SEM image in Figure 4.6a) had a rectangular prism-shaped morphology with an estimated length of 1.3 ± 0.1 μm and a height of 0.2 ± 0.1 μm. If the dimensions were denoted as aL, bL, and L, where L was equal to the height of the particle, then a is 6.5 after assuming that b equals a. The critical size for a rectangular nuclei as a function of Ω* is given by eq 17 [17].

$$L_c = -\frac{4}{3}(1+\frac{1}{b}+\frac{1}{a})\frac{v\sigma}{\Delta G_r} = \frac{4}{3}(1+\frac{2}{a})\frac{v\sigma}{RT\ln\Omega *} \quad (17)$$

where σ is the surface free energy, v is the molar volume (m^3/mol) of chernikovite, R is the universal gas constant (8.314·J/mol/K) and T is the ambient temperature (298 K). Since σ for chernikovite could not be found in the literature, its value was assumed to be 200 mJ/m^2 as it was in the mid range of values experimentally determined for apatite and other minerals [17]. Chernikovite molar volume can be related to its MW (876.14 g/mol) and density ρ (3260 kg/m^3) as v = MW/(ρ*1000).

The SSA, by definition, can be written in terms of L as follows:

$$SSA = \frac{Surface\ \ Area}{Mass} = \frac{2(aL)(aL)+4(aL)(L)}{1000\rho(aL)^2 L} = \frac{2a+4}{1000\rho\ aL} \quad (18)$$

Likewise, the concentration of solids can also be expressed in terms of L as follows:

$$C_{Ch} = \frac{N_p\rho(aL)^2 L}{V} = \frac{1000N_p\rho\ a^2L^3}{V} \quad (19)$$

where N_p was estimated to be $3.1\cdot10^{11}$ by dividing the mass of uranium taken up (from dissolved concentration data at the end of the uptake period) by the mass of a single chernikovite particle (using SEM estimated dimensions and ρ). Ω* and k_p were optimized by minimizing the residual squared error between the measured and modeled uranium and phosphate effluent concentrations. For each set of parameter values, the modeled concentrations were obtained by numerically integrating eqs. 8-10 along with the constraints in eqs. 11, 16-19.

Supersaturated conditions in the presence of goethite. The individual models describing U(VI) uptake due to the ternary surface complex formation and chernikovite precipitation were combined to form a composite model for predicting uranium and phosphate fate. Model simulations were then compared with the experimental data. The optimized parameters from the individual models were preserved.

Uranium LMB: $$\frac{Q}{2}U_{in} - QU_{eff} - VC_g\frac{dU_s}{dt} - k_p SSA\ C_{Ch}\ V\ f(\Delta G) = V\frac{dU_{eff}}{dt} \quad (20)$$

Adsorbed uranium MB: $$\frac{dU_s}{dt} = \gamma_{UP}\left(U_s^{*} - U_s\right) = \gamma_{UP}\left(\frac{65U_{eff}}{1+0.56U_{eff}} - U_s\right) \quad (21)$$

Phosphate LMB:

$$\frac{Q}{2}P_{in} - QP_{eff} - VC_g\frac{dU_s}{dt} - VC_g\frac{dP_s}{dt} - k_p SSA\ C_{Ch}\ V\ f(\Delta G) = V\frac{dP_{eff}}{dt} \quad (22)$$

Adsorbed phosphate MB:

$$\frac{dP_s}{dt} = \gamma_P\left(P_s^{*} - P_s\right) + \gamma_{UP}\left(U_s^{*} - U_s\right) = \gamma_P\left(\frac{81.6P_{eff}}{1+0.79P_{eff}} - P_s\right) + \gamma_{UP}\left(\frac{65U_{eff}}{1+0.56U_{eff}} - U_s\right) \quad (23)$$

Chernikovite MB: $$k_p 10^{-6} SSA\ C_{Ch}\ V\ f(\Delta G)\ \ MW = V\frac{dC_{Ch}}{dt} \quad (24)$$

At t = 0, $$U_{eff} = P_{eff} = U_s = P_s = C_{Ch} = 0 \quad (25)$$

The above five differential equations were solved numerically using eqs. 16-19 and the initial conditions (eq 25).

4.2.5. Remobilization rate calculations

For all the conditions used to investigate uptake, the U(VI) and phosphate remobilization

rates were also calculated by performing mass balances. The key difference between the uptake period and remobilization period models was that in remobilization there was no influent U(VI) or phosphate term (U_{in} = P_{in} = 0). These equations are summarized in Table 4.2. The initial conditions for these governing equations are represented by the end of the uptake period when t_R = 2.5.

Table 4.2. Governing equations for the remobilization of uranium and phosphate

Elution of adsorbed uranium in the absence of phosphate:

Uranium LMB: $$-QU_{eff} - VC_g \frac{dU_s}{dt} = V \frac{dU_{eff}}{dt} \quad (26)$$

Uranium SMB: $$\frac{dU_s}{dt} = -\alpha_U (U_s - U_s^*) \approx -\alpha_U U_s \quad (27)$$

Initial conditions: $$U_{eff} = U_{eff}(t_R = 2.5); U_s = U_s(t_R = 2.5)$$

where α_U, is the remobilization rate constant (min^{-1}) for U(VI) adsorbed as $\equiv FeO_2UO_2$. The desorption was assumed to occur far enough from equilibrium such that $U_s >> U_s^*$.

Elution of adsorbed uranium and phosphate:

Uranium LMB: $$-QU_{eff} - VC_g \frac{dU_s}{dt} = V \frac{dU_{eff}}{dt} \quad (28)$$

Uranium SMB: $$\frac{dU_s}{dt} = -\alpha_{UP} (U_s - U_s^*) \approx -\alpha_{UP} U_s \quad (29)$$

Phosphate LMB: $$-QP_{eff} - VC_g \frac{dP_s}{dt} - VC_g \frac{dU_s}{dt} = V \frac{dP_{eff}}{dt} \quad (30)$$

Phosphate SMB: $$\frac{dP_s}{dt} = -\alpha_P P_s - \alpha_{UP} U_s \quad (31)$$

Initial conditions: $$U_{eff} = U_{eff}(t_R = 2.5); U_s = U_s(t_R = 2.5); P_{eff} = P_{eff}(t_R = 2.5); P_s = P_s(t_R = 2.5)$$

where α_{UP}, and α_P are the remobilization rate constants (min^{-1}) for U(VI) and phosphate adsorbed as $(\equiv FeO)_2UO_2PO_4$ and for phosphate adsorbed as $\equiv FePO_4H_2$, respectively. The desorption was assumed to occur far enough from equilibrium such that $U_s >> U_s^*$.

Dissolution of precipitated chernikovite:

Uranium LMB: $$-QU_{eff} - k_d SSA\ C_{Ch}\ V\ f(\Delta G) = V\frac{dU_{eff}}{dt} \quad (32)$$

Phosphate LMB: $$-QP_{eff} - k_d SSA\ C_{Ch}\ V\ f(\Delta G) = V\frac{dP_{eff}}{dt} \quad (33)$$

SMB: $$k_d 10^{-6} SSA\ C_{Ch}\ V\ f(\Delta G)\ MW = V\frac{dC_{Ch}}{dt} \quad (34)$$

Initial condition: $U_{eff} = U_{eff}(t_R = 2.5); P_{eff} = P_{eff}(t_R = 2.5); C_{Ch} = C_{Ch}(t_R = 2.5)$

where k_d is the chernikovite dissolution rate constant (μmol/m^2.min). Eqs. 16-19 will hold as for the uptake regime. Since the dissolution-precipitation reaction for chernikovite, as written in eq. 12, is not an elementary reaction, k_p/k_d need not equal K_{sp}.

U(VI) and phosphate elution in the presence of goethite for supersaturated conditions:

Uranium LMB: $$-QU_{eff} - VC_g\frac{dU_s}{dt} - k_d SSA\ C_{Ch}\ V\ f(\Delta G) = V\frac{dU_{eff}}{dt} \quad (35)$$

Adsorbed uranium MB: $$\frac{dU_s}{dt} = -\alpha_{UP}U_s \quad (36)$$

Phosphate LMB: $$-QP_{eff} - VC_g\frac{dU_s}{dt} - VC_g\frac{dP_s}{dt} - k_d SSA\ C_{Ch}\ V\ f(\Delta G) = V\frac{dP_{eff}}{dt} \quad (37)$$

Adsorbed phosphate MB: $$\frac{dP_s}{dt} = -\alpha_P P_s - \alpha_{UP}U_s \quad (38)$$

Chernikovite MB: $$k_d SSA\ C_{Ch}\ V\ f(\Delta G)\ MW = V\frac{dC_{Ch}}{dt} \quad (39)$$

Initial condition: $U_{eff}, U_s, P_{eff}, P_s, C_{Ch} = U_{eff}, U_s, P_{eff}, P_s, C_{Ch} \mid t_R = 2.5$

Eqs. 16-19 will hold as for the uptake regime.

4.3. Results and discussion

CFSTR experimental data were used to investigate the effect of phosphate on the mechanism and extent of uranium uptake and remobilization in the presence of goethite under conditions favoring uranium adsorption as well as precipitation. Effluent

concentrations (C) were normalized with respect to the maximum concentration achievable in the reactor (TOTU or C_0) and were plotted against normalized time (t/t_R). Results from the uptake period (up to 2.5 t/t_R) are shown first followed by those from the remobilization period (~6 t/t_R).

4.3.1. Undersaturated conditions

The presence of phosphate significantly enhanced uranium(VI) uptake on goethite. The effluent uranium concentrations after ~0.3 t_R were much lower than in the absence of phosphate for both duplicate reactors (Figure 4.3a). U(VI) uptake in the presence of phosphate was 4.4-4.6 µmol/g (estimated from solid-phase mass balance (Appendix 4-C) divided by the concentration of goethite), which was significantly higher than the 0.3-1.4 µmol/g taken up in its absence. The corresponding phosphate concentrations began to show a breakthrough after ~0.5 t_R when compared with a non-reactive tracer (Figure 4.3b), indicating favorable phosphate uptake. Furthermore, phosphate uptake (64-78 µmol/g) was significantly higher than uranium uptake, which is consistent with observations of U(VI) and phosphate adsorption under static conditions at pH 4 [7]. These results suggest that the uptake of phosphate predominantly occurred by the formation of a binary surface complex not involving uranium, such as $\equiv FePO_4H_2$, that probably formed sooner than a ternary surface complex involving U, phosphate and the goethite surface. Uranium(VI) uptake was enhanced because the surface-bound phosphate made it more favorable for uranium to adsorb through the formation of the ternary surface complex.

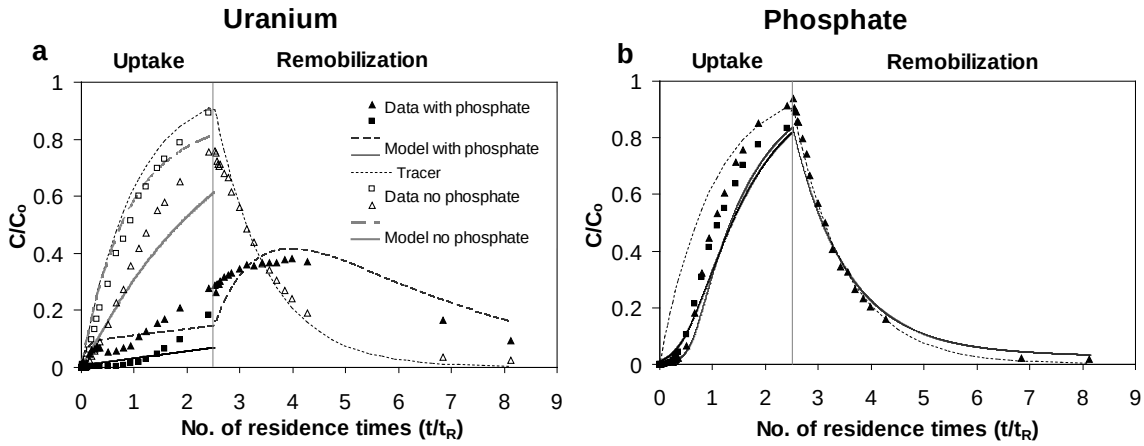

Figure 4.3. Uranium(VI) and phosphate uptake on goethite in the presence (closed symbols) and absence (open symbols) of influent phosphate and subsequent remobilization with 0.01 M $NaNO_3$ solution at pH 4. Influent solutions contained 2 µM U_{in} and either 0 or 200 µM P_{in} at pH 4 and 0.01 M ionic strength. t_R was 210 min. These conditions were undersaturated with respect to chernikovite. Uptake periods were run in duplicates for both conditions, and the remobilization period was only run on one duplicate. Solid lines indicate CFSTR model fits and the dashed line indicates predicted concentrations for a conservative tracer. Of the total uranium and phosphate taken up, ~69% and ~52% respectively eluted during the remobilization period.

Solid phase analysis. As was expected for the undersaturated conditions, SEM images of solids collected at the end of the uptake experiment did not reveal a uranium phosphate precipitate. Goethite particles were present as agglomerates (Figure 4-A4). EDX analysis detected Fe and O but no U, P or Na, which suggested that the agglomerated particles did not include any uranium phosphate. The detection limit of EDX is such that adsorbed U, P, and Na would not be detected.

Spectroscopic evidence for the formation of the ternary surface complex was obtained from XAFS investigations of the coordination environment of uranium (Figure 4.4). The U L_{III}-edge EXAFS spectra for the uranyl-sorbed goethite sample in the presence of phosphate for the undersaturated conditions (Figure 4.4 line c) were compared with the spectra of adsorbed uranium in phosphate-free samples (Figure 4.4

lines d and e) obtained respectively from the CFSTR control experiment at pH 4 and the batch study presented earlier (Figure 3.2 line e). Results from the shell-by-shell fitting of the Fourier transformed EXAFS spectra are shown in Table 4.3.

For the uranyl-sorbed goethite samples in the absence of phosphate at pH 4, a single starting structural model developed earlier (section 3.3.3.1) was refined against the individual spectra. The model included a single axial oxygen shell (U-O_{ax}) at ~1.78 Å, a split equatorial oxygen shell at ~2.3 (U-O_{eq1}) and ~2.5 Å (U-O_{eq2}) commonly observed for inner-sphere U(VI) surface species, the three multiple scattering paths associated with U-O_{ax}, and two iron shells at ~3.48 (U-Fe_1) and ~4.1 Å (U-Fe_2). No U-C paths were included in the model because carbonate was not significant at pH 4 [18]. The Debye-Waller factor was fixed for the U-Fe shells during the optimization at an arbitrarily chosen value that was sufficiently high (typically these values increase with increasing shell distance). The details of this model have been discussed in section 3.3.3.1. Briefly, uranium adsorbed by forming inner-sphere bidentate edge-sharing (E2), $\equiv Fe(OH)_2UO_2$ [18-20], and bidentate corner-sharing (C2), $(\equiv FeOH)_2UO_2$ [21], surface complexes.

Similarly, the ternary surface complex structural model developed previously (details in section 3.3.3.4) was refined to fit the EXAFS spectrum and Fourier-transform corresponding to the uranyl-sorbed goethite sample in the presence of phosphate (Figure 4.4 line c). Besides contributions from the U-O_{ax}, U-O_{eq1}, and U-O_{eq2} shells and associated multiple scattering, a single phosphorus shell at ~3.64 Å (U-P) and a single iron shell at ~4.2 Å (U-Fe) were needed to achieve the best fit. For the undersaturated conditions, phosphate enables the formation of a ternary surface complex, such as $(\equiv FeO)_2UO_2PO_4$, in which uranium acts as a bridging ligand at sites that favored the C2

complex in the absence of phosphate.

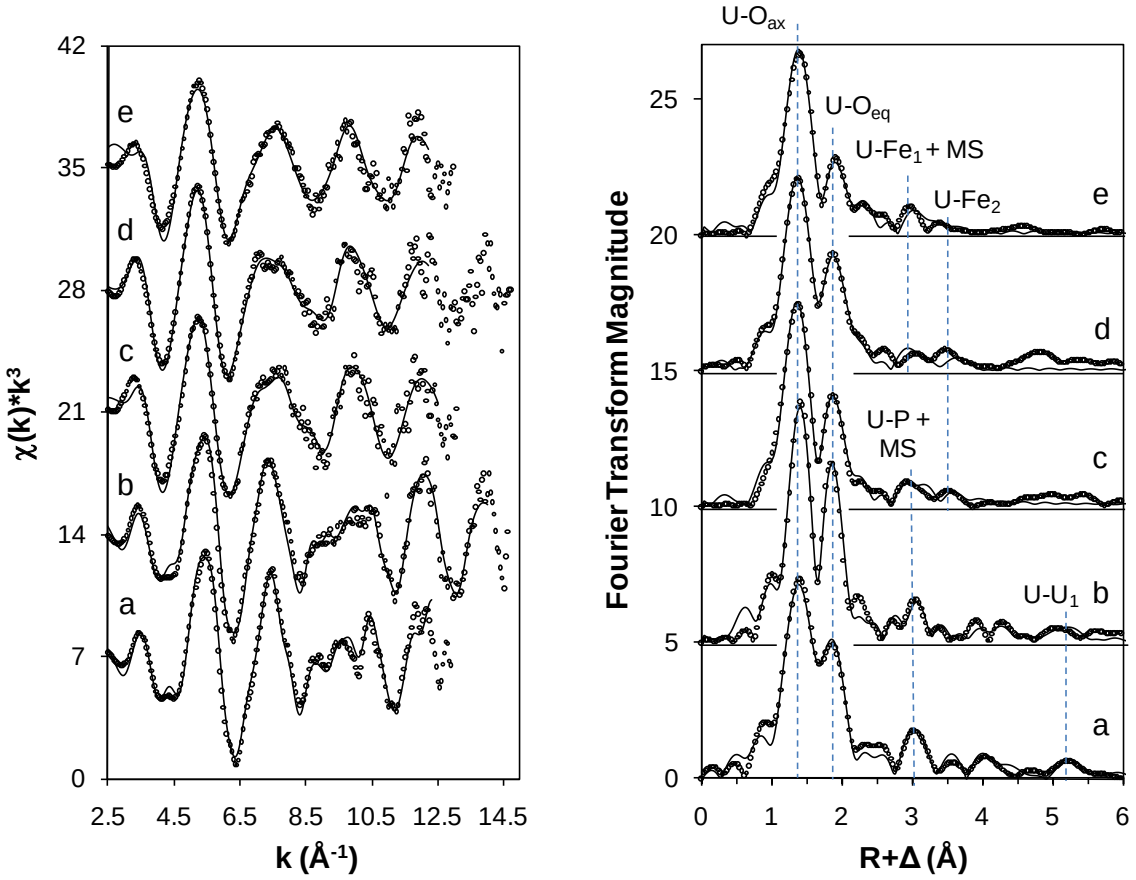

Figure 4.4. U L_{III}-edge EXAFS spectra (left) and Fourier transforms (right) of precipitated and uranyl-sorbed goethite samples for different experimental conditions: a) Batch_chernikovite; b) CFSTR_100 µM TOTU_with phosphate; c) CFSTR_1 µM TOTU_with phosphate; d) CFSTR_100 µM TOTU_no phosphate; e) Batch_100 µM TOTU_no phosphate. Dots represent data and lines represent the least-squares fits to the data.

Table 4.3. EXAFS fitting results

Sample		$U\text{-}O_{ax}$	$U\text{-}O_{eq1}$	$U\text{-}O_{eq2}$	$U\text{-}Fe_1$	U-P	$U\text{-}Fe_2$	$U\text{-}U_1$	$U\text{-}U_2$	ΔE_0 (eV)[e]	χ_r^2 [f]	R-factor[g]
a) Chernikovite	N[a]	2[d]	4.5(3)			4[d]		4[d]	4[d]	5.4(8)	56.93	0.0156
Batch	R (Å)[b]	1.775(4)	2.281(5)			3.64(1)		5.28(2)	6.84(5)			
	σ^2 (Å^2)[c]	0.0023(3)	0.0048(7)			0.003(1)		0.010(2)	0.010			
b) 100 µM TOTU	N[a]	2[d]	3.9(3)			4[d]		4[d]	4[d]	5.1(8)	10.85	0.0223
CFSTR_with phosphate	R (Å)[b]	1.782(3)	2.294(4)			3.61(2)		5.28(3)	6.74(6)			
	σ^2 (Å^2)[c]	0.0017(2)	0.0035(6)			0.007(2)		0.011(2)	0.011			
c) 1 µM TOTU	N[a]	2[d]	2.5(6)	1.7(7)		0.4(8)	0.8(8)			14(2)	7.33	0.0201
CFSTR_with phosphate	R (Å)[b]	1.778(6)	2.33(3)	2.47(4)		3.64(4)	4.19(7)					
	σ^2 (Å^2)[c]	0.0022(4)	0.005[d]	0.005[d]		0.001(10)	0.008[d]					
d) 100 µM TOTU	N[a]	2[d]	3(2)	3(2)	0.4(6)		0.6(4)			12(3)	37.03	0.0224
CFSTR_no phosphate	R (Å)[b]	1.780(9)	2.31(6)	2.45(6)	3.5(1)		4.13(8)					
	σ^2 (Å^2)[c]	0.0027(6)	0.008(8)	0.008	0.009[d]		0.009[d]					
e) 100 µM TOTU	N[a]	2[d]	1.9(6)	1.6(7)	0.3(6)		0.5(9)			12(3)	22.02	0.0231
Batch_no phosphate	R (Å)[b]	1.802(5)	2.36(3)	2.53(4)	3.5(1)		4.1(1)					
	σ^2 (Å^2)[c]	0.0028(6)	0.005(2)	0.005	0.008[d]		0.008[d]					

Note: The estimated standard deviations are listed in parentheses, representing errors in the last digit; the amplitude damping factor, $S_o^2 = 1$, was used for all fits.

[a] coordination number; [b] interatomic distance; [c] Debye-Waller factor; [d] values fixed during fitting; [e] difference in threshold Fermi level between data and theory; [f] reduced χ^2, and [g] R-factor, as goodness of fit parameters.

CFSTR modeling results. U(VI) uptake in the absence of phosphate indicates that formation of the uranium binary surface complexes was not rate-limited but was determined by equilibrium (uptake was insensitive to the adsorption rate constant for the two replicates shown in Figure 4.3a). U(VI) remobilization for these conditions was similar to that of a conservative tracer, which indicates that desorption was also not rate-limited.

Results for the uptake of U(VI) by formation of the $(\equiv FeO)_2UO_2PO_4$ complex and of phosphate by the $\equiv FePO_4H_2$ and $(\equiv FeO)_2UO_2PO_4$ complexes are also shown in Figure 4.3. The rate of formation of the $\equiv FePO_4H_2$ complex was calculated to be higher than the rate of formation of the $(\equiv FeO)_2UO_2PO_4$ complex by about an order of magnitude; the $\equiv FePO_4H_2$ formation rate constant, γ_P, was in the range 0.014-0.1 min^{-1} (Figure 4.3b) while the $(\equiv FeO)_2UO_2PO_4$ formation rate constant, γ_{UP}, was estimated to be within $1.29*10^{-3}$-$1.82*10^{-2}$ min^{-1} (Figure 4.3a). The rate of remobilization was faster for the ternary surface complex ($\alpha_{UP} = 1.49*10^{-3}$ min^{-1}) than for the phosphate binary surface complex ($\alpha_P = 2.91*10^{-4}$ min^{-1}). Interestingly, the rates of formation and remobilization of the ternary surface complex were found to be similar. The ratios of the formation and remobilization rate constants for the two types of adsorbed phosphate complexes indicate that the $\equiv FePO_4H_2$ complex ($\gamma_P/\alpha_P \sim 10^2$-$10^3$) was stronger than the $(\equiv FeO)_2UO_2PO_4$ complex ($\gamma_P/\alpha_P \sim$ 1-10). A faster remobilization of the ternary surface complex may further support the $(\equiv FeO)_2UO_2PO_4$ structure over the $\equiv FePO_4UO_2$ structure for the ternary surface complex (bridged by uranyl), as it would be probably easier to break a uranyl bonded to Fe octahedra than a phosphate.

4.3.2. Supersaturated conditions

The presence of phosphate enhanced uranium(VI) uptake for the supersaturated conditions both in the absence and presence of goethite.

4.3.2.1. Absence of goethite

Uranium and phosphate uptake trends indicate formation of a uranium phosphate solid (Figure 4.5). Effluent uranium and phosphate concentrations show a significant decrease relative to the tracer after ~0.5 residence times indicating the onset of precipitation. Thereafter the effluent concentrations stabilized at ~0.15 C/C_o for both U(VI) and phosphate suggesting precipitation of a solid with a 1:1 U:P molar ratio (14.4-15.2 µmol of U(VI) uptake relative to 14.0-15.8 µmol of phosphate uptake).

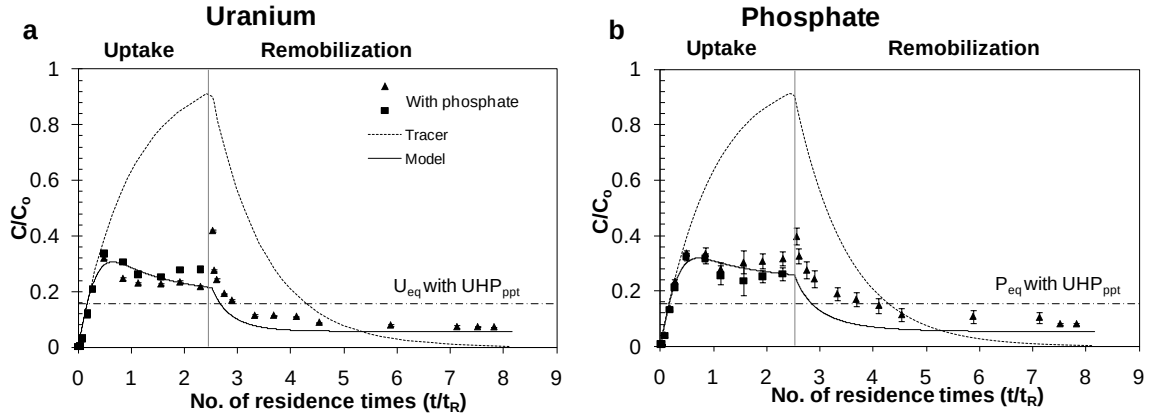

Figure 4.5. Uranium(VI) and phosphate uptake in the absence of goethite and subsequent remobilization with 0.01 M $NaNO_3$ solution at pH 4. Influent solutions contained 200 µM U_{in} and 200 µM P_{in} at pH 4 and 0.01 M ionic strength. t_R was 210 min. These conditions were supersaturated with respect to chernikovite. The uptake period was run with duplicate reactors in the presence of phosphate; one of those duplicates was then used for measuring remobilization. Symbols represent effluent concentrations and solid lines represent model predicted concentrations. The two dashed lines indicate predicted non-reactive tracer concentrations and equilibrium solubility of uranyl hydrogen phosphate (UHP_{ppt}), respectively. Error bars indicate 95% confidence intervals of mean measured concentrations. Of the total uranium and phosphate taken up, ~23% and ~38% respectively eluted during the remobilization period.

Furthermore, a significant fraction of the uranium phosphate solids precipitated as nanoparticulate colloids as suggested by a significant decrease in dissolved uranium and phosphate concentrations after selected effluent samples were filtered again using a 20 nm filter (data not shown).

Solid phase analysis. Direct evidence for chernikovite precipitation was obtained from SEM images of particles collected on the filter membrane capping the CFSTR (Figure 4.6a).

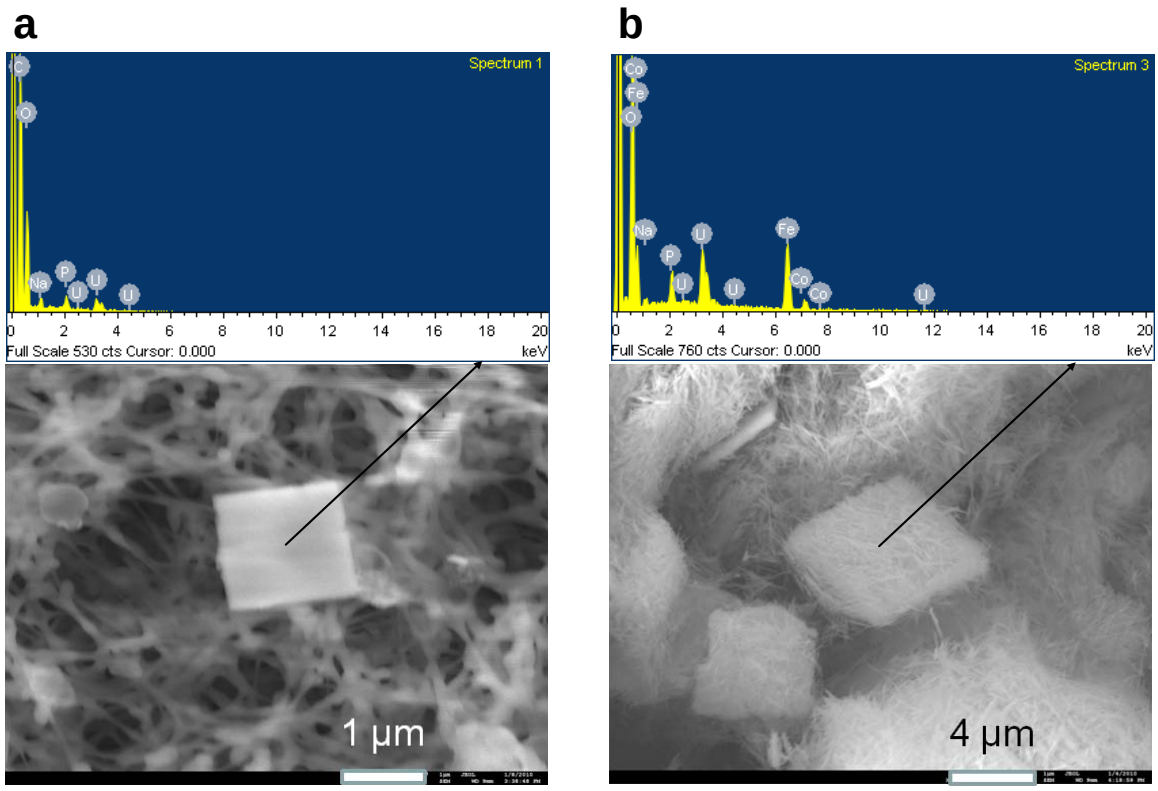

Figure 4.6. Electron micrographs of chernikovite in the (a) absence and (b) presence of goethite collected on 0.2 µm filter membranes for the supersaturated conditions. The corresponding EDX patterns are also shown above the images. Note the different scales of the images.

The particles have the rectangular prism-shapes typical of chernikovite particles observed previously [7, 22, 23]. EDX analysis of these particles confirmed the presence of U and P. Na was also detected but it was most likely from the sodium nitrate used for

fixing the ionic strength. Sodium meta-autunite was not expected as it was not found for similar conditions previously (Chapter 2).

The solids-loaded filter membranes were also analyzed using XRD (Figure 4.7). Although some of the reflections corresponding to the chernikovite diffraction pattern were not recorded due to preferred orientation of crystals on the filter membranes, the most prominent peaks were the same as those of previously synthesized chernikovite crystals and the reference pattern [7].

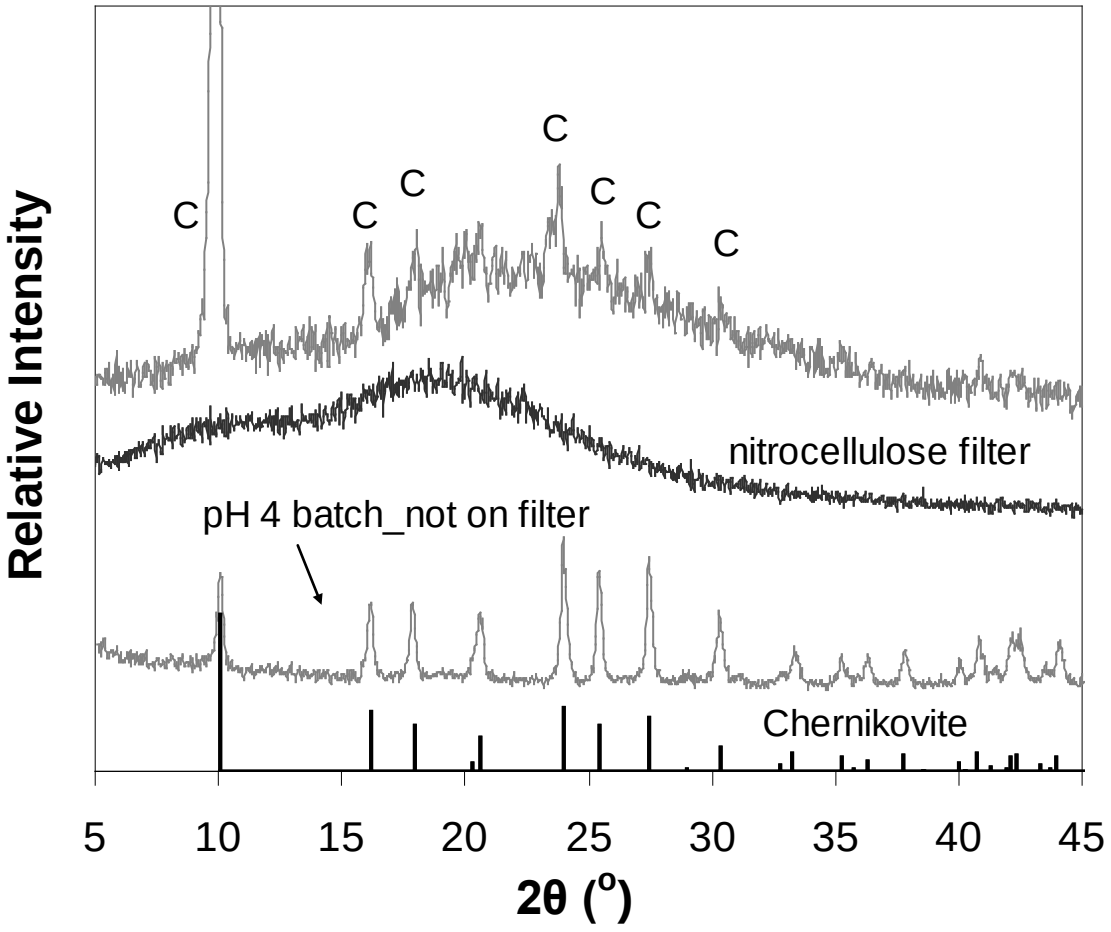

Figure 4.7. X-ray diffraction pattern of the precipitated uranium phosphate in the absence of goethite collected on 0.2 µm nitrocellulose filter membrane for the supersaturated conditions. The chernikovite reference pattern, PDF# 01-075-1106, and the batch-synthesized (Chapter 2) pattern are also shown for comparison. The chernikovite peaks are labeled as C.

CFSTR modeling results. Precipitation of chernikovite in the two replicate reactors resulted in a critical supersaturation for nucleation, Ω*, of 1.23 ($f(\Delta G^*) = 0.23$) and a precipitation rate constant (k_p) of 4.1-4.2*10^{-9} mol/m^2.s. The precipitation rate at steady state, 1.80-1.85*10^{-8} mol/m^2.s ($k_p \cdot f(\Delta G_{ss})$ where $f(\Delta G_{ss})$ is the distance to equilibrium at steady state, and is equal to 4.4), is about three orders of magnitude higher than the measured precipitation rate (4.7-6.5*10^{-11} mol/m^2.s) of chernikovite formed as a secondary mineral during phosphate-promoted uraninite dissolution [24]. Rey et al. estimated these rates by recording time-dependent scanning force microscopy (SFM) topographic profiles of the precipitating solids. The discrepancy in rate estimates could be due to the differences in the minimum time interval for recording successive observations in the two studies; SFM images were recorded at least every ~40 h, which is much higher than the 5-15 min time interval used in the CFSTR study presented here. Secondly, the rate estimates using SFM depended strongly on the accuracy of the average height of chernikovite particles estimated from images at a given time, which may have significant variability. Thirdly, their rate estimates could also be different because the uraninite dissolution could actually be the rate-limiting step in the overall formation of the U(VI) phosphate.

The remobilization of U(VI) and phosphate for these conditions was limited by the dissolution kinetics of the precipitated chernikovite (Figure 4.5). CFSTR modeling results indicate a chernikovite dissolution rate constant (k_d) of 1.4*10^{-9} mol/m^2.s, which is quite similar in magnitude to the k_p. If the reaction were elementary and reversible, k_p/k_d should equal K_{sp}. However, chernikovite dissolution-precipitation is not an elementary reaction (eq. 12), and k_p and k_d are overall rate constants that cannot be

related to K_{sp}. Barring an initial transient region when conditions were switched from uptake to remobilization, U(VI) and phosphate model predictions explained the observed data quite well. However, the remobilized phosphate concentrations were underpredicted by the model that assumed stoichiometric dissolution of chernikovite. Non-stoichiometric dissolution of chernikovite was evident from the release of 4.8 µmol of U(VI) along with 7.3 µmol of phosphate after 6 t_R of the remobilization experiment. These results are similar to the non-stoichiometric dissolution of meta-autunite minerals reported previously [25, 26]. As a result of such non-stoichiometric dissolution, the remaining chernikovite particles may gradually transform into a new phase, such as $(UO_2)_3(PO_4)_2 \cdot xH_2O$, with molar U/P > 1. The chernikovite dissolution rate at steady state, $7.7*10^{-10}$ mol/m^2.s ($k_d \cdot f(\Delta G_{ss})$ where $f(\Delta G_{ss}) = 0.55$), was more than two orders of magnitude higher than the dissolution rates of sodium and calcium meta-autunites (~10^{-13} mol/m^2.s) at pH 4 estimated by Wellman et al. [25] using the steady-state effluent concentrations of uranium and phosphate. To the best of our knowledge the dissolution rate of chernikovite has not been reported previously.

4.3.2.2. Presence of goethite

Phosphate-induced precipitation of chernikovite also occurred for the supersaturated conditions in the presence of goethite (Figure 4.8). The effluent U(VI) concentrations after the onset of precipitation (~0.5 t_R) were significantly lower in the presence of influent phosphate than for the phosphate-free conditions (Figure 4.8a). In the presence of phosphate, the total U(VI) uptake increased from 40 µmol/g to 289-299 µmol/g over the 2.5 t_R run. Before precipitation started, the effluent phosphate concentrations were

similar to those recorded for the undersaturated conditions, which indicates significant initial phosphate uptake due to formation of the $\equiv FePO_4H_2$ surface complex (Figure 4.8b). However, unlike for the undersaturated conditions the phosphate concentrations did not achieve a breakthrough at higher t_R but were limited by chernikovite precipitation. The total phosphate uptake (330-358 µmol/g) was more than the corresponding total U(VI) uptake needed for chernikovite formation (lower U:P uptake ratio than 1:1) because significant phosphate adsorbed to goethite in addition to forming chernikovite. This increased phosphate uptake was similar to the phosphate uptake during undersaturated conditions (64-78 µmol/g). Furthermore, the total µmoles of uranium precipitated (14.3-14.8) during the uptake period were similar to µmoles precipitated in the absence of goethite (14.4-15.2).

Effluent U(VI) and phosphate concentrations also demonstrated an instability that was not observed previously (Figures 4.3 and 4.5). This instability could be due to the interaction of negatively charged colloidal uranium phosphate solids with a positively charged goethite surface. As in the absence of goethite, evidence of the formation of colloids was found from the significant decrease in dissolved concentrations after selected effluent samples were filtered again using a 20 nm filter (Appendix 4-D).

In addition to the differences in uptake, the remobilization curves for the supersaturated and the undersaturated conditions also differ remarkably (Figures 4.8 and 4.3). In the presence of phosphate, while the remobilization curve for the undersaturated conditions had a broad peak, for the supersaturated conditions, the remobilization period had a long tail indicative of elution of a dissolving solid. The dissolution of chernikovite governed uranium (93 µmol/g) and phosphate (86 µmol/g) elution in the presence of

goethite after 6 t_R of the remobilization period.

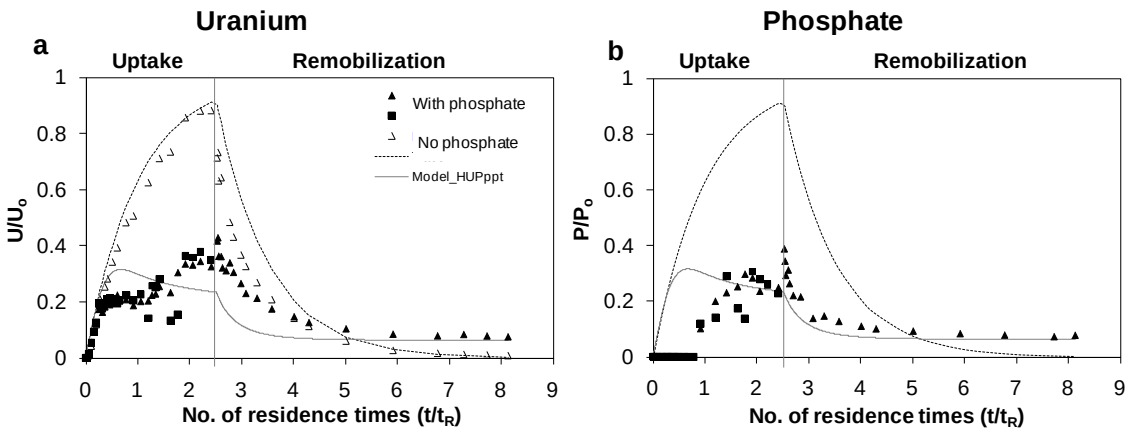

Figure 4.8. Uranium(VI) and phosphate uptake on goethite in the presence (closed symbols) and absence (open symbols) of influent phosphate and subsequent remobilization with 0.01M $NaNO_3$ solution at pH 4. Influent solutions contained 200 µM U_{in} and either 0 or 200 µM P_{in} at pH 4 and 0.01 M ionic strength. t_R was 210 min. These conditions were supersaturated with respect to chernikovite. The uptake experiment was run in duplicate in the presence of phosphate; one of the duplicates was used for recording remobilization. The solid line indicates CFSTR model predictions for saturated conditions in the absence of goethite. Of the total uranium and phosphate taken up, ~31% and ~24% respectively eluted during the remobilization period.

Solid phase analysis. Imaging of solids retained on the filter membranes at the end of the uptake experiments revealed the typical chernikovite-like particles covered with goethite (Figure 4.6b). EDX confirmed the presence of U and P. Na was also detected just as in the absence of goethite. However, since the particle morphology resembled those in the absence of goethite, it appears that Na could be from the sodium nitrate salt. No such solids were observed for conditions in the absence of phosphate, where aggregates of goethite particles were observed. EDX analysis of those aggregates detected only Fe and O.

Spectroscopic evidence for the formation of a solid belonging to the meta-autunite group in the presence of goethite was obtained from XAFS (Figure 4.4). The U L_{III}-edge

EXAFS spectrum for the uranyl-associated goethite sample for the supersaturated conditions (Figure 4.4 line b) was similar to the spectrum of synthetic chernikovite (Figures 4.4 line a) resolved previously (Chapter 3). Both the standard and the sample were fit to the sodium meta-autunite structure [16]. These shell-by-shell fitting results of the Fourier transformed EXAFS spectra are shown in Table 4.3. The meta-autunites are sheets of coordinated uranium and phosphate polyhedra [27]. Since XAFS cannot be used to distinguish the interlayer cations in these structures, sodium meta-autunite is indistinguishable from chernikovite by this technique. However, it was still able to confirm that the solids precipitated in the presence of goethite belonged to the meta-autunite group.

CFSTR modeling results. Predictions for this condition were made by combining U(VI) and phosphate uptake rates due to adsorption and precipitation determined in earlier experiments. The values of rate constants determined for the formation of the ternary and binary uranium and phosphate surface complexes from the undersaturated conditions and for chernikovite precipitation from supersaturated conditions were used. However, the calculations did not converge. This may probably require shorter time steps for integration. Since chernikovite precipitation was the dominant uptake mechanism also in the presence of goethite, results from the CFSTR model in the absence of goethite were used for comparison against the measured data (Figure 4.8). While this model was able to predict U(VI) and phosphate remobilization quite well, the predictions for the uptake period were not as good. Significant phosphate adsorption for the initial residence times, for example, was one factor that was not accounted for in this

precipitation model.

4.4. Implications for uranium remediation

Uranium uptake is enhanced by soluble phosphate either by inducing the formation of a ternary surface complex on dominant mineral matrices such as goethite or by favoring precipitation of chernikovite. The extent of U(VI) immobilization via precipitation is likely to exceed immobilization via adsorption. With adsorption the sites become saturated and breakthrough occurs, while continuous uptake of U(VI) occurs as long as there is sufficient phosphate. Moreover, the formation of the ternary surface complex was found to be rapidly reversible when conditions changed to U-free solutions. The dissolution rate constant of chernikovite, on the other hand, was ~3 times slower than its rate constant for formation.

For phosphate-based in-situ immobilization strategies it is essential to recognize that sufficient phosphate was needed to precipitate U(VI). Although thermodynamic equilibrium calculations predict formation of uranyl orthophosphate and sodium meta-autunite as the long term stable phases of uranium phosphates, chernikovite is the phase that actually forms because it is kinetically favored. In subsurface systems chernikovite may determine the fate of U(VI), particularly in the time immediately after phosphates are injected into the subsurface. Furthermore, the chernikovite formation requires a low degree of supersaturation (1.23) which indicates that not a great excess of phosphate (other than that to overcome the adsorptive capacity of the aquifer) was needed to induce precipitation.

Quantification of uptake and remobilization rate constants from simple systems

such as those presented in this study helps in determining relative reaction rates. These rate constants could be integrated into macroscopic multicomponent reactive transport models used for predictions of contaminant transport and fate.

4.5. Conclusions

The effect of phosphate on the rates and mechanisms of U(VI) uptake and remobilization under flowing-conditions was examined. Flow-through reactor modeling results for undersaturated conditions indicate that U(VI) adsorption and desorption in the absence of phosphate were not rate-limited. U(VI) uptake was enhanced in the presence of phosphate. Rapid phosphate uptake occurred predominantly by the formation of a binary surface complex until the goethite surface was saturated. The adsorption of phosphate made uranium adsorption more favorable through the formation of the $(\equiv FeO)_2UO_2PO_4$ surface complex. While the rate of formation (0.014-0.1 min^{-1}) of the phosphate binary surface complex was much higher than its remobilization rate ($2.91*10^{-4}$ min^{-1}), the rates of formation ($1.29*10^{-3}$-$1.82*10^{-2}$ min^{-1}) and remobilization ($1.49*10^{-3}$ min^{-1}) of the $(\equiv FeO)_2UO_2PO_4$ complex were similar. Although it took longer to immobilize uranium as the $(\equiv FeO)_2UO_2PO_4$ complex than to immobilize phosphate as the binary surface complex, the remobilization of the $(\equiv FeO)_2UO_2PO_4$ complex was faster.

For conditions supersaturated with respect to chernikovite, the presence of phosphate enhanced uranium(VI) uptake both in the absence and presence of goethite by precipitation of chernikovite. In the absence of goethite, the critical saturation ratio (Ω = 1.23) for the nucleation of chernikovite and the rate of chernikovite precipitation (4.1-$4.2*10^{-9}$ $mol/m^2.s$) were estimated. Remobilization of U(VI) and phosphate for these

conditions was limited by the dissolution kinetics ($1.4*10^{-9}$ mol/m^2.s) of precipitated chernikovite. The chernikovite dissolution rate was about four orders of magnitude higher than the dissolution rates (~10^{-13} mol/m^2.s) of sodium and calcium meta-autunites at pH 4 that are thermodynamically predicted as the long-term stable forms of uranium. Furthermore, the dissolution of chernikovite was non-stoichiometric, indicating that the remaining chernikovite particles were gradually transforming into a new phase with molar U/P > 1. A significant fraction of the precipitated chernikovite in the absence and presence of goethite was colloidal in nature. Overall, the extent of U(VI) immobilization via precipitation is likely to exceed immobilization via adsorption by the $(\equiv FeO)_2UO_2PO_4$ complex. Moreover, the formation of the ternary surface complex was found to be rapidly reversible when conditions changed to U-free solutions. The dissolution rate constant of chernikovite, on the other hand, was ~3 times slower than its rate constant for formation.

References

1. U.S.DOE *Limited field investigation plan for the 300 area uranium plume, 300-FF-5 operable unit, Hanford Site. Pacific Northwest National Laboratory, Richland, Washington.*; U.S. Department of Energy: 2005.
2. Vermuel, V.; Fruchter, J.; Wellman, D.; Williams, B.; Williams, M., Site Characterizatio Plan: Uranium Stabilization through Polyphosphate Injection–300 Area Uranium Plume Tre Demonstration Project. In PNNL-16008, Pacific Northwest National Laboratory, Richland, Washin: 2006.
3. Wellman, D.; Fruchter, J.; Vermeul, V. *Experimental Plan: Uranium Stabilization Through Polyphosphate Injection 300 Area Uranium Plume Treatability Demonstration Project*; PNNL-16101, Pacific Northwest National Laboratory (PNNL), Richland, WA (US): 2006.
4. Wellman, D.; Fruchter, J.; Vermeul, V.; Williams, M. *Challenges Associated with Apatite Remediation of Uranium in the 300 Area Aquifer*; PNNL-17480, Pacific Northwest National Laboratory (PNNL), Richland, WA (US): 2008.
5. Cheng, T.; Barnett, M. O.; Roden, E. E.; Zhuang, J. L., Effects of phosphate on uranium(VI) adsorption to goethite-coated sand. *Environmental Science & Technology* **2004,** *38*, (22), 6059-6065.
6. Payne, T. E.; Davis, J. A.; Waite, T. D., Uranium adsorption on ferrihydrite - Effects of phosphate and humic acid. *Radiochimica Acta* **1996,** *74*, 239-243.
7. Singh, A.; Ulrich, K.-U.; Giammar, D. E., Impact of phosphate on U(VI) immobilization in the presence of goethite. *Geochimica et Cosmochimica Acta* **2010 (submitted)**.
8. Fetter, C., *Contaminant hydrogeology*. 2nd ed.; Prentice hall Upper Saddle River, NJ: 1999.
9. Schwertmann, U.; Cornell, R. M., *The Iron Oxides: Structure, Properties, Reactions, Occurrences and Uses*. Second ed.; Wiley-VCH: New York, NY, 2003.
10. Ravel, B.; Newville, M., ATHENA, ARTEMIS, HEPHAESTUS: data analysis for X-ray absorption spectroscopy using IFEFFIT. *Journal of Synchrotron Radiation* **2005,** *12*, (4), 537-541.
11. Webb, S., SIXPACK: a graphical user interface for XAS analysis using IFEFFIT. *Physica Scripta* **2005,** *115*, 1011–1014.
12. Newville, M., IFEFFIT: interactive XAFS analysis and FEFF fitting. *Journal of Synchrotron Radiation* **2001,** *8*, (2), 322-324.
13. Ankudinov, A.; Bouldin, C.; Rehr, J.; Sims, J.; Hung, H., Parallel calculation of electron multiple scattering using Lanczos algorithms. *Physical Review B* **2002,** *65*, (10), 104107.
14. Demartin, F.; Gramaccioli, C.; Pilati, T., The importance of accurate crystal structure determination of uranium minerals. II. Soddyite (UO2) 2 (SiO4). 2H2O. *Acta Crystallographica Section C: Crystal Structure Communications* **1992,** *48*, (1), 1-4.
15. Locock, A.; Burns, P., Crystal structures and synthesis of the copper-dominant members of the autunite and meta-autunite groups: torbernite, zeunerite, metatorbernite and metazeunerite. *Canadian Mineralogist* **2003,** *41*, (2), 489.
16. Locock, A.; Burns, P.; Duke, M.; Flynn, T., Monovalent cations in structures of the meta-autunite group. *Canadian Mineralogist* **2004,** *42*, (4), 973.

17. Lasaga, A., *Kinetic theory in the earth sciences*. Princeton Univ Pr: 1998.
18. Rossberg, A.; Ulrich, K.; Weiss, S.; Tsushima, S.; Hiemstra, T.; Scheinost, A., Identification of Uranyl Surface Complexes on Ferrihydrite: Advanced EXAFS Data Analysis and CD-MUSIC Modeling. *Environ. Sci. Technol* **2009,** *43*, (5), 1400-1406.
19. Waite, T.; Davis, J.; Payne, T.; Waychunas, G.; Xu, N., Uranium (VI) adsorption to ferrihydrite: Application of a surface complexation model. *Geochimica et Cosmochimica Acta* **1994,** *58*, (24), 5465-5478.
20. Bargar, J.; Reitmeyer, R.; Davis, J., Spectroscopic Confirmation of Uranium (VI)-Carbonato Adsorption Complexes on Hematite. *Environ. Sci. Technol* **1999,** *33*, (14), 2481-2484.
21. Sherman, D.; Peacock, C.; Hubbard, C., Surface complexation of U (VI) on goethite ([alpha]-FeOOH). *Geochimica et Cosmochimica Acta* **2008,** *72*, (2), 298-310.
22. Van Haverbeke, L.; Vochten, R.; Van Springel, K., Solubility and spectrochemical characteristics of synthetic chernikovite and meta-ankoleite. *Mineralogical Magazine* **1996,** *60*, 759-766.
23. Vochten, R., Transformation of chernikovite and sodium autunite into lehnerite. *American Mineralogist* **1990,** *75*, 221-225.
24. Rey, A.; Gimenez, J.; Casas, I.; Clarens, F.; De Pablo, J., Secondary phase formation on UO2 in phosphate media. *Applied Geochemistry* **2008,** *23*, (8), 2249-2255.
25. Wellman, D. M.; Gunderson, K. M.; Icenhower, J. P.; Forrester, S. W.; Forrester, S. W., Dissolution kinetics of synthetic and natural meta-autunite minerals, $X_{3-n}^{((n)+)}[(UO_2)(PO_4)]_2 \bullet x\ H_2O$, under acidic conditions. *Geochemistry Geophysics Geosystems* **2007,** *8*.
26. Wellman, D. M.; Icenhower, J. P.; Gamerdinger, A. P.; Forrester, S. W., Effects of pH, temperature, and aqueous organic material on the dissolution kinetics of meta-autunite minerals, $(Na,Ca)_{2-1}[(UO_2)(PO_4)]_2 \bullet 3H_2O$. *American Mineralogist* **2006,** *91*, 143-158.
27. Finch, R.; Murakami, T., Systematics and Paragenesis of Uranium Minerals. In *Uranium: mineralogy, geochemistry and the environment*, Burns, P. C.; Finch, R., Eds. Mineralogical Society of America: Washington, DC, 1999; Vol. 38, pp 91-180.

Appendix 4-A: Equilibrium adsorption modeling

Table 4-A1. Summary of Langmuir isotherm parameters for different approaches

Case	Condition	Data	q_m K_L	q_m[b] (µmol/g)	K_L (L/ µmol)	Normalized Mean RSS
1	U adsorption in the absence of phosphate	Measured[a]	3	28	0.11	0.2
2	U adsorption in the presence of phosphate	Measured[a] and SCM[c]-generated (for intermediate range)	65	115	0.56	0.006
3	Phosphate adsorption in absence of U		81.6	103	0.79	0.22

[a] data recorded after 1 d of reaction.
[b] q_m from estimated total surface sites (~66 µM, assuming 2.3 sites/nm^2) is ~112 µmol/g.
[c] surface complexation model (SCM) was used to generate virtual data.

Uranium adsorption in the absence of phosphate

A non-linear least squares optimization of Langmuir and Freundlich models was performed and the best fits are shown along with the adsorbed uranium data after 1 day of reaction (Figure 4-A1).

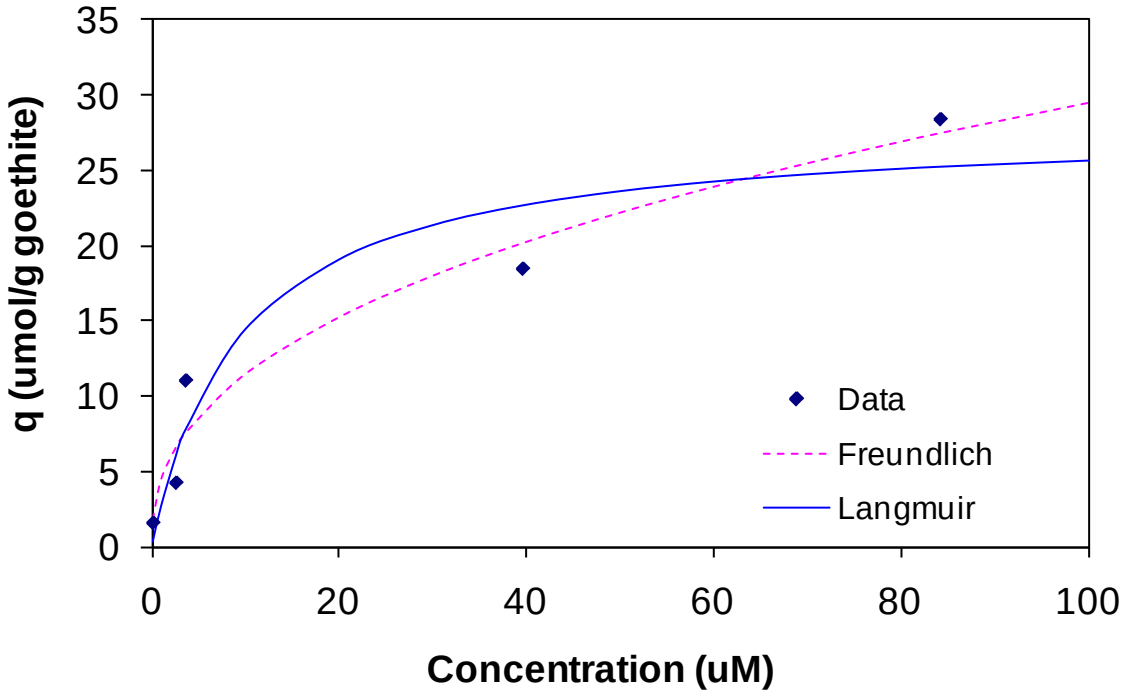

Figure 4-A1. Uranium adsorption on goethite in the absence of phosphate at pH 4

Although the Freundlich model fit had a lower residual squared error (21.5) than the Langmuir model fit (43), the Langmuir model was chosen. The adsorption data indicated an upper limit to the amount of U that could be adsorbed on goethite at pH 4. The optimized parameters for the two models are summarized below in equations 1 and 2,

$$q = K_F C^{1/n} = 4.45C^{0.41} \qquad \text{(A1)}$$

$$q = \frac{q_m K_L C}{1 + K_L C} = \frac{(28.1)(0.11)C}{1 + (0.11)C} = \frac{3C}{1 + 0.11C} \qquad \text{(A2)}$$

where q is the sorption density (µmol U uptake/ g goethite) and C is the concentration of dissolved uranium (µM) at equilibrium.

Presence of 130 µM phosphate Using the surface complexation model [7] total adsorbed and dissolved uranium concentrations for 45 µM TOTU were calculated until

precipitation was predicted. Therefore, calculated values until 40 µM TOTU were used as virtual data points along with the three actual data points recorded after 1 day of reaction (Table 4-A2). All these data points were then used to obtain optimized Langmuir and Freundlich model fits (Figure 4-A2).

The Langmuir model fits the data slightly better than the Freundlich model; both fit much better than the linear model. The Freundlich model fit had a residual squared error of 50 and that of the Langmuir model fit was 12. The corresponding parameters for the two models are summarized below in equations 7 and 6.

$$q = K_F C^{1/n} = 39.1 C^{0.67} \quad \text{(A3)}$$

$$q = \frac{q_m K_L C}{1 + K_L C} = \frac{(115.1)(0.56)C}{1 + (0.56)C} = \frac{65C}{1 + 0.56C} \quad \text{(A4)}$$

Table 4-A2. Actual and virtual data points used for optimizing adsorption model

Concentration (µM)	q (µmol/g goethite)	TOTU (µM)	Source
0.026	1.7	1.01	actual
0.078	5.0	3	SCM
0.11	8.4	5.05	actual
0.162	9.9	6	SCM
0.223	13.2	8	SCM
0.36	16.5	10.1	actual
0.471	24.6	15	SCM
0.691	32.7	20	SCM
0.957	40.8	25	SCM
1.29	48.7	30	SCM
1.7	56.4	35	SCM
2.24	64.0	40	SCM

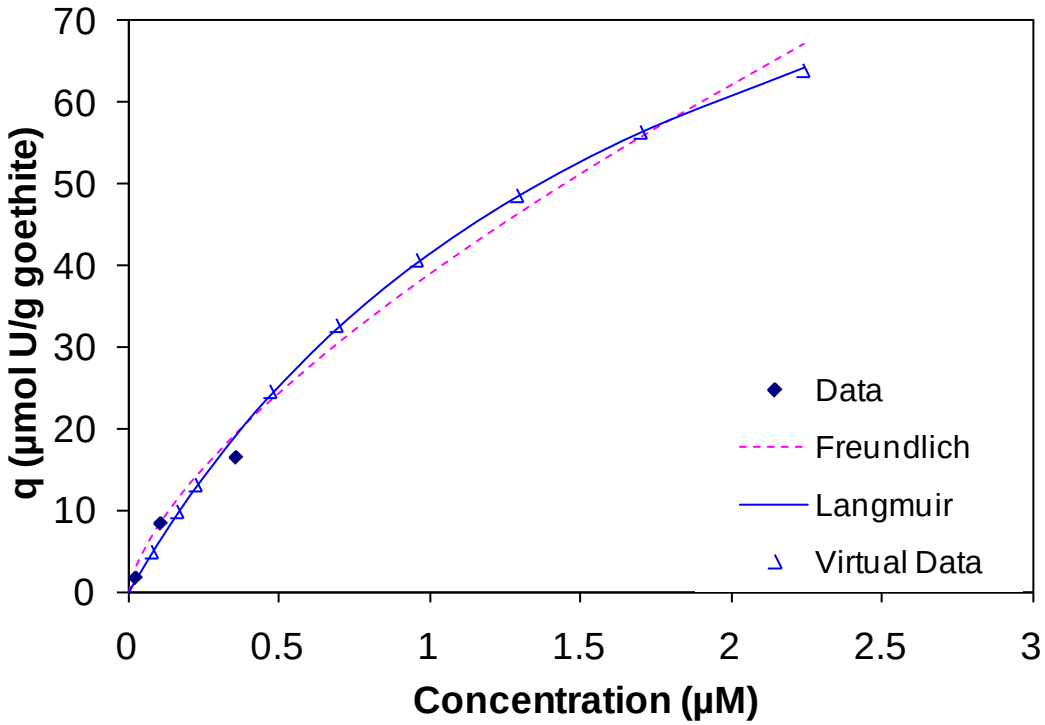

Figure 4-A2. Uranium adsorption on goethite in the presence of phosphate at pH 4

Phosphate adsorption in the absence of uranium

A non-linear least squares optimization of Langmuir and Freundlich models was performed and the best fits are shown along with the adsorbed phosphate actual and virtual data after 1 day of reaction (Figure 4-A3). Since the surface complexation model [7] predicted phosphate adsorption for the two $TOTPO_4$ conditions investigated during the batch study (Chapter 2) very well, the model was used to calculate the total adsorbed and dissolved phosphate concentrations in the absence of uranium for the intermediate $TOTPO_4$ range.

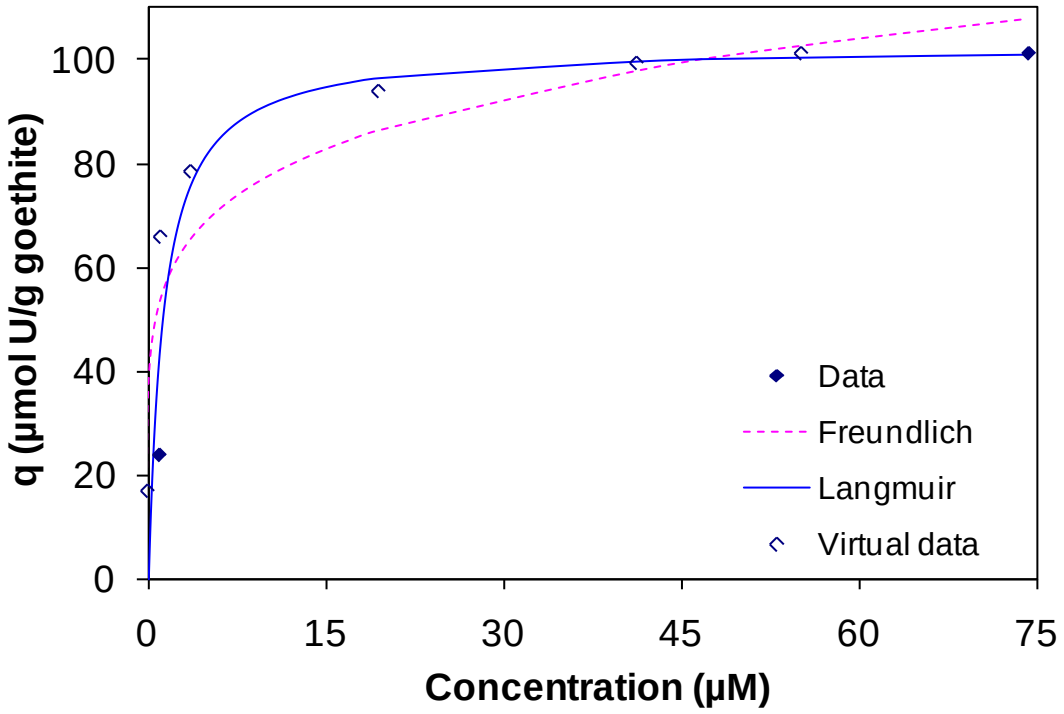

Figure 4-A3. Phosphate adsorption on goethite in the absence of uranium at pH 4

The Langmuir model fit was chosen as it had a lower residual squared error (1045) than the Freundlich model fit (1248). The adsorption data indicated an upper limit to the amount of P that could be adsorbed on goethite at pH 4. The optimized parameters for the two models are summarized below in eqs. A5 and A6.

$$q = K_F C^{1/n} = 52.76C^{0.17} \quad \text{(A5)}$$

$$q = \frac{q_m K_L C}{1 + K_L C} = \frac{(102.8)(0.79)C}{1 + (0.79)C} = \frac{81.6C}{1 + 0.79C} \quad \text{(A6)}$$

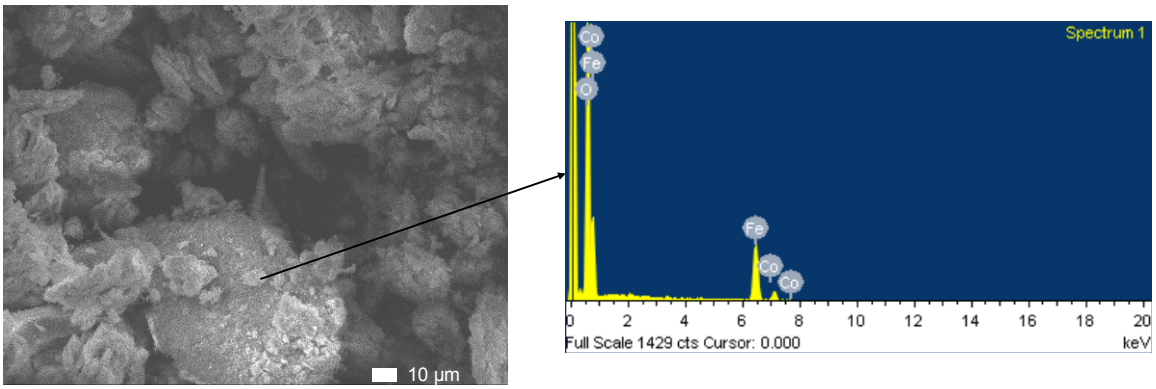

Figure 4-A4 SEM image of goethite agglomerates for undersaturated conditions and the corresponding EDX pattern. Co overlaps with Fe in the EDX pattern; deadtime was ~30%.

Appendix 4-B: Numerical integration of the uptake and remobilization equations

The liquid-phase and solid-phase mass balance equations are a set of coupled ordinary differential equations denoted by the following matrix equation:

$$\frac{d\vec{x}}{dt} = \vec{F}(\vec{\bar{x}}, t) \tag{A7}$$

where $\vec{x}$ is a column matrix containing the dependent variables. The only independent variable is time, t. For U uptake in the absence of phosphate, $\vec{x} = \begin{bmatrix} U \\ U_s \end{bmatrix}$; and matrix

$$\vec{F}(\vec{\bar{x}}, t) = \begin{bmatrix} f_1(U, U_s, t) \\ f_2(U, U_s, t) \end{bmatrix} = \begin{bmatrix} \frac{1}{V}\left[\frac{Q}{2}U_0 - QU - VC_g\gamma_U\left(\frac{3U}{1+0.11U} - U_s\right)\right] \\ \gamma_U\left(\frac{3U}{1+0.11U} - U_s\right) \end{bmatrix} \tag{A8}$$

The initial conditions can also be written in matrix form as in eq A9.

$$\vec{\bar{x}}(0) = \begin{bmatrix} U(t=0) \\ U_s(t=0) \end{bmatrix} = \begin{bmatrix} 0 \\ 0 \end{bmatrix} \tag{A9}$$

Eqs. A8 and A9 were solved using the 4th order Runge-Kutta method that involves the following set of equations for numerical integration.

$$x(n+1) = x(n) + \frac{h}{6}(\vec{k}_1 + 2\vec{k}_2 + 2\vec{k}_3 + \vec{k}_4); \tag{A10}$$

where step size $h = \Delta t = 1$ min

$$\vec{k}_1 = \vec{F}(t_n, x(n)) = \vec{F}(n) \qquad \vec{k}_2 = \vec{F}(t_n + \frac{h}{2}, (x(n) + \frac{h}{2}\vec{k}_1))$$

$$\vec{k}_3 = \vec{F}(t_n + \frac{h}{2}, (x(n) + \frac{h}{2}\vec{k}_2)) \qquad \vec{k}_4 = \vec{F}(t_n + h, (x(n) + hk_3)) \tag{A11a-d}$$

$$\begin{bmatrix} U_{n+1} \\ U_{s,n+1} \end{bmatrix} = \begin{bmatrix} U_n \\ U_{s,n} \end{bmatrix} + \frac{\Delta t}{6}\left\{\vec{k}_1 + \quad 2\vec{k}_2 + \quad 2\vec{k}_3 + \quad \vec{k}_4\right\} \tag{A12}$$

For solving differential equations pertaining to other conditions, matrices $\vec{\bar{x}}$ and $\vec{F}(\vec{\bar{x}}, t)$ were accordingly modified to reflect other dependent variables (P, P_s) and related terms.

Appendix 4-C: Estimation of mass uptake and remobilization from measured effluent CFSTR data

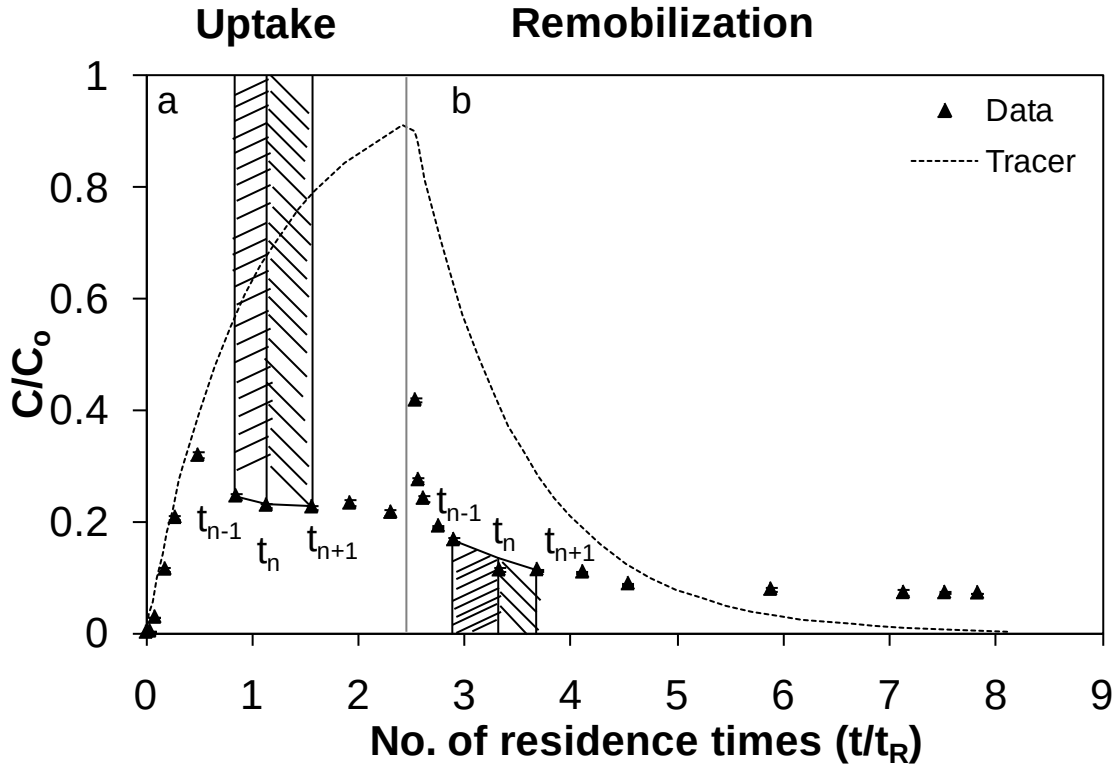

Figure 4-C1. Mass uptake calculations from measured effluent concentrations of a CFSTR during a) uptake and b) remobilization periods. Shaded regions indicate areas for integration by approximating them as successive trapeziums. The data shown is a typical representative data.

For CFSTR uptake period,

$$Rate\ \ mass_{in} - Rate\ mass_{out} - Rate\ mass_{uptake} = Rate\ mass_{accumulated} \tag{1}$$

Elemental LMB:

$$QC_0 - QC - Rate\ mass_{uptake} = V\frac{dC}{dt} \tag{2}$$

$$Rate\ mass_{uptake} = QC_0 - QC - V\frac{dC}{dt} \tag{3}$$

Integrating eq. (3) with respect to time,

$$mass_{uptake} = \int_0^{2.5\ t_R} (QC_0 - QC - V\frac{dC}{dt})dt = Q\int_0^{2.5\ t_R}(C_0 - C)dt - V\int_{C(t=0)}^{C(t=2.5\ t_R)} dC$$

$$= QC_0\frac{t_R}{t_R}\int_0^{2.5\ t_R}(1-\frac{C}{C_0})dt - VC(t = 2.5\ t_R)$$

$$= QC_0 t_R \int_0^{2.5\ t_R}(1-\frac{C}{C_0})d(\frac{t}{t_R}) - VC(t = 2.5\ t_R) \quad (5)$$

$$\approx QC_0 t_R[Sum\ of\ successive\ trapezoidal\ areas\ (Figure\ 4-C1a)] - VC(t = 2.5\ t_R) \quad (6)$$

$$= QC_0 t_R\left[\sum\frac{1}{2}((1-\frac{C}{C_0}\Big|_{t_n}) + (1-\frac{C}{C_0}\Big|_{t_{n+1}}))(\frac{t}{t_R}\Big|_{n+1} - \frac{t}{t_R}\Big|_n)\right] - VC(t = 2.5\ t_R) \quad (7)$$

For CFSTR remobilization period,

$$Rate\ \ mass_{in} - Rate\ mass_{out} + Rate\ mass_{remob} = Rate\ mass_{accumulated} \quad (8)$$

Elemental LMB:

$$0 - QC + Rate\ mass_{remob} = V\frac{dC}{dt} \quad (9)$$

$$mass_{remob} = \int_0^{6\ t_R}(QC + V\frac{dC}{dt})dt = Q\int_0^{6\ t_R} Cdt + V\int_{C(t=0)}^{C(t=6\ t_R)} dC$$

$$= QC_0 t_R\int_0^{6\ t_R}\frac{C}{C_0}d(\frac{t}{t_R}) + V(C(t = 6\ t_R) - C(t = 0)) \quad (10)$$

$$\approx QC_0 t_R[Sum\ of\ trapezoidal\ areas\ (Figure\ 4-C1b)] + V(C(t = 6\ t_R) - C(t = 0)) \quad (11)$$

$$= QC_0 t_R\left[\sum\frac{1}{2}(\frac{C}{C_0}\Big|_{t_n} + \frac{C}{C_0}\Big|_{t_{n+1}})(\frac{t}{t_R}\Big|_{n+1} - \frac{t}{t_R}\Big|_n)\right] + V(C(t = 6\ t_R) - C(t = 0)) \quad (12)$$

Appendix 4-D: Additional data showing colloidal formation of uranium phosphate in the presence of goethite

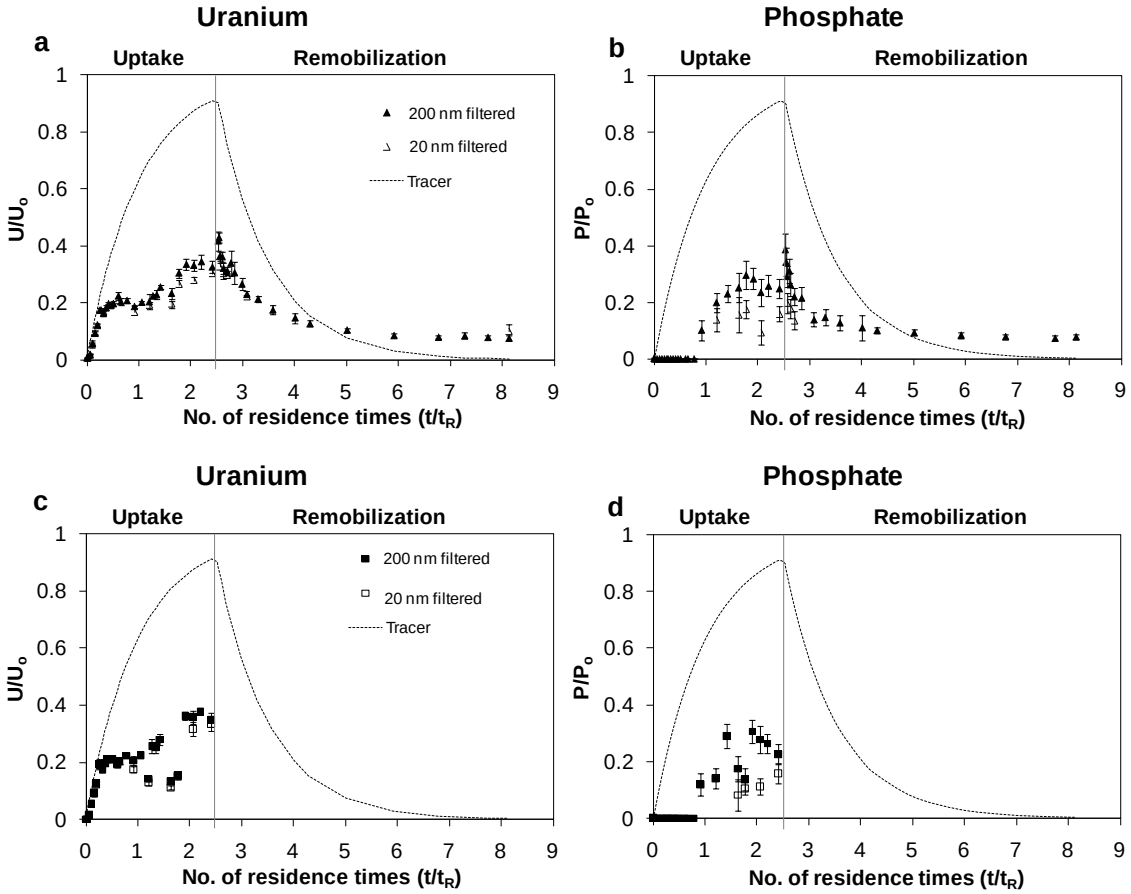

Figure 4-D1. Data for uranium(VI) and phosphate uptake on goethite in the presence of influent phosphate after filtration from 200 nm membrane capping the reactors (closed symbols; data presented in Figure 4.8) and 20 nm post-filtration (open symbols) and subsequent remobilization with 0.01M $NaNO_3$ solution at pH 4. The uptake experiment was run in duplicate in the presence of phosphate (Figures a,b for duplicate 1 and Figures c,d for duplicate 2); one of the duplicates (duplicate 1) was used for recording remobilization. Influent solutions contained 200 µM U_{in} and 200 µM P_{in} at pH 4 and 0.01 M ionic strength. t_R was 210 min. These conditions were supersaturated with respect to chernikovite. Error bars indicate 95% confidence intervals of mean measured concentrations.

Chapter 5 Effect of growth of iron (oxy)(hyr)oxide on the uptake and remobilization of uranium in the absence and presence of phosphate

5.1. Introduction

Uranium phosphates were found to be the dominant solid forms of uranium at several natural and contaminated zones. At the Coles Hill site in south central Virginia (U.S.) natural barium uranyl phosphate deposits were estimated to be stable for the last 150,000 years [1]. Autunite-like uranyl phosphate phases were prevalent in some contaminated soils at the Oak Ridge National Lab [2] and at the Fernald Environmental Management Project (FEMP) in Ohio [3, 4], and metatorbernite [$Cu(UO_2PO_4)_2 \cdot 8H_2O_{(s)}$] was the dominant U solid phase at the Hanford site (Washington, U.S.A.) [5]. The stability of several of these uranium phosphates could possibly be attributed to their co-precipitation with iron oxyhydroxides either as solid solutions or in occluded forms. Stable nanocrystalline uranium phosphates were found to co-exist with iron oxyhydroxides at the Koongarra U ore deposit in Australia [6]. The dynamic conditions favoring transformation of ferrihydrite to goethite and hematite may have incorporated the initially adsorbed uranium into nanocrystals of minerals containing U, P, and Mg or Cu [7, 8]. Moreover, uranium could also be structurally incorporated into iron oxyhydroxide matrices as a uranate species (U^{6+}) [9].

In order to understand the long-term immobilization behavior of uranium it is important to identify conditions that may favor co-precipitation of uranium with iron oxyhydroxides. Information on the rates of uranium uptake and release under these

conditions may be compared with rates of other immobilization mechanisms to design the most effective remediation strategy.

The objective of this study was to investigate how uranium immobilization was affected during uptake of Fe(III). Answers were sought to the following questions: what mechanisms might affect the uptake of the uranium and phosphate complexes? How are these mechanisms related to U(VI) remobilization? Experiments were conducted using CFSTR and column reactor configurations to consider the effects of transport, to mimic environmental conditions and to study the effect of different modes of contact of uranium, phosphate and iron. The experiments tested the hypothesis that phosphate will induce formation of nano-sized U(VI)-phosphate precipitates that are occluded within the growing goethite matrix.

5.2. Materials and methods

5.2.1. Materials

Pure goethite was synthesized and characterized by methods outlined in Chapter 2, and it was maintained as a stock suspension. Details of synthesis and characterization of the goethite-coated sand have been reported previously [10]. Briefly, goethite-coated sand was prepared by mixing the goethite suspension and the acid-washed pre-dried quartz sand (50-70 mesh size) at pH 6.8 for 1 day. The goethite-coated sand was washed repeatedly to remove any loosely-bound goethite from the quartz surface. Goethite-coated sand was used for column experiments to mimic natural subsurface materials; iron oxide grain coatings are products of weathering processes and act as significant sorbents for metals in aquifers [11]. The use of pure goethite in column experiments would cause

iron concentrations to be unrealistically high for subsurface media [12] and create experimental difficulties because of large head loss. Field sediments were not chosen for this study as they would have introduced unwanted complexity to the experiments due to the presence of other minerals that could have obfuscated the effects caused by iron oxyhydroxide.

All chemicals used were certified ACS grade or better. Stock solutions and dilutions were prepared using ultrapure (resistivity > 18.2 MΩ-cm) water. Uranium, iron and phosphate were respectively added as $UO_2(NO_3)_2$, $Fe(NO_3)_3$ and $Na_2HPO_4 \cdot 7H_2O$. Influent and reactor pH before the start of the experiment were adjusted to 4 using trace metal grade HNO_3 and 1 M NaOH. $NaNO_3$ was added to fix the ionic strength at 0.01 M. K^+ (as 0.01M KNO_3 solution at pH 4) was used as a non-reactive tracer for the column experiments.

5.2.2. Column experiments

A packed column reactor design was used to mimic natural subsurface environments. Flow-through experiments were conducted with cylindrical columns of 2.6 cm length (L) and 1 cm diameter (Figure 5.1). Small columns were used in order to minimize changes in the uptake mechanism with reactor length and to minimize transverse dispersion effects. The columns were packed with ~2.76 g of either goethite-coated sand (gcs) or uncoated sand (ucs) with an estimated porosity of 0.37; porosity is the fraction of the volume of voids over the total volume of the column. During the uptake period dissolved Fe(III)-containing influent solutions in the absence or presence of uranium and phosphate were introduced into the column. For a few conditions the uptake period was followed

by a remobilization period when U(VI)-free and Fe(III)-free solutions with or without phosphate were introduced. Table 5.1 lists the experimental conditions investigated.

All experiments were performed at a constant flow rate of 0.05 mL/min (~0.17 cm/min) representative of natural groundwater flow and attainable at lab-scale; pore velocities in the range of 0.02-0.2 cm/min for uranium mine tailings [13] and of 0.001 cm/min for groundwater [14] have been reported. A residence time (t_R) of 15 min was estimated from preliminary tracer studies (Appendix 5-A). All solutions were kept at pH 4 and a fixed ionic strength (0.01M) to be consistent with the batch experiments (Chapter 2) and CFSTR experiments (Chapter 4). Influent Fe(III) concentrations (45 – 120 ppb) were supersaturated with respect to goethite, lepidocrocite and hematite but undersaturated with respect to ferrihydrite.

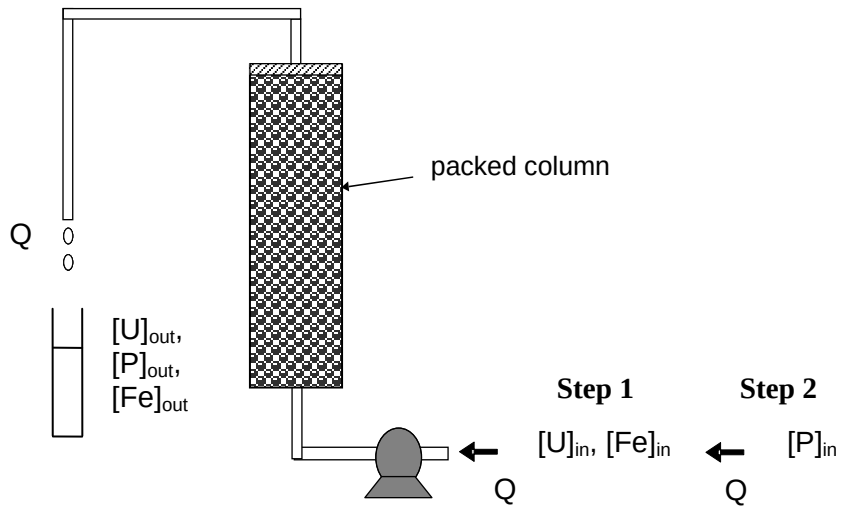

Figure 5.1. Packed column containing uncoated or goethite-coated sand being subjected to step 1) uptake of U(VI) in the absence or presence of dissolved Fe(III) and step 2) remobilization of solid-associated U(VI) with U-free phosphate solution.

Effluent solutions from the reactor were collected at regular time intervals using a fraction collector and analyzed for dissolved Fe, U and P using ICP-MS. When compared with influent concentrations, the effluent concentrations were used to calculate the extent of Fe(III), U(VI) and phosphate uptake and remobilization from the packed columns (Appendix 5-B). The gcs columns used to study the effect of Fe(III) on U(VI)/phosphate uptake were run in duplicates to provide enough material for solid phase characterization of samples at the end of experiments. One of these duplicates was also used for remobilization studies. For each of the conditions an Fe(III)-free control experiment on a gcs column was also run during the uptake and remobilization periods.

Table 5.1. Conditions for packed column experiments at pH 4

S.No.	Solute	Packed material	Uptake period		Remobilization period	
			Influent solution	t/t_R[a]	Influent solution	t/t_R[a]
1	Fe(III)	1 gcs and 1 ucs	0.8 µM Fe(III)	308	None	
2	Phosphate and Fe(III)	3 gcs and 1 ucs	5 µM TOTP with 0.54 µM Fe(III)	288	None	
3	Uranium and Fe(III)	3 gcs and 1 ucs	107 µM TOTU with 1.19 µM Fe(III)	600	None	
4	Uranium and Fe(III)	3 gcs and 1 ucs	11 µM TOTU with 2.1 µM Fe(III)	184	Phosphate and U-free 0.01M $NaNO_3$ solution	467
5	Uranium and Fe(III)	3 gcs and 1 ucs	13 µM TOTU with 2.4 µM Fe(III)	23	U-free 0.01M $NaNO_3$ solution with 100 µM TOTP	97

[a] t/t_R are the total number of residence times the experiment was run

5.2.3. Continuous-flow stirred tank reactor (CFSTR) experiments

The effect of Fe(III) uptake on iron oxides on U(VI) and phosphate uptake was also investigated using the CFSTRs. An experimental set-up identical to the one described in Chapter 4 was used. The only difference for these set of experiments was the presence of 2.5 µM dissolved Fe(III) with the influent uranium stream during the uptake period. To facilitate comparison with results presented in Chapters 2 and 4, the same goethite suspension concentration (0.59 g/L) was chosen for these CFSTR experiments. Table 5.2 lists the specific conditions examined for these CFSTR experiments during the uptake period.

Table 5.2 Experimental conditions for CFSTR dynamic goethite study at pH 4

Conditions[a]	TOTU (µM)	$TOTPO_4$ (µM)	Goethite (g/L)	Reactors	t_R
Undersaturated[a]					
Uptake in the absence of phosphate	1[b]	0	0.59	2	2.5
Remobilization	0	0	0.59	1	6
Uptake in the presence of phosphate	1[b]	100	0.59	2	2.5
Remobilization	0	0	0.59	1	6

[a] with respect to chernikovite ($UO_2HPO_4 \cdot 4H_2O_{(s)}$)
[b] all U-containing influent solutions during the uptake period also contained 2.5 µM Fe(III)

5.2.4. Analysis

Dissolved U, P, and Fe concentrations were measured using ICP-MS (Agilent 7500ce) with respective method detection limits of 0.005 ppb, 0.8 ppb, and 1 ppb. Solution pH was measured using a glass electrode and a pH meter (Accumet Research). Images of residual solids from packed columns and from CFSTR centrifuged pastes were collected by SEM (JEOL 7001LVF). Some of these solids were also analyzed by XRD (Rigaku

Geigerflex D-MAX/A) using Cu-K_α radiation. For the centrifuged pastes from CFSTR experiments, U L_{III}-edge XAFS spectra were collected along with wet pastes from conditions discussed in Chapter 4, and analyzed similarly.

5.3. Results and discussion

Data from the column experiments at pH 4 were used to study the effect of simultaneous uptake of Fe(III) on U(VI)/phosphate uptake. First, evidence for Fe(III) uptake on goethite-coated sand in the absence of any co-solute is presented. Next, the effect of such an Fe(III) uptake on its co-solute (phosphate and U(VI)) is discussed. Finally, the effect of phosphate-containing solution on U(VI) remobilization is presented. Effluent concentrations (C) are normalized with respect to the influent concentration (C_0) and are plotted against normalized time (t/t_R).

5.3.1. Iron uptake on goethite-coated sand

The presence of goethite on sand enhanced the uptake of dissolved Fe(III). For a fixed influent Fe(III) concentration of 45 ± 4 ppb (0.8 µM**)**, dissolved Fe(III) concentrations in the effluent showed a gradual breakthrough for the ucs (Figure 5.2); those for the gcs attained a steady value of ~15 ppb after ~1 day of reaction time (100 t_R). For the ucs an uptake of 0.03 µmolFe/g sand was recorded, while uptake for the goethite-coated sand was 0.053 µmolFe/g sand. Fe(III) uptake on the ucs could be indicative of adsorption made favorable by the electrostatic attraction of the dominant $Fe(OH)_2^+$ species to the negatively charged silica surface (pH_{pZc} ~2 [15]) at pH 4. On the gcs, this adsorptive Fe(III) uptake could be occurring initially due to the significant amount of exposed quartz

surface (goethite coating was 0.1% by wt.). Thereafter, the continuous uptake of Fe(III) indicates either of the three mechanisms: a) adsorption of Fe(III) to goethite, by providing new sites for adsorption as the existing ones were consumed; b) growth of goethite as Fe(III) precipitates on the surface; c) heterogeneous nucleation of an iron oxyhydroxide phase leading to the formation of new particles on the goethite surface. Mechanisms b and c appear more likely since conditions were supersaturated with respect to lepidocrocite, goethite and hematite.

The speciation of Fe(III) taken up by the solid, however, could not be determined. SEM images of the sand particles at the end of the experiment did not provide a direct evidence for the precipitation of an iron oxyhydroxide phase due to the relatively small surface coverage of goethite on sand and the imaging limitations. Advanced studies combining different isotopes of Fe (56 and 57) and Mössbauer spectroscopy could be helpful in identifying the mechanisms of Fe(III) uptake.

5.3.2. Phosphate uptake in the absence and presence of co-influent iron(III)

In the absence of any influent Fe(III), significant phosphate uptake (0.20 µmolP/g) on the gcs occurred from an influent containing 5 µM TOTP (Figure 5.3a). This result agrees well with the favorable adsorption of phosphate to iron oxides at low pH reported under batch conditions [12, 16-18]. On a molar basis, the phosphate uptake was much higher than Fe(III) uptake (0.053 µmolFe/g) on the gcs for a similar uptake period (Figure 5.2).

The uptake of phosphate on the gcs was enhanced (0.22 µmolP/g) when 0.54 µM Fe(III) was present as a co-influent with phosphate (Figure 5.3a). The phosphate breakthrough for both replicate gcs columns occurred (~120 t_R) later than when the

influent contained no Fe(III) (~80 t_R). The breakthrough curves in the presence of Fe(III) were steeper than in the absence of Fe(III), which suggests that the rate of adsorption of phosphate onto the gcs was also faster than in the absence of influent Fe(III).

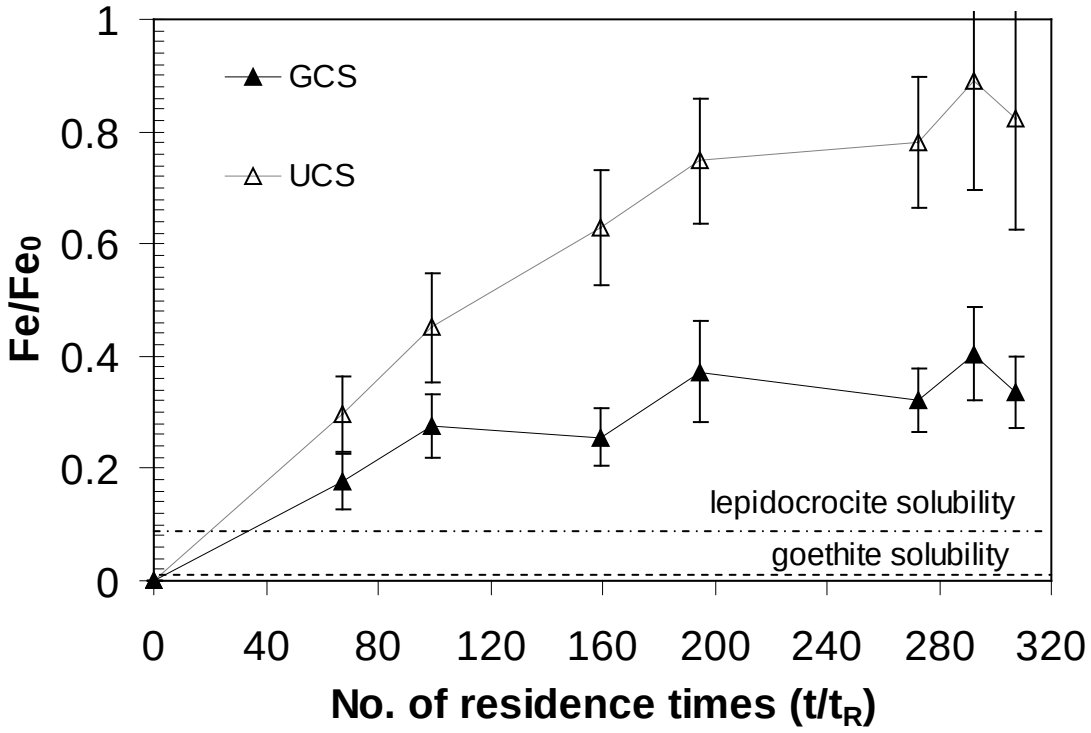

Figure 5.2. Uptake of dissolved Fe(III) on uncoated (ucs) and goethite-coated sand (gcs) columns from a 0.8 µM Fe(III)-containing influent solution at pH 4. Influent Fe concentrations (Fe_0) were supersaturated with respect to goethite but undersaturated with respect to ferrihydrite. Analytical uncertainty is shown with error bars representing 95% confidence intervals of the mean measured concentrations.

While Fe(III) in the influent enhanced phosphate uptake on the gcs, the presence of phosphate lowered Fe(III) uptake from 0.053 µmolFe/g to 0.019 µmolFe/g. This effect was also evident from the similar iron breakthrough curves for the gcs and the ucs, unlike in the absence of phosphate (Figure 5.2). Interestingly, with gcs the increase in molar uptake of phosphate (0.02 µmol/g) in the presence of Fe(III) was equal to the Fe(III) uptake. The increase in phosphate uptake caused by Fe(III) in the influent could

be due to the fresh growth of iron oxyhydroxide, which could provide more sites for phosphate adsorption. Phosphate adsorption was reported to be higher to a poorly crystallized goethite than to a well-crystallized goethite [19]. Alternatively, this concurrent 1:1 uptake of iron and phosphate could be indicative of surface precipitation of an Fe(III)-phosphate on goethite [20].

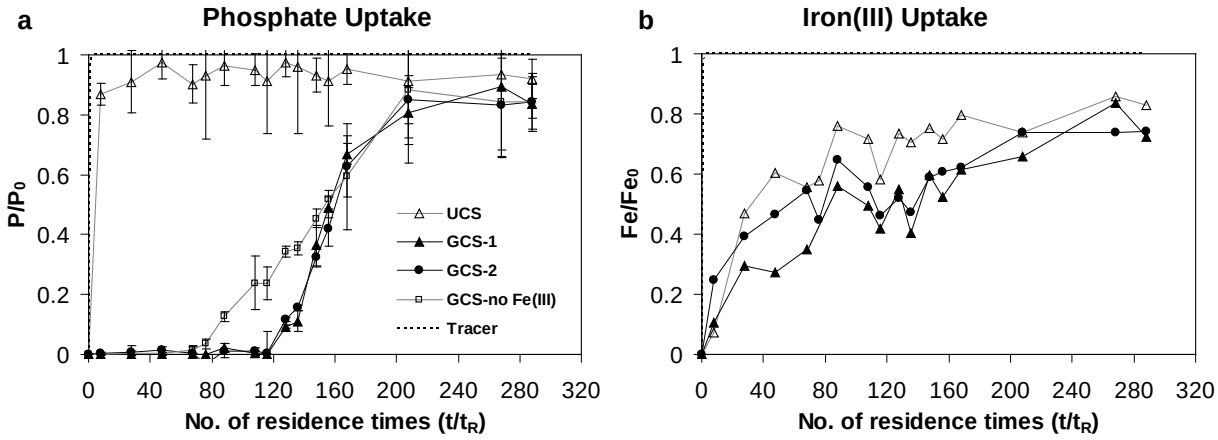

Figure 5.3. Uptake of a) phosphate and b) Fe(III) on ucs (open triangles) and gcs columns (closed symbols) from an influent solution containing 0.54 µM Fe(III) and 5 µM of TOTP at pH 4. Phosphate uptake on gcs in the absence of dissolved Fe(III) is also shown. Influent Fe concentrations (Fe_0) were supersaturated with respect to goethite but undersaturated with respect to ferrihydrite. Influent phosphate (P_0) and Fe_0 were undersaturated with respect to strengite ($FePO_4 \cdot 2H_2O$). Analytical uncertainty is shown for measured concentrations of phosphate with error bars representing 95% confidence intervals of the means.

5.3.3. Uranium uptake in the absence and presence of co-influent iron(III)

5.3.3.1. Results from packed columns

Measured effluent U concentrations from the ucs and the gcs columns indicated uptake of U(VI) both in the absence and in the presence of Fe(III) when compared to a conservative tracer (Figure 4a). The elution of uranium and iron is discussed later in section 5.3.4.1. In the absence of Fe(III), an uptake of 0.010 µmolU/g gcs from an influent solution

containing 11 µM TOTU at pH 4 and 0.01 M ionic strength was recorded. U(VI) uptake, however, decreased slightly to 0.009 µmolU/g gcs in the presence of 2.1 µM Fe(III) resulting in faster U breakthrough (Figure 5.4a). The effluent U concentrations from both the replicate reactors (closed symbols) were in good agreement.

When compared to the ucs (0.006 µmolU/g), U(VI) uptake on the gcs in the presence of Fe(III) was higher (0.009 µmolU/g) due to higher adsorptive affinity of goethite for uranium at pH 4. This U(VI) uptake, however, was about an order of magnitude lower than the corresponding Fe(III) uptake (0.042 – 0.095 µmolFe/g sand, Figure 5.4c). The uptake of iron was unaffected by the presence of U(VI) as effluent iron concentrations from gcs columns were similar to those in the absence of U (Figure 5.2). These results indicate that whereas co-influent Fe(III) enhanced phosphate uptake on the gcs as discussed earlier, its effect on uranium was the opposite. This effect is suggestive of U(VI) and Fe(III) competitive adsorption. U(VI) uptake decreased in the presence of influent Fe(III) probably because the $Fe(OH)_2^+$ species outcompeted the UO_2^{2+} species for adsorption sites on goethite. The Fe(III) uptake did not seem to create new adsorption sites for U(VI) like it did for phosphate.

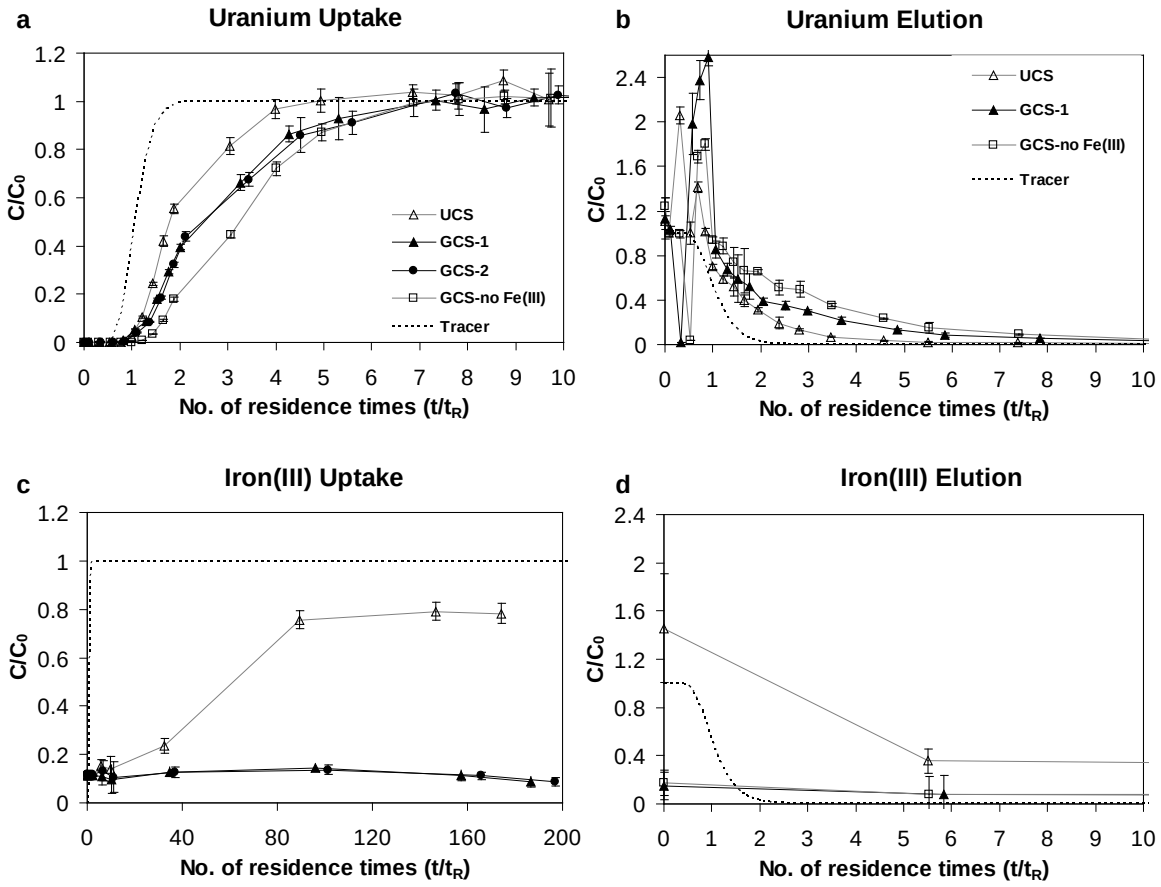

Figure 5.4. Uptake of a) U(VI) and c) dissolved Fe(III) on ucs (open triangles) and gcs columns (closed symbols) from an influent solution containing 2.1 µM Fe(III) and 11 µM of TOTU at pH 4. Uptake on gcs in the absence of dissolved Fe(III) is also shown (open squares). Remobilization curves of b) U(VI) and d) Fe(III) with U-free and phosphate-free solution at pH 4 are shown alongside. Influent Fe concentrations (Fe_0) were supersaturated with respect to goethite but undersaturated with respect to ferrihydrite. Analytical uncertainty is shown for measured concentrations of phosphate with error bars representing 95% confidence intervals of the means.

5.3.3.2. Results from CFSTRs

The decrease in U(VI) uptake during simultaneous Fe(III) uptake on goethite in packed columns was also observed in the CFSTR experiments (Figure 5.5). For a 0.01 M $NaNO_3$ influent solution at pH4 containing 1 µM TOTU, U(VI) uptake decreased slightly from 0.33-1.4 µmol/g in the absence of influent Fe(III) to ≤ 0.40 µmol/g when Fe(III) was present as a co-influent (Table 5.3).

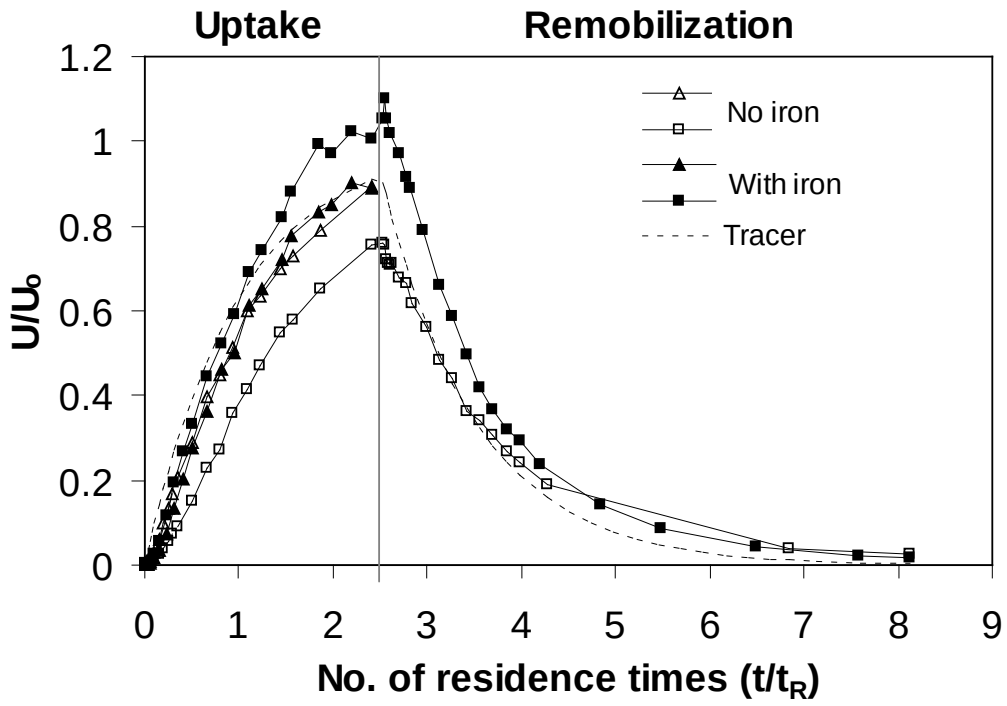

Figure 5.5. U(VI) uptake on goethite in the presence (closed symbols) and absence (open symbols) of influent ~1.25 µM Fe(III) and subsequent remobilization with 0.01 M $NaNO_3$ solution at pH 4. The 1 µM TOTU-containing influent solution and the 0.59 g/L goethite suspension were maintained at pH 4 and 0.01 M $NaNO_3$ ionic strength. Uptake periods were run in duplicate for both conditions, and the remobilization period was only run on one duplicate. The dashed line indicates predicted concentrations for a conservative tracer.

5.3.4. Uranium remobilization with 0.01 M $NaNO_3$ solution at pH 4

The solid-associated uranium resulting from the uptake period was subjected to remobilization with a 0.01 M $NaNO_3$ solution that did not contain uranium, iron or phosphate. The influent pH was maintained at 4. The remobilization experiment was performed with one of the duplicate gcs columns and the CFSTRs following the uptake period.

5.3.4.1. Results from packed columns

Apart from the initial transience in effluent concentrations, U(VI) elution curves were

typical of a desorbing species (Figure 5.4b). The adsorbed uranium was completely remobilized for the three columns. However, times for complete elution were different and were correlated with the quantity of uranium loaded on each of the columns (Table 5.3). Remobilization was the earliest (~10 t_R) for the ucs for which U(VI) uptake was the least. U(VI) elution from the gcs was earlier (~28 t_R) for the column that had seen the influent Fe(III) during the uptake period than the column with no influent Fe(III) (~34 t_R). Furthermore, when U(VI) elution times were compared with the times to attain saturation ($C/C_0 > 0.99$) during the uptake period, U(VI) adsorption was found to be a qualitatively faster process than desorption.

The transient behavior within the first t_R was indicated by an initial decrease and subsequent increase in effluent concentrations to values even higher than the original influent. The initial decrease could be due to the continued adsorption of uranium between the end of the uptake period and the start of the remobilization period. Thereafter upon contact with the U-free remobilizing solution this adsorbed uranium may have desorbed rapidly resulting in the increased effluent concentrations.

While remobilization of uranium was complete for the ucs and the gcs columns, iron elution was complete only for the ucs (Figure 5.4d). For the gcs, only ~23% of the total iron taken up was remobilized after ~466 t_R. These results indicate that most of the iron taken up during the uptake period was probably incorporated in the structure of goethite as it grew or existed as a surface precipitate on goethite, and uranium was taken up as an adsorbed species.

5.3.4.2. Results from CFSTRs

Elution of U(VI) adsorbed on goethite in the presence and absence of influent Fe(III) were typical of a desorbing species (Figure 5.5). U(VI) immobilized during Fe(III) uptake on goethite was completely remobilized by the 0.01 M $NaNO_3$ solution at pH 4 after ~6 t_R. However, only ~51% of the adsorbed uranium in the absence of Fe(III) was remobilized suggesting that the presence of Fe(III) probably promoted a less stable uranium association with goethite.

Table 5.3 Elemental uptake and remobilization results from column effluent data for different conditions

S.No.	Condition	Packed material	Uptake period							Remobilization period						
			Influent solution[a]	Run t/t_R[b]	Fe(III) uptake (µmol/g)	$t/t_{R,s}$[c]	U(VI) uptake (µmol/g)	$t/t_{R,s}$[c]	Phosphate uptake (µmol/g)	Influent solution[a]	Run t/t_R[b]	Fe(III) elution (µmol/g)	$t/t_{R,w}$[d]	U(VI) elution (µmol/g)	$t/t_{R,w}$[d]	Phosphate elution (µmol/g)
1	Fe(III) uptake	gcs	0.8 µM Fe(III)	308	0.053					None						
		ucs	0.8 µM Fe(III)	308	0.030					None						
2	Phosphate uptake	gcs-1	5 µM TOTP with 0.54 µM Fe(III)	288	0.020			208	0.22	None						
		gcs-2	5 µM TOTP with 0.54 µM Fe(III)	288	0.018			208	0.22	None						
		ucs	5 µM TOTP with 0.54 µM Fe(III)	288	0.014			48	0.011	None						
		gcs	5 µM TOTP with no Fe(III)	288				208	0.20	None						
3	Uranium uptake	gcs-1	11 µM TOTU with 2.1 µM Fe(III)	184	0.092	7.3	0.0085			Phosphate-free and U-free 0.01M $NaNO_3$ solution	466	0.021	27.5	0.011		
		gcs-2	11 µM TOTU with 2.1 µM Fe(III)	184	0.097	7.7	0.0088									
		ucs	11 µM TOTU with 2.1 µM Fe(III)	184	0.042	4.9	0.0064				466	0.045	10.2	0.0065	$t/t_{R,s}$[c]	Phosphate uptake
		gcs	11 µM TOTU with no Fe(III)	184		7.8	0.010				466	0.020	33.5	0.012		
Effect of phosphate on uranium uptake and remobilization																
4	Uranium uptake and remobilization with phosphate	gcs-1	13 µM TOTU with 2.4 µM Fe(III)	23	no data	~8	0.010			U-free 0.01M $NaNO_3$ solution with 100 µM TOTP	97	no data	10	0.0088	25	0.291
		gcs-2	13 µM TOTU with 2.4 µM Fe(III)	23	no data	~8.5	0.011				97	no data	11	0.010	30	0.320
		ucs	13 µM TOTU with 2.4 µM Fe(III)	23	no data	6.2	0.0071	$t/t_{R,w}$[d]	Phosphate elution		97	no data	19.7	0.0074	2.42	0.016
		gcs	19 µM TOTU with no Fe(III)	23		~7	0.013				97		8.7	0.010	20.0	0.255
5	Uranium uptake on pre-adsorbed phosphate	gcs-1	104 µM TOTU with 1.2 µM Fe(III)	600	0.19	16.2	0.17		0.041	None						
		gcs-2	104 µM TOTU with 1.2 µM Fe(III)	600	0.19	16.2	0.18		0.046	None						
		ucs	104 µM TOTU with 1.2 µM Fe(III)	600	0.036	4.3	0.10		0.028	None						
		gcs	110 µM TOTU with 0.49 µM Fe(III)	600	0.067	13.6	0.15		0.048	None						

[a] all influent solutions at 0.01 M ionic strength and pH 4; [b] t/t_R are the total number of residence times the experiment was run; [c] $t/t_{R,s}$ are the number of residence times needed to first reach $C/C_0 > 0.99$;
[d] $t/t_{R,s}$ are the number of residence times needed to first reach $C/C_0 < 0.01$

5.3.5. Effect of phosphate on uranium uptake and remobilization in the presence of dissolved Fe(III)

For the binary solute experiments just discussed, presence of influent Fe(III) increased phosphate uptake and decreased U(VI) uptake. Results of experiments on the effect of phosphate on U(VI) and Fe(III) interactions with the gcs are presented here. These results are compared with phosphate-enhanced uranium uptake on goethite in the absence of dissolved Fe(III) under batch (Chapter 2) and flow conditions (Chapter 4).

5.3.5.1. Uranium remobilization with pH 4 solution containing 100 µM phosphate and 0.01M $NaNO_3$

To investigate uranium remobilization when phosphate is in the solution, ucs and gcs-packed columns were loaded with uranium following the procedure used in the uptake study presented in section 5.3.3.1 and by using similar influent U(VI) (13 µM) and Fe(III) (2.4 µM) concentrations. This sequence of contacting uranium and phosphate is associated with phosphate-based immobilization strategies; phosphate is added to a pre-existing contaminated zone of U(VI). Trends in effluent uranium concentrations and calculated U(VI) uptake in the presence of Fe(III) during the uptake period were similar to those in previous experiments for both the ucs and the gcs columns (Figure 5.6a and Table 5.3). U(VI) uptake in the absence of Fe(III), however, was significantly higher (0.013 µmolU/g) than in the previous set of experiments (0.010 µmolU/g) because the influent U(VI) concentration was ~1.5 times higher (19 µM). Although the same influent stock was used in the two experiments, the U(VI) concentrations were higher probably because the solution had become more concentrated due to evaporative losses.

After loading the packed columns with uranium, the influent was immediately

switched to a U-free solution containing 100 μM TOTP at the same pH and ionic strength. Unlike in the previous experiments (section 5.3.4.1) the effluent U concentrations had no transient behavior (Figure 5.6b) because there was no time gap between the end of the uptake period and the start of the remobilization period. While U(VI) elution from the ucs was complete as recorded previously, not all of the goethite-associated uranium was remobilized (Table 5.3). Of the total uranium immobilized in the presence of Fe(III), ~90-92% was remobilized by the phosphate-containing influent after ~97 t_R. In comparison, only ~79% of the total uranium immobilized in the absence of Fe(III) was remobilized by the influent.

Another important distinction for U(VI) elution from the gcs with phosphate was the appearance of a secondary peak (~5.5-8.5 t_R) after an initial washout period that was not observed for phosphate-free remobilization (Figure 5.6b). This secondary peak was present for the gcs columns irrespective of whether they were exposed to influent Fe(III) or not during the uptake period. The secondary elution peak from the gcs columns probably indicated the formation of a phosphate-facilitated adsorbed uranium species that was more stable than the adsorbed uranium species formed in the absence of phosphate. Interestingly, phosphate began to breakthrough around the time that the secondary peaks had completely eluted, which suggests that the influent solution was probably causing desorption of these stronger immobilized uranium species (Figure 5.6c). For the ucs, however, no such secondary peak was observed. Instead, the effluent U(VI) concentrations showed a broad-tailed feature from about ~2-5 t_R which coincided with corresponding effluent phosphate concentrations significantly higher than the influent phosphate concentrations (Figure 5.6c). The broad-tailed feature could be the elution of

uranium phosphate particles that may have formed when the desorbing U(VI) reacted with the influent phosphate.

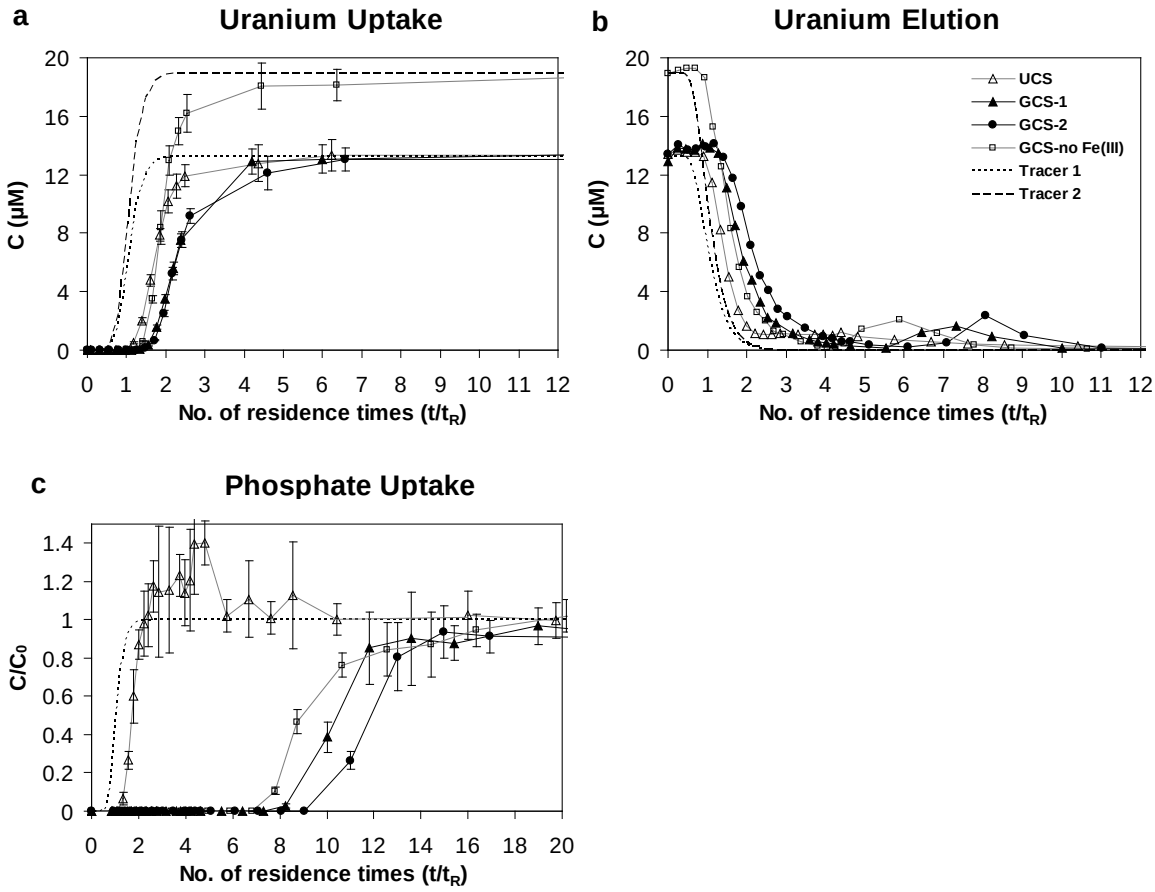

Figure 5.6. Uptake of a) U(VI) and c) dissolved Fe(III) on ucs (open triangles) and gcs columns (closed symbols) from an influent solution containing 2 µM Fe(III) and 11 or 19 µM of TOTU at pH 4. Uptake on gcs in the absence of dissolved Fe(III) is also shown (open squares). Remobilization curves of b) U(VI) and d) Fe(III) with U-free and phosphate-free solution at pH 4 are shown alongside. Influent Fe concentrations (Fe_0) were supersaturated with respect to goethite but undersaturated with respect to ferrihydrite. Analytical uncertainty is shown for measured concentrations of phosphate with error bars representing 95% confidence intervals of the means.

These results indicate that phosphate promotes the formation of uranium surface species that are strongly associated with goethite. The presence of Fe(III) during the uptake of uranium not only decreased U(VI) uptake on goethite but also limited the formation of the stable phosphate-induced uranium surface species. Considering the

strong association of Fe(III) with phosphate on the goethite surface (5.3.2) it is possible that Fe(III) is outcompeting U(VI) for phosphate.

5.3.5.2. Effect of pre-adsorbed phosphate on uranium uptake

U(VI) uptake was investigated in the presence and absence of influent Fe(III) on the phosphate-loaded gcs and ucs columns that resulted from the phosphate uptake experiments (section 5.3.2). For influent solutions containing 104-110 µM TOTU at pH 4 and 0.01 M ionic strength, the uptake on the gcs (0.15-0.18 µmolU/g) was significantly higher than on the ucs (0.10 µmolU/g), and breakthrough occurred for the gcs after ~10 t_R for both levels of influent Fe(III) (1.2 µM and 0.49 µM) (Figure 5.7a).

The presence of pre-adsorbed phosphate seems to have retarded U(VI) breakthrough. When compared to phosphate-free conditions (Figure 5.6a) it took about twice as much time to achieve breakthrough, even though an order of magnitude higher influent TOTU was used. This retarded breakthrough is indicative of phosphate-enhanced U(VI) uptake.

Phosphate elution from the ucs column was complete (Table 5.3). Interestingly, the effluent phosphate concentrations indicated a broad-tailed feature between 4-13 t_R (Figure 5.7b) similar to the effluent uranium concentrations that were remobilized with phosphate (Figure 5.6b). Appearance of this feature indicates that the same interaction might be responsible for the slow elution of a uranium-phosphate species from the ucs whether uranium interacted with pre-adsorbed phosphate or remobilizing phosphate. Elution of phosphate from the gcs columns, on the other hand, was slightly slower than the ucs and was incomplete. Only 19-24 % of the total phosphate taken up (Figure 5.3a)

was remobilized after 600 t_R of phosphate-free influent solution. Slow and incomplete desorption of phosphate from goethite has been reported previously [19, 21, 22].

Influent Fe(III) concentrations indirectly impacted U(VI) uptake by affecting the quantity of phosphate retained on the columns. Effluent iron concentrations from the gcs columns initially increased and then reached a steady state much lower than the influent concentrations, suggesting the continuous uptake of Fe(III) witnessed previously (Figure 5.7c). The effluent Fe(III) concentrations were similar for the two levels of influent Fe(III), which indicated more uptake for the higher influent Fe(III) (Table 5.3). The enhanced uptake of Fe(III) for the higher influent Fe(III) coincided with less elution of phosphate (0.041-0.046 µmol/g) than for the lower influent Fe(III) (0.048 µmol/g). Columns that had the higher concentration of adsorbed phosphate resulted in higher U(VI) uptake, and the presence of higher Fe(III) impacted U(VI) uptake indirectly by causing a higher uptake and retention of phosphate.

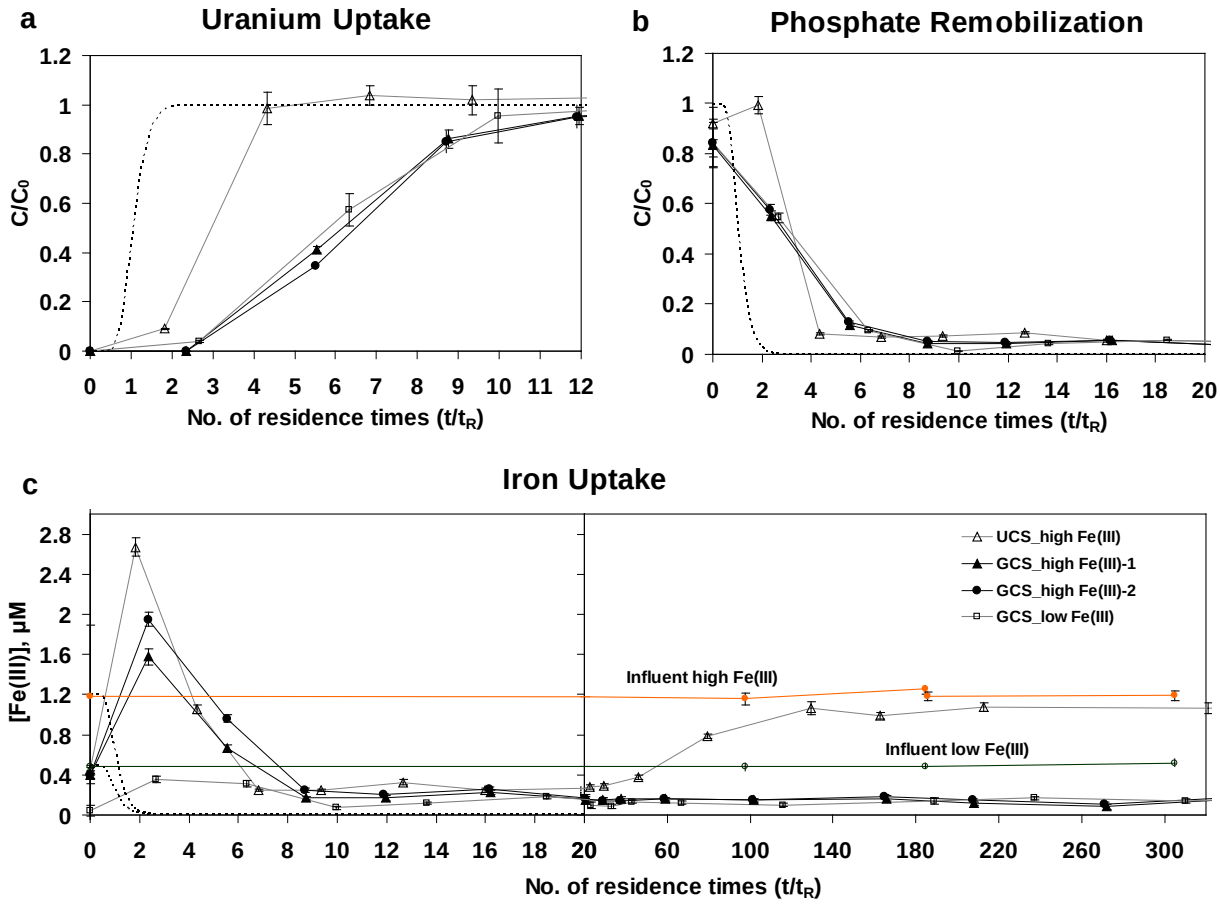

Figure 5.7. Uptake of a) U(VI) and c) dissolved Fe(III) and corresponding remobilization of b) phosphate on ucs (open triangles) and gcs columns (closed symbols) from influent solutions containing ~100 µM of TOTU and 0.49-1.2 µM Fe(III) at pH 4 and 0.01M $NaNO_3$. Columns were preloaded with phosphate. Uptake on gcs for the low (0.49 µM**)** influent Fe(III) is also shown (open squares). Influent Fe(III) were supersaturated with respect to goethite but undersaturated with respect to ferrihydrite. Analytical uncertainty is shown with error bars representing 95% confidence intervals of the means.

5.3.5.2. Simultaneous contacting of phosphate with uranium

Due to the small size of the packed columns, it was not possible to simultaneously contact uranium and phosphate in the presence of goethite. CFSTRs were used to overcome this limitation. Uranium and phosphate interactions in the presence of ~1.25 µM influent Fe(III) were compared with the results obtained in the absence of phosphate (Chapter 4) for the same influent TOTU (1 µM) and TOTP (100 µM) concentrations and by following an identical experimental design.

Phosphate significantly enhanced U(VI) uptake even in the presence of Fe(III) (Figures 5.5a and 5.8a). The presence of Fe(III), however, decreased U(VI) uptake slightly from 4.33-4.59 µmol/g to 3.74-4.19 µmol/g, a result similar to the results from column studies presented earlier. The corresponding phosphate effluent concentrations showed similar uptake (60-104 µmol/g) in the presence of influent Fe(III) than for the Fe(III)-free conditions (64-78 µmol/g).

Remobilization of the goethite-associated uranium (Figure 5.8a) and phosphate (Figure 5.8b) resulted in similar elution profiles in the absence and presence of Fe(III). However, the relative quantities of remobilized uranium and phosphate were higher in the presence of Fe(III). While almost all phosphate and ~76% of total U(VI) immobilized in the presence of Fe(III) were remobilized after ~6 t_R, only ~52% of total phosphate and ~69% of the total U(VI) taken up in the absence of Fe(III) were eluted out during the same period. These results indicate that the presence of Fe(III) not only diminishes phosphate-induced U(VI) uptake on goethite but also promotes the formation of a relatively less stable surface species of U(VI) and phosphate. Interestingly, this U(VI) and phosphate interaction even enhances phosphate elution, a result in contrast with the

slow phosphate desorption recorded for the column studies.

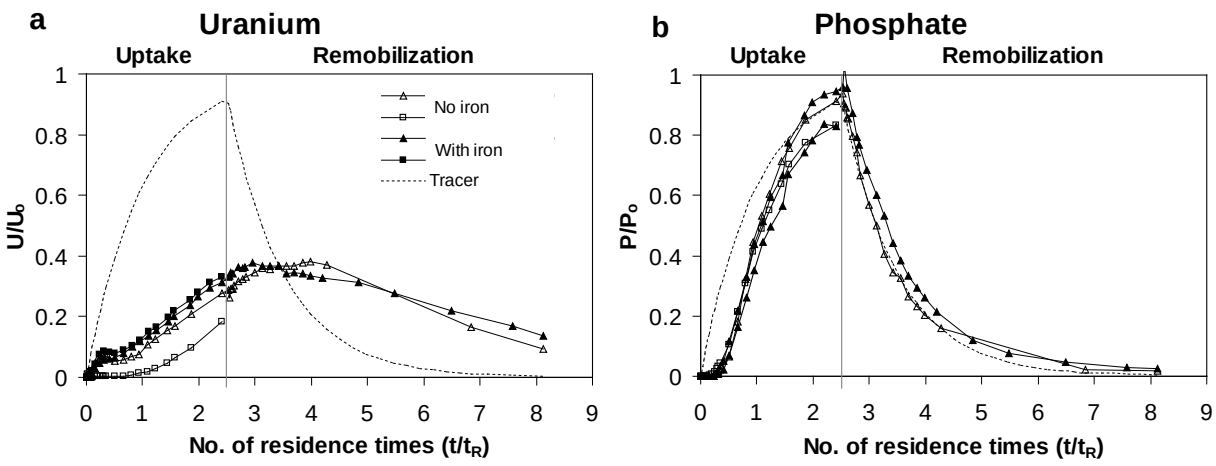

Figure 5.8. Uptake of a) uranium(VI) and b) phosphate on goethite in the presence (closed symbols) and absence (open symbols) of influent ~1.25 µM Fe(III) and subsequent remobilization with 0.01 M $NaNO_3$ solution at pH 4. An influent solution containing 1 µM TOTU was simultaneously contacted with a 100 µM TOTP-containing influent solution in the CFSTR containing 0.59 g/L goethite suspension at the same ionic strength and pH 4. Uptake periods were run in duplicates for both conditions, and the remobilization period was only run on one duplicate. The dashed line indicates predicted concentrations for a conservative tracer.

5.4. Implications for uranium remediation

Dynamic conditions promoting the growth of iron oxides may have significant impact on the U(VI)-phosphate interactions as witnessed in this study. The presence of Fe(III) during uranium and phosphate uptake on goethite had contrasting effects on U(VI) and phosphate uptake. While phosphate uptake was significantly enhanced that of U(VI) was slightly decreased. Furthermore, it was easier to remobilize U(VI) that had been taken up as a co-solute with Fe(III).

The interactions of Fe(III)-phosphate-U(VI) were impacted by the mode of contact between U(VI) and phosphate; whether phosphate was pre-adsorbed, was used as

a remobilizing solution or was contacted simultaneously with U(VI. These considerations could be important while formulating a remediation strategy for sub-surface uranium. In most cases phosphate would be added to soils and sediments already loaded with uranium.

5.5. Conclusions

The effects of simultaneous Fe(III) uptake on iron (oxy)(hydr)oxides on U(VI) and phosphate uptake and remobilization were investigated at pH 4. Goethite-coated sand packed columns and goethite-containing CFSTRs were used to simulate environmental conditions favoring the growth of iron (oxy)(hydr)oxide and establish different modes of contact of uranium, phosphate and Fe(III). Influent Fe(III) concentrations were chosen supersaturated with respect to goethite but undersaturated with respect to ferrihydrite. The presence of goethite on sand enhanced the uptake of dissolved Fe(III). The continuous uptake of Fe(III) indicated either the growth of goethite as Fe(III) precipitated on the surface or heterogeneous nucleation of an iron oxyhydroxide phase leading to the formation of new particles on the goethite surface. In the presence of co-influent Fe(III), the extent and the rate of phosphate uptake on goethite-coated sand increased. The uptake of phosphate was concurrent with Fe(III) uptake (1:1 on molar basis) indicating either surface precipitation of an Fe(III)-phosphate phase on goethite or enhanced phosphate adsorption on the goethite surface poorly crystallized due to Fe(III) uptake. The continuous uptake of Fe(III), however, decreased U(VI) uptake on goethite-coated sand in column experiments and on goethite in CFSTR experiments indicating competitive adsorption of U(VI) and Fe(III). Unlike for phosphate, the Fe(III) uptake did

not seem to create new adsorption sites for U(VI). Elution of goethite-associated uranium with U-free and phosphate-free 0.01 M $NaNO_3$ solution at pH 4 resulted in complete U(VI) desorption, but elution was faster for the condition that had seen the influent Fe(III) during the uptake period indicating that Fe(III) promoted a less stable uranium association with goethite. Only ~23% of the total Fe(III) taken up was remobilized indicating a more stable association of iron with the goethite structure. In comparison, elution with U-free phosphate-containing solution resulted in incomplete and retarded U(VI) desorption. The presence of phosphate probably facilitated the formation of a goethite-associated uranium species that was more stable than the adsorbed uranium species formed in the absence of phosphate. U(VI) desorption was higher when uranium was immobilized in the presence of Fe(III) indicating that Fe(III) during the uptake of uranium not only decreased U(VI) uptake on goethite but also limited the formation of stable phosphate-induced uranium surface species.

References

1. Jerden, J. L.; Sinha, A. K., Phosphate based immobilization of uranium in an oxidizing bedrock aquifer. *Applied Geochemistry* **2003,** *18*, (6), 823-843.
2. Roh, Y.; Lee, S. R.; Choi, S.-K.; Elless, M. P.; Lee, S. Y., Physicochemical and mineralogical characterization of uranium-contaminated soils. *Soil and Sediment Contamination* **2000,** *9*, (5), 463-486.
3. Morris, D. E.; Allen, P. G.; Berg, J. M.; Chisholm-Brause, C. J.; Conradson, S. D.; Donohoe, R. J.; Hess, N. J.; Musgrave, J. A.; Tait, C. D., Speciation of uranium in Fernald soils by molecular spectroscopic methods: characterization of untreated soils. *Environmental Science and Technology* **1996,** *30*, (7), 2322-2331.
4. Buck, E. C.; Brown, N. R.; Dietz, N. L., Contaminant uranium phases and leaching at the Fernald site in Ohio. *Environmental Science and Technology* **1996,** *30*, (1), 81-88.
5. Catalano, J. G.; McKinley, J. P.; Zachara, J. M.; Heald, S. M.; Smith, S. C.; Brown, G. E., Changes in uranium speciation through a depth sequence of contaminated Hanford sediments. *Environmental Science & Technology* **2006,** *40*, (8), 2517-2524.
6. Murakami, T., Ohnuki, T., Isobe, H. and Sato, T., Mobility of uranium during weathering. *American Mineralogist* **1997,** *82*, 888-8999.
7. Murakami, T.; Sato, T.; Ohnuki, T.; Isobe, H., Field evidence for uranium nanocrystallization and its implications for uranium transport. *Chemical Geology* **2005,** *221*, (1-2), 117-126.
8. Sato, T.; Murakami, T.; Yanase, N.; Isobe, H.; Payne, T. E.; Airey, P. L., Iron nodules scavenging uranium from groundwater. *Environmental Science & Technology* **1997,** *31*, (10), 2854-2858.
9. Duff, M. C.; Coughlin, J. U.; Hunter, D. B., Uranium co-precipitation with iron oxide minerals. *Geochimica et Cosmochimica Acta* **2002,** *66*, (20), 3533-3547.
10. Xie, L.; Giammar, D., Influence of Phosphate on Adsorption and Surface Precipitation of Lead on Iron Oxide Surfaces. *Adsorption of metals by geomedia II: variables, mechanisms, and model applications* **2008**, 349.
11. Coston, J.; Fuller, C.; Davis, J., Pb2+ and Zn2+ adsorption by a natural aluminum-and iron-bearing surface coating on an aquifer sand. *Geochimica et Cosmochimica Acta* **1995,** *59*, (17), 3535-3547.
12. Cheng, T.; Barnett, M. O.; Roden, E. E.; Zhuang, J. L., Effects of phosphate on uranium(VI) adsorption to goethite-coated sand. *Environmental Science & Technology* **2004,** *38*, (22), 6059-6065.
13. Gabriel, U.; Gaudet, J. P.; Spadini, L.; Charlet, L., Reactive transport of uranyl in a goethite column: an experimental and modelling study. *Chemical Geology* **1998,** *151*, (1-4), 107-128.
14. Hanshaw, B.; Back, W.; Rubin, M., Radiocarbon determinations for estimating groundwater flow velocities in central Florida. *Science* **1965,** *148*, (3669), 494.
15. Stumm, W.; Morgan, J. J., *Aquatic chemistry*. Third ed.; John Wiley & Sons, Inc.: New York, NY, 1996; p 1022.
16. Arai, Y.; Sparks, D. L., ATR-FTIR spectroscopic investigation on phosphate adsorption mechanisms at the ferrihydrite-water interface. *Journal of Colloid and Interface Science* **2001,** *241*, (2), 317-326.

17. Nilsson, N.; Lovgren, L.; Sjoberg, S., Phosphate Complexation at the Surface of Goethite. *Chemical Speciation and Bioavailability* **1992,** *4*, (4), 121-130.
18. Singh, A.; Ulrich, K.-U.; Giammar, D. E., Impact of phosphate on U(VI) immobilization in the presence of goethite. *Geochimica et Cosmochimica Acta* **2010 (submitted)**.
19. STRAUSS, R.; BRÜMMER, G.; BARROW, N., Effects of crystallinity of goethite: II. Rates of sorption and desorption of phosphate. *European Journal of Soil Science* **1997,** *48*, (1), 101-114.
20. Ler, A.; Stanforth, R., Evidence for surface precipitation of phosphate on goethite. *Environmental Science & Technology* **2003,** *37*, (12), 2694-2700.
21. Cabrera, F.; De Arambarri, P.; Madrid, L.; Toga, C., Desorption of phosphate from iron oxides in relation to equilibrium pH and porosity. *Geoderma* **1981,** *26*, (3), 203-216.
22. Torrent, J.; Barron, V.; Schwertmann, U., Phosphate adsorption and desorption by goethites differing in crystal morphology. *Soil Sci. Soc. Am. J* **1990,** *54*, (4), 1007–1012.
23. Toride, N.; Leij, F. J.; van Genuchten, M. T. *The CXTFIT code for estimating transport parameters from laboratory or field tracer experiments. Version 2.1.*; No. 139; U.S. Salinity Laboratory, Agricultural Research Service, U.S. Department of Agriculture: Riverside, California, April 1999, 1999.

Appendix 5-A: Estimation of column residence time from preliminary tracer studies

The residence time for the goethite-coated and uncoated sand packed columns was estimated by performing K tracer experiments for the uptake and remobilization periods. Effluent K concentrations were modeled to obtain an optimized longitudinal dispersion coefficient and a superficial velocity that was used to calculate the residence time.

Elemental uptake was modeled using the computer program, CXTFIT 2.1 [23]. The program uses equilibrium and non-equilibrium transport models to predict liquid phase concentrations of reactant species based on known parameter values (direct problem). It can also estimate transport parameters by non-linear least squares regression fitting of the observed data to solutions of the convection-dispersion equation (CDE) for unidirectional transport of reactant species (indirect problem).

Equilibrium transport modeling

The CDE for unidirectional transport of a species undergoing simultaneous adsorption, first-order degradation, and zero-order production in a homogeneous medium is given as:

$$R\frac{\partial C_r}{\partial t} = D_L \frac{\partial^2 C_r}{\partial x^2} - v_x \frac{\partial C_r}{\partial x} - \mu C_r + \gamma(x) \qquad (1)$$

where, v_x is the average linear groundwater velocity or pore-water velocity.

R is the retardation factor: $R = 1 + \frac{\rho_b K_d}{\theta}$, where ρ_b is the soil bulk density (kg/cm^3); K_d is the distribution coefficient (L/kg); θ is the porosity of the saturated medium. D_L is the longitudinal dispersion coefficient (cm^2/s), μ and γ are the combined first order degradation and zero-order production rate coefficients, respectively:

$$\mu = \mu_l + \frac{\rho_b K_d \mu_s}{\theta} \qquad \gamma(x) = \gamma_l(x) + \frac{\rho_b \gamma_s(x)}{\theta}$$

where subscript s and l respectively refer to solid and liquid phases.

Case 1a: K-breakthrough curves

For modeling tracer uptake, R was set to 1 and μ and γ were set equal to 0 in eq. 1.

$$\frac{\partial C_r}{\partial t} = D\frac{\partial^2 C_r}{\partial x^2} - v\frac{\partial C_r}{\partial x} \qquad (2)$$

Model predictions to the effluent K data for 3 gcs and 1 ucs packed columns were optimized to obtain D_L and v_x for each of the four columns (Figure 5-A1). Finally, an overall average value was obtained for the two parameters (Table 5-A1).

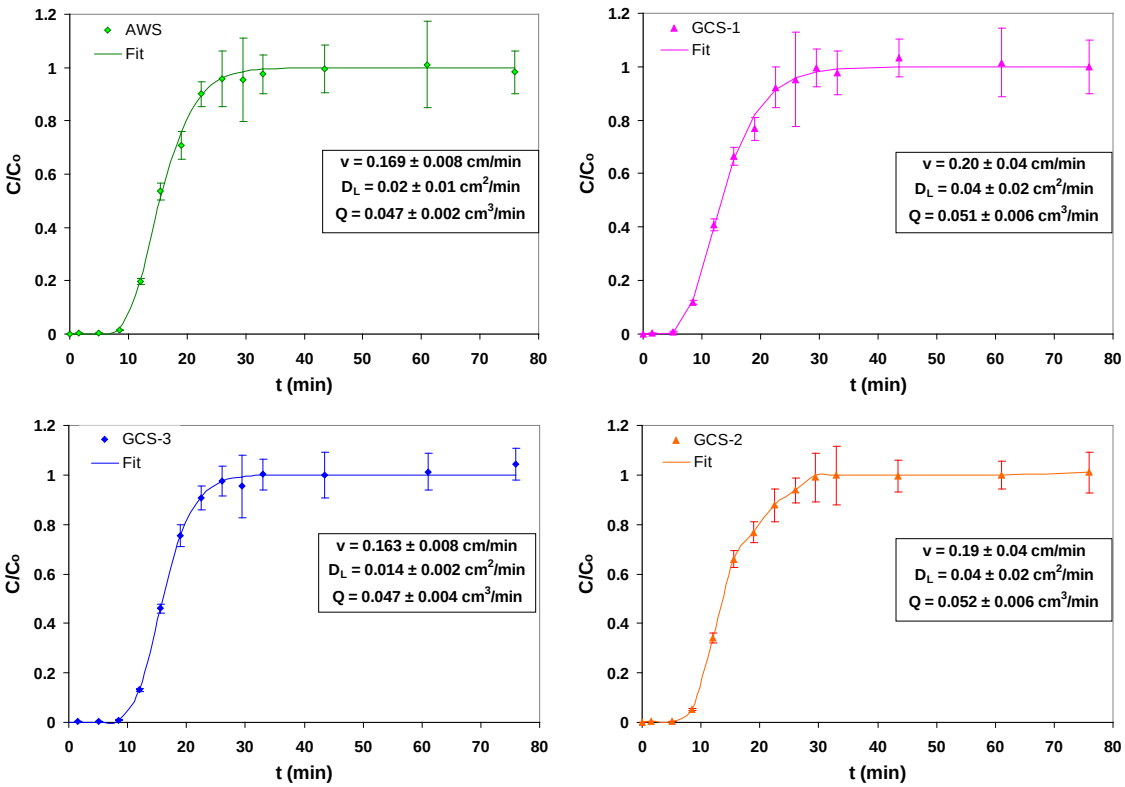

Figure 5-A1 Measured and modeled K effluent concentration profiles for the uptake period. Measured flow rate (Q) specific to each column is also indicated.

Table 5-A1 Optimized parameters for each column and average values

	AWS		GCS-1		GCS-2		GCS-no Fe		Average	95% c.i.
v_x (cm/min)	0.169	0.008	0.20	0.01	0.19	0.01	0.163	0.002	**0.18**	**0.02**
D_L (cm^2/min)	0.02	0.01	0.04	0.02	0.04	0.02	0.014	0.002	**0.03**	**0.02**

Case 1b: K-remobilization curves

For modeling remobilization of K a similar approach as for the uptake period was followed, and optimized D_L and v_x for each of the four columns were obtained (Figure 5-A2). Using these results an overall average value for the two parameters was obtained (Table 5-A1).

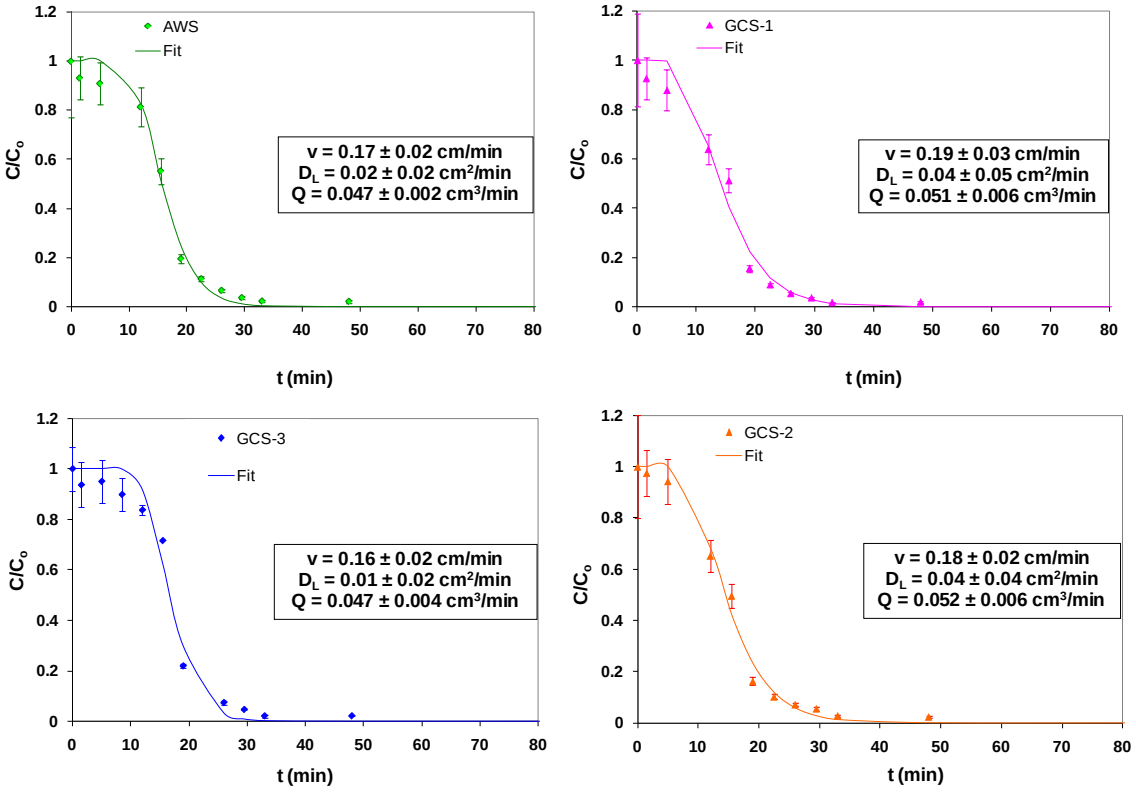

Figure 5-A2 Measured and modeled K effluent concentration profiles for the remobilization period. Measured flow rate (Q) specific to each column is also indicated.

Table 5-A2 Optimized parameters for each column and average values

	AWS		GCS-1		GCS-2		GCS-no Fe		Average	95% c.i.
v_x (cm/min)	0.169	0.008	0.20	0.01	0.19	0.01	0.163	0.002	**0.18**	**0.02**
D_L (cm^2/min)	0.02	0.01	0.04	0.02	0.04	0.02	0.014	0.002	**0.03**	**0.02**

Modeling results for both the uptake and remobilization periods agree very well. While the optimized value of D_L was identical for both periods, estimates for v_x were not significantly different from each other. To estimate column residence time (t_R), an average value of the two optimized v_x estimates was used along with the measured length (L) of these columns.

$$t_R = \frac{L}{v_x} = \frac{2.6\ cm}{\frac{(0.18+0.17)}{2} cm\,\min^{-1}} \approx 15\,\min.$$

Appendix 5-B: Estimation of mass taken up and remobilized from measured effluent packed column data

Typical effluent concentration profiles from a packed column during the uptake and remobilization periods (Figure 5-B1) are used to demonstrate the approach used to estimate the mass uptake and remobilization of a particular species.

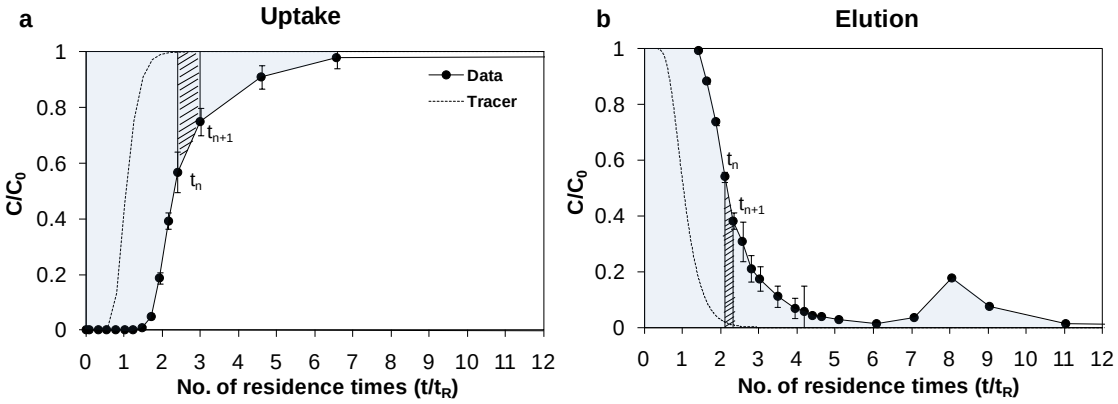

Figure 5-B1. Mass uptake calculations from measured effluent concentrations from a packed column during a) uptake and b) remobilization periods. The data shown is a typical representative data. Shaded regions indicate areas for uptake and remobilization. Calculations involve summation of successive trapeziums. C and C_0 are the measured effluent and influent concentrations, respectively.

For the uptake period, elemental liquid-phase mass balance can be written as:

$$mass_{uptake} = mass_{in} - mass_{out} - mass_{accumulated} \quad (1)$$

Neglecting the accumulation of mass in the liquid hold-up of the packed column with respect to the total volume of water passing through the column, eq. 1 can be written as:

$$mass_{uptake} = mass_{in} - mass_{out} = \int_{C_i}^{C_f} (C_0 - C)\frac{moles}{vol} \bullet elemental\ volume\ of\ water \quad (2)$$

$$= \int_0^T (C_0 - C) \bullet Q \bullet dt = Q\ C_0 \frac{t_R}{t_R} \int_0^T (1 - \frac{C}{C_0}) dt = Q\ C_0 t_R \int_0^T (1 - \frac{C}{C_0}) d(\frac{t}{t_R})$$

$$= Q\ C_0 t_R \bullet (shaded\ \ area\ \ in\ \ Figure\ \ 5-B1a) \tag{3}$$

For the remobilization period, since there is no incoming mass and neglecting mass in liquid hold-up, eq. 1 can be written as:

$$mass_{remob} = mass_{out} = \int_{C_i}^{C_f} (C) \frac{moles}{vol} \bullet elemental\ \ volume\ \ of\ \ water \tag{4}$$

$$= Q\ C_0 t_R \int_0^T \frac{C}{C_0} d(\frac{t}{t_R}) \ = \ Q\ C_0 t_R \bullet (shaded\ \ area\ \ in\ \ Figure\ \ 5-B1b) \tag{5}$$

Chapter 6 Conclusion

6.1. Summary of Dissertation

Injection of soluble phosphate compounds to uranium-contaminated subsurface zones could be an effective remediation strategy. If sufficient phosphate is added to overcome the adsorptive capacity of the soils, then uranium uptake could be enhanced by formation of U(VI)-phosphate-iron oxide ternary surface complexes for low uranium concentrations and by precipitation of U(VI)-phosphates at higher uranium concentrations. The overall objectives of the research were 1) to investigate phosphate-induced immobilization mechanisms of the environmental contaminant uranium at the iron (oxy)(hydr)oxide-water interface over multiple length and time scales, and 2) to relate the rates of uranium transport in phosphate-amended iron oxide-rich sediments to mechanisms of uranium immobilization and release.

First, the effects of geochemical conditions of total U(VI) and phosphate, the presence or absence of goethite, and reaction time on the extent and mechanism of U(VI) uptake were investigated. Dissolved U(VI) and phosphate concentrations were interpreted within a reaction-based modeling framework that included dissolution-precipitation reactions and a surface complexation model to account for adsorption. The batch experiments and associated modeling of equilibrium adsorption and precipitation provided information on the impacts of phosphate on uranium immobilization both in the presence and absence of goethite. Precipitation of uranium phosphates in the presence of goethite was the dominant mechanism at high total uranium (50 - 100 μM) and high total phosphate (130 μM) concentrations. Homogeneous nucleation of chernikovite,

$UO_2HPO_4 \cdot 4H_2O_{(s)}$, occurred rapidly for initially supersaturated suspensions both with and without goethite, although equilibrium calculations predicted uranium orthophosphate, $(UO_2)_3(PO_4)_2 \cdot 4H_2O_{(s)}$, as the most stable phase. Adsorption was the dominant mechanism for low total phosphate conditions (≤15 μM) for most total uranium concentrations, except at 100 μM when heterogeneous nucleation of a uranium phosphate phase on the goethite surface was observed. Adsorption was also dominant at conditions when total phosphate (130 μM) was in large excess of the total uranium (1 - 10 μM). The observed simultaneous uranium and phosphate uptake could be due to the formation of a U(VI)-phosphate-Fe(III)oxide ternary surface complex. Depending on the total adsorption sites available and total uranium concentrations, a critical phosphate concentration (between 15 - 130 μM in this study) must be met to achieve preferential uranium phosphate precipitation over adsorption. The goethite surface acts as a sink for dissolved phosphate, limiting the formation of uranium phosphates and resulting in higher dissolved U(VI) concentrations than would be attainable in goethite-free suspensions for high total uranium concentrations (50 - 100 μM).

Results from goethite-free conditions indicated that U(VI)-phosphate solids nucleated rapidly and gradually transformed from chernikovite to another phase over a period of 1 year. The molar U/P uptake ratio decreased with time for conditions when total phosphate was in excess of total U(VI), which indicated preferential phosphate uptake on the initially nucleated chernikovite phase; the U/P uptake ratio increased when total U(VI) was in excess of total phosphate. The combination of systematic experiments that analyzed both solutions and solids with updated geochemical equilibrium models was essential to identifying the effects of geochemical composition and time on the rates

and mechanisms of U(VI) removal from solution.

Second, molecular-scale structures of uranium immobilized by adsorption and precipitation mechanisms were identified and related to macroscopic uptake of uranium. XAFS spectroscopy was used to probe the coordination environment of uranium for different total U(VI) concentrations over a pH range of 4-7 in the absence and presence of phosphate. For a fixed total uranium concentration (10 µM), U(VI) uptake in the presence of phosphate occurred by adsorption at pH 4 and by precipitation at pH 6-7. EXAFS analysis revealed that the structure of precipitated U(VI) fit the sodium meta-autunite structure. In the absence of phosphate, EXAFS spectra of adsorbed U(VI) for low to circum-neutral pH (4-7) conditions indicated the presence of bidentate edge-sharing, $\equiv Fe(OH)_2UO_2$, and bidentate corner-sharing $(\equiv FeOH)_2UO_2$, surface complexes. In the presence of phosphate, U(VI) existed in precipitated and adsorbed forms. The relative amounts of these U(VI) forms were quantified using linear combinations of the goethite-free precipitated U(VI)-phosphate and phosphate-free adsorbed U(VI) end member spectra, and depended on the total uranium and pH. For low total uranium conditions at pH 4, the EXAFS spectra indicated that uranium adsorbed to the goethite surface as a ternary surface complex involving uranium, phosphate and iron. The ternary surface complex could be written as $(\equiv FeO)_2UO_2PO_4$ where UO_2^{2+} was the bridging molecule between phosphate and corner-sharing iron octahedra.

Third, the effect of phosphate on the rates and mechanisms of U(VI) uptake and remobilization under flowing-conditions was examined. Continuous-flow stirred tank reactor (CFSTR) experiments at pH 4 were conducted under conditions that were supersaturated and undersaturated with respect to chernikovite. The experiments were

interpreted using a combination of macroscopic measurements of dissolved concentrations, microscopy, and XAFS spectroscopy. The rates of dominant U(VI) and phosphate uptake and remobilization mechanisms were quantified using a flow-through reactor model. For undersaturated conditions, U(VI) adsorption and desorption in the absence of phosphate were determined by equilibrium. U(VI) uptake was enhanced in the presence of phosphate. Rapid phosphate uptake occurred predominantly by the formation of a binary surface complex until the goethite surface was saturated. The adsorption of phosphate made uranium adsorption more favorable through the formation of the $(\equiv FeO)_2UO_2PO_4$ surface complex. While the rate constants of formation (0.014-0.1 min^{-1}) of the phosphate binary surface complex was much higher than its remobilization rate constant ($2.91*10^{-4}$ min^{-1}), the rate constants of formation ($1.29*10^{-3}$-$1.82*10^{-2}$ min^{-1}) and remobilization ($1.49*10^{-3}$ min^{-1}) of the $(\equiv FeO)_2UO_2PO_4$ complex were similar. Although it took longer to immobilize uranium as the $(\equiv FeO)_2UO_2PO_4$ complex than to immobilize phosphate as the binary surface complex, the remobilization of the $(\equiv FeO)_2UO_2PO_4$ complex was faster.

For conditions that were supersaturated with respect to chernikovite, the presence of phosphate enhanced uranium(VI) uptake both in the absence and presence of goethite by precipitation of chernikovite. In the absence of goethite, the critical saturation ratio (Ω = 1.23) for the nucleation of chernikovite and the rate constant of chernikovite precipitation ($4.1\text{-}4.2*10^{-9}$ $mol/m^2.s$) were estimated. Remobilization of U(VI) and phosphate for these conditions was limited by the dissolution kinetics ($1.4*10^{-9}$ $mol/m^2.s$) of chernikovite. Furthermore, the dissolution of chernikovite was non-stoichiometric, which indicates that the remaining chernikovite was gradually transforming into a new

phase with a molar ratio of U/P > 1. A significant fraction of the precipitated chernikovite in the absence and presence of goethite was colloidal in nature. Overall, the extent of U(VI) immobilization via precipitation is likely to exceed immobilization via adsorption by the $(\equiv FeO)_2UO_2PO_4$ complex. Moreover, the formation of the ternary surface complex was found to be rapidly reversible when conditions changed to U-free solutions. The dissolution rate constant of chernikovite, on the other hand, was ~3 times slower than its rate constant for formation.

Finally, the effects of Fe(III) uptake on goethite on simultaneous U(VI) uptake and remobilization were investigated at pH 4. Goethite-coated sand packed columns and goethite-containing CFSTRs were used to simulate environmental conditions favoring the growth of goethite and establish different modes of contact of uranium, phosphate and Fe(III). The presence of goethite on sand enhanced the uptake of dissolved Fe(III). The continuous uptake of Fe(III) indicated either the growth of goethite as Fe(III) precipitated on the surface or heterogeneous nucleation of an iron oxyhydroxide phase led the formation of a new phase on the goethite surface. Only ~23% of the total Fe(III) taken up was remobilized with an Fe(III)-free solution indicating a stable association of iron with the goethite structure. In the presence of co-influent Fe(III), the extent and the rate of phosphate uptake on goethite-coated sand increased. The uptake of phosphate was concurrent with Fe(III) uptake (1:1 on molar basis) indicating either surface precipitation of an Fe(III)-phosphate phase on goethite or enhanced phosphate adsorption on the goethite surface gradually turning poorly crystalline due to Fe(III) uptake. The continuous uptake of Fe(III), however, decreased U(VI) uptake on goethite-coated sand in column experiments and on goethite in CFSTR experiments, which suggested

competitive adsorption of U(VI) and Fe(III). Unlike for phosphate, the Fe(III) uptake did not seem to create new adsorption sites for U(VI).

Elution of goethite-associated uranium with U-free, phosphate-free, and Fe(III)-free solution at pH 4 resulted in complete U(VI) desorption, but elution was faster for the condition that had seen the influent Fe(III) during the uptake period, indicating that Fe(III) promoted a less stable uranium association with goethite. In comparison, elution with U-free phosphate-containing solution resulted in incomplete and retarded U(VI) desorption. The presence of phosphate probably facilitated the formation of a goethite-associated uranium species that was more stable than the adsorbed uranium species formed in the absence of phosphate. U(VI) desorption was higher when uranium was immobilized in the presence of Fe(III) indicating that Fe(III) during the uptake of uranium not only decreased U(VI) uptake on goethite but also limited the formation of stable phosphate-induced uranium surface species.

6.2. Recommendations for Future Work

To predict the long-term stability of uranium immobilized following phosphate addition, information on uptake and release mechanisms and rates across the entire range of environmentally relevant pH conditions is warranted. Immobilized uranium in contaminated zones can be subjected to changes in solution chemistry such as pH, temperature, and alkalinity. A particular immobilization strategy that successfully limited uranium release at low pH conditions may not work at higher pH. The work presented in this dissertation primarily focused on low pH conditions. The critical results from this study could be tested against higher pH conditions (6-9) for the batch, flow-

through and column experiments. At higher pH, carbonate complexation would be a dominant reaction pathway that could impact U(VI) immobilization with phosphate. Furthermore, batch equilibration studies at pH 4 indicated that a critical phosphate concentration between 15 and 130 µM was needed to achieve preferential uranium phosphate precipitation over adsorption. By selecting different phosphate concentrations and pH, this range could be constrained further.

The molecular-scale information obtained from the work presented in Chapter 3 could be integrated with the equilibrium speciation model presented in Chapter 2. The current model considers uranium adsorption to goethite surface in the absence of phosphate as an edge-sharing binary surface complex [$\equiv FeO_2UO_2$] and adsorption in the presence of phosphate as an edge-sharing ternary surface complex. U(VI) adsorption data from our experiments in the absence of phosphate was underpredicted and adsorption in the presence of phosphate was overpredicted at high total uranium conditions by this model. The surface complexation model could be refined by including both the edge-sharing and the corner-sharing [$(\equiv FeO)_2UO_2$] surface complexes for uranium adsorption in the absence of phosphate and by rewriting the ternary surface complexation reaction based on the $(\equiv FeO)_2UO_2PO_4$ complex. The updated model could be further evaluated against data from studies at higher pH just proposed.

The structural model for the U(VI)-phosphate-Fe(III)oxide ternary surface complex proposed in this work (Chapter 3) could be further developed. For conditions favoring U(VI) adsorption experiments could be performed at different geochemical conditions of total uranium, total phosphate, pH, and ionic strength, and adsorbed mineral. Wet chemical analysis can be combined with ATR-FTIR and XAFS to

determine the structure of the ternary surface complexes for the varying geochemical conditions. A longer range XAFS data (up to k of 15 $Å^{-1}$) could be helpful in resolving the structure better.

The chernikovite precipitation and dissolution rate constants determined in the CFSTR experimental and modeling study (Chapter 4) indirectly depend on the assumption of an interfacial free energy value for chernikovite. This energy is required to estimate the critical size of nuclei forming at the onset of precipitation. Future work could focus on determining chernikovite interfacial free energy experimentally.

From column studies on the effect of simultaneous Fe(III) uptake on goethite on U(VI) and phosphate uptake, the speciation of the Fe(III) taken up by goethite-coated sand could not be determined (Chapter 5). Advanced studies combining different isotopes of Fe (56 and 57) and Mössbauer spectroscopy, highres-TEM, ATR-FTIR could be helpful in identifying the mechanisms of Fe(III) uptake. Likewise, such studies could also be helpful in identifying the mechanisms for the concurrent 1:1 uptake of iron and phosphate and the decrease in U(VI) uptake in the presence of Fe(III). Furthermore, U(VI)-loaded columns when remobilized with phosphate indicated the presence of a more stable goethite-associated uranium surface species that eluted more slowly than the bulk of the desorbing uranium. It would be interesting to perform these experiments with different concentrations of influent phosphate and analyze the changes in the time and concentration of this secondary eluted species. A critical phosphate concentration could be identified when the secondary elution peak was no longer significant.

To further evaluate how the different immobilization mechanisms identified in this study affected uranium release rates due to changes in solution chemistry, isotope

exchange experiments could be performed. This technique can be used to determine the proportion of solid-associated uranium that is exchangeable with the dissolved phase at close-to-equilibrium conditions. Pre-equilibrated goethite suspensions containing depleted uranium (^{238}U) of known concentration can be spiked with small aliquots of a pure isotope of uranium (like ^{233}U). Changes in isotopic composition of the dissolved phase could be monitored with time until a dynamic equilibrium is reached. The final isotope ratio when compared to the total uranium ratio, which is known at the start of the experiment, gives an indication of the proportion of goethite-associated uranium that can exchange with the dissolved phase. Also, the time-dependent change in isotopic composition of the dissolved phase could be a measure of the rate of exchange of uranium between the two phases. This technique could be used to compare exchange rates of precipitated uranium with adsorbed uranium, and of the adsorbed uranium in the presence of phosphate with adsorbed uranium in the absence of phosphate.

One of the future tasks could be to relate this work to the field-scale. U-contaminated and uncontaminated sediments from an actual field site could be obtained and characterized for its mineral content, including iron oxides. Batch, continuous-flow and column experiments could be performed using these sediments and the results compared to simpler systems such as this work. Thereafter, these mechanistic studies could be tested at an actual site such as Hanford, where phosphate-based U immobilization field-scale demonstration tests are being conducted. Importantly, the reactions and rate parameters derived from this study could be integrated into a reactive transport model being used to predict U fate in subsurface zones.

The effects of microbiology on U(VI)-phosphate-iron oxide interactions can be

explored. In several subsurface environments, microbes play a dominant role in nutrient cycling, including U and Fe, and may utilize phosphate for their metabolism. It would be interesting to see how U(VI)-phosphate precipitation and adsorption on goethite are affected by some of the prevalent microbial communities. Such interactions could be investigated with signature microbial species relevant for both oxidizing as well as reducing conditions. For example, the effect of phosphate on U(VI) reduction by Fe(II) adsorbed to Fe(III) oxyhydroxides could be investigated in the presence and absence of microbes.

Curriculum Vita of Abhas Singh

Department of Energy, Environmental and Chemical Engineering
Washington University in Saint Louis • Campus Box 1180 • One Brookings Drive
St. Louis, MO 63130 • Email: abhas.singh@wustl.edu

Education

Ph.D. in Energy, Environmental and Chemical Engineering — August 2010
Washington University in Saint Louis. Advisor: Dr. Daniel Giammar — G.P.A. 3.93/4.0

Ph.D. coursework in Chemical Engineering — 2004-2005
Indian Institute of Technology (IIT) Bombay, India. — G.P.A. 9.5/10

B.Tech. in Chemical Engineering — 1995-1999
Indian Institute of Technology (IIT) Bombay, India. — G.P.A. 8.3/10

Research Experience

Dissertation titled, *'Geochemical conditions affecting uranium(VI) fate and transport in soil and groundwater in the presence of phosphate'* — Oct 2006 – June 2010

- Determined factors affecting macroscopic uranium uptake mechanisms in uranium(VI)-phosphate-Fe(III) oxide systems under batch conditions.
- Studied molecular-scale effects of phosphate on uranium(VI) interactions with goethite using XAFS.
- Investigated uranium(VI) incorporation mechanisms under dynamic conditions of iron (oxy)hydroxide growth and transport using goethite-coated sand packed columns and flow-through reactors.
- Related uranium remobilization rates to immobilization mechanisms.

Synthesis of abiotic uraninite — May 2006 - Sep 2006

- Installed and operationalized apparatus for creating reducing environment in the glove-box for abiotic synthesis of uraninite.

Research rotation experiences: — Sep 2005 - Apr 2006

- Methane production by anaerobic digestion of corn-to-ethanol waste
  Procured, installed, and operationalized gas-leak free digester assembly.
- Reductive dechlorination of TCE by Fe(II) sorbed onto iron oxide surfaces
  Conducted time series experiments to account for adsorption of Fe(II) on goethite.
  Analyzed vapor phase TCE concentrations by gas chromatography.

Analytical Techniques Used

X-ray Absorption Spectroscopy (XANES and XAFS), X-ray Diffraction (XRD), Scanning Electron Microscopy (SEM), Inductively Coupled Plasma Mass Spectrometry (ICP-MS), Transmission Electron Microscopy (TEM), Attenuated Total Reflection Fourier Transform Infrared (ATR-FTIR) Spectroscopy, Gas Chromatography (GC), Particle Size and Zeta-Potential Measurements, BET Surface Area Analysis.

Professional Experience

Quality Control Officer at Indian Oil Corporation Limited Sep 1999 - Feb 2002

- Benchmarked product formulations and commissioned production of specialty lube chemicals.
- Tested and certified raw materials and products manufactured.

Publications

- Zeng H., Singh A., Basak, S., Ulrich K.U., Sahu, M., Biswas P., Catalano J.G., and Giammar, D.E. (2009) Nanoscale size effects on uranium(VI) adsorption to hematite. *Environmental Science & Technology* **43**(5), 1373-1378.
- Ulrich K.U., Singh A., Schofield, E.J., Bargar, J.R., Veeramani, H., Sharp, J., Bernier-Latmani, R., and Giammar, D.E. (2008) Dissolution of biogenic and synthetic UO_2 under varied reducing conditions. *Environmental Science & Technology* **42**(15), 5600-5606.

(pending)

- Singh A., Ulrich K.U., and Giammar, D.E. (2010) Impact of phosphate on U(VI) immobilization in the presence of goethite (in review *Geochimica et Cosmochimica Acta*).
- Singh A. and Giammar, D.E. (2010) Effect of phosphate on uranium(VI) uptake and remobilization under flow conditions in the presence of goethite (in preparation for submission to *Environmental Science & Technology*).

Selected Presentations

- Singh A., Ulrich K.U., Catalano, J.G., and Giammar, D.E. (2009) Effect of phosphate on uranium(VI) immobilization in the presence of iron(III) (oxy)hydroxides. Poster presentation, Migration Conference, 12th International Conference on the Chemistry and Migration Behavior of Actinides and Fission Products in the Geosphere, Kennewick, WA.
- Singh A., Ulrich K.U., Catalano, J.G., and Giammar, D.E. (2009) Effect of phosphate on uranium fate and transport in soil and groundwater. Oral presentation, AEESP Conference, Iowa City, IA.
- Singh A., Ulrich K.U., Catalano, J.G., and Giammar, D.E. (2009) Uranium(VI) - phosphate interactions in the presence of goethite. Poster presentation, 4th annual DOE-ERSP PI Meeting, Lansdowne, VA.
- Singh A., Ulrich K.U., Catalano, J.G., and Giammar, D.E. (2009) Multiscale uranium(VI) - phosphate interactions in the presence of goethite. Oral presentation, Spring ACS National Meeting, Salt Lake City, UT.
- Singh A., Ulrich K.U., Catalano, J.G., and Giammar, D.E. (2008) Uranium(VI)-phosphate interactions at the goethite-water interface. Poster presentation, Goldschmidt Conference, Vancouver, Canada.
- Singh A., Ulrich K.U., Catalano, J.G., and Giammar, D.E. (2008) Uranium(VI)-phosphate interactions at the goethite-water interface. Poster presentation, Environmental Sciences: Water, Gordon Research Conference, Holderness, NH.

- Singh A., Ulrich K.U., and Giammar, D.E. (2007) Adsorption and surface precipitation of uranyl phosphate on goethite. Oral presentation, Mid-American Environmental Engineering Conference, University of Missouri, Columbia, MO.
- Singh A., Ulrich K.U., and Giammar, D.E. (2007) Adsorption and surface precipitation of uranyl phosphate on goethite. Poster presentation, Spring ACS National Meeting, Chicago, IL.

Proposal Accepted

'An XAFS study of the effect of phosphate on uranium immobilization mechanisms in uranium(VI)-phosphate-iron(III) oxide systems', Advanced Photon Source, Chicago. 2009 - 2010

Teaching Experience

- Guest Lecturer, Environmental Chemistry Fall 2009
  Gave two guest lectures on Sorption Processes.
- Teaching Assistant, Introduction to Environmental Engineering Spring 2008
  Held weekly help sessions; assisted with development of a problem set and final exam; graded weekly course assignment; gave a guest lecture.
  Avg. rating on TA effectiveness: 6.0/ 7.0
- Teaching Assistant, Environmental Chemistry Fall 2008
  Held weekly office hours and an end-semester review session; graded weekly course assignments and part of final exam; gave two guest lectures.
  Avg. rating on TA effectiveness: 6.25/ 7.0

Other Leadership Experience

- Chair, Faculty Search Student Committee Spring 2009
- Mentor, Ph.D. research rotation student Spring 2009
- Treasurer, Environmental Eng. Students Association, Wash. U. 2007 - 2008
- Secretary, WEF Student Chapter, Wash. U 2006 – 2007

Honors/ Awards

- Student Travel Fellowship, 4th Annual DOE-ERSP PI meeting, Lansdowne, VA 2009
- The ENVIRSAN Scholarship 2005 – 2006
- National Talent Search Scholarship (India) 1993 – 1999

Professional Affiliations

- American Chemical Society (ACS) 2007 - Present
- Water Environment Federation (WEF) 12/2005 - 02/2009